Physics of Earth and Space Environments

Vladimir Bychkov
Gennady Golubkov
Anatoly Nikitin *Editors*

The Atmosphere and Ionosphere

Elementary Processes, Discharges and Plasmoids

Springer

The Atmosphere and Ionosphere

Physics of Earth and Space Environments

The series *Physics of Earth and Space Environments* is devoted to monograph texts dealing with all aspects of atmospheric, hydrospheric and space science research and advanced teaching. The presentations will be both qualitative as well as quantitative, with strong emphasis on the underlying (geo)physical sciences. Of particular interest are

- contributions which relate fundamental research in the aforementioned fields to present and developing environmental issues viewed broadly
- concise accounts of newly emerging important topics that are embedded in a broader framework in order to provide quick but readable access of new material to a larger audience

The books forming this collection will be of importance for graduate students and active researchers alike.

Vladimir Bychkov • Gennady Golubkov
Anatoly Nikitin
Editors

The Atmosphere and Ionosphere

Elementary Processes, Discharges and Plasmoids

With 115 Figures and 11 Tables

Springer

Editors
Vladimir Bychkov
Lomonosov Moscow
State University
Moscow, Russia

Gennady Golubkov
Semenov Institute of Chemical Physics
Moscow, Russia

Anatoly Nikitin
Institute of Energy Problems of Chemical
Physics
Moscow, Russia

ISSN 1610-1677 ISSN 1865-0678 (electronic)
ISBN 978-94-007-2913-1 e-ISBN 978-94-007-2914-8 (eBook)
DOI 10.1007/978-94-007-2914-8
Springer Dordrecht Heidelberg New York London

Library of Congress Control Number: 2012937225

Printed on acid-free paper

Springer is part of Springer Science+Business Media (www.springer.com)

Contents

Contributors

N.N. Bezuglov Physical Department, St. Petersburg State University, St. Petersburg, Russia

M. Förster Helmholtz Centre Potsdam, GFZ German Research Centre for Geosciences, Telegrafenberg, Potsdam, Germany

Gennady V. Golubkov Semenov Institute of Chemical Physics, Russian Academy of Sciences, Moscow, Russia

K.V. Khodataev FSUE "Moscow Radiotechnical Institute of RAS" (MRTI), Moscow, Russia

A.I. Klimov Joint Institute for High Temperature, Russian Academy of Sciences, Moscow, Russia

A.N. Klyucharev Physical Department, St. Petersburg State University, St. Petersburg, Russia

A.A. Lushnikov Karpov Institute of Physical Chemistry, Moscow, Russia

A.A. Namgaladze Murmansk State Technical University, Murmansk, Russia

B.E. Prokhorov Helmholtz Centre Potsdam, GFZ German Research Centre for Geosciences, Telegrafenberg, Potsdam, Germany

Applied Mathematics, Interdisciplinary Center for Dynamics of Complex Systems (DYCOS), University Potsdam, Potsdam, Germany

O.V. Zolotov Murmansk State Technical University, Murmansk, Russia

Introduction

In Zelenogradsk, a cozy resort on the coast of the Baltic Sea near Kaliningrad (Russia) city, the 2nd International Conference, "Atmosphere, Ionosphere, Safety" (AIS-2010) took place from June 21 until June 27, 2010. The conference was organized by the State Russian University of I. Kant Institute, Semenov Chemical Physics Institute of the Russian Academy of Sciences and the Pushkov Institute of Terrestrial Magnetism and Radio-waves Propagation of the Russian Academy of Sciences. Financial support was provided by the Russian Fund of Basic Researches, the Presidium of the Russian Academy of Sciences, and the European Office of Aerospace Research & Development (EOARD). Scientists who participated in the conference work were from Russia, Belarus, Ukraine, the United States, Germany, Great Britain, the Netherlands, Belgium, Switzerland, and Japan. During the conference, 12 plenary and more than 60 section reports were delivered, and about 30 posters were presented.

The analysis of reactions in the "atmosphere–ionosphere" system, taking into account the influence of natural and anthropogenic processes, was the central question presented for discussion by the conference participants. Basic attention was given to studying the reasons and cases of the various geophysical and atmospheric phenomena, an estimation of their influence on the biosphere of the Earth and its technological systems, and to development of monitoring systems and decrease in risk of the negative influence of natural processes on mankind's ability to live. These problems are of interest for a wide range of experts working in various areas of science and technology.

The ionosphere of the Earth is subject to powerful natural influences. Its lower part is disturbed by earthquakes, volcanic eruptions, typhoons, and thunderstorms. From above it is influenced by a set of processes essential for geomagnetic storms. As a result of these processes, such influencing factors as powerful atmospheric disturbances, electric currents, electromagnetic disturbances in various spectral ranges, plasma and optical disturbances, accelerated particles, raised levels of radioactivity, and changed ionic and molecular composition are formed. Moreover, the microwave radiation of highly excited ionosphere particles, accompanying increases of solar activity and occurrences of magnetic storms, has a negative influence on the biosphere of the Earth.

Knowledge of the influencing factors of nature allows us to use them as catastrophic process indicators and to create corresponding monitoring systems on this basis. Thus, there is a requirement to undertake additional research, which necessity is defined by the considerable strengthening of people's ability to live in an ionosphere, leading to the occurrence of new risks. Such are connected with the active development of manned and unmanned orbital systems, and aviation (including the middle atmosphere height), using new kinds of communication.

The Conference's work was carried out in the following directions.

Elementary Processes in the Upper Atmosphere and Ionosphere

During this section, the possibilities of laser control by one of the major atmospheric processes, that is, the dissociative recombination reaction of slow electrons and molecular ions of oxygen, which under certain conditions can be accelerated (or slowed down) by two to three orders of magnitude under the influence of an external field, have been analyzed.

Features of the nonequilibrium microwave radiation spectrum of the upper atmosphere disturbed by electron beams thrown out of the ionosphere during solar activity were discussed.

A report devoted to consideration of the mechanisms of collision and radiating quenching of Rydberg atoms and molecules populating the F-, T-, and D-layers of the upper atmosphere under the influence of these electrons was heard.

The analysis of basic elementary processes proceeding in the lower atmosphere (electron collision ionization of molecule bombardment, electron dissociative attachment, etc.) considered taking into account the influence of atmospheric electricity, and prebreakdown fields.

Explanation of the nature of luminescent layers in the stratosphere ("elfs" and "sprites") during thunderstorm activity that were observed from the satellites "Tatyana-1" and "Tatyana-2", moving at a height of about 850 km, was discussed.

A method of electron wave functions of the system "Rydberg atom + a neutral particle of the environment" was presented. Mechanisms and methods of collision and radiating quenching of the Rydberg atoms process calculations in the upper atmosphere were considered.

Ionosphere Dynamics and Atmosphere–Ionosphere Coupling

The subjects of these reports concerned actual problems of experimental and theoretical research on the ionosphere and the upper atmosphere. Discussion included existing theoretical models of the upper atmosphere and the ionosphere for application possibilities, in particular, the UAM (upper atmosphere model) for

interpretation of the results of experimental research, and also the direction of perfection of theoretical approaches. Much attention was given to a discussion of electrodynamic mechanisms of local ionosphere precursors of earthquake formation and the concept of "global electric circuit."

Also, the results of joint research of MSTU (Russia) and GRCG (Germany) on the analysis of wind satellite measurements in the high-altitude thermosphere with the application of a theoretical model of the upper atmosphere (UAM) were presented. Analysis has shown, in both satellite observations and theoretical calculations, that the basic influence on the morphology and dynamics of thermosphere circulation in high latitudes is the impact of the solar wind.

A discussion of results of planetary distribution of the total electron content (TEC) in the atmosphere studied during geomagnetic disturbances and after their termination was presented. It appears that for an explanation of the observable ionosphere dynamics during such periods it is necessary to involve ionospheric physicists in a new class of planetary wave processes, – Poincare's waves.

A new mechanism of a phase delay of satellite signals during the periods of strong geomagnetic disturbances that is caused by the cascade of re-radiations at the Rydberg states of atoms and molecules in the decimeter range, excited by streams of ionosphere electrons, was discussed.

Considerable space in this section's work was given to discussion of theoretical models of different ionosphere areas: the three-dimensional model of "a polar wind," realized with the help of the supercomputer Kant RSU. Also, a one-dimensional model of the ionosphere taking into account a complex set of the photochemical processes developing in the D-area of the ionosphere was considered.

Modeling description of the process of internal gravitational wave propagation from the troposphere to the upper atmosphere was presented. Such research is important to understand the physical mechanisms of the influence of the lower atmosphere on the upper atmosphere and the ionosphere. The results obtained show the possibility of fast (within several minutes) penetration of such waves to the heights of the thermosphere and the influence of this process on upper atmosphere dynamics.

A model of tropical hurricanes, allowing defining the important physical characteristics—the time of the origin and duration of the hurricane, and also its speed of movement—was described. The knowledge of such parameters will allow investigating the influence of large-scale meteorological processes on the dynamics of the upper atmosphere and the ionosphere.

Results of modeling research on the mechanisms of the ionosphere precursors of earthquakes executed within the limits of the theoretical model GSM TIP were discussed. The most effective mechanisms of influence of local disturbances over the earthquake epicenter on parameters of the ionosphere plasmas have been considered, and the conclusion is drawn that the most probable reasons for the occurrence of ionosphere precursors are the disturbance of electric field vertical components and the propagation of short-period internal gravitational waves generated over the epicenter.

The problem of the excited particles, or "hot oxygen" formation, observed in the upper atmosphere was discussed. The results of modeling calculations give us the basis to understand that the schemes of description of the photochemical processes with participation of the excited particles do not now allow us to satisfactorily explain the results of experiments.

Characteristics of longitudinal variations of the ionosphere at the middle latitudes, obtained by observations of the satellite Interkosmos-19, were presented and discussed.

The Lomonosov MSU, Moscow, has presented results of optical and UV radiation observations, and also of streams of high-energy electrons obtained by the satellite "University Tatyana-2." The preliminary analysis has shown high correlation of UV and optical radiation in pulsations with duration of about 1 ms. It has been thus established that a correlation between the streams of high-energy electrons and UV or optical radiations is absent. It is noticed also that splashes in radiations are marked over cloudy sites of the Earth surface.

Although concentrations of aerosol particles in the atmosphere of the Earth are insignificant, it is however impossible to consider their influence on atmospheric conditions as negligibly small. It is enough to recollect the dramatic consequences of the "Eyjafjallajokull" volcanic eruption to Iceland and the smoke blanketing of the air of Central Russia and Siberia by summer fires. All these dramatic consequences grow from the influence of aerosol particles on the conditions of the air environment. There are no doubts that struggle against aerosol particles is one of the central foci of safe maintenance of the existence of all lives on Earth. Meanwhile, data on aerosol particles, the mechanisms of their occurrence, and their interaction with the environment and living organisms have remained unreliable until the present time.

Mechanisms of particle charging were discussed. This problem is important for safety maintenance during emergencies of atomic power stations and other nuclear power objects. The majority of radioactive aerosols are charged. The charged aerosols are also important in aerosol technology because motion of these particles can be controlled by means of external electromagnetic fields. The properties of carbon particles formed in the combustion process in airplane engines were also considered.

Electrochemical and Electromagnetic Phenomena in the Atmosphere Including Long-Lived and Plasma Objects

This section of the 2-nd International Symposium (AIS-2010) included Ball Lightning (ISBL-151) and the 4th International Symposium on Unconventional Plasmas (ISUP-4).

Work on these subjects that appeared during the past 2 years was reviewed. It has been noted that the practice of carrying out joint conferences on plasmoids, plasma structures, ball lightning, and unusual kinds of plasmas appears successful. Within the 2 years that have passed since the previous conference, intensive research

on plasmoid physics plasma structures and BL was conducted, and experiments on realization of long-living plasma formations were made.

An activity shift was outlined in BL research to studying of lightning with an internal source of energy possessing a core and a cover and bearing noncompensated electrical charges.

The method of electric discharge in a closed volume in a polymeric tube with a small aperture has generated "fiery" spheres of some millimeters in diameter on exit from an aperture from this tube. It has appeared that the duration of their luminescence was of the order of 10 ms. As source material, metallic particles and some basalt were used.

Artificial BL, obtained by an explosion of nanostructured porous silicon that was impregnated by a solid oxidizer, potassium nitrate, was discussed. Luminescent spheres from 10 to 80 cm in diameter with a lifetime of about 1 s have been realized.

The influence of new kinds of plasma on the surface of combustible liquids was considered. Results of experiments on the influence of pulse and corona discharges on water (covered with a benzene layer), on kerosene, and also on alcohol and kerosene (covered with a layer of an aluminum powder) were presented.

Results of ongoing research of the Gatchina discharge with formation of large (up to 10 cm in diameter) luminescent objects over a volume with water were reported.

Results of research on the structure and evolution of stretched vortical plasmoids at the microwave discharge fed by the pulse and high-frequency generator were presented. It is revealed that the important role in formation of the stretched vortical plasmoid is played by a vibrational-translation relaxation of the excited molecules. Dusty plasmoids have been considered also. They are generated by means of the erosion plasma generator in which an aluminum powder is inserted into the discharge channel and the high-frequency Tesla generator is applied. It has thus appeared that typical lengths of created plasmoids range from 10 to 100 cm, and their characteristic time of life is about 1 s.

Results of research on erosive discharge characteristics change researches have been presented. To study the conditions of continuous existence of formed plasmoids and control of their spatial localization, research on generation of high-frequency discharges is carried out in gas streams. Thus were observed plasmoids in air streams at the exit from a spiral waveguide, and also at the exit from an aperture in a quartz tube located on its axis or in a lateral wall.

On the basis of experimental results on the influence of electric discharge plasma on various materials (including silicon oxide), the model of the following natural object formation is considered. It can be called BL. At the strike of the linear lightning into the earth (or a melting object of inorganic nature), an area of the melt is formed. At that point, plasma interaction reactions of thermal decomposition of hydrocarbon components, of soil, dust, and organic components and of drops of water to C and H_2 take place. In the field of heating, chemical reactions of oxide reduction to metals and metalloids occur, and pure powder particles (aluminum or silicon) and molecules CO_2 and H_2O appear. (This process is similar to the formation of powders at electric explosions of wires, or the precipitation of metal

powders on a basis of oxides). The area appears to be unipolarly charged at the expense of the charge transferred to it from the linear lightning. So, an object in which the core consists of metal particles and gases, and a cover of fused oxide, is formed. The oxide layer decelerates metal particle oxidation by oxygen arriving from the outside. Inside the cavity there is a slow burning (metal or metalloid particles react with CO_2 and H_2O). Subsequently, an ejection of this object from the earth into air under the influence of gas pressure in the fulgurite areas takes place. Despite its possible large weight, it does not fall because of the Coulomb repulsion from the charged surface of the Earth. Internal reactions caused the object to be heated. The pressure inside the object rises, cracks in the cover appear, and it later scatters under the action of the Coulomb repulsion of charges.

It was shown that, within the limits of the already existing BL electrodynamic model, the energy density of an element of the energy core increases with downsizing of an element. The assumption of the existence of a "composite" object as a system of the tiny objects collected inside the general cover of a dielectric material allows us to explain cases of BL exit from sockets and their passage through small apertures and through intact glass.

Results of observation of radiowave interference in a waveguide of rectangular section were reported. Ceramic plates were located in Fibonacci chain order (quasi-periodic system) or the Cantor series (fractal system). From that it was studied what occurs at infringement of the order of the plate placement, shifting their parts for 1/3, 3/4, or 1/16 of the wavelength, respectively. In some cases, clicks of the electric breakdown in air were discovered in the waveguide; they lead to the occurrence of plasma structures.

A report that vorticity degree growth increases the stability of the atmospheric vortex lifetime was heard. For correct account of their formation mechanism, knowledge of the contribution to the formation process of the nonequilibrium self-consistent vortices structures of the storm cloud charged subsystems and research of their dynamics is necessary. Experimental data concerning high-altitude profiles of electric field specified the presence of strong electric fluctuations in storm clouds with characteristic sizes of 10–500 m. Electric field fluctuations on scales of $L \sim 10$–500 m (where L is the difference of the heights of two atmospheric layers), and also the presence of coherent electric structures, were discovered.

Combustion and Pollution: Environmental Impact

In the reports presented for this section, results of computation and experimental research directed toward the perfection of working processes in burner devices and internal combustion engines to provide maximum fuel economy and to lower the production of harmful substances (soot, NO, etc.) were discussed. Methods of burning and flame acceleration modeling in encumbered space and in pipes, methods of maintenance of fast transition of burning to detonation, and also methods of decreasing harmful substances at the burning of gas and liquid fuel, including safe recycling in an exhaust, were discussed.

Information Systems of Environmental Monitoring and Accident Prevention

In these reports, the following problems were considered: microdipole electromagnetic radiations (of slow-down character) induced by pulse X-ray or gamma sources; detection of the narrow directed pulse source of gamma quanta of high energy and the destructive influence of gamma radiation on electronic equipment; corrections of ionospheric delays at registration of the pulse signal, passing the ionosphere; and interrelation of errors of determination of coordinates and registration of arrival time in the range-difference method of a passive location.

It is shown that microdipole radiation, which spectrum is a pulse noise sending, lies in the field of low frequencies. The spectrum-correlation method is proposed for detection of the pulse sources of gamma quanta with time accumulation, allowing to allocate authentically the accepted radiation at a signal-to-noise ratio greater than two.

Rydberg radiation in the upper troposphere induced by the pulse sources of gamma quanta with energy of 1–3 MeV has been considered. It is shown that at pulse emission of 10^{22} gamma quanta radiation is reliably registered at distances of some hundreds of kilometers.

The question of the registration of electromagnetic radiation on board a space vehicle induced by the pulse sources of gamma quanta with duration of 10–100 ns and energy 1 MB was also considered.

On the basis of the presented reports, the Editorial board has prepared the following reviews for this book on important and interesting areas of atmosphere and ionosphere physics.

In Chap. 1 is discussed the contribution of excited atoms to the ionization processes under conditions of low-temperature plasma that may be regarded as a background for transformation of light excitation energy into electrical energy. Relevance of the dynamics chaos regime to the phenomenon of a diffusion autoionization within Rydberg quasi-molecular complexes is demonstrated, taking as an example collisions between Rydberg and normal alkali atoms. The presented data show the theoretical models of chemoionization processes, exploring "dipole-resonant mechanism" to be in satisfactory agreement with the experiment.

In Chap. 2 is presented a review of the theoretical status of the elementary atomic and molecular processes driven by strong monochromatic laser fields. The discussion is focused on near-threshold processes involving Rydberg intermediate states, which play an important role in the Earth's upper atmosphere. The possibility of the stationary formalism of radiative scattering matrix, based on a renormalized Lippmann–Schwinger equation, is demonstrated. This approach provides a unified description of all near-threshold processes, where the transition amplitudes are represented by the radiative scattering matrix elements corresponding to all possible reaction channels. These processes include predissociation, associative ionization, exchange, and other reactions that cannot be described by the standard time-dependent models.

Chapter 3 is devoted to a number of chemical and photochemical processes in the atmosphere that are responsible for the formation of the tiniest (nanometric) aerosol particles which then increase to larger sizes by condensation and coagulation. Charging of aerosol particles is also of importance for the particle growth processes. Chapter 3 considers all the aforementioned aerosol processes, taking into account that the particle size is less or comparable to the mean free path of molecules in the carrier gas; that is, the molecular transport goes in either the free molecule or the transition regime. The chapter outlines an approach that permits strong simplifications in considering the aerosol processes in the transition regime. This approach forms a common basis for treating molecule, charge, and energy transport toward small aerosol particles.

In Chap. 4 are shown a few examples of the interpretation of experimental results in the upper atmosphere and ionosphere obtained by using the model of the upper atmosphere (UAM). In particular, the influence of the interplanetary magnetic field on the upper atmosphere and ionosphere during geomagnetic disturbances, as well as the problem of the "lithosphere–ionosphere connection," are examined. Numerical experiments allow a statistical description of the GPS TEC measurements, which are regarded as precursors of earthquakes. Ionospheric precursors to earthquakes calculated from the model showed satisfactory agreement between the UAM and the observations of GPS TEC. Guidelines are given for the detection of ionospheric precursors of earthquakes.

Chapter 5 is devoted to the theory analysis of the discharge phenomena called elves and sprites in the stratosphere and mesosphere initiated by tropospheric storm processes. At a quantitative level the process of redistribution of charges in an atmosphere at altitudes up to 150 km during the charging and discharging of a storm cloud is investigated. An important role of the small electric conductivity of the stratosphere and mesosphere is shown. At lightning discharge of a storm cloud, the area of the overcritical field appears under the ionosphere in which the avalanche ionization arises (elf). The account of the small electric conductivity of the atmosphere between the troposphere and the ionosphere has allowed explaining the long duration of discharge processes developing under the ionosphere, basically in the residual electrostatic polarization field.

Chapter 6 presents an experimental work that in essence is a continuation of a well-known work on microwave plasmoid physics carried out by the Nobel prize winner P.L. Kapitsa. The chapter is devoted to high-frequency (HF) plasmoid creation in low-temperature plasma, in swirl flows, which is of interest from the aspect of ball lightning (BL) physics and the creation of artificial ball lightning.

Vladimir L. Bychkov
Gennady V. Golubkov
Anatoly I. Nikitin

Chapter 1
Ionization of Excited Atoms in Thermal Collisions

N.N. Bezuglov, Gennady V. Golubkov, and A.N. Klyucharev

Abstract This book is devoted to the modern theory and experimental investigations of the associative ionization (AI) reaction. The means of their further development are analyzed. Numerous applications in plasma chemistry, aeronomy, chemical physics of the upper atmosphere, and astrophysics have contributed to conducting this study. The threshold behavior of cross sections of the endothermic reaction AI is considered, and it is shown that the dependence of above-threshold energy E is a strictly linear in the quantum case, which differs substantially from the law $E^{3/2}$, resulting in a semiclassical theory. This result has a simple physical explanation because the matrix elements of scattering operator resulting from the tunneling effect are finite at $E = 0$. Comparison with the semiclassical theory has been made. A substantiation of the described possibility of elementary AI reaction dynamics in the diffusion approach is given. A detailed consideration of the applicability conditions of the "quantum chaos" theory for the spectrum of highly excited Rydberg molecules is carried out. A review of experimental studies of AI reaction under different conditions covering vapor cells, single effusive beams, two crossing beams, and cold matters (very briefly) is presented. The importance of accounting for specific distribution functions of atoms over a relative (colliding) velocity in AI rate constant evaluations is discussed, and a proper explanation of noticeable variations in experimental data is provided. Different types of colliding atomic/molecular pairs consisting of low-lying excited states (normal, metastable, and resonance) in inert and alkali gases are considered, and the corresponding futures of AI cross sections are analyzed. Experimental data on AI and Penning ionization processes involving the Rydberg states of hydrogen and alkali atoms

N.N. Bezuglov • A.N. Klyucharev
Physical Department, St. Petersburg State University, St. Petersburg, Russia
e-mail: nikolay.bezuglov@gmail.com; anklyuch@gmail.com

G.V. Golubkov (✉)
Semenov Institute of Chemical Physics, Russian Academy of Science, Moscow, Russia
e-mail: golubkov@chph.ras.ru

V. Bychkov et al. (eds.), *The Atmosphere and Ionosphere*, Physics of Earth and Space Environments, DOI 10.1007/978-94-007-2914-8_1,

are considered on the basis of a number of theoretical models. The relevance of diffusion motion of the optical electron through the Rydberg energy states toward the continuum resulting from appearance of the dynamics chaos regime in its evolution is demonstrated.

Keywords Metastable and Rydberg atoms • Ionization in slow atom collision • Intermediate Rydberg complex • Dynamics chaos

1.1 Introduction

Chemical ionization processes in the thermal and subthermal collisions of heavy particles with participation of the excited atoms are characterized by appreciable values of the reaction rate constants (Klyucharev and Vujnovic 1990; Klyucharev 1993). The universe at the initial stage of its existence was composed mainly of atoms, molecules, and positive and negative ions, containing $HD^{\pm}$, $LIH^{\pm}$, hydrogen, deuterium, helium, and lithium in their variety and different combinations. The results of recent spectroscopic observations of cosmic objects in the infrared range have shown the presence of anomalies, which appear in the disappearance of lines emitted by the hydrogen-like Rydberg atoms (RA) with values of the effective quantum number n_{eff} of the order of 10 (Gnedin et al. 2009). To this range, n_{eff} corresponds to the maximum on dependences of the RA chemical ionization processes $k(n_{\text{eff}})$ rate constants, i.e.:

$$\mathrm{X}^{**}\,(n_{\text{eff}}) + \mathrm{Y} \Rightarrow \begin{cases} \mathrm{XY}^{+} + \mathrm{e}^{-}, \\ \mathrm{X} + \mathrm{Y}^{+} + \mathrm{e}^{-}, \\ \mathrm{X}^{+} + \mathrm{Y} + \mathrm{e}^{-}. \end{cases} \tag{1.1}$$

When the concentration of neutral atoms is $c_{\mathrm{A}} \sim 10^{17}$ cm^{-3} and the rate constant is $k \sim 10^{-9}$ cm^3 c^{-1}, the effective lifetime of RA is about τ_{eff} 10^{-8} s (note that for hydrogen RA with $n_{\text{eff}} = 10$, the table value gives $\tau_{\text{eff}} = 10^{-6}$ s).

The concept of low-temperature plasma physics includes sections of elementary processes and their applications. Interest in development in this direction, which first had appeared in the early twentieth century, not only has not declined but is constantly increasing. Now we can speak about the new field of "chemistry of plasma physics," which is a junction of atomic and molecular collisions and chemistry of elementary gas-phase reactions leading to chemical transformations, including ionization and chemical ionization (Smirnov 1981). Studying the physics of ionization processes involving heavy particles, we have to consider the fundamental statements of atomic collision physics, which makes it possible to detect new phenomena and laws. One is the discovery of the new phenomenon of low-temperature plasma gas medium formation at its irradiation by light with wavelengths corresponding to resonant optical transitions in the atom (photoresonance plasma). Such plasma at the initial stage of its formation cannot be described within the traditional scheme of the gas discharge.

It is known that a direct analogy exists between the processes occurring in space and in laboratory facilities. For example, laboratory studies of laser-hydrogen plasma have shown that the features of the processes taking place in it are similar to the processes occurring in the atmosphere of cooling-type stars of the "white dwarf" class.

Recombination leading to filling of the Rydberg states, and being the main mechanism of the ionization-recombination processes with participation of the molecular ions, is sufficiently popular in the astrophysical literature. An example is low-temperature layers enriched by helium of those white dwarfs' atmosphere and the solar photosphere. At the same time, there remain many unresolved questions relating to the processes of a gas and a dust in the atmosphere of the satellite structures of the giant planet Jupiter: Io rich with sodium, where undoubtedly can take place the ionization processes involving excited sodium atoms, similar to those occurring in the laboratory photoresonance plasma in alkali metals vapors in Earth conditions (Klyucharev et al. 2007).

Recent results on the stochastic dynamics in the processes of chemical ionization (Klyucharev et al. 2010) in frames of the resonant collision model (Smirnov and Mihajlov 1971a) indicate the possibility of shifting the primary selective excitation of the RA over a group of excited states, and thereby of control of the elementary processes. The latter is of great interest, because it allows us to identify the relationship between determinism and stochasticity in atomic physics. Below we restrict ourselves to the effective principal quantum numbers $n_{\text{eff}} \leq 25$, which provide the maximum effect of chemical ionization.

1.2 Collision of Atoms in the Thermal and Subthermal Energy Ranges Leading to Ionization

Depending on the state of particle-collision partners in the entrance and exit channels of reactions, the total set of ionization processes in collisions of atoms and molecules can be divided into the processes of collision ionization and chemical ionization. This is a conditional division, which is determined by the potential energy of the excitation and kinetic energy of relative motion of colliding particles. The range of kinetic energies of the atoms of interest to the physics of collision processes lies in the interval 10^{-9} to 10^{3} K, which extends from a "Bose–Einstein condensate" to high-current arc plasma. Remember that the energy of 8.617×10^{-5} eV corresponds to the temperature of 1 K, which agrees approximately with the temperature of liquid helium. Each interval of temperatures of the gas medium has its own set of preferred processes leading to the ionization; in this case, following the division of the collision energy E_{col} of relative motion: the thermal (10^{-1} to 1 eV), subthermal (10^{-3} to 10^{-1} eV), and cold (less than 10^{-3} eV), i.e., collisions in the experiments on laser cooling of atoms.

In the literature, the chemical ionization process is called the reaction in which the transition to a state of the ionization continuum is the result of the internal

energy (excitation energy) of the colliding particles, and the energy of relative motion plays a minor role in energy balance. In other words, the energy of relative motion of atoms on the characteristic values of the inelastic transition distances in these reactions is much smaller than the ionization potential of the individual atoms partners. In connection with the development of new physical and technical trends in modern physics, such as the physics of active laser media, the interaction of radiation with matter is laser synthesis of chemical substances. Interest in these processes emerging in the past 60 years is markedly increased. However, available literature on the processes of ionization in slow atom–atom collisions in general relates to the reactions involving metastable atoms. The use of tunable dye lasers makes possible to implement a resonant optical excitation of atoms in the vast majority of elements, which markedly stimulated the experimental study of such processes. In this case, from energy considerations it follows that the ionization processes in slow symmetrical collisions are possible only if the pair collisions of resonantly excited atoms take place. At the same time two possibilities can be realized: (1) the doubled excitation energy is greater than the atom ionization potential, and (2) this energy is lower than that potential. The first case (1) takes place, for example, at the ionization of hydrogen and inert gases, halogens, nitrogen, and oxygen. The second one (2) is the ionization of alkali atoms of rare earth elements, uranium, most of the metal atoms, the ionization in collisions of metastable atoms of heavy inert gases with hydrogen.

As a result of the ionization process, in slow symmetrical and asymmetrical atom–atom collisions can be formed the following molecular and atomic ions:

$$\begin{aligned} &\text{Symmetrical collision} \quad \mathrm{X(X^*) + X^* \rightarrow X_2^+ + e^-} \\ &\text{Asymmetrical collision} \quad \mathrm{X(X^*) + Y^* \rightarrow XY^+ + e^-} \end{aligned} \tag{1.2}$$

$$\begin{aligned} &\text{Symmetrical collision} \quad \mathrm{X\left(X^*\right) + X^* \rightarrow X^+ + X + e^-} \\ &\text{Asymmetrical collision} \quad \mathrm{X\left(X^*\right) + X^* \rightarrow X^+ + X + e^-} \end{aligned} \tag{1.3}$$

or a pair of positive and negative ions

$$\begin{aligned} &\text{Symmetrical collision} \quad \mathrm{X\left(X^*\right) + X^* \rightarrow X^+ + X^-} \\ &\text{Asymmetrical collision} \quad \mathrm{X\left(X^*\right) + Y^* \rightarrow X^+ + Y^-} \end{aligned} \tag{1.4}$$

We do not consider here the processes of dissociative ionization and the ionization accompanied by a rearrangement of the particles, which can occur in atom–molecule collisions. Reactions (1.2, 1.3, and 1.4) differ by the process mechanisms. Reaction (1.2) is called associative ionization (AI). Note that reaction (1.3) in the cases where one partner is a metastable atom $\mathrm{Y^*}$ with the excitation energy exceeding the ionization potential of atom X is called the Penning ionization (PI).

The foregoing classification of the ionization processes in thermal collisions of atoms indicates only some of the possible reaction channels and in this sense is relative. For example, in the case of collisions of two highly excited atoms with the comparable ionization potential, six channels of reactions that lead to the formation of only atomic ions are theoretically possible:

$$\rightarrow \quad \begin{cases} X^- \left(e_1^- e_2^-\right) + Y^+ \\ Y^- \left(e_1^- e_2^-\right) + X^+ \end{cases} \tag{1.5}$$

$$X^* \left(e_1^-\right) + Y^* \left(e_2^-\right) \Rightarrow \rightarrow \quad \begin{cases} X^+ + Y \left(e_2^-\right) + e_1^- \\ X \left(e_1^-\right) + Y^+ + e_2^- \end{cases} \tag{1.6}$$

$$\rightarrow \quad \begin{cases} X^+ + Y \left(e_1^-\right) + e_2^- \\ X \left(e_2^-\right) + Y^+ + e_1^- \end{cases} \tag{1.7}$$

In reactions (1.5, 1.6, and 1.7), the indices 1 and 2 refer to the optical electrons of atoms X and Y, respectively.

Quantitative conclusions about the effectiveness of chemical ionization with participation of emitting atoms in a broad range of binding energy of the optical electron by the end of the 1990s were possible primarily for alkali metal atoms (Klyucharev and Vujnovic 1990).

1.3 Basic Principles of the Theory

This section discusses the theory of collision ionization, which is characterized by a variety of methods and approaches developed during the past 20–30 years. We have skipped over those which by now have become generally accepted and widely used to describe various physical phenomena in atomic and molecular collisions and low-temperature plasmas and laser devices in the upper atmosphere and ionosphere, aeronomy, and astrophysics. However, many questions are yet to receive their final consideration.

1.3.1 Semiclassical Approach

If the excitation energy of the atom is greater than the ionization potential of the particle Y, then the Penning AI process proceeds. Then, for all the finite interatomic distances the quasi-molecule is found in the autoionizing states, decaying with the emission of an electron, and the formation of the molecular ion, if its existence is

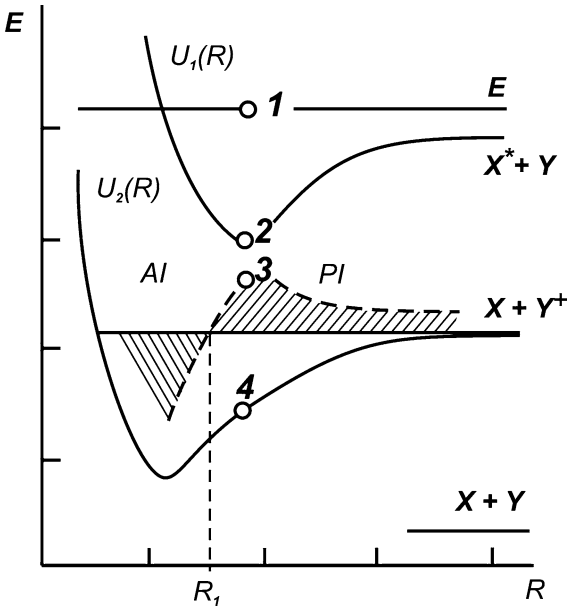

Fig. 1.1 Potential curves for the molecular ion $U_2(R)$ and the quasi-molecular system $U_1(R)$. The value E corresponds to the total energy of the system. The excitation energy of the atom Y^* is greater than the ionization potential of the atom X

possible. A diagram of the electron excited quasi-molecule XY^* potential curves and the ground state molecular ion XY^+, qualitatively illustrating a separation possibility of the processes

$$X^* + Y \rightarrow \begin{cases} XY^+ + e^- & \text{associative ionization (AI)} \quad (1.8) \\ X^+ + Y + e^- & n\text{−type Penning AI reaction (PI)} \quad (1.9) \end{cases}$$

(when the adiabatic approximation takes place), is shown in Fig. 1.1. An implementation of the Franck–Condon principle in the conservation of the nuclei energy is illustrated in this figure by presentation of the ordinate differences of points 1, 2 and 3, 4, respectively: $U_1(R) - U_2(R) = U_3(R) - U_4(R)$. When point 3 lies above the dissociation ion XY^+ limit, the PI channel is preferred. If an autoionization decay from the $U_1(R)$ term for the interatomic distances $R > R(1)$ takes place, the PI-type reaction with formation of the atomic ion and one electron happens (reaction (1.3)). Autoionization decay of $R < R(1)$ leads to the formation of the molecular ion in the stable vibrational excited state. In the same approximation, the energy of electrons releazed in the reaction channels at the interatomic distance R is equal to the $U_1(R) - U_2(R)$ difference. From analysis of the electron energy distribution in the reactions (1.2 and 1.3), we can judge not only about the relative efficiency of the molecular and atomic ion processes as the branching factor of the reaction, but also about the behavior of potential curves of the electronically excited molecules. The limiting value of the atoms (temperature) average energy, where the basic transition

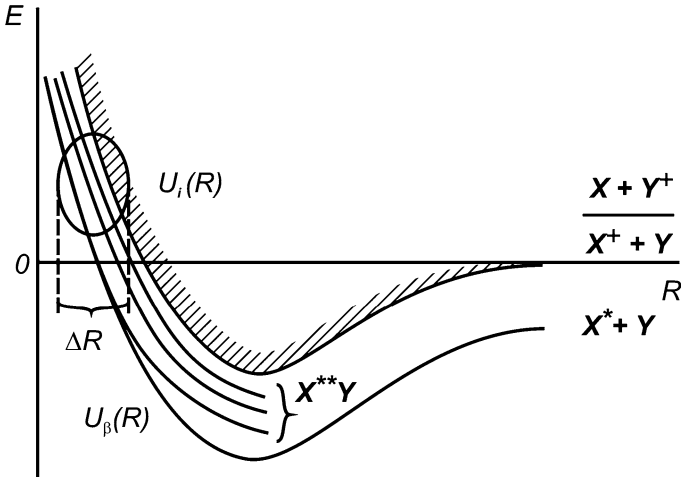

Fig. 1.2 Potential curves for the molecular ion XY^+ and the quasi-molecular XY^*. The excitation energy of the atom Y^* is smaller than the ionization potential of the atom X

preconditions do not violate, can be estimated from the ratio of the de Broglie wavelength of the atom and the characteristic atomic size, a_0. All this has led to the development of Penning electron spectroscopy as a new direction of experimental research.

If the excitation energy X^* is smaller than the Y ionization potential, than there are two possibilities: reaction (1.8) and (1.9) (in the diabatic representation). The first case takes place when the potential curves of the quasi-molecule U_β and the molecular ion U_i do not overlap (Fig. 1.2). In this case, the transition occurs because of the nonadiabatic coupling of the electron and nuclear motions in a wide range of interatomic distances ΔR, when they approach, and the potential curves of Rydberg states of the quasi-molecule $X^{**}Y$ are the Coulomb condensation. The second case corresponds to the situation when, in the vicinity of the point R_c, the potential curve XY^*, and the dissociative term (diabatic picture) intersects a set of curves of the Rydberg and ion U_i terms (Fig. 1.3). When going to the region of interatomic distances $R < R_\mathrm{c}$, the term XY^* becomes autoionization. Consequently, the reaction of the AI here is essentially a multichannel process, as occurs with the participation continuums of the Rydberg, dissociative, and ionized states (see Figs. 1.2, 1.3). As a result of the direct relationship of the Rydberg XY^{**}, the dissociative $X^* + Y$, the intermediate valence X^*Y, and the ionic X^+Y^- configurations, under the atom collisions are possible not only autoionization, but inelastic transitions, that can be accompanied with the increase (or decrease) of the initial atom excitation energies.

Analysis of the discrete level interaction with the states of the continuum and the infinite sequence of the Coulomb levels was carried out (Demkov and Komarov 1966). Strictly speaking, the problem of multiple transitions (associated with the

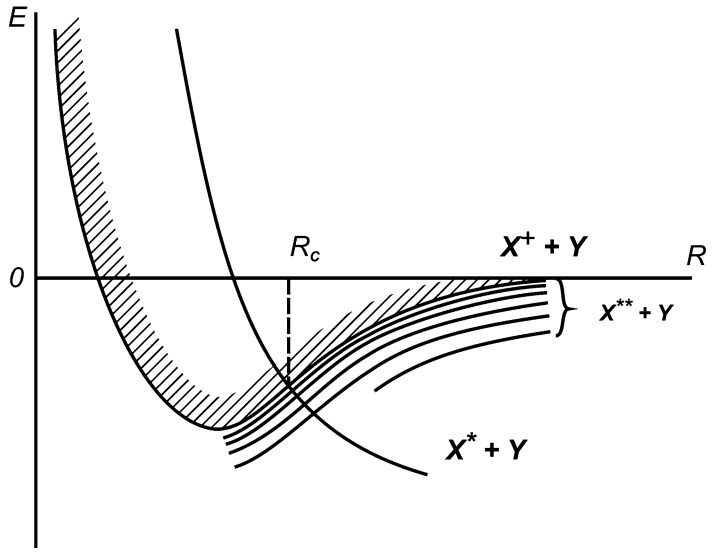

Fig. 1.3 The same as for Fig. 1.2 with a quasi-crossing of the potential curves in the point R_c

Coulomb refinement levels) is solved in the special model case, then the set of Rydberg terms is replaced by a system of the parallel lines, and the diabatic dissociative term is also linearized. In the framework of the Demkov–Osherov contour integral method (Demkov and Osherov 1968), the problem is reduced to multiplying the probabilities to stay on the dissociative term at each point of pseudo-crossing (followed by a summation of the exponents of all these points). This approach is reasonable if the ionization and the transitions to highly excited states are determined by the behavior of the system near the avoided crossing R_c in the small neighborhood L_R, which is the parameter of the problem. Upon reaching the point, $R = R_c$ of the bound state disappears, merging with a continuous spectrum. The ionization cross section in this approximation is equal to πR_c^2.

In the 1970s, the majority of model theoretical studies of the AI process were performed without a set of avoided crossings that occur right up to the potential curve of the quasi-molecule across the border of the molecular ion continuum. Attempts to take them into account in the framework of the traditional approaches based on individual review of each pseudo-crossing for highly excited states were not successful. In this regard, we developed a method that implements the "diffusion-based approach to the collision ionization of excited atoms" (Devdariani et al. 1988). We are talking about the diffusion over the quasi-molecule state energies in a single act of the collision: the main collision parameter is the binding energy of the excited electron. During the "diffusion," the initial single quasi-molecule term is transformed into a "burning" type of conic section at large distances ($R \to \infty$) with decrease in R (Fig. 1.4).

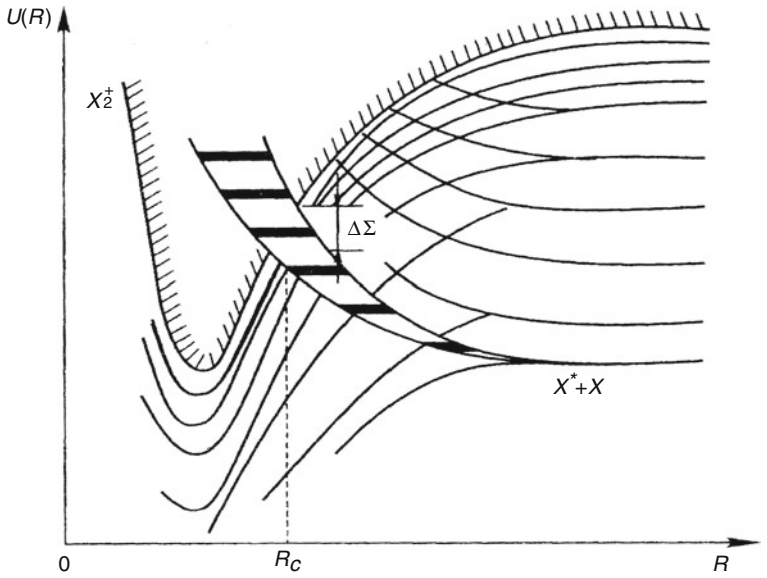

Fig. 1.4 Illustration of the quasi-crossing of covalent and ionic potential curves under the frame of the "diffusion" model

1.3.2 General Equations of the Scattering Theory

In presenting the formal scattering theory of atoms $X + Y^*$ with a transition to the final $e^- + XY^+$ state of the system, it is convenient to use a method of the multichannel quantum defect (MQD) (Golubkov and Ivanov 2001), which gives the most complete and consistent description of the resonant scattering and the reactions leading to the redistribution of particles. For simplicity, we exclude the valent X^*Y^* and ionic X^+Y^- configurations and represent the full Hamiltonian of the system under consideration in the form ($\hbar = m_e = e = 1$)

$$\mathbf{H} = \mathbf{H}_0 + \mathbf{V}, \quad \mathbf{H}_0 = -\frac{1}{2}\mathbf{\Delta}_\mathbf{r} - \frac{1}{r} + \mathbf{H}_q, \tag{1.10}$$

where $-\frac{1}{2}\mathbf{\Delta}_\mathbf{r}$ is the operator of the kinetic energy of a weakly bonding electron, $\mathbf{r}$ is its coordinate read from the XY^+ ion center of mass, and $\mathbf{H}_q$ is the molecular ion Hamiltonian dependent on the coordinate set $\{\mathbf{X}\}$ of the internal electrons (here, $q = \{v, N\}$ is the set of vibrational v and rotational N quantum numbers of the XY^+ ion). Note that the bound and autoionizing Rydberg states of the system belong to the configuration XY^{**} and differ only in sign (and magnitude) of the total energy E of the system, which can be conveniently measured from the ground state of the molecular ion.

The unperturbed Hamiltonian $\mathbf{H}_0$ for Rydberg channels is chosen in such a way that all interactions in the dissociative $X + Y$ configurations are exactly taken into account, but in the scattering $e^- + XY^+$ channel only the Coulomb part $V^c = -\frac{1}{r}$ is contained. Thus, in the total Hamiltonian (Eq. 1.10), the operator $\mathbf{V} = \mathbf{V}^{nc} + \mathbf{V}^{CI}$ includes a non-Coulomb interaction of the electron with the ionic core $\mathbf{V}^{nc}$ and interaction $\mathbf{V}^{CI}$ responsible for the corresponding nonadiabatic transitions between $e^- + XY^+$ and $X^* + Y$ configurations.

A formal solution of the AI problem (or of the inverse process of the dissociative recombination) is reduced to define the collision $\mathbf{T}$−operator (related to the $\mathbf{S}$−matrix by the relationship $\mathbf{S} = \mathbf{1} - 2i\mathbf{T}$), which satisfies the system of the rearranged integral Lippman–Schwinger equations (Golubkov and Ivanov 2001):

$$\mathbf{T} = \mathbf{t} + \mathbf{t}(\mathbf{G} - \mathbf{G}_0)\mathbf{T}, \tag{1.11}$$

$$\mathbf{t} = \mathbf{V} + \mathbf{V}\mathbf{G}_0\mathbf{t}, \tag{1.12}$$

where $\mathbf{G} = (E - \mathbf{H}_0)^{-1}$ is the Green's operator with the interaction $\mathbf{V}$ turned off, and $\mathbf{G}_0$ is weakly dependent on the total energy E operator. We denote the basic wave functions of the unperturbed Hamiltonian $\mathbf{H}_0$ by $|q\rangle$ for the $e^- + XY^+$ configuration and $|\beta\rangle$ for the dissociative $X + Y^*$ configuration. The corresponding matrix elements $\langle q|\,\mathbf{T}\,|\beta\rangle$ are the amplitudes of the transitions $\alpha \Leftrightarrow \beta$ transitions that are symmetrical under permutation of the indices.

The Green's $\mathbf{G}$−operator in Eq. 1.11 is represented by the contribution of noninteracting $e^- + XY^+$ and $X^* + Y$ configurations and has the following form:

$$\mathbf{G}(E) = \sum_i |i\rangle \mathbf{G}^{(c)}(E - E_i)\langle i| + \frac{1}{\pi}\sum_\beta \int \frac{|\beta\rangle\langle\beta|}{E - E_\beta + i\gamma} dE_\beta. \tag{1.13}$$

Here E_i and $|i\rangle$ are the excitation energies and corresponding wave functions of the XY^+ ion, and $\mathbf{G}^{(c)}$ is the Green function describing the electron motion in a Coloumb field. In the representation of spherical harmonics, it has the form

$$\mathbf{G}^{(c)}(\mathbf{r}, \mathbf{r}'; \varepsilon) = \sum_{lm} Y^*_{lm}\left(\frac{\mathbf{r}}{r}\right) G^{(c)}_l(r, r'; \varepsilon) Y_{lm}\left(\frac{\mathbf{r}'}{r'}\right),$$

where $Y_{lm}\left(\frac{\mathbf{r}}{r}\right)$ is the spherical function. It is important for further consideration that the radial function $G^{(c)}_l(r, r'; \varepsilon)$ can be separated into terms with weak and strong energy dependences (Demkov and Komarov 1966):

$$G^{(c)}_l(r, r'; \varepsilon) = \cot \pi\nu(\varepsilon)\,|\varphi_{\varepsilon l}(r)\rangle\langle\varphi_{\varepsilon l}(r')| + g_l(r, r'; \varepsilon). \tag{1.14}$$

The first term in Eq. 1.14 reproduces the position of the Coulomb levels $\nu(\varepsilon) = (-2\varepsilon)^{-1/2}$ at $\varepsilon < 0$ and is expressed through the regular at-zero Coulomb wave functions $\varphi_{\varepsilon l}(r)$ normalized in accordance with

$$\langle \varphi_{\varepsilon l}(r) \, | \varphi_{\varepsilon' l}(r) \rangle = \pi \delta \left(\varepsilon - \varepsilon' \right).$$

After excluding the smoothed real part from (1.13):

$$\mathbf{G}_0(E) = \sum_{i,lm} |i\rangle Y^*_{lm}\left(\frac{\mathbf{r}}{r}\right) g_l\left(r, r'; E - E_i\right) Y_{lm}\left(\frac{\mathbf{r}'}{r'}\right) \langle i| + \frac{1}{\pi} \sum_{\beta} P \int \frac{|\beta\rangle \langle \beta|}{E - E_\beta} \mathrm{d}E_\beta$$

(P means the principal value of the integral), we can write the following equation for the collision **T**–operator:

$$\mathbf{T} = \mathbf{t} + \mathbf{t} \left\{ \sum_q |q\rangle \langle q| \cot\left[\pi \left(-2\varepsilon_q\right)^{-1/2}\right] - i \sum_\beta |\beta\rangle \langle \beta| \right\} \mathbf{T}. \tag{1.15}$$

Here $\varepsilon_q = E - E_q$ is the electron energy in the q-channel of motion, E_q is the energy of its vibrational and rotational excitation. For open channels $\left(\varepsilon_q > 0\right)$, the function $\cot\left[\pi \left(-2\varepsilon_q\right)^{-1/2}\right] = -i$.

Because of the linearity and the separable structure of the nucleus (which follows from the unique properties of the Coulomb Green function), the integral equation (1.15) reduces to a system of linear algebraic equations for the elements of **T**–matrix, in which the dissociative channels are taken into account along with the scattering channels, at the same time consistently ignoring the strong nonadiabatic coupling of the electronic and nuclear motions, which forms a heterogeneous continuum of intermediate Rydberg states interacting with the decaying dissociative terms (Golubkov et al. 1996a). These important properties follow from the formal scattering theory, and automatically provide a unitary **S**–matrix on an arbitrary basis, accounting for the movement of channels, which ensures the controlled precision of carried calculations.

1.3.3 Basic Wave Functions and Elements of Reaction t Matrix

Basic wave functions $|q\rangle$ in the Rydberg configuration (taking into account the vibrational and rotational motion of nuclei) are

$$|q\rangle = |JMlNv\rangle = \varphi_{\varepsilon_v l}(r) \varphi_i(\mathbf{x}) \chi^J_v(R) \Phi^{JM}_{lN}\left(\hat{r}\hat{R}\right). \tag{1.16}$$

Here φ_i is the electron wave function of the XY^+ ion, and $\chi_v^J(R)$ is the vibrational wavefunction. The total angular function of the system $\Phi_{lN}^{JM}(\hat{r}\hat{R})$ is defined in the representation with total angular momentum $\boldsymbol{J}$ and its projection $\boldsymbol{M}$, angular momentum N of the rotational notion of the nuclei, and in the case LS-coupling for σ configuration of XY^+ has the form (Golubkov and Ivanov 2001)

$$\Phi_{lN}^{JM}\left(\hat{r}\hat{R}\right) = \sum_m Y_{lm}\left(\hat{r}\right) Y_{N,M-n}\left(\hat{R}\right)(lNmM-n\,|JM)$$

($\hat{r}$, and $\hat{R}$ are spherical coordinates of the electron and nucleus, and $(lNmM-n\,|JM)$ are the vector summation coefficients, $\boldsymbol{J}=\boldsymbol{l}+\boldsymbol{N}$). The $|q\rangle$ functions are determined in the laboratory frame of reference, where the direction of the z-axis coincides with the electron wave vector.

In the dissociative configuration the electrons are fast enough, so their motion is quantized in the field of the fixed nuclei and is described in the adiabatic approximation. For calculation of the configuration interaction matrix elements it is necessary to expand the channel wave functions (Eq. 1.16) into the adiabatic basis, that is, to pass into the coordinate system associated with the molecule, in which the absolute value of the projection of electronic angular momentum Λ on the molecular axis is fixed. States of a diatomic molecule in this basis are classified according to the values of J (the angular momentum of an electron l is not preserved in general). The total wave function in the adiabatic approximation is a superposition of the channel basis functions:

$$|JM\rho\Lambda v\rangle = \sum_l a_{l\rho}^{J\Lambda}\,|JMl\Lambda v\rangle\,. \tag{1.17}$$

Here ρ is the quantum number given by the largest coefficient of the expansion (1.17) characterizing the effective electron angular momentum of the Rydberg configuration with l mixing taken into account. The wave functions of the dissociative β configuration are determined quite similarly.

To calculate the elements $t^J_{lNv,l'N'v'}$ and $t^J_{lNv,l'\beta\Lambda}$ in the system of Eqs. 1.11 and 1.12 and responsible for the rovibronic and configuration nonadiabatic transitions, it is convenient to introduce the auxiliary $\bar{\mathbf{t}}$ operator, i.e.:

$$\bar{\mathbf{t}} = \mathbf{V} + \frac{1}{\pi}\sum_q P\int \mathbf{V}\frac{|q\rangle\langle q|}{E-E_q-\varepsilon}\bar{\mathbf{t}}\,\mathrm{d}\varepsilon$$

It describes the interaction of the electron with the ion core in an isolated Rydberg $e^- + XY^+$ configuration. Electron parts of matrix elements of the $\bar{\mathbf{t}}$–operator in the mixed basis (1.17), depending on R by definition, are diagonal with respect to subscripts ρ and Λ, and are expressed via the diabatic quantum defects $\bar{\mu}_{\rho\Lambda}$ as

$$\bar{t}^J_{\rho\Lambda,\rho'\Lambda'}(R) = -\tan\pi\bar{\mu}_{\rho\Lambda}(R)\delta_{\rho\rho'}\delta_{\Lambda\Lambda'}. \tag{1.18}$$

So long as the adiabatic basis $|JMl\Lambda v\rangle$ and channel basis (1.16) are connected by the unitary transformation (Golubkov et al. 1997)

$$|JMl\Lambda v\rangle = \sum_N U^{Jl}_{N\Lambda} |JMlNv\rangle \tag{1.19}$$

for $\bar{t}^J_{lNv,l'N'v'}$ elements we have

$$\bar{t}^J_{lNv,l'N'v'} = -\sum_{\rho\Lambda} a^{J\Lambda}_{l\rho} U^{Jl}_{N\Lambda} \times \left\langle \chi^J_v \right| \tan \pi\mu_{\rho\Lambda}(R) \left| \chi^J_{v'} \right\rangle a^{J\Lambda}_{\rho l'} U^{Jl'}_{\Lambda N'}, \tag{1.20}$$

where $U^{Jl}_{N\Lambda}$ is the Fano's rotation submatrix. Therefore, taking the pattern of Rydberg terms and the information about the adiabatic wave functions (1.17) as a basis, one can define by Eq. 1.20 a complete set of the $\bar{\mathbf{t}}$ matrix elements.

According to Eqs. 1.12 and 1.18, the reaction matrix $\mathbf{t}$ satisfies the operator equation

$$\mathbf{t} = \bar{\mathbf{t}} + \bar{\mathbf{t}} \frac{1}{\pi} \sum_\beta P \int \frac{|\beta\Lambda\rangle \langle\beta\Lambda|}{E - E_\beta} \mathbf{t}\, \mathrm{d}E_\beta.$$

From this equation with regard to the smallness of the configuration coupling, we can obtain the following expressions for the matrix elements:

$$t^J_{lNv,l'N'v'} = \bar{t}^J_{lNv,l'N'v'} + \frac{1}{\pi} \sum_\beta P \int \frac{V^{\mathrm{CI}}_{lNv,\beta\Lambda} V^{\mathrm{CI}}_{\beta\Lambda,l'N'v'}}{E - E_\beta} \mathrm{d}E_\beta, \tag{1.21}$$

$$t^J_{lNv,\beta\Lambda} = V^{\mathrm{CI}}_{lNv,\beta\Lambda} + \frac{1}{\pi} \sum_{l'N'v'} P \int \frac{\bar{t}^J_{lNv,l'N'v'} V^{\mathrm{CI}}_{l'N'v',\beta\Lambda}}{E - E_\beta} d\,E_\beta + \frac{1}{\pi} \sum_{\beta'\neq\beta,\Lambda'} P \int \frac{V^J_{lNv,\beta'\Lambda'} V^{\mathrm{CI}}_{\beta'\Lambda',\beta\Lambda}}{E - E_\beta} d\,E_\beta, \tag{1.22}$$

$$t^J_{\beta\Lambda,\beta'\Lambda'} = V^{\mathrm{CI}}_{\beta\Lambda,\beta'\Lambda'}. \tag{1.23}$$

The value of the CI is defined by specific peculiarities of the quasimolecule electron structure. The examples of well-known $e^- + XY^+$ systems show that it is really small, i.e., the values $\left|V^{\mathrm{CI}}_{lNv,\beta\Lambda}\right|^2$ are small in comparison with unity. Elements $t^J_{lNv,l'N'v'}$ in (1.21) are presented in the form of two terms, where the first one is caused by the interaction with the ion core and the second by the mixing of

Rydberg series with the dissociative continuum. The coupling between Rydberg and dissociative channels (1.22) is determined analogously. The direct coupling among dissociative channels dominates the inelastic transitions. The diagonal elements $t^J_{\beta\Lambda,\beta'\Lambda'}$ related to the elastic scattering in the dissociative channels have second-order smallness with respect to the configuration coupling V^{CI} and are absent here.

1.3.4 Matrix Elements of Configuration Coupling

The explicit form of these elements depends significantly on the relative part played by the XY^+ ion rotation and spin–orbit interaction. So long as the role of nucleus rotation is characterized by the distance between the nearest rotation levels, there are two limiting cases only. The first one (Hund's case *a*) takes place when the energy of the spin–axis interaction is large in comparison with this distance. The second one (Hund's case *b*) corresponds to their reverse relation. This case takes place for light molecular ions only, which are the most interesting for us. Taking into account the connection between the *q*-channel (Eq. 1.16) and the adiabatic (Eq. 1.19) basis of states, we put the elements of configuration coupling into the form of two terms

$$\begin{aligned} V^{\mathrm{CI}}_{lN\nu,\beta\Lambda} &= \sum_{\Lambda'} U^{Jl}_{N\Lambda'} V^{\mathrm{CI}}_{l\Lambda'\nu,\beta\Lambda} \\ &= U^{Jl}_{N\Lambda'} V^{\mathrm{rad}}_{l\Lambda\nu,\beta\Lambda} + \sum_{\Lambda'} U^{Jl}_{N\Lambda'} V^{\mathrm{cor}}_{l\Lambda\nu,\beta\Lambda}. \end{aligned} \tag{1.24}$$

The first term describes a nonadiabatic coupling of the intermediate Rydberg complex with the dissociative continuum by means of nuclear radial motion. In the case of weak dependence of the radial part of the CI on the internuclear distance R, the Frank–Condon representation $V^{\mathrm{rad}}_{l\Lambda\nu,\beta\Lambda} = V^{\mathrm{rad}}_{l\Lambda}(R_e)\left\langle \chi^J_\nu \middle| \chi^J_{\beta\Lambda} \right\rangle$ for the matrix elements is equitable, where $\chi^J_{\beta\Lambda}$ is the nuclear wave function of the dissociative channel. The electron part of the matrix elements $V^{\mathrm{rad}}_{l\Lambda}$ complies with the rigorous selection rules:

$$\Delta\Lambda = 0. \tag{1.25}$$

The second term in Eq. 1.25 is caused by the nonadiabatic coupling of electron motion with the internuclear axis rotation (Coriolis coupling) and can be written as (Golubkov et al. 1997)

$$\begin{aligned} V^{\mathrm{cor}}_{l\Lambda'\nu,\beta\Lambda} = -\frac{Q^J_{\nu,\beta\Lambda}}{2M_{\mathrm{c}}} \sum_{\rho} a^{J\Lambda'}_{l\rho} \Big\{ &\lambda^{J\Lambda}_{-} \left\langle \phi^J_{\rho\Lambda'} \middle| L_- \middle| \phi^J_{\rho\Lambda} \right\rangle \delta_{\Lambda',\Lambda-1} \\ &+ \lambda^{J\Lambda}_{+} \left\langle \phi^J_{\rho\Lambda'} \middle| L_+ \middle| \phi^J_{\rho\Lambda} \right\rangle \delta_{\Lambda',\Lambda+1} \Big\}, \end{aligned} \tag{1.26}$$

where M_c is the reduced mass of the quasi-molecule XY^{**},

$$\lambda_{\pm}^{J\Lambda} = [(J \mp \Lambda)(J \pm \Lambda + 1)]^{1/2}, \quad L_{\pm} = L_{\xi} \pm i L_{\eta}.$$

The quantity $Q^{J}_{v,\beta\Lambda}$ is defined as the radial part of the nuclear matrix element and equal to

$$Q^{J}_{v,\beta\Lambda} = \left\langle \chi^{J}_{v} \left| \frac{1}{R^2} \right| \chi^{J}_{\beta\Lambda} \right\rangle.$$

The projections $L_{\pm}$ of the electron angular momentum operator $\boldsymbol{L}$ are defined in the molecular frame system and affect the wave functions of the dissociative channels $\phi^{J}_{\beta\,\Lambda}$ at construction by the common quantum chemical rules. From Eq. 1.26 it implies that unlike Eq. 1.25 the selection rule for Coriolis communication is defined as

$$\Delta\Lambda = \pm 1. \tag{1.27}$$

For homoatomic quasi-molecules X_2^{**} the selection rules (1.25) and (1.27) are provided by the condition: $g \leftrightarrow g$, $u \leftrightarrow u$. Note also that the part of the Coriolis coupling proportional to $\sim \left\langle L^2 \right\rangle_{\Lambda} \delta_{\Lambda\Lambda'}$ is included in the definition of the first term in Eq. 1.24 because the selection rules for this interaction are the same as in Eq. 1.25.

Thus, the formal construction of solutions of the AI problem is completed. Nevertheless, to visualize the physical picture of phenomena is appropriate to turn to the energy spectrum of the intermediate Rydberg quasi-molecule states and, for clarity, to analyze the structure of its adiabatic terms.

1.3.5 *Rydberg States of the XY^{**} Quasi-Molecule*

From the integral equation (1.15) in the operator form, it follows that the eigenvalue spectrum of the Rydberg energy of the intermediate complex XY^{**} is determined by the poles of the collision **T** matrix, which satisfy the matrix equation

$$\mathbf{t}\left\{\sum_{l,v,N} |Jlv N\rangle \langle Jlv N| \cot\left[\frac{\pi}{\sqrt{2(E_v - E_N - E)}}\right] - i \sum_{\beta} |J\beta\rangle \langle J\beta|\right\} = \mathbf{1}, \tag{1.28}$$

where E_v and E_N are the energies of vibrational and rotational motions. Matrix rank for the given value of J equals the total number of channels taken into account in $e^- + XY^+$ and $X^* + Y$ configurations. Solutions of the transcendental equation (1.28) represent a complicated set of complex spectral energy values, the imaginary parts of which depend on the sign and the magnitude of the total energy E of the system.

In the continuum ($E > 0$) there are all the states of the intermediate Rydberg complex XY^{**} associated with the scattering channels, which are divided into the open and closed (resonant states). Recall that in open channels $E > E_v + E_N$ the function

$$\cot\left[\frac{\pi}{\sqrt{2\,(E_v - E_N - E)}}\right] \Rightarrow -i.$$

When the total energy of the system is $E < 0$, Eq. 1.28 describes the rovibronic spectrum of the bound predissociative Rydberg states of the molecule XY^{**} mixed with a dissociative continuum. Depending on the values of the principal quantum number n of the molecule, the energy spectrum can be roughly divided into three main areas. They are determined by the type of the communication between the electronic and nuclear motions and define a hierarchy of the characteristic times: the electronic $T_e \sim n^3$, the vibrational $T_v \sim 1/\omega$ and the rotational $T_N \sim 1/B$ (here ω and B are the vibrational quantum frequency and the rotational constant of the XY^+ ion).

Under the condition $T_e \ll T_v \ll T_N$ for the low-lying electronically excited states, the adiabatic Born–Oppenheimer approximation is true when the electron motion is quantized in the fixed molecular ion, and the projection on the axis Λ is a good quantum number. When n increases, and $T_e \sim T_v$, the adiabatic coupling break takes place with the vibrational motion first and then, if $T_N \sim T_e$, with rotating, or at large values of $Bn^3 \gg 1$, the picture is reversed, i.e., significantly nonadiabatic, when the electron becomes a slow subsystem and the ion core is fast. In this case the states are classified by ranges of the data values of the vibrational v and the rotational N quantum numbers.

Under the condition $\omega n^3 \ll 1$, the transition to the adiabatic terms of the intermediate complex XY^{**} is the subject to the semiclassical approximation by reexpansion of the wave functions $|lvN\rangle$ over the adiabatic $|\rho v\Lambda\rangle$ basis (1.17), following by the summing over all possible quantum numbers v and N (Golubkov and Ivanov 2001). As a result, for each dissociative $\beta\Lambda$–term we can obtain from Eq. 1.28 the following simple transcendental equation:

$$\left[\tan\left(\pi\nu(R)\right) - \bar{t}_{\rho\Lambda,\rho\Lambda}(R)\right]\left[E - U_{\beta\Lambda}(R)\right] = V^2_{\rho\Lambda,\beta\Lambda}(R) \tag{1.29}$$

where $\nu(R)$ is defined as

$$\nu(R) = \frac{1}{\sqrt{2[U_{\mathrm{i}}(R) - E]}},$$

$U_{\mathrm{i}}(R)$ and $U_{\beta\Lambda}(R)$ are the potential curves of the molecular ion XY^+, and the dissociative term $\bar{t}_{\rho\Lambda,\rho\Lambda}(R)$ is the matrix element (1.18). Equation 1.29 reproduces completely the physical situation, which we discussed earlier (in the introduction to this section). Indeed, the zero values of the first square brackets for different values of ρ and Λ correspond to the set of the Rydberg series with the diabatic potential curves:

$$\bar{U}^{**}_{n\rho\Lambda}(R) = U_{\rm i}(R) - \frac{1}{2\left[n - \bar{\mu}_{\rho\Lambda}(R)\right]^2}.$$

At $n \to \infty$ they are close to the ion $U_{\rm i}(R)$ term. Zero values of the second square brackets define a set of the dissociative $U_{\beta\Lambda}(R)$ terms, which intersect the ion term at the pole $E = U_{\rm i}(R)$, in the points $R_{\rm c}(\beta\Lambda)$ determined by the condition $U_{\beta\Lambda}(R_c) = U_{\rm i}(R_c)$. Accounting for the interaction between them leads to a characteristic pattern of the adiabatic terms where the transition of each pseudo-crossing point is accompanied by the increase of adiabatic quantum defect $\mu_{\rho\Lambda}(R)$ by 1. To determine its explicit form is sufficient to replace in the second square brackets in Eq. 1.29 the total energy in the adiabatic Rydberg $U^{**}_{n\rho\Lambda}(R)$ potential using Eq. 1.18 and the expression of $\nu(R) = n - \mu_{\rho\Lambda}(R)$. Then, far from the intersection point it is easy to obtain the $\mu_{\rho\Lambda}(R) \simeq \bar{\mu}_{\rho\Lambda}(R) + \Delta_{\rho\Lambda}(R)$ expression, where

$$\Delta_{\rho\Lambda}(R) \simeq \frac{1}{\pi}\arctan\left[\pi\left(\frac{V^2_{\rho\Lambda,\beta\Lambda}(R)}{U_{\beta\Lambda}(R)}\right)\right].$$

When the value $E > U_{\rm i}(R)$, the magnitude of $\tan\pi\nu(R) \to i$ and the solution of Eq. 1.29 becomes

$$E - U_{\beta\Lambda}(R) - \bar{\Delta}_{\beta\Lambda}(R) = -\frac{i}{2}\Gamma_{\beta\Lambda}(R),$$

where the energy shift and the autoionization width are equal:

$$\bar{\Delta}_{\beta\Lambda}(R) = \frac{1}{2}\sin\left[2\pi\bar{\mu}_{\rho\Lambda}(R)\right],$$

$$\Gamma_{\beta\Lambda}(R) = 2V^2_{\rho\Lambda,\beta\Lambda}(R)\cos^2\pi\bar{\mu}_{\rho\Lambda}(R).$$

Note: the autoionization width $\Gamma_{\beta\Lambda}(R)$ arises here by the jump at the transition $R_{\rm c}(\beta\Lambda)$ point, which is typical for the Coulomb problem (Golubkov and Ivanov 2001).

We considered the approximate approach, which can be described as "quasi-adiabatic," if the potential curves appear. Nevertheless, it is very useful, because it allows without much difficulty demonstrating its effectiveness in addressing a number of nonstationary problems of quantum mechanics (Demkov and Golubkov 2003). The disadvantage of the approach is that the ionization channel is open only when the $R < R_{\rm c}$ region. In fact, as is shown next, the ionization process strictly arises in the case of $E \geq U_{\rm i}(R) + \omega/2$.

The next principal drawback is that the heterogeneity of the ionization continuum associated with the existence of closed channels of motion, which is the result of the strong nonadiabatic coupling of the electronic and nuclear motions in the intermediate Rydberg XY^{**} complex, has disappeared in this approach.

1.4 Theory of AI reaction

1.4.1 Near-Threshold AI Reactions of Atoms

We demonstrate the foregoing theory by the example of the behavior of the endothermic AI reaction of atoms near its threshold. In presenting the general theory, we have omitted a consideration of the subtle effects associated with the manifestation of the resonance structure of the valence (non-Rydberg) and the ionic configurations, which are particularly important when they are situated near the threshold of the spectrum. Although the described formal scattering theory allows us to analyze these special cases, we focus here on the simpler situation where during a motion along the dissociative term $U_{\beta\Lambda}(R)$ only the nearest closed vibronic channel (main series) in the Rydberg states is populated, leaving aside the peculiarities of the nonadiabatic rotational coupling. A semiclassical theory of the endothermic reaction near the threshold $E = E_\beta$ for AI was considered by Cohen (1976), Devdariani (1979), and Smirnov (1981). The total cross section can be represented as follows:

$$\sigma_{\mathrm{AI}}(E) = \frac{2\pi}{M_c} \sum_{\beta} \frac{g_\beta}{E + E_\beta} \sum_{v,j} (2j+1) \left\langle \left| T^{(j)}_{\beta,v}(E) \right|^2 \right\rangle \tag{1.30}$$

where g_β is the statistical weight of the dissociative state, M_c is the reduced mass of the colliding atoms, X and Y, j is their angular momentum, and E_β is the threshold energy of AI for the reaction in the center of mass system for β channel (summation over v is carried out over all open channels). For the case of the quasi-classical motion neglecting the j and l momentum coupling, the situation $j \neq 0$ differs from $j = 0$ by the shift of the electronic terms through the value $j^2/2M_\mathrm{c}R^2$. If for $j \neq 0$ the distortion of their form in the R range, responsible for transitions, can be neglected, then the probability $\langle |T^{(j)}_{\beta,v}(E)|^2 \rangle$ does not depend on the momentum j (this averaging corresponds to the conditions realized in the experiment). The corresponding criterion may be formulated as

$$\varepsilon_v \left| R_\mathrm{c}(\beta) - R_\mathrm{e} \right| R_\mathrm{e}^{-1} \ll \omega$$

where $R_\mathrm{c}(\beta)$ is the crossing point of ionic and valence terms in the vicinity of which the Frank–Condon transitions occurs, and R_e is the equilibrium internuclear distance in the XY^+ ion. When summing over j one must take into account also that the transition to the $XY^+(v)$ state is possible only if $\varepsilon_v > Bj^2$, where $B = 1/2M_\mathrm{c}R^2$ is the rotational constant of the XY^+ ion.

Under these conditions the averaged Rydberg resonances of the square modulus of the amplitudes are equal to (Golubkov and Ivanov 1988):

$$\left\langle \left| T^{(j)}_{\beta,v}(E) \right|^2 \right\rangle = \begin{cases} \bar{V}^2_{\beta v'}, & v' < v-1, \\ \bar{V}^2_{\beta v-1} \left[1 + \frac{\gamma_i(v)\bar{V}^2_{\beta v}}{\gamma(v)\bar{V}^2_{\beta v-1}} \right], & v' = v-1. \end{cases} \tag{1.31}$$

The quantities $\gamma_i(v)$ and $\gamma(v) = \gamma_i(v) + \gamma_\beta(v)$ are the rate of ionization and the total decay determined by the t expressions, $\gamma_i(v) = t^2_{vv-1}$, and $\gamma_\beta(v) = \bar{V}^2_{\beta v}$. The matrix element $\bar{V}_{\beta v}$ is equal to $\bar{V}_{\beta v} = \langle \chi_\beta | V_{\beta v}(R) | \chi_v \rangle = V_\beta(R_e)\alpha_{\beta v}$, where $\alpha_{\beta v} = \langle \chi_\beta | \chi_v \rangle$ (the index v' refers to the Rydberg channels open with the vibrational quantum number $v' \leq v - 1$). Substituting Eq. 1.31 in the general expression (Eq. 1.30) and summing over j for the partial cross sections, one has

$$\sigma^{(\beta)}_{AI}(E) = g_\beta \frac{4\pi^2 R_e^2 V_\beta^2}{E + E_\beta} \times \sum_{v'=0}^{v-1} \left[\alpha^2_{\beta v'} \varepsilon_{v'} + \alpha^2_{\beta v'+1} \frac{\gamma_i(v'+1)}{\gamma(v'+1)} \left(\varepsilon_{v'} \delta_{v',v-1} + \omega \left(1 - \delta_{v',v-1}\right) \right) \right]. \tag{1.32}$$

Here $\varepsilon_v = E - E_v$ is the electron energy in the v-th motion channel, and $\delta_{v,v'}$ is the Kronecker symbol. Note that all the parameters in Eq. 1.32 are the adiabatic system parameters that can be calculated in the framework of the existing theoretical methods or reconstructed from the absorption spectra.

Near the threshold, the total cross section of the AI reaction is a linear function of the energy ($E < \omega$):

$$\sigma_{\mathrm{AI}}(E) = \kappa E, \tag{1.33}$$

where the quantity κ is equal to

$$\kappa = 4\pi^2 R_e^2 \sum_\beta \frac{g_\beta V_\beta^2}{E + E_\beta} \left[\alpha^2_{\beta 0} + \alpha^2_{\beta 1} \frac{\gamma_i(1)}{\gamma(1)} \right]$$

That is, the threshold behavior in the quantum case is absolutely different from the law $E^{3/2}$, resulting in the semiclassical theory (Smirnov 1981; Devdariani 1979). This result has a simple explanation, because the transition matrix elements in the presence of the Coulomb field do not vanish at $E = 0$. Therefore, in the region $0 < E < \omega$ the cross section is proportional to the phase space angular momentum $\left(\sigma \sim j^2_{\max}\right)$, corresponding to the given value of the E energy, i.e., linearly with energy. Moreover, if Eq. 1.32 is to exclude the communication with the Rydberg states (putting $\gamma_1 = 0$) and to ignore the tunneling effects and calculate the Franck–Condon factors using the Landau–Zener approximation for their estimation, then

$$\alpha^2_{\beta v}(E) = \frac{\omega M_c^{1/2}}{\pi (2\varepsilon')^{1/2} F^{(c)}_\beta},$$

where $\varepsilon' = E - E_\beta^{(c)}$ (here $E_\beta^{(c)}$ and $F_\beta^{(c)}$ are the energy and the absolute value of the difference of forces at the crossing point of the ionic and dissociative terms). Then the formula (Eq. 1.32) may be rewritten as

$$\sigma_{\mathrm{AI}}^{(\beta)} = \frac{2\pi^2 R_e^2 V_\beta^2 (2M_c)^{1/2}}{F_\beta^{(c)}\left(E + E_\beta\right)} \sum_{\nu'=0}^{\nu-1} \left(\frac{\omega}{\nu'}\right)^{1/2} \left(E - \nu'\omega\right).$$

Replacing the summation over ν' by the integration, it is easy to obtain the known semiclassical result (Smirnov 1981):

$$\sigma_{\mathrm{AI}}^{(\beta)} = \frac{4\pi R_e^2 \Gamma_\beta (2M_c)^{1/2} \varepsilon'^{1/2}}{3F_\beta^{(c)}\left(E + E_\beta\right)}, \quad \left(\Gamma_\beta = 2V_\beta^2\right) \tag{1.34}$$

(the effective reaction threshold is equal to $E'_\beta = E_\beta + E_\beta^{(c)}$).

At the threshold of the new open channel $E = E_\nu$, the cross section (Eq. 1.32) shows a bend, the magnitude of which is characterized by the change in the cross-section derivative $\mathrm{d}\sigma_{\mathrm{AI}}/\mathrm{d}E$ in this point. The overall AI cross section behaves as

$$\sigma_{\mathrm{AI}}^{(\beta)} = \frac{f(E)}{E + E_\beta},$$

where $f(E)$ is increasing monotonically as a result of the successive opening of the new channels of the Rydberg XY^{**} complex autoionization decay. From Eq. 1.32 it is also implied that when

$$\alpha_{\beta\nu}^2 \left(\gamma_i / \gamma\right) \gg \sum_{\nu'}^{\nu-1} \alpha_{\beta\nu'}^2,$$

a virtual population mechanism of the intermediate Rydberg states is dominant. The formulae (1.31) and (1.32) refer to the case when the energy spread δ of the atomic beam exceeds the maximum interval $E_{\nu-1} < E < E_\nu$ between the Rydberg levels of the closed channels, i.e., $\delta > 1/\nu_\nu^3$. For the opposite case near the appearance threshold of each newly opened up channel, generally speaking, a fine structure has to be seen in the AI spectrum, namely in that part of it where $\delta \leq 1/\nu_\nu^3$.

At $\delta \to 0$ for the small Rydberg level widths $\left(\Gamma_\nu \ll 1/\nu^3\right)$, the AI cross section can be written as (Golubkov and Ivanov 1988)

$$\sigma_{AI}^{(\beta)} = \frac{4\pi^2 R_e^2 V_\beta^2}{\left(E + E_\beta\right)} \sum_{\nu'=0}^{\nu-1} \left[\alpha_{\beta\nu'}^2 \varepsilon_{\nu'} + \alpha_{\beta\nu'+1}^2 \Delta_{\nu'+1}\right], \tag{1.35}$$

$$\Delta_{\nu'+1} = \frac{\gamma_i\,(\nu'+1)}{\gamma\,(\nu'+1)}\left[\omega\,(1-\delta_{\nu',\nu-1}) + \delta_{\nu',\nu-1}\sum_{\nu\geq\bar{\nu}}^{\infty}\frac{1}{\nu^3}\eta\left(\frac{1}{2\nu^2}+\varepsilon_\nu\right)\right]$$

$$\bar{\nu} = \min\{\nu\}, \quad \nu \geq (2\omega)^{-1/2}$$

($\eta(x)$ is the step function), which indicates that along with breaks for the threshold values $E = E_\nu$ should be observed a "small" step (at the energies $E_* = E_\nu - 1/2\nu^3$) associated with the individual contribution of the individual Rydberg resonances. In particular, the discrete structure cross section should be clearly observed for weakly exothermic processes that do not require an initial kinetic energy to overcome the reaction threshold. In this case, the calculation should be carried out by the general formulas of the quantum scattering theory, without resorting to the pre-averaged probability of the process (Eq. 1.31). If $\delta \sim 1/\nu^3$, the step is naturally smoothed out, and for $\delta \gg 1/\nu^3$ it completely disappears. In this case, formula (1.35) transforms in Eq. 1.32.

According to Eq. 1.35, the general formula for the rate constant $k_{\mathrm{AI}}(T)$ of the endothermic reaction AI at temperatures $T \ll \omega$ can be written as

$$k_{AI}(T) = AS(T)T^{1/2}\exp\left(-\bar{E}_\beta/T\right), \tag{1.36}$$

where

$$A = 8\pi^2 R_e^2\left(\frac{2}{\pi M_c}\right)^{1/2}, \quad \bar{E}_\beta = \min\left\{E_\beta\right\},$$

$$S(T) = \sum_{\beta'} g_{\beta'} V_{\beta'}^2\left(\alpha_{\beta' 0}^2 + \alpha_{\beta' 1}^2\frac{\gamma_i}{\gamma T}\sum_{\nu>\bar{\nu}}^{\infty}\frac{\exp\left(-\bar{\varepsilon}_\nu/T\right)}{\nu^3}\right).$$

Here $\bar{\varepsilon}_\nu$ is the position of the Rydberg resonance, measured from the threshold of the reaction (the sum is taken over the configurations β' in $S(T)$ having a common threshold $\bar{E}_\beta$ of reaction). At low temperatures $T \leq 1/\bar{\nu}^3$ (where $\bar{\nu} \approx (2\omega)^{-1/2}$), Rydberg resonances can greatly affect the temperature dependence of the quantities $S(T)$ in Eq. 1.36. If $T \ll \bar{E}_\beta$, it occurs in the region with the exponentially small $k_{\mathrm{AI}}(T)$. The exception is the reaction with a low energy threshold $\left(\bar{E}_\beta \ll \omega\right)$. At higher temperatures ($T \gg 1/\bar{\nu}^3$), the value $S(T)$ becomes a constant (i.e., $S \approx \alpha_{\beta 0}^2 + \alpha_{\beta 1}^2\gamma_i/\gamma$) and the presence of the Rydberg resonances only affects its value. At $T \geq \omega$, for the evaluation of AI rate constant it is convenient to make use of the linear approximation of the cross section (Eq. 1.33), inserting $\kappa = \sigma_{\mathrm{AI}}(\omega)/\omega$. In this case the AI rate constant can be represented as follows:

$$k_{AI}(T) = A\left(1+\frac{2T}{\bar{E}_\beta}\right)T^{1/2}\exp\left(-\bar{E}_\beta/T\right), \tag{1.37}$$

where

$$A = \left(\frac{8}{\pi M_c}\right)^{1/2} \kappa \bar{E}_\beta .$$

To illustrate the foregoing theory we consider the reaction

$$\mathrm{N}\left(^2\mathrm{D}\right) + \mathrm{O}\left(^3\mathrm{P}\right) \rightarrow \mathrm{NO}^+\left(\mathrm{X}^1\Sigma^+\right) + \mathrm{e}^-, \left(\bar{E}_\beta = 0.38\ \mathrm{eV}\right) \tag{1.38}$$

The dependence of the total cross section for this reaction on the energy of the colliding particles was measured by Ringer and Gentry (1979), where it was shown that the process is most effective when the nitrogen atom is in the metastable ^{2}D–state and the oxygen atom is in the ground ^{3}P–state. The valent term positions of the molecule NO were taken from Lee (1977), where it is shown that the ion term U_i intersects with the diabatic terms of three valence configurations $\mathrm{A}'^2\Sigma^+, \mathrm{B}^2\Pi$, and $\mathrm{B}'^2\Delta$ near the equilibrium position. The state $\mathrm{B}'^2\Delta$ interacts with the Rydberg $nd\delta^2\Delta\left(\mathrm{X}^1\Sigma^+\right)$–series. The configuration $\mathrm{A}'^2\Sigma^+$ (correlating with the ground $\mathrm{N}\left(^4\mathrm{S}\right)$ and $\mathrm{O}\left(^3\mathrm{P}\right)$ states) interacts with the $p\sigma^2\Sigma^+\left(\mathrm{X}^1\Sigma^+\right)$–series. It is populated by the Landau–Zener transition from the term $\mathrm{I}^1\Sigma^+$ (the intersection occurs at the distance $R_\mathrm{c} \approx 3$, which lies outside the main transition region). The state $\mathrm{B}^2\Pi$ interacts with the $p\pi^2\Pi\left(\mathrm{X}^1\Sigma^+\right)$ series. We have not considered the configuration $L^2\Pi$ because of the smallness of the corresponding coupling constants (Golubkov and Ivanov 2001).

The general rule is when the atoms $\mathrm{N}\left(^2\mathrm{D}\right)$ and $\mathrm{O}\left(^3\mathrm{P}\right)$ approach and produce the nine valence states with the spin of 1/2, which spin weight is equal to 1/3. These states include three (two $^2\Sigma^+$ and one $^2\Sigma^-$) nondegenerate and six (respectively, three $^2\Pi$, two $^2\Delta$, and one $^2\Phi$) doubly degenerate states, the statistical weight of which is defined as $g_\beta = s_\beta/45$, where s_β is the degeneracy. The configuration interaction $\Delta_{\beta\nu}$ characterizes the splitting of the Rydberg and the valence dissociative terms and is related to the value V_β by the relationship $\Delta_{\beta\nu} = \pi^{-1/2} V_\beta$. The characteristics of the dissociative terms

$$F_\beta = \left|\frac{dU_\beta}{dR}\right|_{R_c^{(\beta)}}, \quad \varepsilon_\beta = \left(U_\beta - U_i\right)_{R_\mathrm{e}}$$

the potential splitting values, and the corresponding statistical weights of these configurations are taken from Golubkov and Ivanov (2001).

The calculation results performed using the formula (1.35), taking into account the three vibrational states ($\nu = 0$, 1, and 2) of the ion NO^+, are shown in Fig. 1.5. When calculating the total cross section corresponding to the partial cross section for the term $\mathrm{A}'^2\Sigma^+$, the term was multiplied by the probability of transition from the $\mathrm{I}^1\Sigma^+$ term, which is given by the Landau–Zener model with the $V_{\mathrm{IA}'} = 6\times10^{-3}$, the difference in the strength $F_{\mathrm{IA}'} = 1.22 \times 10^{-1}$, and the energy $E_{\mathrm{IA}}^{(\mathrm{c})} = 2.1 \times 10^{-2}$ at

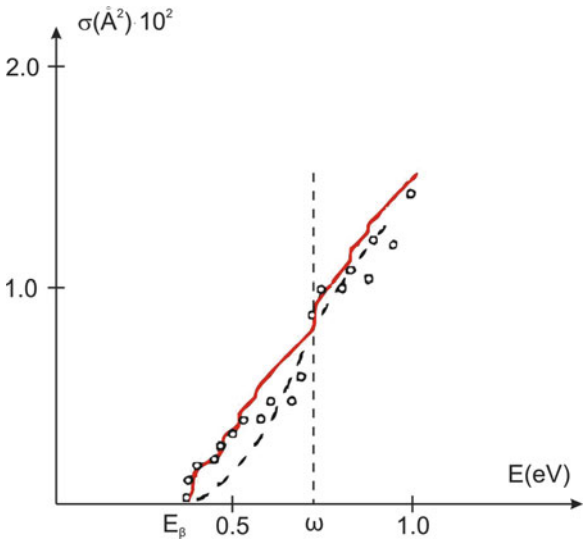

Fig. 1.5 The near-threshold AI cross-section behavior of the $N(^2D) + O(^3P) \rightarrow NO^+ + e^-$ reaction. The circles show the dependence of the experimental cross section on the collision energy (Ringer and Gentry 1979), the broken curve gives the theoretical results obtained in (Nielsen and Dahler 1979), and the full curve presents the result obtained from (1.35)

the intersection point of the terms (Lee 1977). A comparison with the experiment of Ringer and Gentry (1979) shows that satisfactory agreement is observed only near the threshold (at $E \leq 0.2$ eV). It should be noted that the data used in the calculation are not accurate enough, but the possibilities of experiments to measure the absolute reaction cross sections for associative ionization are limited (for example, the reaction systematic error is estimated as 35% (Ringer and Gentry 1979)). However, the experiment detects the "fine" structure of the cross section resulting from the contribution of the Rydberg states. The first step is near the reaction threshold; it corresponds to the contribution of the autoionizing states with $n = 7$ and $v = 1$. In addition, the linear approximation of the cross section near the threshold is fair here in the broad range of temperatures from 4,500 to 7,500 $K°$ with accuracy up to 15%. In particular, at the temperature $T = 4{,}500\,K°$ formula (1.37) gives $k_{AI} \approx 3.6 \times 10^{-13}\text{cm}^3/\text{s}$. Obtained at the same temperature dependence is in good agreement with the experiment.

Thus, the theory of MQD allows you to set the near-threshold dependence of the cross sections and reaction rate constants of associative ionization of atoms with the quantum effects and the contribution of the Rydberg states of the intermediate autodecay complex XY^{**} for endothermic (weakly exothermic) processes. In this case, the threshold behavior of cross sections of the endothermic reaction strictly follows the linear law $\sigma_{AI} \sim E$, in contrast to the predictions of the semiclassical theory (Nielsen and Dahler 1979). It also demonstrates the emergence of some important features of the "thin" sections of the structure (steps from the contribution of the Rydberg resonances) and the conditions of their manifestation in the temperature dependences of the rate constants.

1.4.2 Potential Curves of the Rydberg and Dissociative Configurations

Calculation of the matrix elements and Franck–Condon factors $\alpha_{\beta v}$ included in the near-threshold AI reaction theory for the case when the threshold energy $E_\beta \gg \omega$, and the excitation energy E^* of the X^* and Y atoms lies in infinity below the ionization limit requires information about the adiabatic potential curve behavior of the Rydberg $U^{**}_{n\rho\Lambda}(R)$ and the dissociative states at interatomic distances (from the equilibrium position R_e to the points of crossings $R_c^{(\beta)}$). Under these conditions, the integral theory of MQD (Golubkov and Ivanov 2001) allows us to obtain sufficiently reliable results for the direct AI process and the reverse reaction of dissociative recombination.

Modern quantum chemical methods for calculating of the adiabatic potential curves are well developed and widely used in the determination of the dissociation $X^* + Y$ and ionic XY^+ terms (Golubkov et al. 2002, 2003; Adamson et al. 2009). To construct the potential curves of the Rydberg states XY^{**}, they are of little use because this does not take into account the influence of states of the continuum. Nevertheless, this problem can be solved by the method of matching, as proposed by Golubkov et al. (2010). The problem solving here is possible because the quantum chemical calculations for small- and medium-sized atomic distances $R \leq n$ reproduce well the shape of the potential curves but have no control over the accuracy of their position on the energy scale. At the same time at large distances, $R \geq n$, the Rydberg terms are calculated simply in the framework of the MQD with the use of the finite radius pseudo-potential (Golubkov et al. 2010). Reliability of the results of this procedure is controlled by the precision used in the theory of scattering characteristics of slow electrons by the perturbing particle.

With increasing of the kinetic energy E_k of colliding X^* and Y particles, the theory should include more dissociative intermediate and final vibrational (and rotational) motion channels. However, as clearly demonstrated in Fig. 1.5, the AI cross section starting with $E_k > s\omega$ (where $s \geq 3$) is quite adequately described by the semiclassical theory (Nielsen and Dahler 1979), which essentially simplifies the situation. The overall picture (without regard to the dissociative continuum) is fundamentally changing with increase of the excitation energy E^*. Starting with the values of $n \geq 10$ the adiabatic potential curves of the intermediate complex XY^{**} (along with the increase in the total number of motion channels) in a wide range of distances $\Delta R \sim n$ have the pseudo-crossings of Rydberg states with different values of n and l with orbitally degenerate states (for $3 \leq l \leq n-1$), which split off from the Coulomb interaction because of the X atom (Golubkov et al. 2010).

Under these conditions, the overall pattern of pseudo-crossings essentially depends on the principal quantum number n and displays complicated "stochastic" behavior. Then the operator $\mathbf{t}$ in Eq. 1.28 becomes a function of the total energy E, which must be determined from the integral equation (1.12), giving the specificity pattern of terms for each discrete value of n. Additionally, there is a calculation problem of the matrix elements, determining the nonadiabatic coupling with the

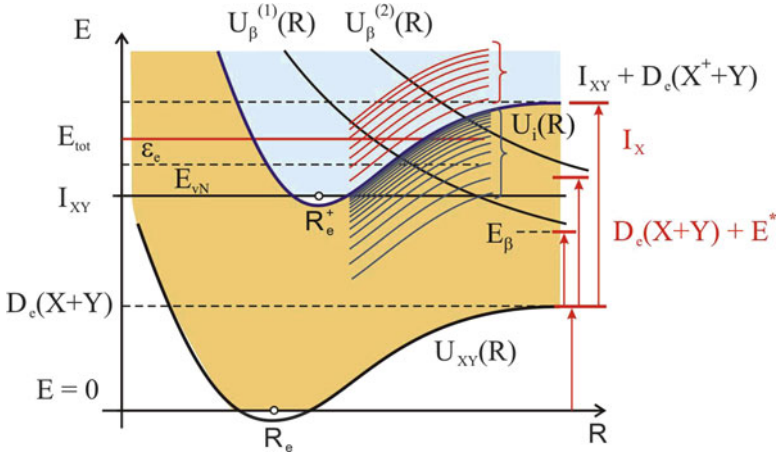

Fig. 1.6 Diabatic potential curves of the molecule XY for the case of $I_X < I_Y$. Terms $U_\beta^{(1)}(R)$ and $U_\beta^{(2)}(R)$ are responsible for the exothermic and endothermic AI reaction, respectively

vibrational motion, as it is necessary to account a broad range of the interatomic coordinates, which is a separate independent task. The problem becomes even more complicated when the bound states of the intermediate valence (non-Rydberg) X^*Y and ionic X^+Y^- configurations are included in the general scheme (Eqs. 1.13, 1.15, 1.21, 1.22, 1.23).

1.4.3 Stochastic Regime of AI Reaction Diffusion Approach

Provided at $I_X < I_Y$, the heat of the AI reaction depends on the initial excitation energy E^* of the X^* atom. Indeed, when at a distance of $R \to \infty$ the energy position $E^* + D_e(X+Y) > I_{XY}$ is located over the ionization threshold of the XY molecule, the AI reaction is exothermic (here I_{XY} and $D_e(X+Y)$ are the ionization potential and the dissociation energy of the XY molecule, respectively). In the opposite case, the endothermic process with a reaction threshold of $E_\beta = I_{XY} - D_e(X+Y) - E^*$ takes place. Moreover, subject to

$$E = E_k + E^* + D_e\ (X+Y) > I_{XY} + D_e\left(X^+ + Y\right) \tag{1.39}$$

(E, and $D_e(X^+ + Y)$ are the total and dissociation energies of the XY^+ ion), when the total energy of the system exceeds the threshold for dissociation of the $X^+ + Y$ ion channel, the exothermic reaction of the AI reaction should be suppressed markedly. The presence of exact equality (Fig. 1.6)

$$D_e(X+Y) + I_X = I_{XY} + D_e\left(X^+ + Y\right)$$

(I_X is the ionization potential of the X atom) permits us to rewrite Eq. 1.39 as $E_k + E^* > I_X$. Assuming that the difference $I_X - E^* = \frac{1}{2n^2}$ is the energy of the Rydberg electron, we finally get that it arises when $E_k > 1/2n^2$. Consequently, for a given initial kinetic energy of E_k the suppression of the AI reaction will occur when the principal quantum numbers

$$n > n_* = \frac{1}{\sqrt{2E_k}}. \tag{1.40}$$

From the law of conservation of the total energy conservation expressed in the form of

$$E_k + E^* + D_e(X + Y) - I_{XY} = \varepsilon_e + E_{vN}$$

(ε_e and E_{vN} are the released electron energy and the energy of the XY^+ ion rovibrational excitation), it follows that because of the strong nonadiabatic coupling of electronic and nuclear motions in the intermediate complex XY^{**} (which is responsible for the inhomogeneity of the ionization continuum spectrum), the formation of the ion XY^+ can be accompanied by vibrational and rotational excitation with the $E_{vN} \leq E^*$ energy. It is also expected, by Eqs. 1.15, 1.21, and 1.22, for the electron energy $\varepsilon \leq \omega$ the final rotational quantum number N can be large enough ($N \gg 1$) that it leads to a strong twisting of the XY^+ ion. It takes place as the result of the ionization continuum inhomogeneity through the nonadiabatic coupling between auto-decaying (ionization and predissociative) states of the closed channels. The latter can be a kind of manifestation of the AI dynamics, because statistically it is more advantageous (exothermic process).

This point means that in the general scheme must be included a large number of the vibrational v and the rotational N quantum ones. Therefore, the resulting spectrum of highly excited quasi-molecular states will contain a large number of interacting Rydberg series, and as a consequence, the dependence of the levels of the principal quantum numbers n for each series will be significantly irregular. The procedure for determining the quantum defect levels and their distribution on the relevant series in the general case is not unique. Moreover, starting with certain values, the classification levels of highly excited states of the system generally becomes impossible, i.e., comes to the stochastic regime (Casati et al. 1985; Lombardi et al. 1988; Gutzwiller 1990; Lombardi and Seligman 1993). A special technique is required because the solution of such a multichannel problem is extremely difficult. Expansion coefficients of the total wave function for this series for large values of n and N behave almost unpredictably, as is typical for multichannel-quantum systems (Golubkov and Ivanov 2001). It is also known that in regions of the strong nonadiabatic coupling (when the levels belonging to different series of energy are close) there is repulsion of the levels of the degenerate states by the interaction between them. Giving all these circumstances, it is advisable, in general, to refuse a classification of the interacting highly excited states and go to a random walk over the Rydberg levels in the transitions between them.

This is a strong justification for the utilization of the "diffusion model" in describing the stochastic dynamics exothermic AI process (Devdariani et al. 1988). Below we discuss the question about the stochastization of the molecular Rydberg states spectrum in more detail.

In the "diffusion model," it is believed that for the endothermic process under the passage of the image point of each pseudo-crossing of the dissociative $\beta-$state potential curve $U_\beta(R)$ and intermediate Rydberg $U^{**}_{n\rho\Lambda}(R)$ states of the XY^{**} quasi-molecule (mixed by the nonadiabatic coupling of electronic and nuclear motions), a change in the electron energy $\delta\varepsilon$ is small compared to the energy change for the entire act of collision, E_β. As a result, the act of the collisions leading to ionization is regarded as the diffusion of the initial excitation energy ε of the intermediate complex states. As a result of its semiclassical motion nature, the Rydberg electron collision process can be described in terms of the probability density population states $W(\varepsilon, t)$ with the energy ε at time t, which is known to be associated with R.

The quantity of the density $W(\varepsilon, t)$ satisfies the following equation (Devdariani et al. 1988):

$$\frac{\partial W(\varepsilon, t)}{\partial t} = -\frac{\partial j(\varepsilon, t)}{\partial \varepsilon} \tag{1.41}$$

where $j(\varepsilon, t) = -D(\varepsilon, t)\left(\partial W(\varepsilon, t)/\partial\varepsilon\right)$ is the excitation flow in the point ε at the time t, and $D(\varepsilon, t)$ is the diffusion coefficient in the energy space, equal to

$$D(\varepsilon, t) = \frac{1}{2}\int p\left(\varepsilon\varepsilon', t\right)\left(\varepsilon' - \varepsilon\right)^2 d\varepsilon' \cong \frac{\overline{\delta\varepsilon^2}}{2\delta t}. \tag{1.42}$$

Here $p(\varepsilon\varepsilon', t)$ is the transition probability per unit time between the states with energies ε and ε', $\overline{\delta\varepsilon^2}$ is the characteristic energy change in δt time transition. Equation 1.41 is solved together with the initial condition

$$W(\varepsilon, t \to -\infty) \to \delta(\varepsilon - \varepsilon_o)$$

and the boundary condition $W\left(\varepsilon = U_\beta(R), t\right) = 0$ corresponding to the single ionization probability. Analysis of the Eq. 1.41 solution shows that the initial delta distribution at the time of convergence to the distances at which the ionization exists broadens. For example, for thermal collisions of alkali atoms and $n \sim 10$ such a broadening is equal to $\Delta\varepsilon \approx 3.6 \div 7.3 \cdot 10^{-3}$ (Devdariani et al. 1988). The ionization probability as a function of the parameter ε_o increases to a maximum value when this parameter is of the order of $\Delta\varepsilon$ in the vicinity of $\varepsilon_o \sim U_\beta(R_c)$. The ionization rate constant decay with further rise of n is associated with the decrease of the ionization probability at small ε, that in this model takes into account the appropriate modification of the boundary conditions at $\varepsilon = U_\beta(R)$. It is true if this

value is the bound energy of one excited atom or the summed bound energies of both excited atoms. In this model, the value of the ionization is mainly determined by the parameter ε_o only, and this does not depend on whether it is the binding energy of one excited atom or the total binding energy of two excited atoms.

Concluding this section, we discuss the issue that is associated with the behavior of the considered quantum system for the case of the weak exothermic (or endothermic) AI process, when the bound electron energy E^* of the atom X^* and the electron energy ε satisfy the conditions $E^* + D_e(X + Y) \sim I_{XY}$, and $\varepsilon \leq \omega$, a number of the final rotational states of the formed XY^+ ion, is still large enough to take advantage of the diffusion model.

On the other hand, the dynamics of the AI for this situation can be studied in the framework of the MQD, and from the direct comparison of the results it can directly define the range of applicability of the diffusion model. It is of undoubted interest because the final settlement of this model is much simpler. Thus, it is desirable to reformulate the model so as to include the random motion over the states of the closed channels in an ionization continuum.

1.4.4 Stochastic Approach to the Highly Excited Intermediate Rydberg Complex

The term stochastization in the theory of complex systems is usually used in cases in which time is an argument of a function of random variable that determines the efficiency of process or phenomenon efficiency. The problem of the oscillator strengths of transitions to high molecular Rydberg states is also related to one of the fundamental problems of modern physics—"quantum chaos" (Cutzwiller 1990; Bellissard 1991; Knauf and Sinai 1997; Stockmann 1999). As is known, the hydrogen atom in an external magnetic field displays level fluctuations similar to those in complex atomic nuclei (Hasegawa 1988). Randomization of the energy spectrum can also be caused by interactions with buffer gas atoms (Golubkov et al. 2010).

We now discuss the possible causes of the spectrum randomization of the isolated highly excited Rydberg molecules, focusing on the conclusions of Lombardi and Seligman (1993), arising from a semiclassical consideration. According to the general theory the total wave function of the Rydberg molecule is represented as (Golubkov and Ivanov 2001)

$$\left|\Psi_q\right\rangle = \mathbf{G}\boldsymbol{\tau}\,|q\rangle. \tag{1.43}$$

Here $|q\rangle$ is the basic wave function of Rydberg configuration, $\mathbf{G}$ is Green's operator defined in Eq. 1.13, and $\boldsymbol{\tau}$ is the level-shift operator. It meets the equation similar

to Eq. 1.11 without a free **t** term. Therefore, the total wave function (Eq. 1.43) has the form:

$$\left|\Psi_q\right\rangle = \sum_i |i\rangle G^{(c)}\left(E - E_i\right) \langle i \,|\, \boldsymbol{\tau} \,|q\rangle + \frac{1}{\pi} \sum_\beta \int \frac{|\beta\rangle \langle \beta \,|\, \boldsymbol{\tau} \,|q\rangle}{E - E_\beta + i\gamma} \mathrm{d}E_\beta. \tag{1.44}$$

Hence, it is the superposition of a complete set of noninteracting basis states in a coordinate wide range of the selected electrons. In the case of diatomic molecule wave functions, $|q\rangle$ and $|i\rangle$ are given by Eq. 1.16, which are valid for arbitrary quantum numbers l and N.

A transition to the "chaotic" description of the orbitally degenerated and split by nonadiabatic rotation coupling of highly excited levels of diatomic Rydberg molecules was carried out by Lombardi and Seligman (1993). This approach does not account for coupling with vibrational and dissociative channels. The authors of this paper suggested that for the large quantum numbers l and N of Rydberg states the angular momenta $\boldsymbol{J}$, $\boldsymbol{l}$, and $\boldsymbol{N}$ are fixed, so they retained only one term in the expansion (Eq. 1.44) with fixed l and N. They applied MQD theory (Golubkov and Ivanov 2001) for determining the positions of the molecular energy levels. Essentially, this approximation eliminates the kinematic relationship between the weakly bound electron motion and molecule rotations for given total angular momentum $\boldsymbol{J}$. Use of such "truncated" Rydberg molecular wave functions for determining the respective dipole matrix elements (or time-dependent autocorrelation functions of dipole moments) on the basis of a correctly calculated energy spectrum can indeed reveal a random behavior.

This approximation is justified, once only one matrix element $\langle i \,|\, \boldsymbol{\tau} \,|q\rangle$ is large, with other ones being ignored. For large principal quantum numbers n such situations are rare. In most cases (especially in the case of strong nonadiabatic coupling), these matrix elements are generally comparable (Balashov et al. 1984). In this case, the repulsion of two closely spaced Rydberg levels belonging to different rotational series is determined substantially by the nonadiabatic interaction, which may be comparable to the distance between these levels. As in the case "d" by Gund, the energy difference between the ionization thresholds of these series under the condition $N \sim \omega / 2B$ is of the order of the oscillation frequency ω (B is the rotational constant of the molecular ion), where there is no reason to exclude the vibrational degrees of freedom from general consideration. Moreover, most highly excited Rydberg molecular states considered by Lombardi and Seligman (1993) are the autoionization states (see Fig. 1.6). The dynamics of electron behavior for these states is described in terms of the scattering theory, where the energy eigenvalues and corresponding wave functions are complex (Golubkov and Ivanov 2001).

The problem becomes even more confused if the valent (non-Rydberg), ionic, and dissociative configurations being essential components of the electronic structure of the excited molecules and having a significant effect on the resulting

spectrum picture are included in the consideration. For example, in the presence of predissociative valent configurations their level widths could exceed significantly the distance between the Rydberg levels (Golubkov and Ivanov 1990). Giving all these circumstances, the approach developed by Lombardi and Seligman (1993) should be regarded as a model, although not without its appeal.

The science of "quantum chaos," having been actively developed during the past 20 years, is still fairly young. As we can see, it is still far from completeness for investigating molecular systems. As in the stationary formulation of the problem random effects are absent, and the quantum mechanics of excited molecules is in itself a complex and self-discipline, chaotic solutions can occur in exotic situations using the approximate approaches only. The ranges of applicability of these approximations are not always obvious, although sometimes they can lead to positive results. This limitation is especially true of the Coulomb problem, where a striking example of this kind is the coincidence of the results of the numerical calculations of the dipole elements (Picart and Edmonds 1979), and of analytical ones (Golubkov et al. 1996b), obtained in the semiclassical approximation, respectively.

1.5 Chemo-Ionization Involving Atoms in Low-Lying Excited States

Let us now discuss the experimental facts accumulated over the past two decades that are an illustration of the theory just presented and put it ahead of fundamentally new problems. Therefore it is natural that we begin with a presentation of the results obtained for the AI and PI reactions involving atoms in low-lying excited states.

1.5.1 Metastable Atoms

1.5.1.1 Pair Collisions of Metastable Atoms of Inert Gases

Shock radiation kinetics of plasma taking into account the electron–atom and photo processes does not overlap all possible types of the charged particle balance in the plasma. For example, the ionization processes involving $He(2^3S)$ atoms can proceed through the following channels:

$$\mathrm{He}\left(2^3\mathrm{S}\right) + \mathrm{He}\left(2^3\mathrm{S}\right) \rightarrow \mathrm{He}^+ + \mathrm{He} + \mathrm{e}^- \quad \mathrm{PI} \tag{1.45}$$

$$\rightarrow \mathrm{He_2}^+ + \mathrm{e}^- \quad \mathrm{AI} \tag{1.46}$$

$$\mathrm{He}\left(2^3\mathrm{S}\right) - \mathrm{He}\left(2^1\mathrm{S}\right) \rightarrow \mathrm{He}^+ + \mathrm{He} + \mathrm{e}^- \quad \mathrm{PI} \tag{1.47}$$

$$\rightarrow \mathrm{He_2}^+ + \mathrm{e}^- \quad \mathrm{AI} \tag{1.48}$$

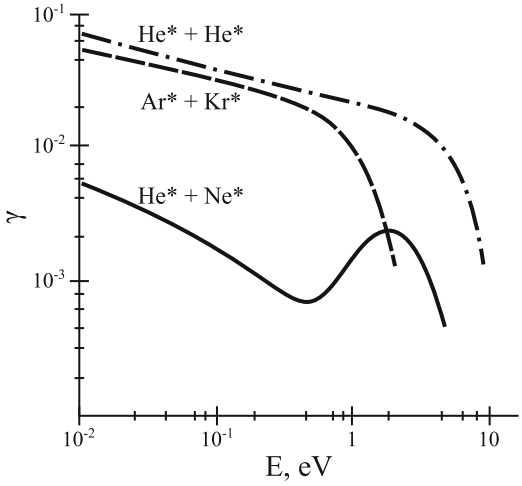

Fig. 1.7 Branching ratio $\gamma = \sigma_{AI}/(\sigma_{AI} + \sigma_{PI})$ as a function of the particle energy

where electrons produced in the channel (Eq. 1.45) have the energy 14.6–15.6 eV, and the spectrum is shifted to higher energies in the channel of Eq. 1.46. The total excitation energy of heavy particles in low-temperature plasma is much greater than the kinetic energy of free electrons. Therefore, PI and AI channels (Eqs. 1.45, 1.46, 1.47, 1.48), called chemo-ionization, play an important role in low-temperature plasma, and especially in cryogenic plasma and plasma without current. The possibility of the simultaneous existence of these two channels takes place because the total energy (kinetic + potential) conservation of the heavy particles before and after the collision is required (Fig. 1.7).

The PI and AI cross sections involving the metastable helium atoms were calculated by Neynaber et al. (1978). The resulting $\sigma_{AI} + \sigma_{PI}$ total cross section of the reaction $He(2^3S) + He(2^3S)$ in the energy range $E = 0.01$–0.13 eV within an experimental error ($\pm 30\%$) coincides with the results of the beam experiments (Garrison et al. 1973). However, the value of the branching factor $\gamma = \sigma_{AI}/(\sigma_{AI} + \sigma_{PI}) = (4.6 \pm 0.6) \cdot 10^{-2}$ obtained in by Bellissard (1991) at the collision energy $E = 0.033$ eV essentially differed from the calculated data (Müller et al. 1991; Devdariani et al. 1983) (see Fig. 1.7). The foregoing is clearly illustrated in Table 1.1.

For inert gases, a part of the spectrum regarding the reasonably fast electrons is associated with the AI process, but for the slower electrons it mainly results from the PI process. The spectra of plasma electron spectroscopy is averaged over the Maxwellian distribution of particles (Fig. 1.8) at $T = 300$ K.

The concentration of the metastable atoms in the active phase of the discharge is of the order of 10^{11} cm^{-3} here, but the electron energy resolution is 0.2 eV. The origin of the energy is located at the maximum of the electron energy

Table 1.1 Total chemoionization cross sections $\sigma_t = \sigma_{AI} + \sigma_{PI}$ and branching ratios of the reactions $\gamma = \sigma_{AI}/(\sigma_{AI} + \sigma_{PI})$ for the $He(2^3S) - He(2^3S)$ and $He(2^3S) - He(2^1S)$ collisions as functions of kinetic energy E

References	E, 10^{-3} eV	σ_t (10^{-16} cm^2)	γ
$He(2^3S) + He(2^3S)$			
Müller et al. (1991) theory	1	318	0.09
	33	106	0.032
	60	92	0.023
Müller et al. (1991) experiment	1.6	—	0.07 ± 0.03
	61	—	0.03 ± 0.03
Garrison et al. (1973) experiment	33	112 ± 30	0.046 ± 0.006
Garrison et al. (1973) experiment	33	135 ± 23	0.07 ± 0.04
Kolokolov and Kudryavtsev (1989) theory	33		0.07 ± 0.03
$He(2^3S) + He(2^1S)$			
Müller et al. (1991) experiment	1.6	859 ± 255	0.14 ± 0.03
	61	193 ± 92	0.08 ± 0.03
Devdariani et al. (1983) theory	33		0.16 ± 0.06

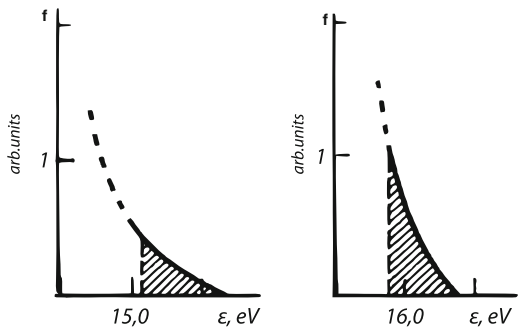

Fig. 1.8 Electron energy distribution function under the afterglow discharge conditions (Adapted from Bezuglov et al. 1994)

distribution function. The electronic spectra correspond to two channels of the chemo-ionization: (1) $He(2^3S) + He(2^3S)$ and (2) $He(2^3S) + He(2^3S)$. The shaded region (in Fig. 1.8) corresponds to the process of AI. A quantitative interpretation of the spectrum allows us to draw the following conclusions. The share of AI in the ionization of symmetrical collisions of 2^3S atoms is 7% ± 4%. For the asymmetrical $2^3S - 2^1S$ transition involving the formation of molecular ions in high vibrational excited states, it is 16% ± 6%. If the concentration of metastable atoms considerably exceeds the plasma electron concentration, which is realized with the fast decrease of the electron temperature T_e in the afterglow plasma with nonequilibrium recombination, increase of degree of ionization is observed after the discharge current disappears.

A comparative analysis of theoretical and experimental spectra of plasma electron spectroscopy allows us to estimate the dissociation energies of the quasi-molecules $He(2^3S) + He(2^3S)$ and $He(2^3S) + He(2^1S)$, which are equal to 0.9 ± 0.2 eV and 0.6 ± 0.2 eV, respectively. The calculation of the rate constants of

the polarization capture demonstrated an increase in the values of the rate constants for the colliding pairs $He(2^3S) - He(2^1S)$ and $He(2^1S) - He(2^1S)$ comparable with $He(2^3S) - He(2^3S)$, which was confirmed in the experiment (see Table 1.1). It follows that the measured and calculated value of the rate constants of reactions (1.45, 1.46, 1.47, 1.48) should depend significantly on the relative populations of the metastable states in the entrance channel of reaction.

The main component in the decaying plasma is the triplet metastable $He(2^3S)$ atoms as a result of an effective quenching of the singlet metastable $He(2^1S)$ atoms by an electron impact at the time of the order of 10^{-4}s. The singlet metastable states play the main role in the active phase of the discharge and the early afterglow of plasma. The He^{2+} ions are formed here in the upper vibrational states. The time of the arrival at the ion collector in the beam experiments is of the order of 5×10^{-6}s; therefore, the vibrationally excited molecular ions with shorter lifetimes should not register.

In addition, destruction channels of the upper vibrationally excited states of the molecular ions leading to their dissociation in plasma usually occur. Therefore, we should expect a decrease of the value γ obtained by the mass spectrometric diagnostics of the helium plasma if the helium pressure increases. It is possible that this is connected with one of the reasons for the difference of the value γ with the results obtained in plasma experiments. The ionization constants measured in the decaying plasma by plasma electron spectroscopy for binary metastable atom collisions of helium, neon, argon, krypton, and xenon atoms at $T = 300$ K are 1.0–$1.5{\cdot}10^{-9}$ cm^3 s^{-1} (Kolokolov and Kudryavtsev 1989).

Constants measured for reactions involving two atoms $Ne(^3P_2)$ are three times smaller. According to the same data, the values γ lie in the range 0.05–0.10, close to similar values for helium and the value of γ for the asymmetrical Ar + Kr process. In the latter case, the constant value is $3.1 \pm 0.6{\cdot}10^{-9}$ cm^3 s^{-1} (Kolokolov and Kudryavtsev 1989).

As a result, we distinguish the following two important implications for low-temperature plasma physics. First, the ionization rate constant for the pair collisions of metastable atoms of the inert gases at room temperature, where the dominant channel is the formation of the atomic ions, is of the order of 10^{-9} cm^3 s^{-1}. Second, at the energy $E < 0.1$ eV, the coefficient γ increases with decrease in energy. Consequently, the relative yield of the molecular ions in the cryogenic plasma is markedly increased.

1.5.1.2 Interactions Between Metastable and Normal Atoms (Asymmetrical Collisions)

Investigations of chemo-ionization in thermal PI collisions with $He(2^3S)$ and $H(1^2S)$ (or deuterium) atoms

$$He\left(2^3S\right) + H\left(1^2S\right) \rightarrow He + H^+ + e^- \tag{1.49}$$

Table 1.2 Total quenching constants of the metastable states of the inert gas atoms by unexcited alkali atoms and zinc atoms (Klyucharev and Vujnovic 1990)

Collision partners		$k,\cdot 10^{-10}$ cm^3 s^{-1}	
		Theory[a] $T = 300$ K	Experiment
He(2^3S)	Zn	9.2	5.1 ± 1.5
	Na	8.1	7.7 ± 1.5
	K	9.0	12.0 ± 2.4 $T = 350$ K
	Rb	9.1	4.5 ± 0.9
	Cs	9.7	4.4 ± 1.6 $T = 450$ K
He(2^1S)	Cs	–	15 ± 6
Ne(^{3}P$_0$)	–	31 ± 9 $T = 450$ K	
Ne(^{3}P$_2$)	–	30 ± 9	

[a]Estimates are obtained in the framework of the polarization model (all the values of the quenching constants with the exception of the neon atom can include the components of ionization)

were carried out by Merz et al. (1994) by high-resolution electron spectroscopy, aimed at increasing of the types of collision partners: hydrogen and deuterium, and the metastable atoms of heavy inert gases.

The rate constant of the dissociative recombination reaction

$$K_\beta\left(T_\mathrm{i}^\mathrm{f}, T_\mathrm{e}\right) = \left(\frac{8}{\pi T_\mathrm{e}^3}\right)^{1/2} \int_0^\infty \sigma_\beta\left(T_\mathrm{i}^\mathrm{f}, \varepsilon\right) \exp\left(-\varepsilon / T_\mathrm{e}\right) \mathrm{d}\varepsilon \tag{1.50}$$

as a inverse process of the AI reaction has been studied earlier in the framework of the MQD theory (Hasegawa 1988), where the rate constants of the dissociative recombination of H_2^+, HD^+, and D_2^+ were calculated and a two-temperature dependence of the rate constant of the dissociative recombination was proposed. Here T_i^f is the rotation molecular temperature, T_e is the temperature of electrons, ε is the electron energy, and σ_β is the cross section of the reaction.

Note that according to the reported data (Hasegawa 1988; Balashov et al. 1984) the rates of the dissociative recombination for the asymmetrical molecular ions were correlated with the relevant sections of their formation in the reaction (Eq. 1.49).

Data obtained from the total quenching constants of metastable states, which were measured in the afterglow of a pulsed discharge for the reaction PI, involving the rare gas metastable atoms and the normal atoms Zn, Na, K, Rb, and Cs, are presented in Table 1.2. By definition, these results correspond to the upper boundary values of the process constants. As can be seen from the table, in accordance with the rule of conservation of total spin angular momentum of the system, the constant k_PI for the He($2^3\mathrm{S}_1$) + Cs($6^2\mathrm{S}_{1/2}$) pair is greater than for the He($2^1\mathrm{S}_0$) + Cs($6^2\mathrm{S}_{1/2}$) pair.

There are also papers that demonstrate conservation of total electron spin for the optically oriented metastable helium atoms in the reaction He $(2^3S_1) + A$, where A are the atoms of Cd, Ca, Zn, Sr, Ba, Mg, Pb, Yb, and Eu (for instance, Klyucharev (1993)).

The optical orientation of metastable helium atoms can be used to study the PI reactions with unexcited molecules M:

$$\mathrm{He}\left(2^3S_1\right) + \mathrm{M} \rightarrow \mathrm{He}\left(1^1S_0\right) + \mathrm{M}^+ + \mathrm{e}^- \tag{1.51}$$

It is found that the value of polarization of the electrons in experiments on ionization of CO, CO_2, and N_2O molecules by the optically oriented 2^1S_0 helium atoms is close to the initial polarization of metastable atoms (Klyucharev 1993). The effect of polarization transfer (with conservation of the total electron spin) was also noted in the case of collisions of metastable helium atoms in the 2^3S_1 states with the nitrogen molecules (Klyucharev 1993). There are also papers that demonstrate the conservation of total electron spin for the optically oriented metastable helium atoms in the reaction He$(2^3S_1) + A$, where A are the atoms of Cd, Ca, Zn, Sr, Ba, Mg, Pb, Yb, and Eu (Klyucharev and Bezuglov 1983).

The efficiency of the atomic and molecular processes involving rare gas metastable atoms is different for the singlet and triplet states, and at a collision velocity $\upsilon >> 105$ cm s^{-1} their ratio asymptotically tends to 1 (Klyucharev and Vujnovic 1990). The molecular ions in the reactions involving the atoms Ne$(^3P_2)$ and the molecules N_2, CO, and CO_2 are more than 90% of the product yield, and an isotope effect plays a significant role here (Klyucharev 1993). A drop in the values of the PI reaction rate constants in the thermal collisions of the metastable inert atoms with CO, CO_2, H_2, O_2, N_2, and nitrogen-containing molecules is common for all these pairs with a energy decrease in the range 0.03–0.1 eV. The rate constants are of the order of 10^{-10} to 10^{-9} cm^3 s^{-1} ($E \approx 0.03$ eV), which indicates that intermediate quasi-molecule weakly bound states with a potential depth less than 0.03 eV are formed during the reaction.

Note that, in general, the total electron spin S of the interacting particles must not be conserved, as it takes place in the case of the excitation transfer from the resonant excited xenon atom $^3P_1$ to the CO molecule. The case of LS coupling is an exception to the rule only when the spin of the system is a "good" quantum number. This relationship breaks down if the atomic weight of the interacting particles is increasing. If the reaction occurs at the internuclear distances where a relativistic interaction is of the order of (or greater than) the electrostatic one, the projection of the total electron angular momentum on the internuclear axis Ω is the motion integral. At the same time, the width of the quasi-stationary term should decrease with increase of a projected Ω, because the ionizing electron acquires a large orbital momentum and interacts weakly with the ion core. The simultaneous use of the results of the optical measurements and electron spectroscopy techniques allows us to evaluate the efficiency of the forming of the excited charged particles in the PI reaction.

Table 1.3 Rate constants of the excited ion formation in the asymmetrical thermal collisions of zinc subgroup atoms with metastable helium atoms

Collision partners	Ion state	$k,\cdot 10^{-11}$ cm^3 s^{-1}
$He(2^1S_1) + Zn(4^1S_0)$	$3d^9\ 4s^2\ ^2D_{5/2}$	8 ± 2
	$3d^9\ 4s^2\ ^2D_{3/2}$	2.0 ± 5
$He(2^1S_1) + Zn(4^1S_0)$	$3d^9\ 4s^2\ ^2D_{5/2}$	30 ± 6
	$3d^9\ 4s_2\ ^2D_{3/2}$	16 ± 6
$He(2^1S_1) + Zn^*(4^3P_2)$	$6s^2\ S_{1/2}$	30 ± 7
	$5p^2\ P_{3/2}$	60 ± 15
	$5p^2\ P_{1/2}$	25 ± 5
$He(2^3S_1) + Cd(5^1\ S_0)$	$4d^9\ 5s^2\ ^2D_{5/2}$	18 ± 6
	$4d^9\ 5s^2\ ^2D_{3/2}$	12 ± 5
$He(2^3S_1) + Cd^*(5^3P_2)$	$5f^2\ F_{7/2}$	2 ± 1
	$5p^2\ P_{3/2}$	2.0 ± 0.7
	$6d^2\ D_{5/2}$	30 ± 8
	$6d^2\ D_{3/2}$	20 ± 6
	$4f^2\ F_{7/2}$	50 ± 10
	$4f^2\ F_{5/2}$	40 ± 10
	$7s^2\ S_{1/2}$	8 ± 2
	$6p^2\ P_{3/2}$	2.0 ± 5
$He(2^3S_1) + Hg^*(6^3P_2)$	$7p^2\ P_{1/2}$	30 ± 6

For example, we present the data on the formation of ions in the ground and excited states in this reaction:

$$He\left(2^3S_1\right) + Cd\left(5^1S_0\right) \rightarrow He\left(1^1S_0\right) + Cd^+ + e^- \tag{1.52}$$

which were obtained using the optical and the electron spectroscopy. Within their error they give the following results. The 20% of the quenching collisions in the optical spectroscopy and 30% in the electron spectroscopy lead to the formation of excited cadmium ions, ^2D_J.

Table 1.3 shows the rate constants of the ion excitation state by collisions of the zinc subgroup atoms with the metastable helium atoms (Tolmachev 1982).

1.5.1.3 Pair Collisions of the Metastable Atoms

The lower triplet $^3P_2$ and $^3P_0$ metastable states of the zinc subgroup atoms (Zn, Cd, Hg) can be occupied by the intercombination optical transitions from the ground atom state. In this case, the following chemo-ionization scheme can be implemented, which includes a set of processes:

$$Hg\left(6^1S_0\right) + h\upsilon \rightarrow Hg\left(6^3P_1\right) \tag{1.53}$$

$$Hg\left(6^3P_1\right) + N_2 \rightarrow Hg\left(6^3P_0\right) + N_2{}^* \tag{1.54}$$

$$\mathrm{Hg}\left(6^3\mathrm{P}_1\right) + \mathrm{Hg}\left(6^3\mathrm{P}_1\right) \rightarrow \mathrm{Hg}^+{}_2 + \mathrm{e}^- \tag{1.55}$$

$$\mathrm{Hg}\left(6^3\mathrm{P}_1\right) + \mathrm{Hg}\left(6^3\mathrm{P}_0\right) \rightarrow \mathrm{Hg}^+{}_2 + \mathrm{e}^- \tag{1.56}$$

$$\mathrm{Hg}\left(6^3\mathrm{P}_0\right) + \mathrm{Hg}\left(6^3\mathrm{P}_0\right) \rightarrow \mathrm{Hg}^+{}_2 + \mathrm{e}^- \tag{1.57}$$

Collisions of the second kind of the optically excited $6^3\mathrm{P}_1$ hydrargyrum (helium) atom and a molecule of nitrogen lead to the population of $6^3\mathrm{P}_0$ metastable state with a concentration three orders of magnitude greater than the population of the emitting $6^3\mathrm{P}_1$ level.

The rate constant of the process (Eq. 1.57), which is the main ionization channel under the experimental conditions, equals $k = (4.0 \pm 0.8)\cdot 10^{-10}$ cm^3 s^{-1} at $T = 295$ K. It agrees with the calculation result obtained in the framework of the polarization capture theory and allows us to treat this process as a zero-threshold one (Klyucharev 1993). For the case of the cadmium atom, the values of the chemoionization constants obtained in the same way for the unit $5^3\mathrm{P}_{0,1,2}$-state value are equal to 4×10^{-12} cm^3 s^{-1} at $T = 575$ K. The double excitation energy of the $6^3\mathrm{P}_0$ state of the hydrargyrum (mercury) atom is 9.34 eV, which is higher than the ionization potential of 10.43 eV of the normal atom, leading to the assumption of the zero-threshold nature of the process and to an estimate of the molecular ion dissociation energy equal to $\mathrm{De}^+\left(\mathrm{Hg}_2^+\right) \geq 1$ eV.

Change of the electrokinetic parameters of the gas discharge plasma and the formation of the current-free plasma in the hydrargyrum vapor in the resonance radiation are associated, for example, with the reaction (Eq. 1.57) of chemoionization (Fig. 1.9). The resulting free electrons may participate in the balance of the level populations of the laser to mercury vapor.

Discussion of the literature data on the constants of chemoionization in thermal collisions with metastable atoms shows that the rate constants of zero-threshold reactions may be as high as 10^{-6} to 10^{-10} cm^3 s^{-1}.

1.6 Ionization in Collisions Between Atoms in the Resonant Excited States

The sequence of related collisional processes leading to the effective ionization of the medium can be realized when atoms are excited into a resonant state. Let us consider the main types of the symmetrical collisions for this case, which include (1) the chemoionization process in pair collisions of the excited atoms,

$$\mathrm{A}^* + \mathrm{A}^* \rightarrow \begin{cases} \mathrm{A}_2^+ + \mathrm{e}^-, & (1.58) \\ \mathrm{A}^+ + \mathrm{A} + \mathrm{e}^-; & (1.59) \end{cases}$$

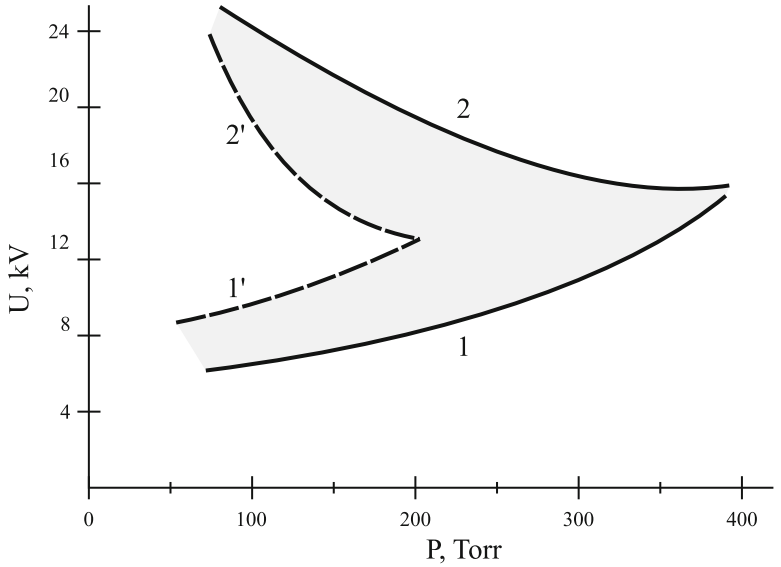

Fig. 1.9 *Upper* and *lower* ranges of values for the stress field of the discharge in nitrogen without (curves $1'$, $2'$) and with the addition of (curves 1, 2) a small admixture of mercury atoms

(2) the two-step ionization processes with the transfer of excitation energy,

$$A^* + A^* \rightarrow A^{**} + A, \tag{1.60}$$

and transition processes in the ionization continuum by the AI and PI, as well as the formation of the ion pair

$$A^{**} + A \rightarrow \begin{cases} A_2^+ + e^-, & (1.61) \\ A^+ + A + e^-; & (1.62) \\ A^+ + A^-. & (1.63) \end{cases}$$

At the same time there is a wide range of conditions in which the collisional processes involving atoms in the emitting states can give a significant contribution to the ionization. Thus, an ensemble of the excited states formed in an absorbing medium, irradiated by light, in general, is a potential source of the processes leading to the ionization. For example, if the external light field is "weak" (for the field strength $E < 10^6$ V cm^{-1}), and multiphoton excitation and ionization do not occur, the population of excited alkali metal atoms resulting from absorption can be induced by collisions.

Considering the ionization of the absorbing medium in the single-component weak light fields with photon energy less than the ionization potential of the atom, there are two primary ionization mechanisms: the photo-ionization of the excited states and ionization in thermal collisions of atoms. Reactions of this type occur in experimental facilities and in various plasma chemical devices in

which there are excited atoms and photons, although the fundamental difference between multiphoton ionization of the collision step process takes place when the characteristic lifetimes of the excited atom absorption and scattering are separated in time. Moreover, in the case of "weak" light fields, nonlinearity in the external radiation intensity process of the ionization by the collision of two pairs of excited particles, for example, the resonant excited alkali metal atoms, is possible.

1.6.1 Binary Collisions of Alkali Atoms

The first series of quantitative measurements of the constants AI of alkali metal atoms was carried out using the optical excitation of the medium in the regime of a radiation transport, which allows obtaining a uniformly excited medium volume of 100 cm^3 to be relatively easy (Bezuglov et al. 1994). The photo-ionization of excited atoms can be used as a diagnostic method in studies of chemo-ionization processes. Recently, a method for measuring the ionization rate constants of the optically excited atoms has been developed that can be used for measurement of photo-ionization currents in relatively simple form. However, for atoms with a low vapor pressure, for example, rare earth elements, such studies are hard to conduct because it is difficult to obtain the vapor of these elements in the volume of the reaction (Klyucharev 1993). However, this difficulty can be eliminated by using optical excitation of the atomic beam.

Previously it was thought that the role of collisions inside the beam is negligible. However, as calculations show, the real atomic beam average relative velocity is reduced by approximately three times compared to the gas-filled cell at the same temperature (Bezuglov et al. 1987).

For a qualitative analysis of the mechanism of AI atoms, it is necessary to know the parameters of the terms of the molecular ions and quasi-molecules involved in the entrance and exit channels of the reaction. For ions of alkali atoms, the dissociation energy D_e^+ exceeds the dissociation energy of the molecules; therefore, it is realized otherwise in the molecule and hydrogen molecular ions.

The AI processes from the first excited levels of the alkali metal atoms are so specific that they should be, apparently, in a separate class of endothermic ion–molecule reactions. These conditions are associated with dipole transitions from the atom ground states and can be efficiently populated by the optical excitation, which opens wide possibilities of experimental investigations of AI in binary collisions of the resonantly excited atoms. The first quantitative results were obtained under the optical excitation of a vapor-filled cell in the mode of the resonance radiation transfer, which is formed by the equilibrium Maxwell distribution of energies of the excited atoms at a controlled temperature T (Devdariani et al. 1978).

In the next stage, the temperature dependence of the photo-ionization rate constants of the reaction, occurring in collisions of resonantly excited atoms, is found. It is determined by the activation energy and the AI cross section as a function

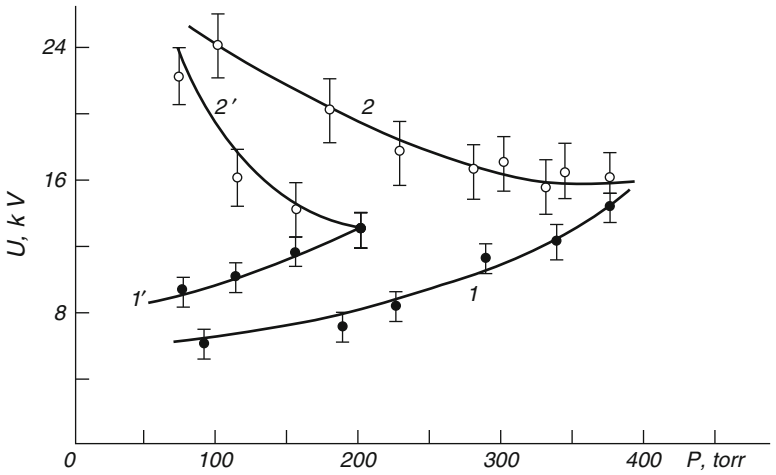

Fig. 1.10 Dependence of the molecular ion current on the square of the resonance level concentration

of energy. Figure 1.10 shows the dependence of the IAI ion current from the cell with cesium vapor on the square of the concentration of excited atoms produced in the optical excitation resonant states, in the mode of the resonance radiation transfer. The measurements were made when the cesium vapor pressure was 10^{-3} to 10^{-2} mmHg at $T = 425$ K. We see that the dependence IAI $= f(\mathrm{N}^2(6^2\mathrm{P}))$ is linear in the entire range of the vapor pressure. Similar associations were observed for other alkali atoms (Rb, Na, K). The temperature dependence of the chemo-ionization rate constants shows that this process has a threshold with the corresponding value of the activation energy ΔE.

A model representation of the unsplit covalent potential curve is valid for the quasi-molecule states formed from the atoms in the ^{2}S state. In fact, 24 of the intermediate quasi-molecule states correlated at $R \to \infty$ with two n^2P excited alkali atom states are involved in the reactions (1.58) and (1.59). The model used assumes that the resulting values describe one effective potential curve instead of the beam real terms.

There are few theoretical studies of AI processes involving the resonantly excited heavy alkali atoms in the literature. The expression for the constant $k(T)$ of the endothermic process for cesium and rubidium atoms, with taking into account the twist effect, was obtained by Klyucharev and Vujnovic (1990) (Table 1.4).

Devdariani (1979), based on the experiment to pair collisions of atoms 2Cs(6^2P) and 2Rb(5^2P), and using the semiclassical approximation to the Maxwellian atomic velocity distribution in the thermal energy range, described the constant process of Eq. 1.58 by the expression

$$k_i(T) = \pi V_c R_c^2 \gamma(T) \exp\left(-U_0(R_c)/T\right) \tag{1.64}$$

Table 1.4 Rate constants and activation energy ΔU in binary collisions of resonantly excited alkali atoms

Collision partners	ΔU, eV	k,·cm^3 s^{-1}	
2Cs(6^2P)	0.33 ± 0.04	(2 ± 0.2)·10–13,	$T = 425$ K
2Rb(5^2P)	0.20 ± 0.03	(3.2 ± 0.4)·10–13,	$T = 470$ K
2K(4^2P)	≤ 0.1	(9 ± 2)·10–13,	$T = 500$ K
2Na(3^2P)	–	(3.8 ± 0.4)·10–11,	$T = 580$ K
2Li(2^2P)	>0.5	10–15 ÷ 10–16,	Estimate

Table 1.5 Constants of the AI process in the binary collisions of the sodium atoms in resonance states

Experiment	Excited states	T, K		k, 10^{-11}, cm^3 s^{-1} (Bezuglov et al. 1987, 1989)
Gas cell	$3^2P_{1/2,3/2}$	T_g	580	3.8
Gas cell	$3^2P_{1/2,3/2}$	T_g	650	1.1*
Gas cell	$3^2P_{1/2,3/2}$	T_g	596	2.8
Single beam	$3^2P_{3/2}$	T_s	580	0.03*
Crossing beams	$3^2P_{3/2}$	T_s	575	3.4*
Laser cooling	$3^2P_{3/2}$	T_{cool}	0.75×10^{-3}	1.1

Note: Here T_g is the temperature in the gas cell, T_s is the temperature of the source beams, and T_{cool} is the temperature of ultracold atoms in the laser trap. The asterisk (*) indicates constant values that were obtained self-consistently by Bezuglov et al. (1989) from the experimental data incorporating measurements in a vapor cell, a single effusive beam, and two crossing beams

where

$$\gamma(T) = (2\pi\mu T)^{1/2}\,\Gamma\,/\,E$$

Here U_0 is the potential value corresponding to a point in terms of the avoided crossing $R = R_c$, Γ is the value of the autoionization width at R_{max}, V_c is the relative velocity of the particles, μ is the reduced mass, and T is the temperature expressed in eV.

It became apparent that the accumulation of the experimental data on chemoionization reveals differences between the results of the beam experiments and the experiments carried out in a gas cell (plasma). The values are significantly higher than the possible experimental errors (Table 1.5). The question arose about the correctness of the published values of the rate constants (the "paradox of sodium"). This situation has been analyzed by Bezuglov et al. (1989). It was shown that the main reason for the scatter of the published experimental data is the peculiarities of the distribution function of the excitation over atomic velocity $F(\upsilon)$ in different experiments.

Calculations showed that $F(\upsilon)$ in the gas-cell plasma is significantly different from the distribution function for a single beam. Intersecting beams with this respect occupy an intermediate position. The function $F(\upsilon)$ at the same temperature of the

beam source and the gas cell is enriched, in the latter case, by the fast particles as compared to the single beam. The maximum $\sigma(E)$, along with the threshold behavior of the cross sections at $E \geq 0.1$ eV, was found by Wang et al. (1985). It is consistent with the model (Devdariani 1979) where the maximum dependence $\sigma(E)$ in the region $0.005 \leq E \leq 0.10$ eV is comparable in magnitude with the cross section at 0.3 eV. From this it follows that the process for sodium atoms AI (1.60) is a multichannel one.

The cross section of $\mathrm{Na}\left(3^2\mathrm{P}\right) + \mathrm{Na}\left(3^2\mathrm{P}\right) \rightarrow \mathrm{Na}_2^+ + -\mathrm{e}^-$ for the temperature range 0.75 mK to 650 K was calculated in the semiclassical approximation by Geltman (1988). This cross section of the order of magnitude coincided with the measurement result at the point $T = 0.75$ mK (see, for instance, Huennekens and Gallagher 1983). However, it was by two to three orders of magnitude greater than the experimental values in the thermal collision energy range.

The energy dependence of the cross section was measured in an experiment with two intersecting beams for $3^2\mathrm{P}$ (Wang et al. 1987) and $3^2\mathrm{P}_{3/2}$ (Kircz et al. 1982) states of sodium. This dependence has a minimum at $E = 0.15$ eV in the range of 0.08–0.26 eV collision energy and increases with increasing energy.

A joint analysis of the experimental data obtained in the gas cell, single, and crossing beams conducted by Bezuglov et al. (1987) reduces to determining the dependence of reaction rate on the relative velocity (energy) of the colliding particles, which is equivalent to obtaining the temperature dependence of the rate constant. It turns out that this approach is helpful in the case of large values of the reaction energy threshold ΔU, and at lower values of ΔU, where the exponential factor $\mathrm{e}^{-\Delta U/KT}$ is not dominating in the magnitude of the rate constant.

At the same time, simultaneous estimation of the autoionization width $\Gamma(\mathrm{R})$ carried out in the framework of the AI model with two resonantly excited alkali metal atoms (Devdariani 1979) is possible in the field of $R \leq R_\mathrm{c}$, where R_c is the intersection point of the ion and the covalent potential curves.

Graphic solution of systems of nonlinear equations for the AI rate constants in the cases of the gas cell $\mathrm{Na}(3^2\mathrm{P}_{3/2,1/2})$, single effusion beam $\mathrm{Na}(3^2\mathrm{P}_{3/2})$, and two intersecting beams of $\mathrm{Na}(3^2\mathrm{P}_{3/2})$ allowed estimation of the possible values of the process parameters $\Delta U \leq 0.05$ eV and $\Gamma \geq 8 \times 10^{12}$ s^{-1} for two $3^2\mathrm{P}_{3/2}$ sodium atoms.

Kircz et al. (1982) found that the yield of the molecular ions during the excitation of $3^2\mathrm{P}_{3/2}$ atom Na states increased by 1.7 times at changing the light polarization from perpendicular to parallel with respect to the beam direction. Blange et al. (1997) showed that the contribution of the $3^2\mathrm{P}_{1/2}$ state of sodium in the ionization depends on the polarization of the exciting radiation, and the initial spin orientation does not affect the yield of the molecular ions at the electron beam energy of 25 MeV. The differences of the results of experiments performed for the atomic beam and the gas-filled cells (Huennekens and Gallagher 1983; De Iong and van der Valk 1979) may be related to the polarization effects.

In the first case the polarization vector was perpendicular to the beam direction, and in the second one the resulting polarization effect was insignificant. At the

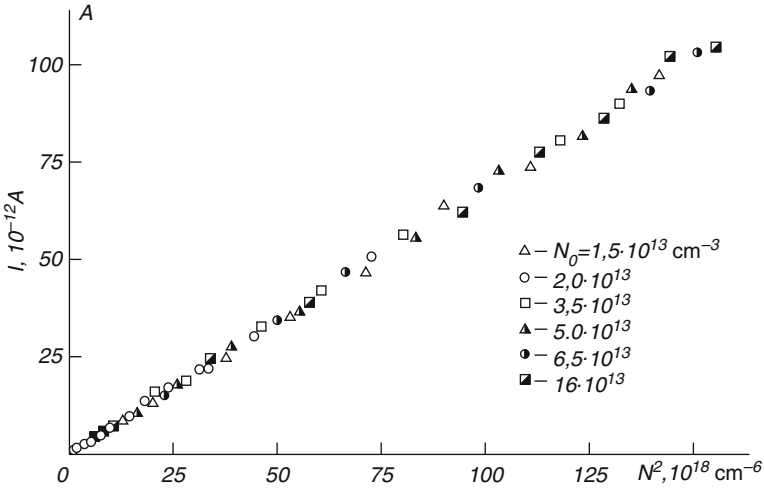

Fig. 1.11 Experimental energy spectrum of electrons with energy from 0 to 2.1 eV formed during resonance excitation of sodium atoms

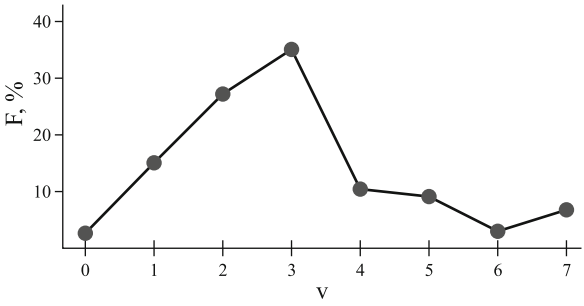

Fig. 1.12 Relative populations of the vibrational states of the molecular ion Na_2^+ in the vicinity of the first peak in Fig. 1.12, obtained by electronic high-resolution spectroscopy (Blangé et al. 1997)

same time, the main contribution, which leads to a difference in the measured AI constants in both cases, may be caused by the marked difference in the collision energy threshold for the ionization (Klyucharev and Vujnovic 1990).

Electron spectroscopy methods enable receiving reliable information not only about the different ionization processes, but also about the second kind of collisions of excited atoms with electrons. Figures 1.11 and 1.12 show an overview spectrum of the electrons, which can be registered for selective excitation of the 3^2P state of the sodium atoms. The first maximum of the electron energy distribution close to zero energy corresponds to the AI process. The maximum at $E = 2.1$ eV is caused by the heating of slow electrons produced by the photo-ionization during collisions of the second kind with excited 3^2P atoms. Along with the second kind of collisions of $Na^* + e^- \rightarrow Na + e^-$, we can observe the processes of the triple collisions $Na^* + Na^* + e^- \rightarrow 2Na + e^-$; they correspond to the maximum of the electron spectrum at $E = 4.2$ eV.

The intermediate peaks are associated with the processes of the photo-ionization and PINa $\left(3^2\mathrm{P}\right)+\mathrm{Na}^*\ (\mathrm{n}, l) \rightarrow \mathrm{Na}^+ + \mathrm{Na} + \mathrm{e}^-$ with the participation of atoms in the upper excited states populated by the *excitation energy transfer* (EET) processes.

At the same time, the position of the first electron peak $\leq$0.1 eV agrees well with the idea that the autoionization decay of the quasi-molecular potential curve occurs in the vicinity of the pseudo-crossing with the ion curve.

1.7 The Processes of a Double Excitation in the Binary Collisions of Excited Atoms

The chain of interrelated collisional processes leading to ionization can be realized when atoms are excited into the resonance states. One such example is the transfer of energy primary excitation with the population of upper excited states, where almost all the total internal energy is transferred to one of the partners (Eq. 1.60). For the first time, researchers have encountered the phenomenon of EET in experiments with activated crystals, where the process of the excitation transfer occurs as a result of the electron–phonon interaction, which is called a *cooperative luminescence* (Ovsiyankin and Feofilov 1968).

The AI channel opens in experiments with the resonantly excited states of the alkali atoms, which is accompanied by the heating of primary electrons and the formation of the photo-plasma in the working volume. Thus, in addition to EET the population of the upper atomic states by fast electrons should be taken into account. Concentration of excited atoms and ionization value during saturation of a resonance transition are both determined by vapor pressure. Studies conducted to date of electrical kinetic parameters of the plasma sodium show that the electron heating from the second kind of collisions in the sodium vapor under saturation of a resonance transition starts from the density of normal atoms $N_0 = 2 \times 10^{13}\mathrm{cm}^{-3}$.

Inelastic thermal energy collisions can be considered as the transitions between the terms of a quasi-molecule, corresponding to the initial and final states of the colliding atoms. The EET processes occur in localized areas, concentrated in the vicinity of the fixed values of the interatomic distance (see curves $\mathrm{A}^* + \mathrm{B}^*$ and $\mathrm{A} + \mathrm{B}^{**}$ for $R_2 \gg R_1$ in Fig. 1.13).

The total rate constant of these processes in binary collisions of the resonant excited sodium atoms is 7×10^{-11} cm^3 s^{-1}. In the case of thermal collisions between two resonantly excited sodium atoms, the EET processes have virtually no effect on the efficiency of the AI reaction. Because the EET takes place at internuclear distances where the covalent terms correlated as $R \rightarrow \infty$ with the 2Na(3^2P) states are well known, calculation of the effective cross sections is possible in the theory (Borodin and Komarov 1974).

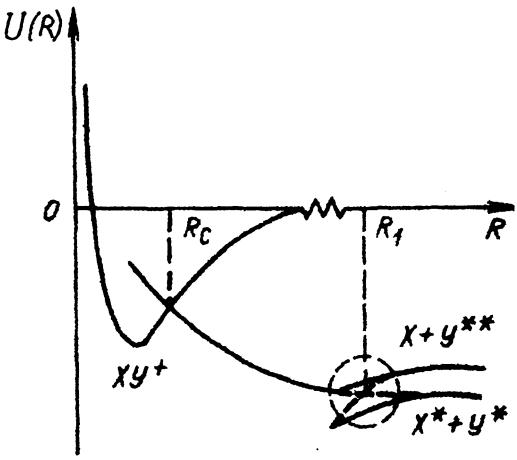

Fig. 1.13 Potential curves of the XY^+ and XY^{**} molecular states. AI and energy exchange process collisions

1.8 Chemo-Ionization Processes Involving Rydberg Atoms

We can distinguish two typical ranges of distances between the ion and the perturbing atom considering the slow collision of the Rydberg atom A^{**} (n) with the unexcited atom B. First, we use a quasi-free representation of the Rydberg electron when the atom B is in the classically allowed region of electron motion, taking into account its scattering on atom B. Second, atom B is located in the classically forbidden zone. Here you can see the process of the chemo-ionization with partners A^+ and B (Fig. 1.14).

The charge–recharge and ion–molecule reactions

$$A^+ + B \rightarrow A + B^+ \tag{1.65}$$

$$A^+ + BC \rightarrow AB^+ + e^- \tag{1.66}$$

should be also attributed here to the inelastic processes. In this connection, we should mention two works in which a model of the ion core Rydberg atom A^{**} is used. In the first study (Zhdanov and Chibisov 1976), the interaction of the ion core of the sodium atom with a dipole moment of the inert gas atom is considered as the general mechanism leading to a change in the principal quantum number n of the Rydberg sodium atom induced by their collisions. In the second paper (Devdariani et al. 1978), the ionization process in the collision of the atom A^{**} with the atom B is accompanied by a transition of the valence electron of the atom B to the atom A^{**}, when the optical electron of the atom A becomes free, i.e., the exchange decay of the quasi-molecule AB^{**} takes place.

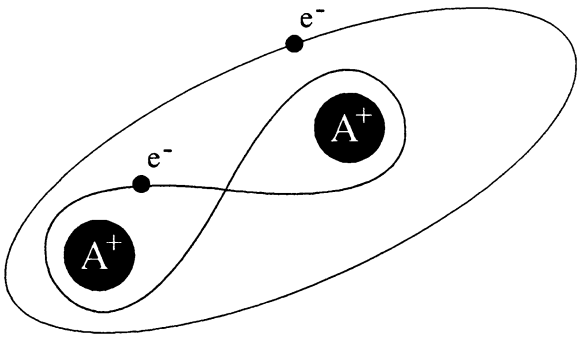

Fig. 1.14 Qualitative illustration of the Rydberg atom–atom collision according to *E*. Fermi

1.8.1 Symmetrical Collisions

The following data from review papers (Gnedin et al. 2009; Smirnov 1981) and results in the chemo-ionization of Rydberg atoms of alkali metals obtained by Nielsen and Dahler (1979) and by Huennekens and Gallagher (1983) will be used. The effectiveness of the chemo-ionization in the thermal ($E > 10^2$ K) and the subthermal ($E < 10^2$ K) ranges of the symmetrical Rydberg atom collisions was investigated. The atom motion dynamics is not described classically in the case of the ultracold collisions ($E < 10^{-3}$ K). The rate constants of the chemoionization in the thermal and subthermal regimes can be calculated in the semiclassical approximation. In these papers, laser excitation of n^2S and n^2D Rydberg states of the sodium atom is carried out with the help of two pulsed tunable lasers with the repetition rate 50 kHz.

A signal corresponding to the AI channel is measured in most of the beam experiments. At the same time, these theoretical calculations include information about two possible AI and PI ionization channels. We should take into account, comparing the experimental data and the theory, that the resulting signal in the cross-beam conditions (cross-beam conditions, CB) and the calculated rate constant kAI correspond to both the signal caused by particle collisions of different beams and the particle collisions within one beam (single-beam conditions, SB). It is known that the different values of relative velocities of the partner particles correspond to CB and SB conditions (Klyucharev and Vujnovic 1990). The experimental data obtained without regard to the latter circumstance can be considered as the upper values of the CB constants:

$$k_{\mathrm{AI}}^{\mathrm{tot}} = k_{\mathrm{AI}}^{\mathrm{CB}} + k_{\mathrm{AI}}^{\mathrm{SB}}. \tag{1.67}$$

Attention was drawn to this fact only very recently. The comparison of the experimental and theoretical data of the AI constants for intersecting beams, taking into account the collision contribution of one beam (Eq. 1.67) for the excited ^{2}S and ^{2}D sodium atoms (Beterov et al. 2005), is represented in Fig. 1.15. The data of the

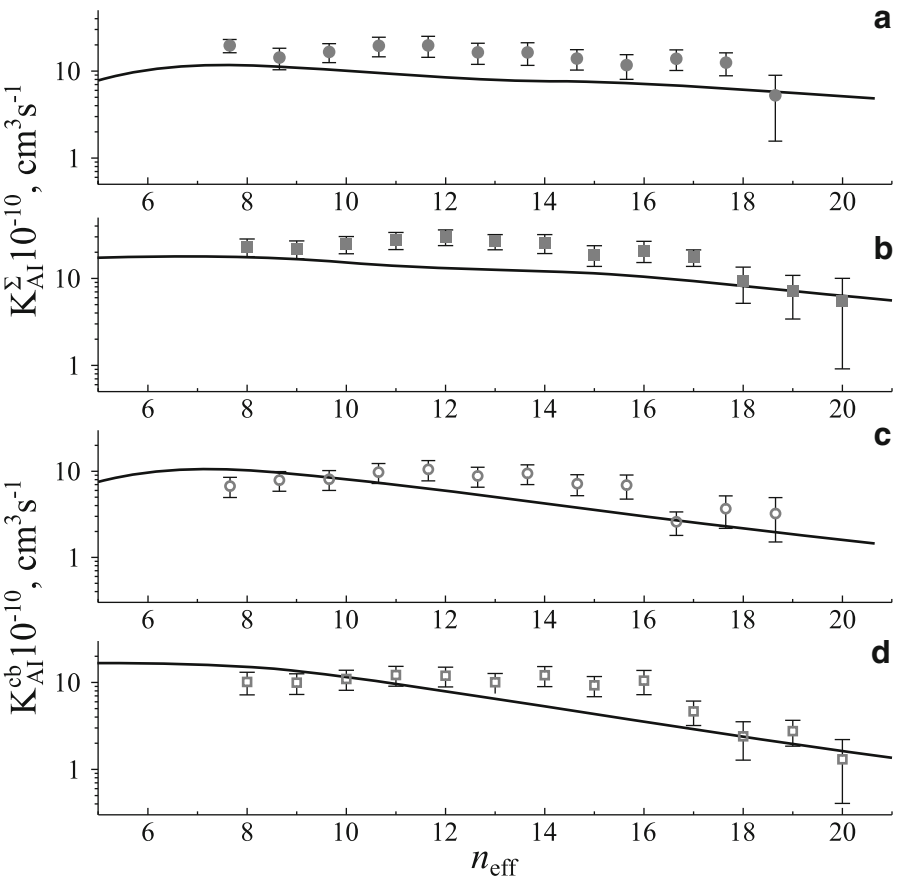

Fig. 1.15 Experimental and theoretical AI rate constants of reaction $Na^*(n_{eff}, l) + Na$ under the crossed atomic beam condition for $T = 600$ K and $8 \le n_{eff} < 20$: (**a**) k^{Σ}, $l = 0$ case is denoted by dots; (**b**) k^{Σ}, $l = 2$ is shown by *perfect squares*; (**c**) *open circles* represent the k^{cb}, $l = 0$ case; (**d**) *open squares* indicate k^{cb}, $l = 2$ case; *full curves* give the stochastic theory results

total constants $k_{AI} + k_{PI}$ and branching factor $\gamma = \sigma_{AI}/(\sigma_{AI} + \sigma_{PI})$ calculations for the chemoionization $Na(n^2P) + Na$ process as a function of n_{eff} are presented in Fig. 1.16.

Comparison of the calculated and experimental data for AI and PI cross sections in the collisions of resonantly excited $Rb(5^2P_{3/2})$ atoms and atoms of rubidium in the ^2S and ^2D Rydberg states was carried out by Barbier et al. (1987). The calculation of the total autoionization width of the excited quasi-molecule $\Gamma(R) = \Gamma_{dir}(R) + \Gamma_{rev}(R)$ takes into account two possible ionization channels: a "direct" one (with the detachment of an electron of the highly excited atom) and a "reverse" one (with exchange of electrons of excited atoms). Table 1.6 shows the values k_{PI} and k_{AI} at $T = 450$ K.

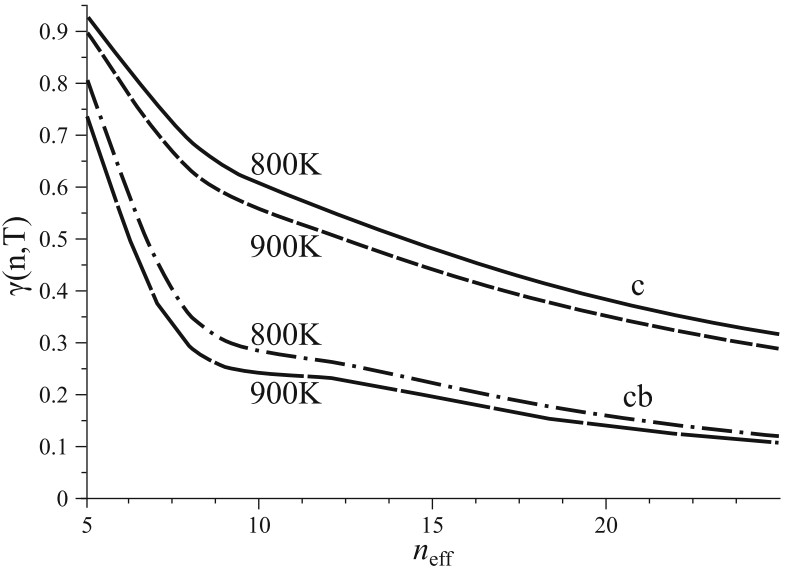

Fig. 1.16 Theoretical results for the total chemo-ionization rate constants in hydrogen

Table 1.6 Values of the coefficients of PI and AI reactions at $T = 450$ K

States	k_{PI} 10^{-10} $cm^3 \cdot s^{-1}$	k_{AI} 10^{-10} $cm^3 \cdot s^{-1}$
7^2S	0.5	0.6
5^2D	1.7	Negligible
6^2D	1.4	
7^2D	1.2	
8^2D	1.0	
9^2D	0.9	

A difference between the values k_{PI} and k_{AI} is defined by the difference of contributions of the direct and the reverse processes to the total autoionization width for n^2S and n^2D states of the excited atom. Qualitatively, this can be seen in the experiments on the hydrogen chemoionization of the alkali atoms and the calculations for the hydrogen atom (Fig. 1.16). A quantum mechanical model of the chemoionization was considered by Duman and Shmatov (1980). The power dependence $n_{max} \sim T^{-1/2}$, where n_{max} is the value of the principal quantum number, corresponds to the maximum of the rate constant.

1.8.2 Asymmetrical Collisions

The signals corresponding to the excitation states n^2P of the sodium atoms present as minor impurities at optical excitation of the potassium vapor, as reported by

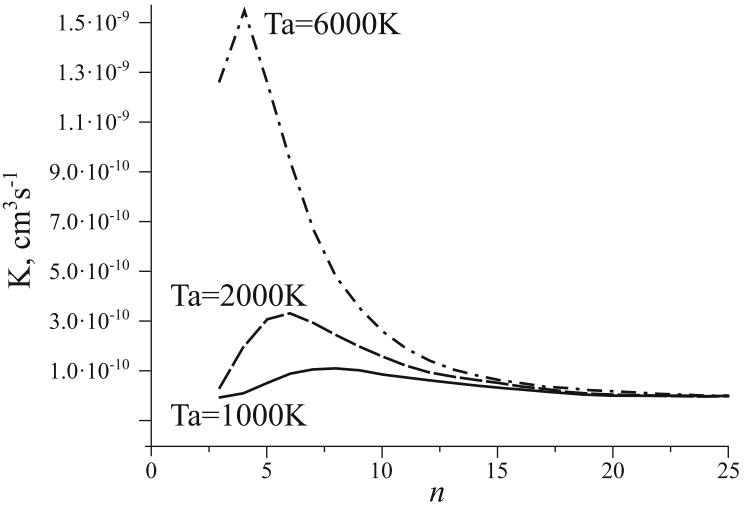

Fig. 1.17 Branch coefficients γ for the chemo-ionization in $Na^*(n_{eff}, l = 1) + Na$ collisions; *cb* and *c* denote the crossed beams and vapor cell, respectively. $T = 800$–900 K

Table 1.7 Rate constants of AI reaction with the formation of homogeneous and heterogeneous molecular ions, $T = 450$ K

	$k_{AI}\ 10^{-10}$ $cm^3 \cdot s^{-1}$	$k_{AI}\ 10^{-10}$ $cm^3 \cdot s^{-1}$
State	Ion KRb^+	Ion Rb_2^+
6^2D	2.4 ± 0.6	1.6 ± 0.4
8^2S	2.4 ± 0.6	2.2 ± 0.7
7^2D	2.5 ± 1.0	2.3 ± 0.9

Klyucharev and Lazarenko (1980). As a result, it is possible to estimate the constant value lower limit $k_{min} > 10^{-10}$ cm^3 s^{-1} for the asymmetrical chemo-ionization processes. Thus, the values of the constants of the asymmetrical processes involving Rydberg atoms in the thermal range of speeds can reach significant values. The process of the ion $HeNe + (Ne^* + He)$ was studied by Harth et al. (1986). In this case the measured value of the cross-section maximum at $n_{eff} \approx 10$ was an order of magnitude smaller than those for the symmetrical $Ne^* + Ne$ case.

A two-step excitation scheme via intermediate metastable states is used in this work and in most of the others on studies of the inert gas Rydberg atoms. To do this, the direct optical methods using a synchrotron and a laser (photon) excitation have been actively used in recent years (Hu et al. 2000). Estimates show that the ratio of the effective rate constants of the reaction Na^* $(n^2P) + Na$ (Li) for the principal quantum numbers $8 \le n \le 14$ with the formation of homogeneous and heterogeneous molecular ions should be smaller than unity. The experimental rate constants of the AI reaction $Rb(n,l) + K(4S) \rightarrow KRb^+ + e^-$ are given by Djerad et al. (1985). In Table 1.7 are presented the rate constant values for the 6^2D, 8^2S, and 7^2D states, and a comparison with the reaction $Rb(n,l) + Rb(5^2S)$.

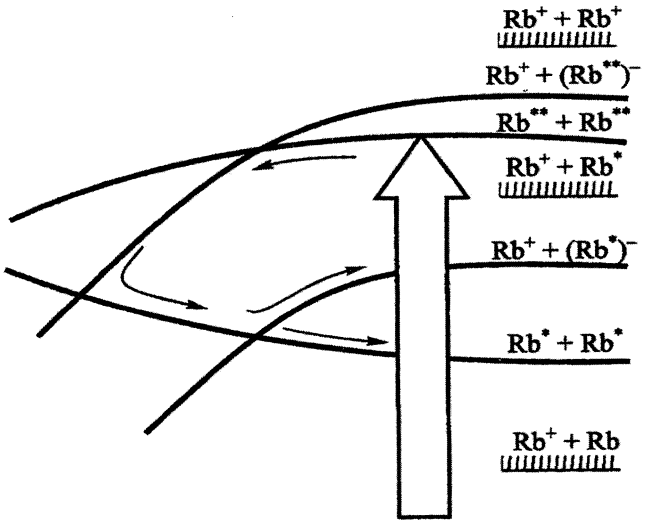

Fig. 1.18 Schematic illustration of potential curves quasi-crossing in the case of collisions of two highly excited atoms (rubidium)

The temperature dependence of the total chemoionization rate constant $k_{\mathrm{AI}} + k_{\mathrm{PI}}$ and the branching for the factor γ are calculated in the framework of the dipole resonance model for the Li(n^2P) + Na collision with the formation of $(\mathrm{LiNa})^+$ and Li^+ ions in the case of the filled vapor cell (Ignatovic et al. 2008).

The theoretical works just cited on the calculation of the constants of the chemo-ionization processes in varying degrees use the so-called dipole model of the resonant mechanism proposed by Smirnov and Mihajlov (1971b) for inelastic processes involving Rydberg atoms (see also Ianev and Mihajlov 1980).

1.8.3 Binary Collisions of Two Rydberg Atoms

The following process can proceed in collisions of two Rydberg atoms at thermal and subthermal energies (Fig. 1.18).

$$\rightarrow \mathrm{A}^+ + \mathrm{A}^* + \mathrm{e}^-, \tag{1.68}$$

$$\mathrm{A}^{**} + \mathrm{A}^{**} \rightarrow \left(\mathrm{A}_2{}^+\right)^* + \mathrm{e}^-, \tag{1.69}$$

$$\rightarrow \mathrm{A}^+ + (\mathrm{A})^*. \tag{1.70}$$

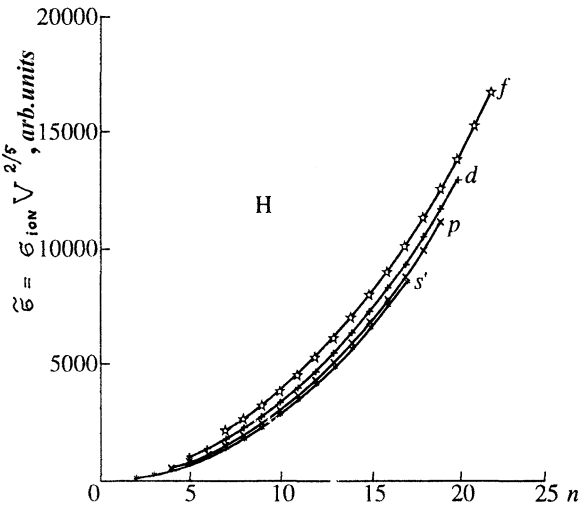

Fig. 1.19 Penning ionization (PI) cross section in the pair collisions of Rydberg hydrogen atoms in the *S*, *P*, *D*, and *F* states

Cross sections (Eqs. 1.68, 1.69, 1.70) for symmetrical collisions of two highly excited atoms are calculated by the Monte Carlo method in McGeogh et al. (1988). Experiments carried out in this work show that a good agreement between the calculated and the experimental results is obtained at relative velocities of collisions $V_c \geq \upsilon_e$, where υ_e is the characteristic velocity of the Rydberg electron. The calculated values at lower velocities of V_c are greater than the experimental ones. Written in atomic units, the cross section of the molecular ions (Eq. 1.69) in the temperature range 10–10^3 K is equal to

$$\sigma\,(\mathrm{n}, V_c) = 0.703 V_c^{-0,65} \mathrm{n}^{3.35} \tag{1.71}$$

The Penning ionization rate constants in the binary collisions of the Rydberg hydrogen atoms, the alkali atoms, and the ions of strontium are calculated by Bezuglov et al. (1995). The calculation is carried out using the model approach of Katsuura-Smirnov (Galitskii et al. 1981) for the long-range dipole–dipole ionization mechanism at large internuclear distances.

Autoionization widths of the intermediate quasi-molecular states are expressed in terms of the photo-ionization cross section $\sigma^{\mathrm{f}}(nl)$ of the Rydberg atomic *nl* levels and the line strengths of the transitions between them. These quantities are calculated in the semiclassical approximation taking into account the quantum character of the Rydberg electron motion in the approximation of the straight line motion of particles (see Figs. 1.19 and 1.20).

Features of the ionization cross section of the strontium ion were calculated in the framework of the dipole–dipole ionization mechanism caused by the nonmonotonic dependence of photo-ionization cross sections of the singly charged strontium ions on *n*. In this case the dipole–dipole approximation of the atom–atom interaction is best for the subthermal collisions because the interaction time increases at large internuclear distances.

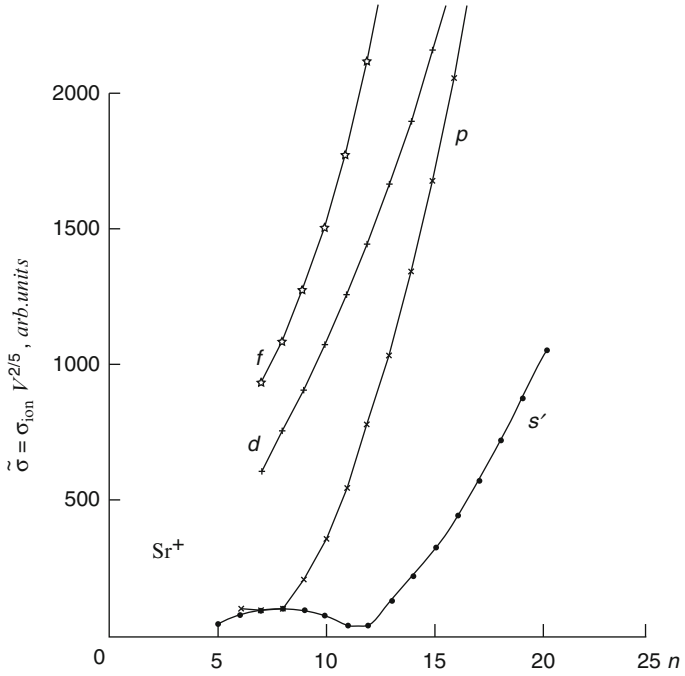

Fig. 1.20 Identical with Fig. 1.19 for the case of single-charged strontium ions

The ionization in collisions of two Rydberg alkali atoms in the n^2P state was studied by Bezuglov et al. (1997), taking into account the influence of the interaction of close configurations n^2P, n^2S, and $(n+1)^2$S on the efficiency of the process:

$$\mathrm{A}\,(\mathrm{n}l) + \mathrm{A}\,(\mathrm{n}l) \rightarrow \left(\mathrm{A}\,(\mathrm{n}_1 l_1) + \mathrm{A}^+\right) + \mathrm{e}^-. \tag{1.72}$$

with the transitions to the nearest (over energy) level of the ion state, in the case when the energy of $nl \rightarrow n_1 l_1$ transition into the lower $n_1 l_1$ state exceeds the bound energy of the nl state of another atom (near-threshold ionization). High efficiency of the reaction (1.72) at large interatomic distances takes place as a result of the dipole–dipole interaction, which in this case is the most effective of all multipole interactions. Results of the numerical calculation of the cross section of the molecular ion formation process are shown in Fig. 1.21.

The cross section oscillates with respect to n within the principal quantum numbers $7 < n < 26$, which is associated with the oscillations depending on the frequency of the intraatomic transitions. The weak components in the electronic spectra of the reaction under certain conditions can become apparent, which corresponds to the forbidden in the dipole–dipole approximation ($\Delta L = \pm 1$) optical transitions $[\mathrm{A}\,(n\mathrm{P}) + \mathrm{A}\,(n\mathrm{P})] \rightarrow [\mathrm{A}\,(n\mathrm{S}) + \mathrm{A}\,((n+1)\,\mathrm{S})]$, induced by the interconfiguration interaction.

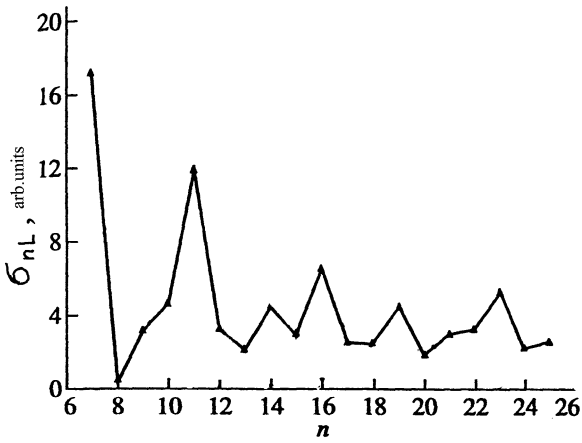

Fig. 1.21 Cross section $\sigma(n)$ of near-threshold ionization in Rydberg atom–Rydberg atom collisions

The constants of the atomic ion formation in the binary collisions of Rb(11^2P) measured by Borodin et al. (1995) were compared with the results of the calculation within the model approximations, which were used in two previous studies. The measured value $k = (1.5 \pm 0.4) \cdot 10^{-8}$ cm^3·s^{-1} within a factor of 2 coincided with the calculated value.

Recently, interest in the processes has increased, such as PI reactions with the participation of the Rydberg atoms, caused by the effects of the cold plasma formation in the magneto-optical traps (Amthor et al. 2009).

1.9 Formation of Negative Ions in Thermal Collisions with Rydberg Atoms

1.9.1 Symmetrical Collisions

Let us discuss the possibility of negative ions in thermal collisions of the excited and normal atoms of one kind.

Figure 1.22 shows the scheme of the terms of the excited molecule X_2^*, ground state molecule X_2, and the potential curve of the Coulomb ion pair $X^+ + X^-$. We assume that at large interatomic distances R the Coulomb interaction is the main. The value of R_c, at which a pseudo-crossing of the covalent X_2^* and the Coulomb X^+X^- potential curves can be estimated from the approximate relationship $\Delta E \approx -e^2/R_c$, where ΔE is the energy defect of the reaction. From this it follows that the formation of the pair $X^+ + X^-$ can occur from the excited states of X^*, for which ΔE is of the order of kT_a. In real cases, the effectiveness of such a reaction is determined not only by the value of ΔE. Thus, it was shown that the preferential population of the excited states with a zero-energy defect does not take place in the

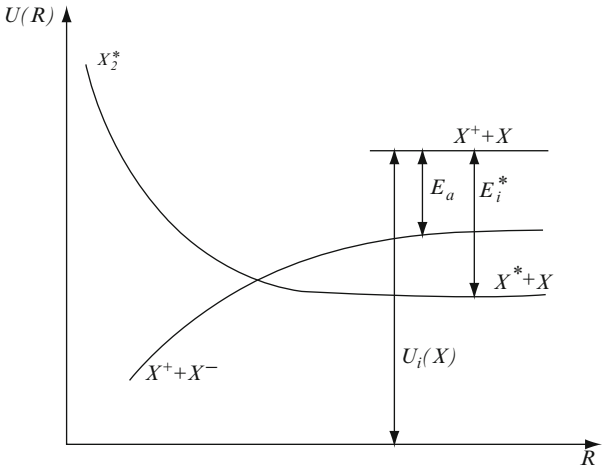

Fig. 1.22 Illustration of the mechanism of $X^{**} + X \rightarrow X^+ + X$ collision process

framework of the Landau-Zener transition mechanism as the result of the reverse process of the ion–ion recombination. For the highly excited states, the crossing of the covalent repulsive s term of the quasi-molecule and the Coulomb term of the $X^+ + X^-$ does not occur. Then, the formation of the positive and negative ions can take place through the transitions such as the Rosen-Zener at small internuclear distances, or with a help of a third covalent term, which correlates with the lower excited states at $R \rightarrow \infty$. A formation of the negative ions in the system

$$\mathrm{Rb}\,(nl) + \mathrm{Rb}\left(5^2\mathrm{S}\right) \rightarrow \mathrm{Rb}^+ + \mathrm{Rb}^- \tag{1.73}$$

is considered at the temperature $T_a = 540$ K by Barbier et al. (1986). The specificity of the Rydberg atoms, which manifests itself in collisions with heavy particles, is that the ionic cores and the valence electrons have different effects on the nature of the collision. The ion core controls the diffusion of the Rydberg atoms in a gas. Formation efficiency of the negative ions in collisions with heavy electronegative particles is caused by the scattering of the outer electrons. The formation of the negative ion Ca^- in the thermal collisions with the neon Rydberg atoms in *ns* and *nd* states, in the range of $8 < n_{\mathrm{eff}} < 14$, was investigated by Reicherts et al. (1997). The dependence of $k(n_{\mathrm{eff}})$ has a maximum $k_{\max} \approx 10^{-8}$ cm^3·s^{-1} at the point of $n_{\mathrm{eff}} = 11.5$, which was not observed in this range for the pair $Ne^{**} + SF_6$. This finding is in good agreement with the results of the model calculations of the calcium atoms.

1.9.2 Asymmetrical Collisions with Molecules

In this case we can speak about the internal degrees of freedom of the complex with a large number of possible reaction channels, respectively, and the number of possible resonances with an energy defect $\Delta E \approx 0$. A model of the energy transfer of the molecular rotation to the Rydberg electron used to explain the experimental data was suggested by Matsuzawa (1979). The experimental values of the ionization cross sections in collisions with the polar and the quadrupole molecules at $T \approx 300$ are of the order of 10^{-14} to 10^{-12} cm^2. These cross sections are proportional to n^{-3} and the square of the dipole moment of the polar molecules and weakly dependent on the quantum numbers n and l.

Because the frequencies of transitions in the atom can be of the order of energies of the vibrational transitions in the molecule, one can observe the resonant character of the energy transfer of the excited atom to the vibrations of the molecule

$$\mathrm{Na}^*(n) + \mathrm{CH_4} \rightarrow \mathrm{Na}^* + (\mathrm{CH_4})^* \tag{1.74}$$

Collisions of the Rydberg atoms with the halogen molecules with the positive electron affinity

$$\mathrm{PA} + \mathrm{BC} \rightarrow \mathrm{A}^+ + \mathrm{BC}^- \tag{1.75}$$

lead to negative ion formation. For example, the negative H^- and He^- ions appear according to this scheme in the tandem (double) electrostatic charged-particle accelerators using the same potential difference, when the ion A^+ changes its sign in the result of the charge exchange.

The exothermic process cross sections of the ion pair formation depend on the value of the vibrational excitation of the electronegative molecules. The influence of the vibrational excitation has several reasons, such as a decrease in the energy threshold of the reaction and the change in the vertical energy of the electron affinity. Rise of vibrational excitation leads to a significant increase in the cross sections and the corresponding rate constants. For example, the value of the rate constant is approximately 10^{-7} cm$^3 \cdot$s^{-1} in the case of halogen-containing molecules.

The yield of the negative ions in thermal collisions with Rydberg atoms is determined by the efficiency of the attachment process. This concept is confirmed by the theory and measurements of the rate constants of the Rydberg atom ionization with principal quantum numbers $n = 20$–100 in collisions with halide molecules. For example, the slow Rydberg atom–molecule collisions with the formation of negative ions and free electron capture by the molecules are similar in effectiveness, as it follows from the Fermi quasi-free electron representation. Therefore, the cross section of the collision of highly excited atoms A^{**} with the halogen molecules, calculated in the impulse approximation, is determined by the cross section of the free electron scattering at the energies of about 3.10 eV.

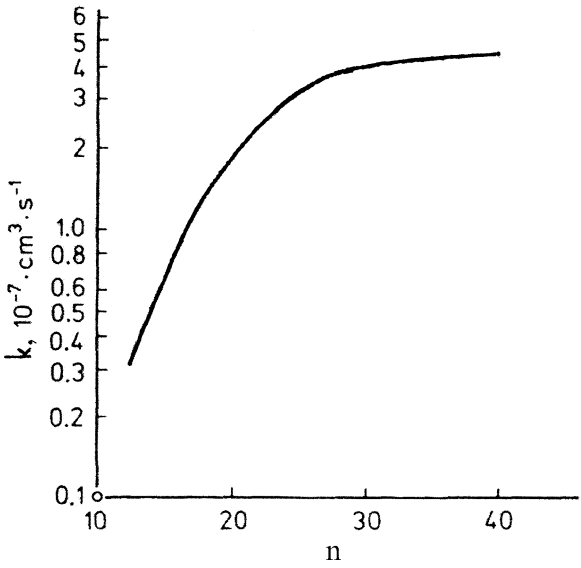

Fig. 1.23 Rate constant of impact ionization in nonsymmetrical case: $X_n^{**} + SF_6 \rightarrow X^+ + SF_6^-$, Na($n^2$P), $12 \leq n \leq 40$, $T = 500\,\kappa$

The reaction cross section $A^{**} + SF_6 \rightarrow A^+ + SF_6^-$ is inversely proportional to the characteristic velocity of the electron in the excited orbit. When changing the principal quantum number values from 23 to 106, the rate constant values of this reaction lie in the range $(4–4.5)\cdot 10^{-17}$ cm$^3\cdot$s^{-1} and are almost independent of n (Beterov et al. 1987; Zollars et al. 1986) (Fig. 1.23).

Large values of the rate constants of the reaction are connected here with the fact that the excited ion SF_6^{-*} formed during reaction is a long-lived one with the lifetime $\tau > 10$ s.

Another situation in collisions of the alkali atoms with the molecule of O_2 is realized for the intermediate values of the principal quantum number n. In this case, the lifetime of the excited ion O_2^{-*} is small, i.e., it is of the order of $\tau \approx 10^{-9}$ s, and effective electron auto-detachment in the absence of a stabilizing mechanism takes place. The interaction with the ionic core of the Rydberg atom, which is especially effective for small n, can be the stabilizing mechanism. Therefore, the rate constant with the participation of the O_2 molecule should decrease with the increase of n in contrast to SF_6. This change explains the small value of the constant (10^{-12} cm$^3\cdot$s^{-1}) and its decrease with increase of n.

1.10 Conclusion

Returning to the above diffusion approximation (1.41) and (1.42), we note the following. For exothermic AI reactions at low relative kinetic energies of colliding atoms, entry of the representation point to the spatial domain of the intermediate

Rydberg complex XY^{**} is accompanied by a transition to the highly excited states with large angular momentum N. Their energy level positions are different appreciably from the states close to the regular distribution.

Classical motion of nuclei along the random trajectories converged at pseudo-crossing points of the potential curves of the Rydberg and dissociative configurations should correspond to the dynamic "quantum chaos." However, this scenario is totally unsuitable, because representation of the potential curves lying near the ionization continuum is not applicable. Therefore, the motion of the quantum system takes place in time for the energy levels to be irregularly arranged because of the strong nonadiabatic coupling of the electron and nuclear motions.

However, it should be borne in mind that the intermediate states with large principal quantum numbers n make a small contribution to the dynamics of the AI process. On the one hand, as was shown, there is a dynamic factor (1.40). On the other, this region of the spectrum is passed fairly quickly, because the characteristic energy transfer for a certain period of time is much greater than the distance between closely spaced levels, including levels of the autoionizing states of the continuum, despite the fact that in this region of motion resulting from the inclusion of direct transitions in the ionization continuum, diffusion approximation is formally not applicable, and the total contribution to the diffusion flow is small here (Golubkov et al. 1979).

Our theoretical model is supplemented with an extended review of experimental data on AI constants measured under a vapor cell, a single atomic beam, and crossing-beam conditions. Various colliding pairs involving both low-lying and highly excited (Rydberg) states are considered here, with discussion provided on the corresponding features of the accompanying AI processes. A proper understanding of the presented experimental findings within the framework of the theoretical treaty developed here is important for our further activity.

Acknowledgments The work was supported by the EU FP7 IRSES Project COLIMA, No. 247475.

References

Adamson SO, Buenker RG, Golubkov GV et al (2009) Laser stimulation of low-temperature dissociative recombination of dissociative recombination of electrons and oxygen molecular ions. Russ J Phys Chem B3(2):195–210

Amthor T, Denskat J, Giese C et al (2009) Autoionization of an ultracold Rydberg gas through resonant dipole coupling. Eur Phys J D53:329–335

Balashov EM, Golubkov GV, Ivanov GK (1984) Radiative transitions between Rydberg states of molecules. Sov Phys JETP 59(6):1188–1194

Barbier L, Djerad MT, Cheret M (1986) Collisional ion-pair formation in an excited alkali-metal vapor. Phys Rev A34:2710–2718

Barbier L, Pesnelle A, Cheret MJ (1987) Theoretical interpretation of penning and associative ionization in collisions between two excited rubidium atoms. J Phys B28:1249–1260

Bellissard J (1991) Non commutative methods in semiclassical analysis. Transition to chaos in classical and quantum mechanics. Springer, Berlin

Beterov IM, Vasilenko GL, Riabtsev II et al (1987) Collisional chemiionization of highly excited sodium atoms. Z Phys D At Mol Clust 6–7:55–63

Beterov IM, Tretyakov DV, Riabtsev II et al (2005) Collisional and thermal ionization of sodium Rydberg atoms. III. Experiment and theory for nS, nP and nD states with $n = 8 \div 20$ in a cross beam geometry. J Phys B38:4349–4361

Bezuglov NN, Klyucharev AN, Sheverev VA (1987) Associative ionization rate constants measured in cell and beam experiments. J Phys B20:2497–2513

Bezuglov NN, Vujnovic VV, Klyucharev AN, Sheverev VA (1989) The efficiency of collision processes involving optically excited atoms in crossed atomic beams. Opt Spectrosc 66: 721–725

Bezuglov NN, Klyucharev AN, Stacewicz T (1994) Photoplasma of optically excited metal vapors. Opt Spectrosc 77:304–326

Bezuglov NN, Borodin VM, Klyucharev AN et al (1995) Ionization in subthermal collisions of Rydberg alkali metal atoms. Opt Spectrosc 79:680–684

Bezuglov NN, Borodin VM, Klyucharev AN et al (1997) Near-threshold ionization in collisions of two Rydberg atoms in identical states. Opt Spektrosc V 83:338–344

Blangé JJ, Aben G, Rudolph H et al (1997) Associative ionization in collision between excited Na atoms in $3^2P_{3/2}$ and $3^2P_{1/2}$ states. J Phys B30:2789–2800

Borodin VM, Komarov IV (1974) Redoubling of the excitation induced by collisions between two resonance excited cesium atoms. Opt Spectrosc 36:250–257

Borodin VM, Dobrolezh BV, Klucharev AN et al (1995) Investigation of ionization processes in subthermal collisions of rubidium n^2P atoms with one another and with the ground state Rb atoms. Opt Spectrosc 78:15–19

Casati G, Chirikov BV, Guarneri I (1985) Energy-level statistics of integrable quantum systems. Phys Rev Lett 54:1350–1353

Cohen JS (1976) Multistate curve-crossing model for scattering: associative ionization and excitation transfer in helium. Phys Rev A13:99–110

Cutzwiller MC (1990) Chaos in classical and quantum mechanics. Pergamon Press, New York

De Iong A, van der Valk F (1979) Associative ionization of laser-excited sodium in an atomic beam. J Phys B12:L561–L566

Demkov YuN, Golubkov GV (2003) Adiabatic approximation in time-dependent problems of quantum mechanics. Khim Fiz 22(10):7–24

Demkov YuN, Komarov IV (1966) Ionization under slow collisions of two atoms. Sov Phys JETP 23:189–196

Demkov YuN, Osherov VI (1968) Stationary and time-dependent quantum problems solved by the contour integral method. Sov Phys JETP 26:916–923

Devdariani AZ (1979) Influence of the characteristic feature of elastic scattering on the temperature dependence of the rate constant on nonadiabatic reactions. Opt Spectrosc 47:58–64

Devdariani AZ, Klyucharev AN, Lazarenko AB et al (1978) Collisional ionization processes of Rydberg states of the alkali atoms. Sov Tech Phys Lett 4:408–411

Devdariani AZ, Demidov VI, Kolokolov NB et al (1983) Electronic spectra under the low excited atoms collision in inert gases. JETP 84:1646–1653

Devdariani AZ, Klyucharev AN, Penkin NP et al (1988) Diffusional approach to the process of collisional ionization of excited atoms. Opt Spectrosc 64:425–426

Djerad MT, Harima H, Cheret M (1985) Associative ionization in Rb(nL) – K(4S) collisions. J Phys B18:L815–L819

Duman EA, Shmatov IP (1980) Ionization of highly excited atoms in the own gas. Sov Phys JETP 51:1061–1069

Galitskii VM, Nikitin EE, Smirnov BM (1981) Theory of the collisions of atomic particles. Nauka, Moscow (in Russian)

Garrison BJ, Miller WH, Shaefer HF (1973) Penning and associative ionization of triplet metastable helium atoms. J Chem Phys 59:3193–3198

Geltman S (1988) Semiclassical analysis of the associative process $Na(3p) + Na(3p) \rightarrow Na_2^+ + e$. J Phys B21:L735–L740

Gnedin YN, Mihajlov AA, Ignatovic LM et al (2009) Rydberg atoms in astrophysics. New Astron Rev 53:259–265

Golubkov GV, Ivanov GK (1988) Near-threshold associative ionization reaction of atoms. J Phys B21:2049–2062

Golubkov GV, Ivanov GK (1990) Interaction of auto-decayed states in molecular photodissociation processes. IL Nuovo Cimento 12D(1):1–20

Golubkov GV, Ivanov GK (2001) Rydberg states of atoms and molecules and elementary processes with their participation. URSS, Moscow

Golubkov GV, Kuznetsov NM, Egorov VV (1979) The role of single-step ionization by thermal electron-atom collisions. J Phys Colloq C7 40:89

Golubkov GV, Ivanov GK, Golubkov MG (1996a) Nonadiabatic effects in dissociative recombination of electrons with hydrogen molecular ions. Chem Phys Rep 15:503–513

Golubkov GV, Ivanov GK, Balashov EM (1996b) Manifestation of nonadiabatic electron-rotational coupling in radiative transitions between Rydberg states of H_2 molecule. Opt Spectrosc 80(1):33–40

Golubkov MG, Golubkov GV, Ivanov GK (1997) Low-temperature dissociative recombination of electrons with H_2^+, HD^+ and D_2^+ molecular ions. J Phys B30:5511–5534

Golubkov GV, Golubkov MG, Romanov AN (2002) Dissociative recombination of electrons and O_2^+ in intense visible laser radiation. JETP 94(3):489–497

Golubkov GV, Golubkov MG, Romanov AN et al (2003) Dissociative recombination $e^- + O_2^+ \rightarrow O(^1D) + O(^3P)$in a strong laser field. Phys Chem Chem Phys 5:3174–3182

Golubkov GV, Golubkov MG, Ivanov GK (2010) Rydberg states of atoms and molecules in a field of neutral particles. In: Bychkov VL, Golubkov GV, Nikitin AI (eds) The atmosphere and ionosphere: dynamics, processes and monitoring. Springer, New York, pp 1–67

Gutzwiller MC (1990) Chaos in classical and quantum mechanics. Springer, Heidelberg

Harth K, Hotop H, Ruf MW (1986) Ionization and charge transfer in collisions of neon Rydberg atoms with $n \leq 30$. Invited papers, Oji international seminar on highly excited states of atoms and molecules. Fyji-Yoshida, Japan, pp 117–121

Hasegawa H (1988) Stochastic formulation of energy level statistics: application to the hydrogen atom in a magnetic field. In: Taylor KT, Nayfeh MH, Clark CW (eds) Atomic spectra and collisions in external fields. Plenum Press, New York, p 297

Hu XK, Mitchell JBA, Lipson RH (2000) Resonance-enhanced multiphoton ionization-photoelectron study of the dissociative recombination and associative ionization on Xe_2^+. Phys Rev A62:052712

Huennekens J, Gallagher A (1983) Associative ionization by collision between two $Na(^3p)$ atoms. Phys Rev A28:1276–1287

Ianev RK, Mihajlov AA (1980) Resonant ionization in slow atom-Rydberg atom collisions. Phys Rev A21:819–826

Ignatovic LjM, Mihajlov AA, Klyucharev AN (2008) The rate coefficient for the chemi-ionization in slow $Li(n)^* + Na$ collisions. J Phys B41:025203

Kircz JG, Morgenstern R, Nienhuis G (1982) Polarization dependence of associative ionization of laser-excited Na $3^2P_{3/2}$ atoms. Phys Rev Lett 48:610–613

Klyucharev AN (1993) Chemi-ionization processes. Phys Usp 36:486–512

Klyucharev AN, Bezuglov NN (1983) Excitation and ionization of atoms during the absorption of light. LGU, Leningrad

Klyucharev AN, Lazarenko AV (1980) Collisional ionization processes in the optical excitation of Rydberg states of potassium. Opt Spectrosc 48:229–230

Klyucharev AN, Vujnovic V (1990) Chemoionization in thermal-energy binary collisions of optically excited atoms. Phys Rep 188:55–81

Klyucharev AN, Bezuglov NN, Matveev AA et al (2007) Rate coefficient for the chemi-ionization processes in sodium and other alkali-metal geocosmical plasma. New Astron Rev 51:547–562

Klyucharev AN, Bezuglov NN, Mihajlov AA et al (2010) Influence of inelastic Rydberg atom: Rydberg atom collision process on kinetic and optical properties of low-temperature laboratory and astrophysical plasmas. J Phys Conf Ser 257:012027

Knauf F, Sinai YG (1997) Classical nonintegrability, quantum chaos. Birkhauser, Basel

Kolokolov NB, Kudryavtsev AA (1989) Hemi-ionization processes in low-temperature plasma. In: Smirnov BM (ed) Chemistry of plasma, vol 15. Energoatomizdat, Moscow, pp 127–162

Lee SM (1977) Multichannel dissociative recombination theory. Phys Rev A16:109–122

Lombardi M, Seligman TH (1993) Universal and nonuniversal statistical properties of levels and intensities for chaotic Rydberg molecules. Phys Rev A47(5):3571–3586

Lombardi M, Labastie P, Bordas MC et al (1988) Molecular Rydberg states: classical chaos and its correspondence in quantum mechanics. J Chem Phys 89(6):3479–3491

Matsuzawa M (1979) State-changing collision of a high-Rydberg atom with polar molecule. Phys Rev A20:860–866

McGeoch MW, Schlier RE, Chawla GK (1988) Associative ionization with cold Rydberg lithium atoms. Phys Rev Lett 61:2088–2091

Merz A, Ruf M-W, Hotop H et al (1994) Ionization of hydrogen and deuterium atoms in thermal energy collisions with metastable $He^*(2^3S)$ atoms. J Phys B27:4973–4990

Müller MW, Merz A, Ruf MW et al (1991) Experimental and theoretical studies of the bi-excited collision systems $He^*(2^3S) + He^*(2^3S, 2^1S)$ at thermal and subthermal kinetic energies. Z Phys D At Mol Clust 21:89–112

Neynaber RH, Magnuson GD, Tang SY (1978) Chemi-ionization in collisions of metastable helium with metastable helium. J Chem Phys 68:5112–5117

Nielsen SE, Dahler JS (1979) Endoergic chemi-ionization in $N - O$ collisions. J Chem Phys 71:1910–1925

Ovsiyankin VV, Feofilov PP (1968) The summation of the electronic excitations in activated crystals. In: Nonlinear optics, proceedings of the 2-union symposium on nonlinear optics. Novosibirsk, Nauka

Picart J, Edmonds A (1979) Tables for computation of radial integrals in the Coulomb approximation. J Phys B12(17):2781–2787

Reicherts M, Roth TE, Gopalan A et al (1997) Controlled formation of weakly bound atomic negative ions by electron transfer from state-selected Rydberg atoms. Europhys Lett 40: 129–130

Ringer G, Gentry WR (1979) A merged molecular beam study of the endoergic associative ionization reaction $N(^2D) + O(^3P) - NO^+ + e^-$. J Chem Phys 71:1902–1909

Smirnov BM (1981) Ionization in low-energy atomic collisions. Phys Usp 24:251–275

Smirnov VM, Mihajlov AA (1971a) Nonelastic collisions involving highly excited atoms. Opt Spektrosc 30:984–987

Smirnov VM, Mihajlov AA (1971b) Nonelastic collisions involving highly excited atoms. Opt Spectrosc 30:525–527

Stockmann H-J (1999) Quantum chaos (an introduction). Cambridge University Press, Cambridge

Tolmachev YuA (1982) Excited ions states settling under penning ionization. In: Smirnov BM (ed) Chemistry of plasma, vol 9. Energoatomizdat, Moscow, pp 80–100

Wang M-X, de Vries MS, Boulmer J et al (1985) Direct measurement of velocity dependence of the associative ionization cross section in $Na(3p) + Na(3p)$ collisions. Phys Rev A32:681–684

Wang M-X, Keller J, Boulmer J et al (1987) Spin-selected velocity dependence of the associative ionization cross section in $Na(3p) + Na(3p)$ collision energy range from 2.4 to 290 meV. Phys Rev A35:934–937

Zhdanov VP, Chibisov MI (1976) Penning ionization of the nonmetastable atoms. Zh Eksp Teor Fiz 70:2087–2097

Zollars BG, Walter CW, Lu F et al (1986) Ionization in K(nd)-SF_6 and K(nd)-CCl_4 collisions at intermediate n. J Chem Phys 84:5589–5593

Chapter 2
Elementary Processes Involving Rydberg Molecules in a Strong Laser Field

Gennady V. Golubkov

Abstract Possibilities of the quasi-classical, Born, and semiclassical approximations for the description of the processes of bremsstrahlung, multiphoton ionization, and elastic and inelastic atomic collisions in the field of intensive laser radiation are considered. Large energy of electrons is a general characteristic for the specified processes in which ponderomotive interaction plays the important role. For processes with participation of slow electrons, proceeding near an ionization continuum border, the ponderomotive interaction has weak influence. Features of processes with participation of slow electrons and molecular ions in a strong light field, which proceed through a stage of intermediate Rydberg complex formation, are discussed. The main feature of these complexes is connected with the presence of the strong nonadiabatic connection of electronic and nuclear movement. For description of its display in various elementary processes, the perturbation theory is essentially inapplicable. The inverse problem in a possibility of restoration of the spectroscopic parameters entering into the theory of multichannel quantum defect is discussed.

Keywords Rydberg molecule • Elementary process • Strong laser field

2.1 Introduction

The elementary processes involving diatomic Rydberg molecules XY^{**} can be represented schematically as follows. First of all, they include the collisional processes

$$\left.\begin{matrix} e^- + XY^+ \\ X + Y^* \end{matrix}\right\} \Leftrightarrow XY^{**} \Leftrightarrow \left\{\begin{matrix} e^- + XY^+ \\ X + Y^* \end{matrix}\right., \tag{2.1}$$

G.V. Golubkov (✉)
Semenov Institute of Chemical Physics, Russian Academic of Sciences, Moscow, Russia
e-mail: golubkov@chph.ras.ru

V. Bychkov et al. (eds.), *The Atmosphere and Ionosphere*, Physics of Earth and Space Environments, DOI 10.1007/978-94-007-2914-8_2,

of the elastic and inelastic scattering of slow electrons by molecular ions, the dissociative recombination between electrons and molecular ions, and the associative ionization of atoms, as well as elastic and inelastic collisions between atoms involving the dissociative states whose potential curves lie closely to the minimum of the ion's potential energy (Golubkov and Ivanov 2001). Another important group comprises the processes

$$XY + h\nu \rightarrow XY^{**} \Leftrightarrow \begin{cases} e^- + XY^+ \\ X + Y^* \end{cases} \tag{2.2}$$

(photoionization and photodissociation) induced by the single- or multiphoton absorption. The processes in question also include free–free radiative transitions, such as the electron bremsstrahlung

$$e^- + XY^+ \rightarrow XY^{**} \rightarrow XY^+ + e^- + \hbar\Omega \tag{2.3}$$

where Ω is the bremsstrahlung frequency.

Processes (2.1, 2.2, and 2.3) play a substantial role in gas discharge lasers, low-temperature plasmas, and various atmospheric and astrophysical phenomena (Stebbings and Danning 1983). The effects of external physical factors on their dynamics are also of great interest. In particular, laser control of elementary atomic and molecular processes is a fundamental problem in modern chemical physics. As a tool for controlling these processes, the laser has a number of advantages over classical light sources. First, a highly monochromatic laser beam can be used to achieve the frequency selectivity required to obtain detailed information about a quantum system, such as energy levels, their decay widths, and radiative lifetimes. Second, varying the beam intensity and using a tunable laser, one can determine these characteristics as functions of a laser field strength and frequency, respectively (Ivanov and Golubkov 1991). Third, owing to the high intensities attainable, the present-day laser technology provides tools for a direct control of gas-phase reaction rate constants (Hirschfelder 1989).

2.2 Status of the Theory

Laser–atom interaction has been discussed in a vast literature (Delone et al. 1983; Delone and Krainov 1978; Rapoport et al. 1978; Delone 1989; Lambropoulos 1976; Swain 1980; Rosenberg 1982; Mittleman 1982). The perturbation theory generally describing the behavior of a molecular system interacting with an external electromagnetic field is inapplicable when the field is strong. The concept of the *strong field* is explained as follows. If the amplitude of the laser field strength f is comparable with the atomic field strength $f_a \simeq 5.14 \cdot 10^9$ V/cm (which corresponds to beam intensities of $\sim 10^{17}$ W/cm^2), then the multiphoton ionization rearranges

the electronic structure of the molecule (Ivanov and Golubkov 1999). Accordingly, a field is naturally referred to as strong if it is weak on an atomic scale but is strong enough to mix the states of a Rydberg molecule XY^{**} that are stationary (or quasi-stationary) in the absence of an external field. If the mixing strengths are large, then perturbative treatment is inapplicable (Rosenberg 1982).

To date, a variety of methods have been developed for modeling laser-induced nonlinear resonances embedded in the continua (Geller and Popov 1981), interference between autoionizing states in strong laser fields (Gontier and Nrahin 1980; Zakrewski 1984; Bachau et al. 1986; Movsesyan and Fedorov 1989), adiabatic stabilization of excited states of atoms in strong laser fields (Fedorov and Movsesyan 1988; Fedorov 1987; Horbatsch 1981; Su et al. 1990; Dubrovskii et al. 1991; Gavrila 1992; Peatross et al. 1992; Vos and Gavrila 1992), multiphoton ionization (Hoogenraad et al. 1994; Ivanov et al. 1994, 1997a; Delone and Krainov 1995; Moiseyev and Cederbaum 1999; Fedorov 1999; Kundliya and Mohan 2001; Theodosiou et al. 1979; Reiss 1987; Fedorov and Ivanov 1990), and other phenomena (Connerade et al. 1982; Jetzke et al. 1987; Bucksbaum et al. 1992; Zavriev and Bucksbaum 1993; Brumer and Shapiro 1993; Meyerhofer 1997; Akramine et al. 1999; Makhoute and Khalil 2008; Deb and Sinha 2009; Purohit and Mathur 2010; Musa et al. 2010; Andryushin et al. 1982, 1985; Fedorov and Roshchupkin 1984; Akulin and Karlov 1987; Delone and Fedorov 1989; Ivanov et al. 1996; Khalil et al. 1997; Deb et al. 2009; Itatani et al. 2004).

The main differences between the radiative collisions and collisions occurring in the absence of the field should be highlighted. First of all, the external field influences the asymptotic states of colliding particles, so instead of the usual solutions taken in the form of the plane waves, it is necessary to involve the state describing the motion of particles in the presence of the field. With this purpose, the "dressed" (Cohen-Tannoudji and Reynaud 1977) or the quasi-energy (Zel'dovich 1973) states are used. In both cases, the total wave function is expanded into an infinite series, each term of which corresponds to a particular photon number in the field; that is, account is taken of the virtual absorptions and emissions that are kinematically forbidden because of the momentum conservation. Thus, the problem is reduced to calculating the transition probabilities between the dressed asymptotic states. Moreover, some processes can be only field induced. Actually, at the expense of photon emission in the effective area of the interaction, total energy of the quantum system can decrease to the level corresponding to its bound state, which in this case will be unstable because of an exchange of energy with the field. Such states are referred to as *laser-induced resonances*. The best understanding of the physics of radiative collisions has been achieved in the low-frequency approximation, which decouples the projectile–field and projectile–target interactions and thus greatly simplifies the analysis of the system's behavior (Kelsey and Rosenberg 1979; Rosenberg 1989).

The nonperturbative analysis of laser-assisted collisional processes was initiated by Bunkin and Fedorov (1966), where the electron–atom bremsstrahlung stimulated by the single-mode electromagnetic field was calculated. A similar treatment was

developed by Krol and Watson (1973). In those studies, collisions were treated as the instantaneous elastic scattering events, the spontaneous emission being neglected.

Because we are interested in the processes involving electrons, we must first discuss the free electron dressing effects. It is known, that in the strong electromagnetic field with a frequency ω_f we can use the semiclassical approximation to describe a motion of the nonrelativistic electron with the energy $E_{\mathbf{p}}$ and momentum $\mathbf{p}$, in which the corresponding wave function has the form ($\hbar = m_e = e = 1$):

$$\Phi_{\mathbf{p}}(\mathbf{r}, t) = \sum_{m=-\infty}^{m=+\infty} \gamma_m \exp\left[-i\left(E_{\mathbf{p}} - m\omega_f\right)t + i\left(\mathbf{p} - m\mathbf{k}\right)\mathbf{r}\right] \tag{2.4}$$

where $\mathbf{k}$ is the photon momentum. Expression (2.4) is a superposition of terms corresponding to the number of virtual absorbed (or emitted) photons in the external field. The properties of the expansion coefficients γ_m were discussed in references (Nikishov and Ritus 1964; Brown and Ribble 1964; Leubner 1981; Reiss 1962, 1980).

When the target has an internal structure, the atomic system dressing effects should be taken into account (Ehlotzky 1985). A consistent treatment of field-dressed electron and target states is primarily based on two approaches. One of these approaches uses perturbation series in the coupling between the laser field and the atom–electron system (Francken et al. 1988). In the other, the laser–electron interaction is described exactly while the target dressing is treated perturbatively (Martin et al. 1989; Dimou and Faisal 1987a).

Theoretical studies of intense laser radiation effects on the scattering of slow electrons by the ion targets were carried out (Francken et al. 1988; Martin et al. 1989; Dimou and Faisal 1987a; Giusti-Suzor and Zoller 1987; He et al. 1989; Ivanov et al. 1988; Vartazaryan et al. 1989; Golubkov et al. 1993). In three studies (Ivanov et al. 1988; Vartazaryan et al. 1989; Golubkov et al. 1993), the laser-induced continuum–continuum coupling between free electron states was ignored. In terms of the quasi-energy states, this approximation discards the contributions to Eq. 2.4 from the harmonics corresponding to changes in total photon number ($\Delta m = 0$), which is justified if the following condition is realized:

$$\rho = \frac{f\, p_{\mathrm{e}}}{\omega_f^2} \ll 1 \tag{2.5}$$

(p_{e} is the electron momentum). This result means that the oscillation amplitude of the laser-driven electron is smaller than its wavelength. The condition in Eq. 2.5 implies that the electron can be treated as the free particle with well-defined momentum and energy at an asymptotic region. If the target is an unstructured particle, then the only channel at small ρ is the elastic scattering. Therefore, the laser radiation can have a significant effect on the electron–target system under the condition (2.5) only if the target has a internal structure. If the target is a positive molecular ion, this structure causes by formation of a Rydberg complex XY^{**}.

Therefore, when ρ is small, the electromagnetic field influence on the processes (2.1, 2.2, and 2.3) must appear at the complex formation stage only, where Rydberg electron dynamics is multichannel. The problem was analyzed in the one-channel approximation by Giusti-Suzor and Zoller (1987), and multichannel treatment was developed subsequently (He et al. 1989; Ivanov et al. 1988, 1995, 1997b, c, 1999; Vartazaryan et al. 1989; Golubkov et al. 1993; Golubkov and Ivanov 1993, 1994, 1997). Note that the time-independent theory reported in references (Ivanov et al. 1988, 1995, 1997b, c, 1999; Vartazaryan et al. 1989; Golubkov et al. 1993, 1999a, b; Golubkov and Ivanov 1993, 1994. 1997) automatically takes into account the Stark effect.

Another limitation of the time-independent theory discussed here is imposed by requiring that

$$f\omega_f^{-5/3} \ll 1, \tag{2.6}$$

which means negligible probabilities of the transitions between Coulomb continuum states (Ivanov and Golubkov 1991). Under these conditions, the field effect on the complex XY^{**} is quantified in terms of the Rydberg resonance widths $\Gamma^{\mathrm{f}}_{n_q} \sim \left(f\omega_f^{-5/3}\right)^2 / n_q^3$, where n_q is the principal quantum number of the qth Rydberg resonance series associated with a closed channel (index q subsumes the incident angular momentum l, its projection Λ on the molecular axis, and the set of the ion's internal quantum numbers). The resonance width $\Gamma^{\mathrm{f}}_{n_q}$ should be compared with the natural decay width $\Gamma^{\mathrm{e}}_{n_q} \sim \gamma / n_q^3$, where the decay rate is $\gamma \ll 1$, in line with the concept of the existence of an intermediate complex. Accordingly, one criterion for strong field effect on the intermediate state should be that

$$\gamma < \left(f\omega_f^{-5/3}\right)^2 \ll 1. \tag{2.7}$$

However, the external field can affect the complex XY^{**} at much lower intensities f if resonances of the different Rydberg series (for example, n_q and $n'_{q'}$) overlap or happen to lie closely to one another. In this case, the field interaction between the resonance states

$$V^{\mathrm{f}}_{n_q n'_{q'}} \sim f\omega_f^{-5/3} \Big/ \left(n_q n'_{q'}\right)^{3/2}, \tag{2.8}$$

must be comparable with their half-widths or the level separation $\Delta^{\mathrm{e}}_{n_q n'_{q'}} = \left|E_{n_q} - E_{n'_{q'}}\right|$ (Golubkov et al. 1993); i.e.,

$$V^{\mathrm{f}}_{n_q n'_{q'}} \sim \begin{cases} \Gamma^{\mathrm{e}}_{n_q}, \Gamma^{\mathrm{e}}_{n'_{q'}}, & \Gamma > \Delta, \\ \Delta^{\mathrm{e}}_{n_q n'_{q'}}, & \Delta > \Gamma. \end{cases} \tag{2.9}$$

Note that the account of the strong field effect on the intermediate complex differs substantially from the traditional time-dependent theory of the laser radiation interaction with atoms and molecules (Delone and Krainov 1985, 1994, 2001), because the formation time of the intermediate state cannot be well defined in the quantum mechanical framework, and the coupling between closed channels and continua must be taken into account in the analysis. These requirements motivated the use of special methods for analyzing of the processes (1)–(3) in studies performed in the 1990s. In particular, analysis of the elastic electron scattering by the atomic hydrogen ions in the excimer laser field using numerical integration of the strong coupling equations detected the fine resonance structure in the scattering cross section (Dimou and Faisal 1987b). Analogous features were also demonstrated by Collins and Csanak (1991). Behavior of the Rydberg electrons in laser fields was considered in the theory of radiative collisions of slow electrons with atoms (Giusti-Suzor and Zoller 1987) and molecular ions (Ivanov et al. 1988) and in studies of the photodissociation and photoionization of diatomic molecules (He et al. 1989; Vartazaryan et al. 1989). Laser-assisted collisions involving bremsstrahlung from electrons were also analyzed in (Berson 1981; Krainov and Roshchupkin 1983; Lisitsa and Savel'ev 1987; Balashov et al. 1984; Klinskikh and Rapoport 1987).

2.3 Multiphoton Processes

The problem of laser field effect on the near-threshold photoabsorption spectra in the processes (1) is closely related to that of the multiphoton ionization of atoms (Rapoport et al. 1978). Compared to atoms, molecules are more complex quantum systems where the key role is played by nonadiabatic coupling between the electronic and nuclear degrees of freedom (Golubkov and Ivanov 2001). In particular, the theory of near-threshold photoionization must not only describe vibrational and rotational dynamics but also rigorously take into account a predissociation. Characteristics of the molecular structure play an important role in bound–bound and bound–free radiative transitions (Lisitsa and Savel'ev 1987), which makes the well-developed theory of electron–atom and electron–ion bremsstrahlung (Bunkin and Fedorov 1966; Berson 1981; Krainov and Roshchupkin 1983; Lisitsa and Savel'ev 1987) inapplicable to Rydberg molecules.

Laser-assisted interaction of an electron with a target involves emission by stimulated bremsstrahlung and the absorption of field photons. The problem of the laser-assisted bremsstrahlung emission and absorption was originally analyzed in the Born approximation (Bunkin and Fedorov 1966). The electron–field interaction was taken into account accurately in this work, i.e., the electron wave functions (4) were employed. The authors have found the transition probabilities as the sum of the probabilities of absorption (emission) of a definite number of field photons. To go beyond the Born approximation, a semiclassical impact-parameter

method applicable to high-energy electrons was proposed by Lisitsa and Savel'ev (1987). The scope of that study was limited by the condition (5). The theory was extended to $\rho \gg 1$ and $f \gg 1$ by Klinskikh and Rapoport (1987), where a general expression was obtained for the n-photon differential cross section. In the alternative approach to the same problem used by Golovinskii (1988), the semiclassical wavefunction was found for an electron scattered by the finite-range potential in an electromagnetic field. Moreover, the resulting expression for the potential scattering cross section allows transitions to the limit of the Born approximation and the case of classical scattering.

It should be noted here that the phenomena described by the time-independent theory of radiative collisions developed in several studies (Ivanov et al. 1988, 1995, 1997b, c, 1999; Vartazaryan et al. 1989; Golubkov et al. 1993, 1999a, b; Golubkov and Ivanov 1993, 1994, 1997) occur in the near-threshold energy region of $E_{\mathbf{p}} \leq \omega$ (ω is the oscillation frequency of the molecular ion), where the Born approximation and semiclassical description are strongly inapplicable. According to (5), the electron quiver amplitude satisfies the relationship

$$a_f \cong \frac{f}{\omega_f^2} \ll \lambda_e \sim n^2, \tag{2.10}$$

where the electron wavelength λ_e is comparable with the dimensions of the Rydberg XY^{**} complex. Because of the multichannel Rydberg electron dynamics, electron energy is not conserved during the complex formation stage. The ponderomotive energy (cycle-averaged quiver energy) of the slow electron in a laser focal region is $\Delta E = \langle f \rangle^2 \Big/ 4\omega_f^2$ (Collins and Csanak 1991). If the energy and momentum of the incident electron are $E_{\mathbf{p}} \ll \Delta E$, $p_e \ll \Delta p \sim \langle f \rangle \Big/ \omega_f$, and the transit time $L_f / \Delta p$ through a beam with size L_f is much longer than the laser pulse duration τ_l, then the limitation on the field strength becomes

$$\langle f \rangle \ll L_f \omega_f / \tau_l . \tag{2.11}$$

The conditions depicted by Eqs. 2.6, 2.7, 2.8, 2.9, 2.10, and 2.11 allow ignoring the ponderomotive interaction, which would be significant for relatively fast electrons (Kibble 1966; Corkum et al. 1989, 1992; Reiss 1990; Salamin and Faisal 1997; Salamin 1997). Indeed, as a result of the analytical properties of the Coulomb wave functions, the corresponding ponderomotive contributions to matrix elements, resulting from the electric field inhomogeneity across the laser focal region, are independent of $E_{\mathbf{p}}$ and the scattering channel characteristics. The resulting general shift of all energy levels in the "electron + molecular ion" system can easily be eliminated by introducing a phase factor. For example, in the case of a typical laboratory laser with $\omega_f \sim 10^{-1}$, $L_f \sim 10^8$, and $\tau_l \sim 10^7$, it takes place when the incident electron energy and the average field strength are $E_{\mathbf{p}} \ll 10^{-1}$, and $\langle f \rangle \ll 1$, respectively.

2.4 Effects of Monochromatic Laser Radiation

Even though the basic mechanisms of the interaction between monochromatic laser radiation and autodissociating intermediate states are known and can be described by well-developed mathematical methods (e.g., see Geller and Popov 1981; Andryushin et al. 1982, 1985; Ivanov et al. 1995; Yakovlenko 1982; Lambropoulos and Zoller 1981; Alber and Zoller 1983; L'Huillier et al. 1988), the theory of the continuum–intermediate-state–continuum-type processes is far from complete. As already mentioned, this problem is substantially different from those generally solved in the theory of atom/molecule–field interaction. It also differs from the problems solved in the theory of the radiative collisions (Dubov et al. 1982; Yakovlenko 1984), where the semiclassical approach has proved to be most successful in the study of collisions between atoms in a radiation field. Quantum mechanical analysis of the relative motion using conventional methods of the theory of radiative collisions is a more complicated task, particularly when particle structure is changed by reaction. In particular, the rotational and vibrational degrees of freedom have been found to manifest themselves in the resonant multiphoton ionization (RMPI) and the dissociation (RMPD) of diatomic molecules, when their bound or autodissociating states are significantly populated at the intermediate stage (before transition to a continuum state). These findings motivate a detailed study of the laser-induced coupling of the bound or quasibound states between themselves and to continuum states.

The quantum scattering formalism (including multichannel quantum defect theory (Golubkov and Ivanov 2001)) is applicable because the molecule–field interactions in $e^- + XY^+$ and $X + Y$ configurations are strong only at the XY^{**} formation stage, when the laser-induced coupling $\mathbf{V}^f$ can be treated as comparable to the electrostatic interaction $\mathbf{V}^e$, which formally increases the number of channels in the scattering problem. The spectrum of the resulting unperturbed Hamiltonian consists of noninteracting states with quasi-energies defined as modulo ω_f; this provides a simple method for constructing a $\mathbf{T}$-matrix and wave functions that can be used to calculate RMPI and RMPD processes involving large groups of states (including infinite Rydberg resonance series) while keeping precise track of the coupling of the intermediate states to the continua and transitions between them.

When the process occurs via a single intermediate resonant state (as in k^*-photon absorption for $k^* < k_m$, where k_m is the minimum number of ω_f photons required for ionization), the photoelectron spectrum can be described by the Breit–Wigner-type formula with resonance width corresponding to the $(k^* - k_m)$-photon transition from this state to the continuum (Letokhov 1987). In other words, the single-resonance approximation can be applied to the simplest transition state that is formed at an intermediate stage.

The next step in theory focused on systems where resonance conditions are satisfied simultaneously for two intermediate states, such as those populated by $(k^* - 1)$ and k^* photon absorption. Processes of this kind were examined by analyzing equations for the intermediate-state population amplitudes when a coupling field was rapidly switched on (Andryushin et al. 1982, 1985; Lambropoulos

and Zoller 1981). This work required the use of a special procedure developed to describe the continuum coupling because the widespread relaxation parameter matrix method had proved to be inapplicable. Both RMPI and RMPD characteristics revealed nonmonotonic variation in molecular dynamics with laser intensity (Jolicard and Atabek 1992). This behavior is most clearly manifested in above-threshold dissociation (ATD), which is significant at laser intensities $I \sim 10^{13}$ W/cm^2 (Jolicard and Atabek 1992; Giusti-Suzor et al. 1990; Zavriyev et al. 1990). The process competing with ATD is the ordinary single-photon absorption, and their relative rates depend on the molecule's initial vibrational state and the laser intensity and frequency. An increase in intensity to $I \sim 10^{14}$ W/cm^2 has a considerable bond-softening effect because the molecular potential is distorted by the laser field (Zavriyev et al. 1990; Yao and Chu 1992). Details of the intensity-dependent dynamics underlying these phenomena were examined by Yang et al. (1991). Laser effects on molecular ions were investigated by Zavriyev et al. (1993) and Aubanel et al. (1993). It should also be noted that a bichromatic driving field (the fundamental harmonic and a phase-shifted higher one of the same laser) provides a means for the coherent control of dissociation (Charron et al. 1994; Abrashkevich et al. 1998), in particular for the isotope separation (Atabek et al. 1994; Charron et al. 1995). These experimental observations stimulated theoretical studies intended to explain and predict the laser-driven phenomena. Let us discuss these matters in some detail. Two essentially different approaches were developed to solve problems of this kind (e.g., see Giusti-Suzor et al. 1995; Guo 1998).

In one of these, the stationary equations of the Floquet theory are used (Shirley 1965), which is valid to describe processes driven by dye lasers with typical pulse durations of 10^{-10} to 10^{-9} s, when the field is switched on at $t = 0$ and applied for a sufficiently long time. The approach is true if the laser pulse is sufficiently long and the process dynamics does not vary from cycle to cycle ($\tau_l \gg \tau_r$, where τ_r is a reaction time). The total wave function is represented as a superposition of dressed states, and the system of coupled equations is solved numerically (Chu 1991; He et al. 1990; Bandrauk et al. 1993). For short laser pulses ($\tau_l < 10^{-12}$ s), the Schrödinger equation describing the time evolution of the emerging wave packet is generally computed by using a Gaussian pulse shape. Finding of such solutions is a formidable task. However, a number of assumptions can be made that greatly simplify theoretical analysis, such as the one-dimensional approximation where the internuclear vector is collinear to the laser polarization vector. The resulting solution is only slightly different from those of the three-dimensional problem (Charron et al. 1994).

2.5 The Role of Rotational Degrees of Freedom

One of the issues most widely discussed in the literature is the role of molecular rotation (Ivanov et al. 1996, 1997b; Charron et al. 1994; Giusti-Suzor et al. 1995; McCann and Bandrauk 1992; Banerjee et al. 1994; Sukharev and Krainov 1998),

whose contribution to the laser-driven RMPI and RMPD processes is not evident a priori. In most cases, a rotation can increase the reaction rate by adding new open channels as a consequence of the laser-induced nonadiabatic coupling between the electronic and rotational degrees of freedom, which occurs when electronically excited molecules are produced at the intermediate stage of the process. In other situations, rotation has an inhibiting effect on the reaction, e.g., when RMPI of diatomic XY molecules involves laser-induced bound states situated on the $X + Y$ dissociative continuum background (Charron et al. 1994).

The vast majority of results in the RMPI theory based on the concept of field-dressed states pertain to atomic systems. As already noted, molecules are much more difficult to study. Generally, the intermediate molecular states are degenerate (e.g., with respect to the projection M of total angular momentum J when $J \geq 1$). Furthermore, their upper levels usually predissociate; that is, the corresponding set of dissociation continua is more diverse than atomic continua. Molecules have the vibrational and rotational degrees of freedom, which complicate the laser-driven dynamics of even the simplest diatomic systems; i.e., analyses of photoinduced processes must take into account rovibronic states. The best developed model of interaction between a monochromatic field and a molecule is that of the two-photon ionization and dissociation (Chen et al. 1993), with a single intermediate state or a few mutually interacting ones.

The field-induced coupling between resonances can be sufficiently strong that the corresponding Rabi frequency becomes comparable with the rotational level separations. Under such conditions, RMPI involves large groups of levels, that is, the observed phenomenon has no analogue in atomic systems. It is obvious that the positions and widths of these levels must manifest themselves in the photoelectron spectra, each of which is a hybrid that is mixed with the other states. The radiative scattering matrix method provides a very convenient formalism for analyzing the combined effect of a weak probe field and a strong monochromatic one (Ivanov et al. 1988, 1995, 1997b, c, 1999; Vartazaryan et al. 1989; Golubkov et al. 1993, 1999a, b; Golubkov and Ivanov 1993, 1994, 1997). In the ionization scheme, the system is supposed to be excited to the intermediate (working) level by the probe (or via off-resonant multiphoton processes induced by the strong field), and the strong field drives a cascade of transitions between excited or high-lying excited states and transitions to the continuum.

The rotational alignment of ions can be used to select energy-unresolved states because the field-induced coupling strength between molecular states depends on the projection M of total angular momentum on the laser polarization axis. As a result, molecular ions with given M values can be produced by varying the frequency and strength of the laser field.

When $f \sim 10^{-4} \div 10^{-3}$, the contribution from the groups of dressed states gives rise to the strongly mixed "diatomic molecule + light field" hybrid states. An analysis of the field-strength dependence of their widths has revealed a nonmonotonic behavior (in particular, a decrease in width with increasing f), which suggests molecular stabilization in a certain interval of f.

2.6 Predissociation

The next issue to be addressed is the role of the predissociative XY^{**} states. It turns out that they both open up the new dissociation channels, $XY^{**} \rightarrow X^{*} + Y$, and affect the characteristics of transitions to the ionization continuum. The contribution of predissociation to the anomalous vibrational distribution of $H_2{}^{+}$ ions produced by the photoionization of molecular hydrogen has been discussed (Hickman 1987; Dixit et al. 1989; O'Halloran et al. 1987).

One low-temperature exothermic reaction of the particular importance is that of dissociative recombination (DR) of $O_2{}^{+}$ ions, responsible for the rate of charge loss processes in the upper atmosphere. The DR cross section can be increased by several orders of magnitude by choosing suitable values of the laser parameters, which makes the laser-assisted reaction feasible (Golubkov et al. 2002, 2003, 2011; Adamson et al. 2009). The problem reduces to finding the optimal conditions for the laser control of low-temperature DR and formulating recommendations for future experiments.

Laser control efficiency depends on the incident electron energy, the field strength and frequency, and the angle between the electron and laser beams. The laser pulse duration here is much longer than the transition times between the intermediate molecular states. For example, the predissociation times for high-lying states of XY^{**} are of the order of 10^{-11} s. Note that the tunable lasers widely used in various photo-induced processes are characterized by strengths of $\sim 10^{12} \div 10^{14}$ W/cm^2 and pulse repetition rates of $\Delta\tau \sim 10^{-3}$ s. The corresponding saturation and rotational widths do not exceed 10^{-1} cm^{-1}, and the Doppler broadening is routinely eliminated by splitting the laser beam (Letokhov 1987). Because the energy dependence of the DR cross section cannot be measured to accuracy better than $\Delta E \sim 10^{-3}$ eV, the spread in the pulse frequency ω_f is negligible and the beam can be considered monochromatic.

The problem of quantitative description of DR reaction in the framework of MQD theory directly stems from the following feature of MQD theory: it is highly sensitive to the variation of quantum defects and configuration interactions as functions of internuclear distance. The analysis of partial and total low-temperature DR rate constant as a function of parameters of the theory was carried out by Golubkov et al. (2000a). It was demonstrated that even an insignificant variation of quantum defect may lead to the variation (of the of one to two orders of magnitude) in the rate constant. The dependence of rate constant on the configuration interaction is smoother. Because quantum chemistry is incapable of providing the necessary accuracy, the further development of the theory is impossible without invoking additional modern high-resolution experiments (for example, REMPI, REMPD). Restoration of MQD theory parameters from the experimental data represents the reverse problem, which is incorrect by definition (Golubkov et al. 2000b). It was shown that it can be solved because (1) the direct and reverse problems both are solved in the framework of universal unitary MQD theory; (2) intensities of the photo-processes are analytical functions; (3) the solution is unique only if a

sufficient amount of experimental data is available because this solution is obtained as a result of optimization of a large number of experiments in different spectrum regions; and (4) the reverse problem is reduced to analysis of the sets of simple algebraic equations.

2.7 Conclusion

In conclusion, we discuss the effects associated with a field mixing of the Rydberg resonances. The presence of an external field leads to the fact that the resonance structure of the intermediate Rydberg complexes XY^{**} may overlap some of the resonances belonging to the different vibronic series of the quasi-energy spectrum, which can occur at any ratio between the vibrational ω and field ω_f frequencies. If the field widths are smaller compared with the natural ones, the Rydberg states experience almost no exposure to laser radiation. The situation changes significantly if a resonance level of a predissociative Rydberg series overlaps with the field-induced resonant level. The composite resonant vibronic (hybrid) states will arise in these conditions. The mechanisms of population and decay of these states during the DR reaction must differ significantly from those discussed here. In this case, new channels of the process will arise, when the effective $l\Lambda$-harmonics take place, which occurs as the result of a weak configuration interaction with the dissociative channels being in the field excluded from the process. Because the existence conditions of the field-induced resonances of composite $e^- + XY^+$ systems are very critical to the positions of the unperturbed resonance levels, the rotational structure of the intermediate Rydberg complexes should be included in consideration.

Let us demonstrate the main features of the resonance state field mixing on an example of the DR reaction in the most important case, when the incident electron energy E in a given $(l\Lambda, v = 0, m = 0)$ state is located below the ion vibrational excitation threshold. We consider the situation when the "natural" vibronic resonance of 1 $(l\Lambda, v = 1, m = 0)$ with the energy E_1 overlaps with the laser-induced resonance of 2 $(l'\Lambda', v = 1, m = \pm 1)$, whose energy is equal to E_2, and denote the continuum $e^- + XY^+(m = 0)$ and $X + Y$ $(m = \pm 1)$ states by 0 and β, respectively. Then, the DR reaction, taken in the field absence $(f = 0)$ of the direct and resonant mechanisms and described by the Fano outline, obtains additional features in energy dependence under a field mixing with the laser-induced resonance 2. Indeed, neglecting the field-induced shift and broadening of the levels, the transition probability can be written as (Golubkov and Ivanov 1993)

$$W_{\beta 0} = W_0 \left| \frac{(\varepsilon_1 - \Delta_1)\left(\varepsilon_2 + i\,\Gamma_2^{\mathrm{e}}\right) - \left(V_{12}^{\mathrm{f}}\right)^2}{\left(\varepsilon_1 + i\,\Gamma_1^{\mathrm{e}}\right)\left(\varepsilon_2 + i\,\Gamma_2^{\mathrm{e}}\right) - \left(V_{12}^{\mathrm{f}}\right)^2} \right|^2 \tag{2.12}$$

Here W_0 is the probability of direct transition in the absent external field, $\varepsilon_{1(2)} = E - E_{1(2)}$ are the values measured from the resonant level energies, $\Gamma_{1(2)}^{\mathrm{e}}$ are the natural half-widths of these levels expressed in terms of partial ionization rate

and predissociation, V_{12}^{f} is the field interaction, and Δ_1 is the shift of level 1. In these conditions, isolated laser-induced resonance is weak. However, according to Eq. 2.12, it can greatly affect the line profile if that is close to the natural resonance. In general, the contour form is described by a curve with two peaks.

An alternative situation arises if $\Delta_1 \ll \Gamma_{1(2)}^{\mathrm{e}}$ when the "anti-resonances" appear instead of resonances. In accordance with the formula (2.12) for $f = 0$, only one Fano "anti-resonance" is formed, which is described by the dependence

$$W_{\beta 0} \simeq W_0 \left| \frac{\varepsilon_1}{\varepsilon_1 + i\,\Gamma_1^{\mathrm{e}}} \right|^2$$

In the opposite case (under condition $\left|V_{12}^{\mathrm{f}}\right| \gg \Delta_{12},\ \Gamma_{1(2)}^{\mathrm{e}}$, where $\Delta_{12} = |E_1 - E_2|$), it turns into the two "anti-resonances" located symmetrically at the points $\varepsilon = \pm V_{12}^{\mathrm{f}}$ with half-widths $\left(\left(\Gamma_1^{\mathrm{e}} + \Gamma_2^{\mathrm{e}}\right)/2\right.$. The next important reaction channel DR is characterized by an increase $(m = -1)$ or decrease $\left((m = 1)\right)$ of the translational energy of the reaction products caused by a field mixing, when the probability of resonant process is given by the expression

$$W_{\beta 0} = \frac{\Gamma_1^{\mathrm{i}} \left(V_{12}^{\mathrm{f}}\right)^2 \Gamma_2^{\beta}}{\left| \left(\varepsilon_1 + i\,\Gamma_1^{\mathrm{e}}\right)\left(\varepsilon_2 + i\,\Gamma_2^{\mathrm{e}}\right) - \left(V_{12}^{\mathrm{f}}\right)^2 \right|^2} \tag{2.13}$$

where $\Gamma_1^{\mathrm{i}(\beta)}$ is the autoionizing (i) or predissociative (β) half-widths of the states 1 and 2, respectively. The expression (Eq. 2.13) by analogy with (Eq. 2.12) provided by $\left|V_{12}^{\mathrm{f}}\right| \gg \Delta_{12}, \Gamma_{1(2)}^{\mathrm{e}}$ describes the energy dependence with the two symmetrically situated maxima.

The product features of the process depend not only on the total angular momentum J and its projection M: averaging over M should lead to a smoothing of the observed relationships. However, if $V_{12}^{\mathrm{f}}/J \geq \Gamma_{1(2)}^{\mathrm{e}}$, the spectrum should reproduce the individual resonances for each value M (Ivanov et al. 1995).

References

Abrashkevich DG, Shapiro M, Brumer P (1998) Two-pulse coherent control of electronic branching in Li_2 photodissociation. J Chem Phys 108(9):3385–3390

Adamson SO, Buenker RJ, Golubkov GV, Golubkov MG, Dement'ev AI (2009) Laser stimulation of low-temperature dissociative recombination of electrons and oxygen molecular ions. Russ J Phys Chem B3(2):195–210

Akramine OEl, Makhoute A, Khalil D et al (1999) Effect of laser polarization in laser-assisted electron–helium inelastic collisions: a Sturmian approach. J Phys B At Mol Opt Phys 32(12):2783–2800

Akulin VM, Karlov NV (1987) Intense resonant interactions in quantum electronics. Nauka, Moscow

Alber G, Zoller P (1983) Harmonic generation and multiphoton ionization near an autoionizing resonance. Phys Rev A27(3):1373–1388

Andryushin AI, Kazakov AE, Fedorov MV (1982) Effect of resonant electromagnetic field on the autoionizing states of atoms. Sov Phys JETP 55(1):53–58
Andryushin AI, Kazakov AE, Fedorov MV (1985) Resonant excitation and decay of autoionising states in a strong electromagnetic field. Sov Phys JETP 61(4):678–686
Atabek O, Chrysos M, Lefebvre R (1994) Isotope separation using laser fields. Phys Rev A49(1):R8–R11
Aubanel EE, Gauthier J-M, Bandrauk AD (1993) Molecular stabilization and angular distribution in photodissociation of H_2^+ in intense laser fields. Phys Rev A48(3):2145–2152
Bachau H, Lambropoulos P, Shakeshaft R (1986) Theory of laser-induced transitions between autoionizing states of He. Phys Rev A34(6):4785–4792
Balashov EM, Golubkov GV, Ivanov GK (1984) Radiative transitions between Rydberg states of molecules. Sov Phys JETP 59(6):1188–1194
Bandrauk AD, Aubanel EE, Gauthier JM (1993) Theory of molecules in intense laser fields. In: Bandrauk AD (ed) Molecules in laser fields. Dekker, New York, pp 109–180
Banerjee S, Bhattacharyya SS, Saha S (1994) Nonadiabatic effects on resonance-enhanced two-photon dissociation of H_2. Phys Rev A49(3):1836–1846
Berson IYa (1981) Multiphoton ionization of Rydberg states and stimulated bremsstrahlung at Coulomb field. Izv Akad Nauk SSSR Ser Fiz 45(12):2289–2292; (1981) Semiclassical approximation for stimulated bremsstrahlung. Sov Phys JETP 53(5):891–895
Brown LS, Ribble TWB (1964) Interaction of intense laser beams with electrons. Phys Rev 133(3):A705–A719
Brumer P, Shapiro M (1993) Coherence and laser control of chemical reactions. In: Bandrauk AD (ed) Molecules in laser field. Dekker, New York, pp 287–348
Bucksbaum PH, Bashkansky M, Mcllrath TJ (1992) Scattering of electrons by intense coherent light. Phys Rev Lett 58(4):349–352
Bunkin FV, Fedorov MV (1966) Bremsstrahlung in a strong radiation field. Sov Phys JETP 22(6):844–847
Charron E, Giusti-Suzor A, Mies FH (1994) Fragment angular distribution in one- and two-color photodissociation by strong laser fields. Phys Rev A49(2):R641–R644
Charron E, Giusti-Suzor A, Mies FH (1995) Coherent control of isotope separation in HD^+ photodissociation by strong fields. Phys Rev Lett 75(15):2815–2818
Chen Z, Shapiro M, Brumer P (1993) Theory of resonant two-photon dissociation of Na_2. J Chem Phys 98(11):8647–8659
Chu S-I (1991) Complex quasivibrational energy formalism for intense-field multiphoton and above-threshold dissociation: complex-scaling Fourier-grid Hamiltonian method. J Chem Phys 94(12):7901–7909
Cohen-Tannoudji C, Reynaud S (1977) Dressed-atom description of resonance fluorescence and absorption spectra of a multi-level atom in an intense laser beam. J Phys B At Mol Opt Phys 10(3):345–363
Collins LA, Csanak G (1991) Multiphoton resonances in $e^- + H^+$ scattering in a linearly polarized radiation field. Phys Rev A44(9):R5343–R5345
Connerade JP, Gay JC, Liberman S (1982) Atomic and molecular physics close to Ionization thresholds in high fields. J Phys Colloq (France) 43(C2)
Corkum PB, Burnett NH, Brunel F (1989) Above-threshold ionization in long-wavelength limit. Phys Rev Lett 62(11):1259–1262
Corkum PB, Burnett NH, Brunel F (1992) Multiphoton ionization in large ponderomotive potentials. In: Gavrila M (ed) Atoms in intense laser fields. Academic, New York
Deb SG, Sinha C (2009) Multiphoton effects in laser-assisted ionization of a helium atom by electron impact. Eur Phys J D56(2):173–177
Deb SG, Roy S, Sinha C (2009) Multiphoton (e,2e) process of hydrogen atom in strong laser field. Eur Phys J D55(3):591–600
Delone NB (1989) Interaction of laser radiation with matter. Nauka, Moscow
Delone NB, Fedorov MV (1989) New effects in the multiphoton ionization of atoms. Sov Phys Usp 32(6):500–520

Delone NB, Krainov VP (1978) Atom in a strong light field. Atomizdat, Moscow
Delone ND, Krainov VP (1985) Atoms in strong laser fields. Springer, Heidelberg
Delone ND, Krainov VP (1994) Multiphoton processes in atoms. Springer, Heidelberg
Delone NB, Krainov VP (1995) Atomic stabilization in a laser field. Phys Usp 38(11):1247–1268
Delone ND, Krainov VP (2001) Nonlinear ionization of atoms by laser radiation. Fizmatlit, Moscow
Delone NB, Krainov VP, Shepelyanskii DL (1983) Highly excited atoms in the electromagnetic field. Sov Phys Usp 26(7):551–572
Dimou L, Faisal FHM (1987a) In: Photon and continuum states of atoms and molecules. Rahman NK, Guidotti C, Allegrini M (eds) Photon and continuum states of atoms and molecules. Springer proceedings in physics 16. Springer, Berlin p. 240
Dimou L, Faisal FHM (1987b) In: Photon and continuum states of atoms and molecules. New class of resonance in the $e^- + H^+$ scattering in an excimer laser field. Phys Rev Lett 59(8):872–875
Dixit SN, Lynch DL, McKoy BV, Hazi AU (1989) Electronic autoionization and vibrational-state distributions in resonant multiphoton ionization of H_2. Phys Rev A40(3):1700–1703
Dubov VS, Lapsker YaE, Gurvich LV (1982) Chemical radiative collisions: a new type of elementary processes. Khim Fiz 1(12):1642–1659
Dubrovskii YuV, Ivanov MYu, Fedorov MV (1991) Resonant excitation and stabilization of atomic Rydberg levels during multiphoton ionization in a strong laser field. Sov Phys JETP 72(2): 228–237
Ehlotzky F (ed) (1985) Fundamentals of laser interactions. Lecture Notes in Physics 229. Springer, Berlin
Fedorov MV (1987) Electron in strong light field. Nauka, Moscow
Fedorov MV (1999) Stabilization of atoms in a strong laser field. Phys Usp 42(1):61–66
Fedorov MV, Ivanov MYu (1990) Coherence and interference in a Rydberg atom in a strong laser field: excitation, ionization, and emission of light. J Opt Soc Am B7(4):569–573
Fedorov MV, Movsesyan AM (1988) Field-induced effects of narrowing of photoelectron spectra and stabilization of Rydberg atoms. J Phys B At Mol Opt Phys 21(7):L155–L158
Fedorov MV, Roshchupkin SP (1984) Suppression of interference in $e - e$ scattering by the field of a strong electromagnetic wave. J Phys A Math Gen 17(16):3143–3149
Francken P, Attaourti Y, Joachain CJ (1988) Laser-assisted inelastic electron-atom collisions. Phys Rev A38(4):1785–1796
Gavrila M (1992) Atomic structure and decay in high-frequency fields. In: Gavrila M (ed) Atoms in intense laser fields. Academic, New York, pp 435–510
Geller YuI, Popov AK (1981) Laser stimulation of nonlinear resonances in continuous spectra. Nauka, Novosibisrsk
Giusti-Suzor A, Zoller P (1987) Rydberg electrons in laser fields: a finite–range-interaction problem. Phys Rev A36(11):5178–5188
Giusti-Suzor A, He X, Atabek O, Mies FH (1990) Above-threshold dissociation of H_2^+ in intense laser fields. Phys Rev Lett 64(5):515–518
Giusti-Suzor A, Mies FH, DiMauro LF et al (1995) Dynamics of H_2^+ in intense laser fields. J Phys B At Mol Opt Phys 28(3):309–339
Golovinskii PA (1988) Stimulated bremsstrahlung effect in the scattering of electrons by atoms subject to the polarization of a target. Sov Phys JETP 67(7):1346–1350
Golubkov GV, Ivanov GK (1993) Dissociative recombination of electrons and molecular ions in monochromatic IR light. JETP 77(4):574–586
Golubkov GV, Ivanov GK (1994) Dynamic behavior of highly excited molecular states in the strong monochromatic laser field. Russ Chem Bull 43(3):327–345
Golubkov GV, Ivanov GK (1997) Elementary reactions in a field of monochromatic laser radiation. Chem Phys Rep 16(6):101–111
Golubkov GV, Ivanov GK (2001) Rydberg states of atoms and molecules and elementary processes with their participation. URSS, Moscow
Golubkov GV, Ivanov GK, Vartazaryan AS (1993) Effect of strong electromagnetic field on collisional and radiative processes involving Rydberg states of atoms and molecules. Khim Fiz 12(1):16–31

Golubkov GV, Golubkov MG, Ivanov GK (1999a) The possibility of general MQDT parameter determination from high resolution optical spectra. Khim Fiz 18(1):63–78

Golubkov GV, Golubkov MG, Ivanov GK (1999b) Difficulties inherent in the theory dissociative recombination and possible ways of their obviation. In: Larsson M, Mitchell JBA, Schneider IF (eds) Dissociative recombination: theory, experiment, and application IV. World Scientific, Singapore, pp 106–110

Golubkov MG, Golubkov GV, Ivanov GK (2000a) Difficulties in the theory of low-temperature dissociative recombination and possible ways of their obviation. In: Larson M, Mitchell JBA, Schneider IF (eds) Dissociative recombination. Theory, experiment and applications, vol IV. World Scientific, Singapore

Golubkov MG, Golubkov GV, Ivanov GK (2000b) On the feasibility of reconstruction the MQD theory parameters from high-resolution optical spectra. Chem Phys Rep 18(7):1305–1333

Golubkov GV, Golubkov MG, Romanov AN (2002) Dissociative recombination of electrons and O_2^+ molecular ions in the field of intense visible laser radiation. JETP 94(3):489–497

Golubkov GV, Golubkov MG, Romanov AN, Buenker RJ (2003) Dissociative recombination of electrons and $e^- + O_2^+ \rightarrow O\left(^1D\right) + O\left(^3P\right)$ in a strong laser field. Phys Chem Chem Phys 5:3174–3182

Golubkov GV, Golubkov MG, Buenker RJ (2011) Laser control of low-temperature reaction $e^- + O_2^+$. JETP 112(2):187–192

Gontier Y, Nrahin M (1980) Energetic electron generation by multiphoton absorption. J Phys B At Mol Opt Phys 13(12):4381–4390

Guo H (1998) A time-dependent theory of photodissociation based on polynomial propagation. J Chem Phys 108(6):2466–2472

He X, Atabek O, Giusti-Suzor A, Zoller P (1989) Laser-induced resonances in molecular dissociation in intense fields. Phys Rev A38(11):5586–5594

He X, Atabek O, Giusti-Suzor A (1990) Semiadiabatic treatment of photodissociation in strong laser fields. Phys Rev A42(3):1585–1591

Hickman AP (1987) Non-Franck–Condon distributions of final states in photoionization of $H_2\left(C^1\prod_u\right)$. Phys Rev Lett 59(14):1553–1556

Hirschfelder JN (1989) Where are laser–molecule interactions headed? Adv Chem Phys Laser Mol Methods 73:1–79

Hoogenraad JH, Vrijen RB, Noordam LD (1994) Ionization suppression of Rydberg atoms by short laser pulses. Phys Rev A50(5):4133–4138

Horbatsch M (1981) Suppression of ionization in short high-frequency laser pulses of high intensity. Phys Rev A44(9):R5346–R5349

Itatani J, Levesque J, Zeidler D et al (2004) Tomographic imaging of molecular orbitals. Nature 432:867–871

Ivanov GK, Golubkov GV (1991) Bremsstrahlung from slow electrons scattered by ions in an external electromagnetic field. Sov Phys JETP 72(5):783–789

Ivanov GK, Golubkov GV (1999) Multiphoton ionization of molecules under the conditions of strong field-induced perturbation of Rydberg states. JETP 88(6):1087–1094

Ivanov GK, Vartazaryan AS, Golubkov GV (1988) Radiative collisional processes involving Rydberg states of diatomic molecules. Dokl Akad Nauk SSSR 303(2):390–394

Ivanov GK, Golubkov GV, Manakov DM (1994) Rydberg states in multiphoton atomic ionization processes of Rydberg atoms. JETP 79(5):707–713

Ivanov GK, Golubkov GV, Drygin SV (1995) Resonant multiphoton ionization and dissociation of molecules with simultaneous action of a weak field and intense monochromatic radiation. JETP 80(5):840–847

Ivanov GK, Golubkov GV, Drygin SV (1996) Rotational orientation of molecular ions in multiphoton ionization of molecules. Chem Phys Rep 15(5):641–647

Ivanov GK, Manakov DM, Golubkov GV (1997a) Multiphoton ionization of atoms via a series of intermediate Rydberg states. Chem Phys Rep 16(6):1013–1023

Ivanov GK, Golubkov GV, Drygin SV, Cherlina IE (1997b) Multilevel rotational transitions in the intermediate stage of three-photon ionization of molecules. JETP 84(5):888–892

Ivanov GK, Golubkov GV, Manakov DM (1997c) Multiphoton ionization of atoms via a series of intermediate Rydberg states. Chem Phys Rep 16(6):112–123

Ivanov GK, Golubkov GV, Manakov DM (1999) Characteristics of manifestations of Rydberg resonance structure in multiphoton ionization of molecules. Khim Fiz 18(1):33–39

Jetzke S, Broad J, Maquet A (1987) Electron–hydrogen collisions in the presence of a laser field: one-photon excitation. J Phys B At Mol Opt Phys 20(12):2887–2897

Jolicard G, Atabek O (1992) Above-threshold-dissociation dynamics of H_2^+ with short intense laser pulses. Phys Rev A46(9):5845–5855

Kelsey EJ, Rosenberg L (1979) Generalized low-frequency approximation for scattering in a laser field. Phys Rev A19(2):756–765

Khalil D, Maquet A, Taieb R et al (1997) Laser-assisted (*e*,2*e*) collisions in helium. Phys Rev A 56(6):4918–4928

Kibble TWB (1966) Mutual refraction of electrons and photons. Phys Rev 150(4):1060–1069

Klinskikh AF, Rapoport LP (1987) Quasi-classical theory of potential scattering of an electron in the field of a laser wave. Sov Phys JETP 66(1):53–57

Krainov VP, Roshchupkin SP (1983) Bremsstrahlung of a slow electron at a Coulomb center in an external electromagnetic field. JETP 57(4):754–757

Krol NM, Watson KM (1973) Charged-particle scattering in the presence of a strong electromagnetic wave. Phys Rev A8(2):804–809

Kundliya R, Mohan M (2001) Stabilization of hydrogen atom in intense laser fields. Phys Lett A291(1):22–26

L'Huillier A, Tang X, Lambropoulos P (1988) Multiphoton ionization of rare gases using multichannel quantum defect theory. Phys Rev A39(3):1112–1122

Lambropoulos P (1976) Topics on multiphoton processes in atoms. Adv At Mol Phys 12:87–164

Lambropoulos P, Zoller P (1981) Autoionizing states in strong laser fields. Phys Rev A24(1): 379–397

Letokhov VS (1987) Laser photoionization spectroscopy. Academic, New York

Leubner C (1981) Uniform asymptotic expansion of a class of generalized Bessel functions occurring in the study of fundamental scattering processes in intense laser. Phys Rev A23(6):2877–2890

Lisitsa VS, Savel'ev YuA (1987) Soft-photon emission in collisions in an external electromagnetic field. Sov Phys JETP 65(2):273–280

Makhoute A, Khalil D (2008) Phase signatures in laser-assisted electron-atom collisions. Eur Phys J D46(1):77–82

Martin P, Veniard V, Maquet A et al (1989) Electron-impact ionization of atomic hydrogen in the presence of a laser field. Phys Rev A39(12):6178–6189

McCann JF, Bandrauk AD (1992) Laser induced stabilization and alignment in multiphoton dissociation of diatomic molecules. J Chem Phys 96(2):903–910

Meyerhofer DD (1997) High-intensity-laser-electron scattering. IEEE J Quant Electron 33(11):1935–1941

Mittleman MH (1982) Introduction to the theory of laser–atom interaction. Plenum Press, New York

Moiseyev N, Cederbaum LS (1999) Suppression of electron correlation and of autoionization by strong laser fields. J Phys B At Mol Opt Phys 32(12):L279–L284

Movsesyan AM, Fedorov MV (1989) Interference effects in the photoionization of Rydberg atoms in a strong electromagnetic field. Sov Phys JETP 68(1):27–33

Musa MO, MacDonald A, Tidswell L et al (2010) Laser-induced free–free transitions in elastic electron scattering from CO_2. J Phys B At Mol Opt Phys 43(17):175201

Nikishov FI, Ritus VI (1964) Quantum processes in the field of a plane electromagnetic wave and in a constant field I. Sov Phys JETP 19(2):529–541

O'Halloran MA, Pratt ST, Dehmer PM, Dehmer JL (1987) Photoionization dynamics of H_2 $\left(C^1\prod_u\right)$: vibrational and rotational branching ratios. J Chem Phys 87(6):3288–3298

Peatross J, Fedorov MV, Meyerhofer DD (1992) Laser temporal and spatial effects on ionization suppression. J Opt Soc Am B9(8):1234–1239

Purohit SP, Mathur KC (2010) Resonant laser assisted elastic scattering of electrons by lithium and sodium atoms. Eur Phys J D53(1):1–8

Rapoport LP, Zon BA, Manakov IL (1978) Theory of multiphoton processes in atoms. Atomizdat, Moscow

Reiss HR (1962) Absorption of light by light. J Math Phys 3(1):59–67

Reiss HR (1980) Effect of an intense electromagnetic field on a weak bound system. Phys Rev A22(5):1786–1813

Reiss HR (1987) Electron spectrum in intense-field photoionization. J Opt Soc Am B4(5):726–730

Reiss HR (1990) Relativistic strong-field photoionization. J Opt Soc Am B**7**(4):574–586; (1996) Energetic electrons in strong-field ionization. Phys Rev A54(3):R1765–R1768

Rosenberg L (1982) Theory of electron–atom scattering in a radiation field. Adv At Mol Phys 18:1–52

Rosenberg L (1989) Second-order correction to the low-frequency approximation for scattering in a laser field. Phys Rev Lett A39(9):4525–4530

Salamin YI (1997) Strong-field multiphoton ionization of hydrogen: nondipolar asymmetry and ponderomotive scattering. Phys Rev A56(6):4910–4917

Salamin YI, Faisal FHM (1997) Ponderomotive scattering of electrons in intense laser field. Phys Rev A55(5):3678–3683

Shirley JH (1965) Solution of the Schrödinger equation with a Hamiltonian periodic in time. Phys Rev 138(4):B979–B987

Stebbings R, Danning F (eds) (1983) Rydberg states of atoms and molecules. Cambridge University Press, Cambridge

Su Q, Eberly H, Javanien J (1990) Dynamics of atomic ionization suppression and electron localization in an intense high-frequency radiation field. Phys Rev Lett 64(8):862–865

Sukharev ME, Krainov VP (1998) Rotation and alignment of diatomic molecules and their molecular ions in strong laser fields. JETP 86(2):318–322

Swain S (1980) Theory of atomic processes in a radiation field. Adv At Mol Phys 16:159–200

Theodosiou CE, Armstrong L, Crance M Jr, Feneuille S (1979) Short-time behavior in multiphoton ionization. Phys Rev A19(2):766–775

Vartazaryan AS, Ivanov GK, Golubkov GV (1989) Near-threshold ionization and dissociation of diatomic molecules by weak UV and intense IR radiation. Opt Spectr 67(3):557–561

Vos RJ, Gavrila M (1992) Effective stabilization of Rydberg states at current laser performances. Phys Rev Lett 68(2):170–173

Yakovlenko SI (1982) Absorption of powerful resonance radiation accompanying collisional line broadening. Sov Phys Usp 25(4):216–230

Yakovlenko SI (1984) Radiative collisional phenomena. Energoatomizdat, Moscow

Yang B, Saeed M, DiMauro LF et al (1991) High-resolution multiphoton ionization and dissociation of H_2 and D_2 molecules in intense laser fields. Phys Rev A44(3):R1458–R1461

Yao G, Chu SI (1992) Laser-induced molecular stabilization and trapping and chemical bond hardening in intense laser fields. Chem Phys Lett 197(5):413–418; (1993) Molecular bond-hardening and dynamics of molecular stabilization and trapping in intense laser fields. Phys Rev A48(5):485–494

Zakrewski J (1984) Laser-induced autoionization in the presence of additional atomic continua. J Phys B At Mol Opt Phys 17(5):719–728

Zavriev F, Bucksbaum PY (1993) H_2 in intense laser field. In: Bandrauk AD (ed) Molecules in laser fields. Dekker, New York, pp 71–108

Zavriyev A, Bucksbaum PH, Muller GH, Schumacher DW (1990) Ionization and dissociation of H_2^+ in intense laser fields at 1.064 μm, 532 nm, and 355 nm. Phys Rev A42(9):5500–5513

Zavriyev A, Bucksbaum PH, Squier J, Saline F (1993) Light-induced vibrational structure in H_2^+ and D_2^+ in intense laser fields. Phys Rev Lett 70(8):1077–1080

Zel'dovich YB (1973) Scattering and emission of a quantum system in a strong electromagnetic wave. Sov Phys Usp 16(3):427–433

Chapter 3
Nanoaerosols in the Atmosphere

A.A. Lushnikov

Abstract This chapter presents an overview of the modern state of the kinetics of aerosol processes in the atmosphere. The first part focuses on the principles of modeling the dynamics of nanoaerosols in the atmosphere. Attention is then given to the kinetics of single aerosol particles whose size is less than or comparable to the mean free path of gaseous molecules in the atmosphere (less than 0.1 μm). The Introduction states a concept overview of the circle of atmospheric problems related to the particles suspended in the atmospheric air (atmospheric aerosols). The atmospheric aerosols are known to play an important role in the formation of the climatic conditions on our planet. Although optically active aerosol particles are relatively large, the processes of formation, growth, and behavior of smaller particles (atmospheric nanoaerosols) attract the attention of many researchers because the larger particles result from the smaller ones. The questions of where are these particles from, how they grow, and what are the mechanisms of their losses are of primary importance for modeling the aerosol states of the atmosphere at local and global scales. The main body of this presentation popularizes an analytical approach to the kinetics of a single aerosol particle in the transition regime (the particle size is of the order of the molecular mean free path). I consider the condensational growth of particles, diffusion charging of particles in the free molecule and transition regimes, and heat exchange between the particle and the carrier gas. The version of the flux-matching theory of Lushnikov and Kulmala serves as a basis for the consideration of all the aforementioned processes whose efficiencies are found analytically.

Keywords Nanoaerosols • Principles of modeling • Condensation • Charging • Heat transfer

A.A. Lushnikov (✉)
Karpov Institute of Physical Chemistry, 10, Vorontsovo Pole, 105064 Moscow, Russia
e-mail: alex.lushnikov@mail.ru

V. Bychkov et al. (eds.), *The Atmosphere and Ionosphere*, Physics of Earth and Space Environments, DOI 10.1007/978-94-007-2914-8_3,

3.1 Introduction

The term "aerosol" is quite familiar to everyone. Every day we see dust particles suspended in air, fumes from cigarettes, releases from transport, smoke from chimneys, etc. And almost nobody suspects that most aerosol particles are simply invisible. Despite this fact, these particles whose sizes do not exceed a fraction of a micrometer are of great importance for the formation of the present-day state of the atmosphere. It is these particles that serve as the condensation centers for the formation of cloud particles which cannot otherwise form at low water vapor supersaturation in the atmosphere (Charlson and Heitzenberg 1995; Seinfeld and Pandis 2006; Lohman and Feichter 2005; Friedlander 2000). Meanwhile, little is known about the nature of atmospheric aerosol particles or about the processes leading to their production in the atmosphere. The reasons for this are clear: the particles are so small that we are not able to distinguish them in optical microscopes. Electron microscopes are also powerless because the particles are unstable under the incident electron beam. Still, some speculations about the properties of the aerosol particles are admissible, and we can formulate some theories allowing us to come to conclusions concerning the consequences of the interactions of aerosol particles with our instruments and the environment.

The tiniest aerosol particles are produced by a number of specific mechanisms. All include spontaneous nucleation as the first stage; that is, the particles are assumed to form from vapors of sufficiently low volatile substances produced in the atmosphere from anthropogenic or natural organic releases. After chains of chemical and photochemical intraatmospheric processes, these releases convert to aerosol particles, which then grow by condensing other low volatile substances that are not able to form particles by nucleation (for example, if their vapor concentrations are not sufficient for initiating the nucleation process).

A huge amount of literature is devoted to atmospheric nanoaerosols. For extensive citations of the work of the past century, see the books of Seinfeld and Pandis (2006) and of Friedlander (2000). The goal of this review is to direct the attention of atmospheric scientists to some part of efforts that have remained beyond the mainstream of current atmospheric studies.

3.1.1 Atmospheric Aerosol Processes

Although more than a century has passed since Aitken's discovery of the secondary background aerosols, interest in these did not diminish until the present time. Recently, the dynamics of particle formation has again received considerable attention. Papers reporting on the results of field measurements continue to appear in connection with climatological and ecological needs (Boy and Kulmala 2002; Boy et al. 2003; Castelman 1982; Kulmala et al. 2004; Lyubovtseva et al. 2005, 2010; Stolzenburg et al. 2005; Yu and Turko 2001).

Attempts at modeling this important and still enigmatic process also appeared rather long ago. Here we avoid the long history of this problem and cite only the last models that appeared in the twenty-first century (Stolzenburg et al. 2005; Yu and Turko 2001; Anttila et al. 2004; Kerminen et al. 2004; Korhonen et al. 2003, 2004; Lehtinen and Kulmala 2003; Grini et al. 2005; Lushnikov et al. 2008, 2010; Lushnikov 2010a, b). Earlier citations can be found in these works. All models (without exception) started from the commonly accepted point of view that the chemical reactions of trace gases are responsible for the formation of nonvolatile precursors, which then give life to subnano- and nanoparticles in the atmosphere. In their turn, these particles are considered as active participants of the atmospheric chemical cycles leading to particle formation (see, e.g., Janson et al. 2001).

Many facts concerning the natural background aerosols have been well established. The major features of the phenomenon can be summarized as follows:

- The smallest (nanometer) aerosol particles form by nucleation of low volatile vapors resulting from intra-atmospheric chemical and photochemical transformations. The complete chemical cycles responsible for this very complicated process are not yet fully known, and its output is therefore characterized by the volume productivity $I(t)$ of the cycle: the number of molecules produced in a unit volume at a time. The source productivity is likely a periodic function of time (diurnal cycle).
- Very often observed size spectra reveal a multimodal (mostly trimodal) structure: a peak at 10–25 nm (nucleation or highly dispersed mode) and two submicrometer peaks at 25–100 nm and at 100–200 nm (Aitken and submicrometer modes) (Kulmala et al. 2004 and citations therein).
- The spontaneous nucleation of low volatile vapors is believed to give rise to the production of highly dispersed particles, whose number concentration is strongly dependent on the vapor concentration level.
- Submicrometer particles are often suspected to result from aging smaller particles as a result of their growth by condensing the molecules of low volatile substances. On some occasions the submicrometer particles can be transported from somewhere else.

As is seen from this list, the theoretical modeling of the particle formation–growth process is not a simple task: the point is that the process envelops a very wide range of particle sizes: from nanometers to parts of micrometers (three decimal orders) and masses (nine decimal orders). The respective kinetic processes proceed in various regimes: from free molecular to continuous ones, and the characteristic time scales are also stretched from minutes to hours and even weeks. These facts require one to seek for some simplifications or to sacrifice a part of the picture. For example, the most widespread of models in the past described the process in terms of interacting particle modes, each of which was characterized by its size interval and the number concentration. The time evolution of these values was described by a set of differential equations. These equations included the sources, the sinks of the particles, and the terms describing the aerosol processes. The quality of the models depended on the number of modes taken into account and the way of their introduction. The simplest results were obtained for a single-mode case.

Another direction of modeling is the use of the moment method, which reduces the full rather complicated set of equations describing the kinetics of particle formation–growth to a finite set of ordinary differential equations for some integral characteristics of the particle-size spectra (Friedlander 1983, 2000; Williams and Loyalka 1991). Sometimes the moment methods allow for obtaining exact results even in practically important cases. In particular, Friedlander (1983) established that free-molecular condensational growth can be described by a set of only four first-order differential equations. Lushnikov and Kulmala (1998a) reported on a set of condensational coefficients affording the exact description of nucleation–condensation kinetics in terms of a finite number of moments and applied these results to the analysis of the condensational growth of dimers (Lushnikov and Kulmala 1998b). Rigorous asymptotic analysis of the kinetics of nonbarrier nucleation in the presence of a source of condensable vapor was given by Lushnikov and Kulmala (2000) for algebraic dependencies of the condensation efficiencies on particle size. Then, this approach was extended to the transition regime of particle growth (Lushnikov and Kulmala 2001; Dal Maso et al. 2005).

Here we consider the development of the aerosol state of the atmosphere assuming the following:

- At the initial moment of time, the source of a condensable vapor is switched on. The productivity of the source (the number of particles produced per unit volume at a given time) is $I(t) = I_0 i(t)$, where I_0 is the dimensionality carrier and the dimensionless function $i(t)$ describes the time (t) dependence of the productivity.
- At $t = 0$ there exists a foreign aerosol with known size distribution, distributed over particle masses g as $N(g, 0) = N_0 n(g, 0)$ where $N_0 = \sum N(g, 0)$ is the particle number concentration and the particle mass g is measured in the units of the masses of condensable molecules.

The qualitative picture of the development of the situation appears as follows (Fig. 3.1) (Friedlander 1983). At the initial period, concentration grows linearly with time (for simplicity, we consider $i = 1$), then it begins to bend because part of the vapor condenses onto foreign particles. At $t = t^*$ when the vapor concentration reaches a sufficiently high level for the spontaneous nucleation process to start, newly born particles appear and also begin to consume the vapor. The vapor concentration thus passes a maximum, whose value is determined either by the nucleation rate or the rate of vapor losses by condensation onto foreign particles. The nucleation process stops at $t = t^{**}$ when the vapor concentration level drops lower than the critical value c^* and results in the formation of a highly dispersed mode. The number concentration of the latter depends on the characteristics of foreign particles: their number concentration and some geometric characteristics (more complex than simply average particle radius or average particle surface).

At the post-nucleation stage, evolution mainly continues owing to the growth of foreign particles by simultaneous joining of the vapor molecules and the smaller nanometric particles. The growing particles reach submicrometer sizes.

Although a huge number of papers considered the condensation process in the transition regime (extensive citations are given by Lushnikov and Kulmala (2001),

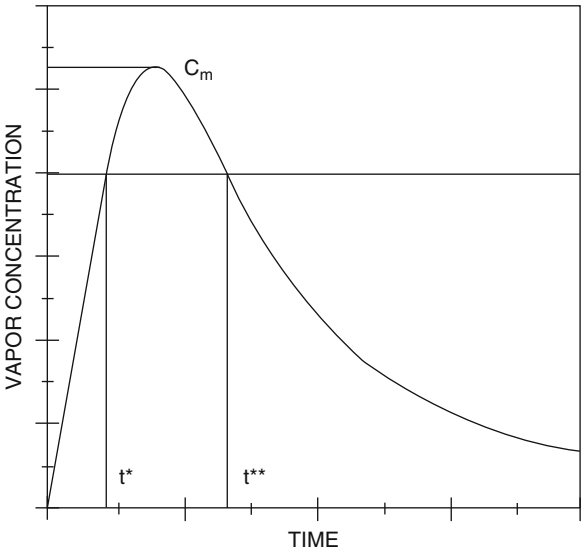

Fig. 3.1 Shown is the qualitative picture of the particle formation in the presence of a constant in time source of low volatile vapors. At the initial period the concentration grows linearly with time. At $t = t^*$ it begins to bend as the vapor concentration reaches a sufficiently high level for the spontaneous nucleation process to start. Newly born particles appear and begin to consume the vapor. The vapor concentration thus passes a maximum. The nucleation process stops at $t = t^{**}$ where the vapor concentration level drops lower than the critical value c^*. At the postnucleation stage the evolution continues mainly owing to the growth of the particles by simultaneous joining the vapor molecules and the smaller nanometric particles to larger submicrometer ones. The period of intense particle formation $t^* < t < t^{**}$ is referred to as the nucleation burst

for example), the main difficulty of the route toward the final solution of this problem has not been overcome. The point is that condensation efficiency is a rather complicated function of particle size. Its exact form is not known, and instead the interpolation formulas (see Seinfeld and Pandis 2006; Friedlander 2000; Williams and Loyalka 1991 for a collection of such interpolations) are used in almost all aerosol calculations. However, even the use of this semi-empirical approach does not eliminate the necessity to introduce further approximations, based mainly on the "isolated mode approximation," where the particle-size distribution splits into several narrow modes, each of which grows independently. The dynamics of the nucleation modes is described within a lognormal theory (Lushnikov and Kulmala 2000, 2001).

Now it becomes more and more evident that the nucleation bursts in the atmosphere can contribute substantially to cloud condensation nuclei production and can thus affect the climate and the weather conditions on our planet (Charlson and Heitzenberg 1995; Kulmala et al. 2004). Commonly accepted opinion connects the nucleation bursts with an additional production of nonvolatile substances that can then nucleate, producing new aerosol particles, or condense on newly born

particles, foreign aerosols, or atmospheric ions. The production of nonvolatile substances, in turn, demands some special conditions to be fulfilled imposed on the emission rates of volatile organics from vegetation, the current chemical content of the atmosphere, rates of stirring and exchange processes between lower and upper atmospheric layers, and the presence of foreign aerosols (accumulation fraction, first of all) serving as the condensational sinks for trace gases and the coagulation sinks for the particles of nucleation mode, the interactions with air masses from contaminated or clean regions (Boy and Kulmala 2002; Boy et al. 2003; Kulmala et al. 2004; Kerminen et al. 2004; Dal Maso et al. 2005; Aalto et al. 2001; Arey et al. 1990; Juozaitis et al. 1996). Such a plethora of very diverse factors, most of which have a stochastic nature, prevents direct attacks of this effect. A very large number of field measurements of the nucleation bursts dynamics appeared during the past two decades (see a review article Kulmala et al. 2004 and references Boy and Kulmala 2002; Boy et al. 2003; Lyubovtseva et al. 2010; Stolzenburg et al. 2005; Kerminen et al. 2004; Arey et al. 1990; Juozaitis et al. 1996). The attempts at modeling this important and still enigmatic process also appeared rather long ago. Here we avoid the long history of this problem and cite only the models that appeared in the twenty-first century (Stolzenburg et al. 2005; Anttila et al. 2004; Korhonen et al. 2003, 2004; Grini et al. 2005). The earlier citations can be found in these works. All models (without exception) started from the commonly accepted point of view that the chemical reactions of trace gases are responsible for the formation of nonvolatile precursors, which then give the life to subnano- and nanoparticles in the atmosphere. In their turn, these particles are considered as active participants of the atmospheric chemical cycles leading to particle formation (Janson et al. 2001). Hence, any model of nucleation bursts included (and includes) *coupled* chemical and aerosol blocks. This coupling leads to strong nonlinearities whose appearance, on the other hand, is not surprising. Indeed, all intra-atmospheric chemical processes are described by a set of nonlinear equations, not all of which are, in addition, firmly established, and there is no assurance that we know all the participants of the chemical cycles leading to the production of low volatile gas constituents which then convert to the tiniest aerosol particles.

3.1.2 Models of Aerosol Processes

Our main idea is to *decouple* the aerosol and chemical parts of the particle formation process and to consider only the aerosol part of the problem. We thus introduce the concentrations of nonvolatile substances responsible for particle growth and the rate of embryo production as *external* parameters whose values can be found either from measurements or calculated independently, once the input concentrations of reactants and the pathways leading to the formation of these nonvolatile substances are known. Next, introducing the embryo production rate allows us to avoid the rather slippery problem of the mechanisms responsible for embryo formation.

Because neither the pathways nor the mechanisms of production of condensable trace gases and the embryos of the condensation phase are well established so far, our semi-empirical approach is well approved. Moreover, if we risk starting from the first principles, we need to introduce too many empirical (fitting) parameters.

Aerosol particles throughout the entire size range beginning with the smallest ones (with sizes of the order 1 nm) and ending with sufficiently large particles (submicrometer and micrometer size) are shaped by some well-established mechanisms: condensation and coagulation. Little is known, however, about atmospheric nucleation. This is the reason why this very important process together with intramode coagulation is introduced here as an external source of the particles of the smallest sizes. The final productivity of the source is introduced as a fitting parameter whose value is controlled by two of these processes simultaneously and thus is always lower than the productivity of the nucleation mechanism alone. Next, coagulation produces particles distributed over a size interval, rather than the monodisperse ones of a critical size (as in the case of nucleation alone). Productivity should be introduced as a function of particle size and time, respectively. In principle, the size dependence of the source can be found theoretically, but it is better to refuse this idea and to introduce it as the product of a lognormal function and the time-dependent total production rate.

Condensational growth depends on the concentrations of condensable vapors, with the condensational efficiencies being known functions of the particle size. The concentrations of condensable trace gases are introduced as known functions. They can also be calculated, once all reactions responsible for conversion of volatile trace gases to low volatile ones and respective reaction rates are known (+ stoichiometry of the reactions + initial concentrations of all participants and many other unpleasant things). Of course, nothing like this is known, and there is no chance to get all this information in the near future.

The losses of particles are caused mainly by preexisting submicrometer and micrometer particles (Boy et al. 2003). There are also other types of losses: deposition of particles onto leaves of trees, soil losses, scavenging by deposits, and mists. Here the loss term is introduced as a sink of small particles on preexisting submicrometer- and micrometer-sized aerosol particles.

Self-coagulation of particles with sizes exceeding 3 nm is entirely ignored in the model. Many authors (e.g., Kulmala et al. 2004 and references therein) estimated the characteristic times of the coagulation process and found them to exceed 10^5 s. In what follows, we ignore this process. In contrast, the intermode coagulation (the deposition of newly born particles onto preexisting aerosols) is of great importance and should be taken into account.

The remainder of this chapter focuses on the interactions of a single aerosol particle with surrounding carrier gas that can contain some condensible vapors (condensation and evaporation), ions (particle charging processes), and the energy exchange between the particle and the surrounding gas. The kinetics of all these processes is very complex, because the particle sizes are comparable to the molecular mean free path. In principle, in this situation one must solve the Boltzmann

kinetic equation. Below I wish to popularize an approximate approach that allows one to avoid the solution of the full Boltzmann equation and to consider the aforementioned transport effects from a unified point of view. The final results are analytical.

3.2 Flux-Matching Theories of Molecular Transport in the Transition Regime

We introduce the reader to the ideology of the flux-matching theories by considering the condensation of a nonvolatile vapor onto the surface of an aerosol particle. The central idea of existing flux-matching procedures is a hybridization of the diffusion and the free molecule approaches. The concentration profile of a condensing vapor far away from the particle is described by the diffusion equation. This profile coincides with the real one down to the distances of the order of the vapor molecule mean free path. A limiting sphere is then introduced inside which the free molecule kinetics governs the vapor transport. The concentration profile in the free molecule zone is considered to be flat. The equality of the fluxes in both zones and the continuity of the concentration profile at the surface of the limiting sphere define the flux and the reactant concentration at the particle surface. The third parameter, the radius of the limiting sphere, cannot be found from such a consideration.

We apply a more sophisticated scheme (Lushnikov and Kulmala 2004a). We also introduce a limiting sphere outside of which the density profile of condensing vapor can be described by the diffusion equation. But inside the limiting sphere we solve the collisionless Boltzmann equation subject to a given boundary condition at the particle surface (incomplete sticking in our case) and put an additional condition: the concentration at the surface of the limiting sphere coincides with that found from the solution of the diffusion equation. Even in the absence of any potential created by the particle, the vapor profile in the free molecule zone depends on the radial coordinate, because the particle surface adsorbs all incoming molecules. We thus gain the possibility to call for the continuity of the first derivatives of the profile on both sides of the limiting sphere. This additional condition defines the radius of the limiting sphere.

3.2.1 Flux Matching for Mass and Charge Transport

The steady-state ion flux $J(a)$ onto a particle of radius a can always be written as

$$J(a) = \alpha(a) n_\infty, \tag{3.1}$$

i.e., the flux is proportional to the ion density n_∞ far away from the particle. The proportionality coefficient $\alpha(a)$ is known as the charging efficiency. The problem is to find $\alpha(a)$. Nothing, however, prevents us from generalizing Eq. 3.1 as follows:

$$J(a, R, n_R) = \alpha(a, R) n_R, \tag{3.2}$$

where n_R is the ion concentration at a distance R from the particle center. It is important to emphasize that n_R is (still) *an arbitrary value* introduced as a boundary condition at the distance R (also arbitrary) to a kinetic equation which is necessary to solve for defining $\alpha\,(a, R)$. The flux defined by Eq. 3.1 is, thus,

$$J(a) = J\,(a, \infty, n_\infty) \quad \text{and} \quad \alpha(a) = \alpha\,(a, \infty)\,. \tag{3.3}$$

The value of $\alpha\,(a, R)$ does not depend on n_R because of the linearity of the problem.

Let us assume for a moment that we know the exact ion concentration profile $n_{\text{exact}}(r)$ corresponding to the flux $J(a)$ from infinity (see Eq. 3.1). Then, using Eq. 3.2 we can express $J(a)$ in terms of n_{exact} as follows:

$$J(a) = J\,(a, R, n_{\text{exact}}(R)) = \alpha\,(a, R)\, n_{\text{exact}}(R). \tag{3.4}$$

Now let us choose R sufficiently large for the diffusion approximation to reproduce the exact ion concentration profile

$$n_{\text{exact}}(R) = n^{(J(a))}(R), \tag{3.5}$$

with $n^{(J)}(r)$ being the steady-state ion concentration profile corresponding to a given total ion flux J. The steady-state density of the ion flux $j(r)$ is the sum of two terms

$$j(r) = -D\frac{\mathrm{d}n^{(J)}(r)}{\mathrm{d}r} - B\frac{\mathrm{d}U(r)}{\mathrm{d}r}n^{(J)}(r), \tag{3.6}$$

where D is the ion diffusivity, $U(r)$ is a potential (here the ion–particle interaction), and B is the ion mobility. According to the Einstein relationship, $kTB = D$. On the other hand, ion flux density is expressed in terms of total ion flux as follows: $j(r) = -J/4\pi r^2$, with $J > 0$. Equation 3.6 can be now rewritten as

$$\mathrm{e}^{-\beta U(r)}\frac{\mathrm{d}}{\mathrm{d}r}\left(n^{(J)}(r)\mathrm{e}^{\beta U(r)}\right) = \frac{J}{4\pi D r^2},$$

where $\beta = 1/kT$. The solution to this equation is

$$n^{(J)}(r) = \mathrm{e}^{-\beta U(r)}\left(n_\infty - \frac{J}{4\pi D}\int_r^\infty \mathrm{e}^{\beta U(r')}\frac{\mathrm{d}r'}{r'^2}\right). \tag{3.7}$$

Substituting Eqs. 3.5 and 3.7 into Eq. 3.4 gives the equation $J(a) = \alpha(a, R)n^{(J)}(R)$, or

$$J(a) = \alpha(a, R)\mathrm{e}^{-\beta U(R)}\left(n_\infty - \frac{J(a)}{4\pi D}\int\limits_R^\infty \mathrm{e}^{\beta U(r')}\frac{\mathrm{d}r'}{r'^2}\right). \tag{3.8}$$

We can solve this equation with respect to $J(a)$ and find $\alpha(a)$:

$$\alpha(a) = \frac{\alpha\,(a, R)\,\mathrm{e}^{-\beta U(R)}}{1 + \frac{\alpha(a,R)\mathrm{e}^{-\beta U(R)}}{4\pi D}\int\limits_R^\infty \mathrm{e}^{\beta U(r')}\frac{\mathrm{d}r'}{r'^2}}. \tag{3.9}$$

Equation 3.9 is exact. We, however, know neither $\alpha(a, R)$ nor R. It is pertinent to notice here that if we have some grounds to neglect unity on the right-hand side of Eq. 3.10; then, $\alpha(a)$ depends only on the separation distance R:

$$\alpha(a) = \frac{4\pi D}{\int\limits_R^\infty \mathrm{e}^{\beta U(r')}\frac{\mathrm{d}r'}{r'^2}}. \tag{3.10}$$

There is no way to find $\alpha(a, R)$ exactly. We thus call upon two approximations:

- We approximate $\alpha(a, R)$ by its free molecule expression

$$\alpha(a, R) \approx \alpha_{\mathrm{fm}}(a, R) \tag{3.11}$$

- We define R from the condition

$$d_r n_{\mathrm{fm}}(r)|_{r=R} = d_r n^{(J(a))}(r)|_{r=R}, \tag{3.12}$$

where $n_{\mathrm{fm}}(r)$ is the ion concentration profile found in the free molecule regime for $a < r < R$. The distance R separates the zones of free molecule and continuous regimes.

3.2.2 *Flux-Matching for Enthalpy Transport*

Let us consider a spherical particle of radius a heated to temperature T_* suspended in the carrier gas with temperature $T_\infty < T_*$. In what follows we operate with the mean energy per a particle q and the flux of this energy $\mathcal{Q}$ rather than with the temperature and temperature flux. The reasons for this are explained later, when we define these values in terms of the distribution function.

The steady-state heat flux $\mathcal{Q}(a)$ from the particle of radius a can always be written as

$$\mathcal{Q}(a) = \gamma(a)\,(T_* - T_\infty)\,. \tag{3.13}$$

The heat flux is directed outward from the particle. The proportionality coefficient $\gamma(a)$ is referred to as the heat transfer efficiency of the particle. Our goal is to find $\gamma(a)$.

We also introduce the generalized efficiency $\gamma(a, R)$ defined as follows:

$$\mathcal{Q}\,(a, R, T_R) = \gamma\,(a, R)\,(T_* - T_R)\,, \tag{3.14}$$

where q_R is the temperature at a distance (yet arbitrary) R from the particle center.

Let us assume for a moment that we know the exact temperature profile $T^{\text{exact}}(r)$ corresponding to the heat flux $\mathcal{Q}$. Then, using Eq. 3.14 we can express $\mathcal{Q}(a)$ in terms of T_{exact} as follows:

$$\mathcal{Q}(a) = \gamma\,(a, R)\,(T_* - T_{\text{exact}}(R))\,. \tag{3.15}$$

Now let us choose R sufficiently large for the macroscopic approximation (the thermoconductivity equation) to reproduce the exact temperature profile:

$$T_R^{\text{exact}} = T^{\mathcal{Q}}(R) = T_\infty + \mathcal{Q}/\,(4\pi\Lambda R)\,, \tag{3.16}$$

with $q^{\mathcal{Q}}(r)$ being the steady-state q-profile corresponding to a given total heat flux $\mathcal{Q}$ and Λ being the thermoconductivity of the carrier gas. Combining this with Eq. 3.15 gives

$$\mathcal{Q}(a) = \gamma\,(a, R)\left(T_* - T_\infty - \frac{\mathcal{Q}(a)}{4\pi\Lambda R}\right). \tag{3.17}$$

We can solve this equation with respect to $\mathcal{Q}(a)$, use Eq. 3.14, and find $\gamma(a)$:

$$\gamma(a) = \frac{\gamma\,(a, R)}{1 + \frac{\gamma(a,R)}{4\pi\Lambda R}}. \tag{3.18}$$

There is not a chance to find $\gamma\,(a, R)$ exactly. We again call upon two approximations:

- We approximate $\gamma\,(a, R)$ by its free molecule expression:

$$\gamma\,(a, R) \approx \gamma_{\text{fm}}\,(a, R)\,. \tag{3.19}$$

- We define R from the condition

$$d_r n_{fm}(r)|_{r=R} = d_r n^{\mathcal{Q}}(r)|_{r=R}, \tag{3.20}$$

where $n_{\rm fm}(r)$ is the gas density profile found in the free molecule zone $a < r < R$. The distance R separates the zones of free molecule and continuous regimes, and

$$n^{\mathcal{Q}}(r) = \frac{T_\infty n_\infty}{T(r)}$$

in the continuous zone. The latter equality expresses the constancy of pressure in the continuous zone.

3.2.3 Kinetic Equation

The description of ion transport in the free molecule regime to a spherical particle requires the solution of the steady-state collisionless Boltzmann kinetic equation for ion distribution $f(\mathbf{r}, \mathbf{v})$:

$$v_i \frac{\partial f}{\partial x_i} - \frac{1}{m}\frac{\partial U}{\partial x_i} \cdot \frac{\partial f}{\partial v_i} = 0. \tag{3.21}$$

Here f $(\mathbf{r}, \mathbf{v})$ is the ion distribution over coordinates $\mathbf{r}$ and velocities $\mathbf{v}$, m is the ion mass, and U $(\mathbf{r})$ is the potential of an external field. The convention on summation over repeating indexes is adopted.

In what follows we consider only spherical particles. The potential U is then a function of $r = |\mathbf{r}|$ and ion distribution depends only on three variables, the ion radial coordinate r, absolute ion velocity $v = |\mathbf{v}|$, and $\mu = \cos\theta$, with θ being the angle between the directions of $\mathbf{r}$ and $\mathbf{v}$.

In spherically symmetrical systems another set of variables is more convenient. Namely, instead of r, v, μ we introduce the variables r, E, L, with

$$E = mv^2/2 + U(r), \quad L = m|[\mathbf{v} \times \mathbf{r}]| = mvr\sqrt{1-\mu^2} \tag{3.22}$$

being the total ion energy and the ion angular momentum, respectively. It is important to emphasize that E and L are ordinary current variables such as r and μ rather than the integrals of motion.

In these variables the Boltzmann equation takes the form:

$$s\sqrt{L^2(r) - L^2} \cdot \frac{\partial f_s}{\partial r} = 0, \tag{3.23}$$

where $s = \pm 1$ is an auxiliary variable defining the direction of ion motion along the radial coordinate ($s = -1$ corresponds to motion toward the particle) and

$$L^2(r) = 2mr^2\left(E - U(r)\right). \tag{3.24}$$

The derivation of Eq. 3.21 is simple. Indeed,

$$\frac{\partial f}{\partial x_i} = \frac{\partial f}{\partial E}\frac{\partial E}{\partial x_i} + \frac{\partial f}{\partial L^2}\frac{\partial L^2}{\partial x_i}$$

$$\frac{\partial f}{\partial v_i} = \frac{\partial f}{\partial E}\frac{\partial E}{\partial v_i} + \frac{\partial f}{\partial L^2}\frac{\partial L^2}{\partial v_i}$$

Substituting the evident equalities

$$\frac{\partial E}{\partial x_i} = -\frac{\partial U}{\partial x_i}, \quad \frac{\partial E}{\partial v_i} = m v_i,$$

$$\frac{\partial L^2}{\partial x_i} = \frac{\partial L^2}{\partial v_i} = 0,$$

and

$$mv\mu = \pm\sqrt{L^2(r) - L^2}$$

into Eq. 3.21 gives Eq. 3.23.

The ion flux toward the particle is expressed in terms of f as follows:

$$J = -\int d^3v \int (\mathbf{v}\cdot\mathbf{dS})\, f(\mathbf{r},\mathbf{v}). \tag{3.25}$$

The integrals on the right-hand side of this equation are taken over all $\mathbf{v}$ and the surface of a sphere of radius r. The sign "−" in the definition of the flux makes J positive. In spherical coordinates, Eq. 3.24 is rewritten as

$$J = -8\pi^2 r^2 \int_0^\infty v^3 \mathrm{d}v \int_{-1}^{1} f\,(r, v, \mu)\,\mu\,\mathrm{d}\mu. \tag{3.26}$$

Now let us change the variables. The rule for replacing the variables $(r, v, \mu) \to (r, E, L)$ readily follows from definition (3.22) of the variables E and L:

$$2\pi v^2 \mathrm{d}v q \mathrm{d}\mu \to \frac{\pi}{m^2 r}\sum_s \frac{\mathrm{d}E\,\mathrm{d}L^2}{\sqrt{L^2(r) - L^2}}. \tag{3.27}$$

The restrictions on the intervals of integration over E and L^2 are defined by two conditions, $L^2 \le L^2(r)$ and $L^2(r) \ge 0$. The latter is equivalent to $E \ge U(r)$. In what follows we do not specify the limits of integration except for the cases, where they play a decisive role.

The expressions for the ion density profile $n(r)$ and the ion flux J in r, E, L variables are as follows:

$$n(r) = \frac{\pi}{m^2 r} \sum_s \int \mathrm{d}E \int \frac{\mathrm{d}L^2}{\sqrt{L^2(r) - L^2}} \cdot f_s\,(r, E, L) \tag{3.28}$$

and

$$J = -\frac{4\pi^2}{m^3} \sum_s s \int \mathrm{d}E \int \mathrm{d}L^2\, f_s\,(r, E, L). \tag{3.29}$$

The ion flux is independent of r.

The boundary conditions to the kinetic equation should be formulated individually for each concrete case.

3.3 Condensation

Trace gases are commonly recognized to react actively with the aerosol component of the Earth's atmosphere. Substantial changes to atmospheric chemical cycles resulting from the presence of aerosol particles in the atmosphere make us look more attentively at the nature of the processes depending on the activity of the atmospheric aerosols (Seinfeld and Pandis 2006). The processes of gas–particle interactions are usually the first-order chemical reactions going along the route:

$$(\mathrm{A}) + (\mathrm{P}) \rightarrow (\mathrm{AP}), \tag{3.30}$$

where (A), (P), and (AP) stand, respectively, for a reactant molecule, an aerosol particle, and the final product resulting from the reaction Eq. 3.30.

As an example we refer to ozone, a key substance for the Earth atmosphere protecting living systems on our planet against the sun UV radiation. Since the discovery of the ozone hole in the mid-1970s (Farman et al. 1985), it has been well established that ozone is subject to periodical large depletion events at the Poles and to continuous decay in the global stratosphere. The amplitudes of ozone level variations are partly driven by heterochemical reactions occurring on the surfaces of polar stratosphere cloud particles that transform the stable reservoir molecules into radical precursors (see Lohman and Feichter 2005 and references therein). Processes such as Eq. 3.30 are also of importance in the aerosol catalysis (Weber et al. 1999; Feng et al. 2001).

The interconnection between uptake and mass accommodation efficiencies was studied by several groups (Kulmala and Wagner 2001; Finlayson-Pitts and Pitts 2000; Davidovits et al. 1991, 1995; Natanson et al. 1996; Laaksonen et al. 2005; Davis 1983; Shi and Seinfeld 1991; Zagaynov et al. 1976). The condensational

aspects of the problem were considered earlier by Wagner (1982). Respective theoretical interpretations were presented in several works (Clement et al. 1996; Widmann and Davis 1997; Qu and Davis 2001; Li and Davis 1995). The models of uptake process were also proposed by Smith et al. (2003) and Tsang and Rao (1988).

Data of experimental measurements of mass accommodation efficiencies were reported by Li et al. (2001) and Winkler et al. (2004, 2006). In two recent papers (Pöschl et al. 2007; Ammann and Pöschl 2007), the authors summarized the state of art in this problem and tried to unify existing very diverse terminology applied by different authors working in this direction.

As shown in the review article (Clement 2007) and by Pöschl et al. (2007), since the very end of the last century the discrepancies in approaches to the kinetics of uptake have almost disappeared. Commonly accepted schemes now assume the sequential transports of the gaseous reactant through the gas phase, then through the interface, and then in the bulk of the particle, including possible chemical reactions inside accompanying the transport process.

This section considers only a part of the uptake process: reactant transport through the gas phase. Transport in the gas phase is normally assumed to be described by semi-empirical theories that connect the total flux of the reactant with its concentration far away from the particle.

The main idea is to replace the semi-empirical approaches by a theory that applies the Boltzmann kinetic equation with Maxwell's boundary conditions (Cercignani 1975) corresponding to noncomplete sticking of the reactant molecule to the particle surface and to derive analytically the expression for the efficiency of trapping the reactant molecules. It is possible to do for not very great cost. The final formula is even simpler than those proposed by the semi-empirical approaches. The theory itself is also simple and transparent.

Let a particle of the radius a initially containing N_B molecules of a substance B be embedded in the atmosphere containing a reactant A. The reactant A is assumed to be able to dissolve in the host particle material and to react with B. The particle will begin to consume A molecules and will do this until the pressure of vapor A over the particle surface is enough to block the diffusion process. Our task is to find the consumption rate of the reactant A as a function of time. Next, we focus on sufficiently small particles whose sizes are comparable to or less than the mean free path of the reactant molecules in the carrier gas. The mass transfer to such particles is known to depend strongly on the dynamics of the interaction between incident molecules and the particle surface. In particular, the value of the probability S_p for a molecule to stick to the particle surface is suspected to strongly affect the uptake kinetics.

The first simplest theories of mass transfer from gas to particles applied the continuous models (the particle radius a much exceeds the condensing molecule mean free path l). Such models were not able to describe very small particles with sizes less than l. It was quite natural therefore to try to attack the problem starting with the free molecule limit, that is, to consider a collisionless motion of condensing molecules. Respective expressions for the condensational efficiencies had been

derived and can be found in several studies (Seinfeld and Pandis 2006; Friedlander 2000; Williams and Loyalka 1991; Li and Davis 1995; Fuchs and Sutugin 1971). An important step directed to reconciliation of these two limiting cases was taken in the prominent book of N. A. Fuchs (1964), who invented the flux-matching theory. The general consideration of the kinetic problems in the transition regime can be found in Cercignani's book (1975).

The flux-matching theories are well adapted for studying mass transfer to aerosol particles in the transition regime. Although these theories mostly had no firm theoretical basis, they successfully served for systematizing numerous experiments on growth of aerosol particles, and until now these theories remain rather effective and very practical tools for studying kinetics of aerosol particles in the transition regime (see Seinfeld and Pandis 2006; Friedlander 2000; Williams and Loyalka 1991). On the other hand, these theories are always semi-empirical ones; that is, they contain a parameter that should be taken from somewhere else, not from the theory itself.

We introduce the readers to the ideology of the flux-matching theories by considering the condensation of a nonvolatile vapor onto the surface of an aerosol particle. The central idea of the flux-matching procedure is a hybridization of the diffusion and the free molecule approaches. The concentration profile of a condensing vapor far away from the particle is described by the diffusion equation. This profile coincides with the real one down to the distances of the order of the vapor molecule mean free path. A limiting sphere is then introduced wherein the free molecule kinetics governs the vapor transport. The equality of the fluxes in both zones and the continuity of the concentration profile at the surface of the limiting sphere define the flux and the condensing vapor concentration at the particle surface. The third parameter, the radius of the limiting sphere, cannot be found from such a consideration.

We apply the more sophisticated approach of Lushnikov and Kulmala (2004a). This approach starts with an *exact* expression for the trapping efficiency. This step, however, does not solve the whole problem. The point is that this exact expression contains two unknown functions that should be found from the solution of respective transport equation. However, this formal step is of great use, because some ideas arise as to how to introduce efficient approximations.

We also introduce a limiting sphere outside of which the density profile of condensing vapor can be described by the diffusion equation. Inside the limiting sphere we solve the collisionless Boltzmann equation subject to a given boundary condition at the particle surface and put an additional condition: the vapor concentration at the surface of the limiting sphere coincides with that found from the solution of the diffusion equation. This condition has also been applied in older theories. The next step forward was done by Lushnikov and Kulmala (2004a), where the authors noticed that even in the absence of any potential created by the particle the vapor profile in the free molecule zone depends on radial coordinates. We thus gain the possibility to call for the continuity of the first derivatives of the profile on both sides of the limiting sphere. This additional condition defines the radius of the

limiting sphere. This very ideology applies here for determining the efficiency of trapping the reactant molecules by an aerosol particle as a function of the mass accommodation coefficient.

3.3.1 Basic Equations

Below, an exact (formal) expression for the condensational efficiency is derived. This expression eventually contains some parameters that can be defined only on solving the full transport problem. However, it is possible to introduce simple approximations and to restore these parameters approximately. This program is performed in this section.

3.3.1.1 Trapping Efficiency

Let us assume that the reactant molecules (A molecules) move toward the particle that captures them (see Eq. 3.30). The further fate of reactant molecules depends on the results of chemical processes that proceed inside the particle. Let us denote $n_{\pm}$ as the concentration of A right beneath (n_+) or right underneath (n_-) the particle surface. Already here we emphasize that the surface concentrations $n_{\pm}$ depend on the nature of physicochemical processes on the surface and inside the particle. Let then n_∞ be the number concentration of A molecules far away from the particle. It is commonly accepted that the concentration difference $n_\infty - n_+$ drives a flux of A toward the particle surface. The particle begins to grow and to change its chemical composition. The rate of change in the number of A molecules inside the particle is equal to the total molecule flux J minus the total number of molecules deposited per unit time at the particle surface minus the rate of consumption of A by chemical processes inside the particle. The A molecules are assumed to escape from the particles. In steady-state conditions, the flux J can be written as

$$J = \alpha(a)\,(n_\infty - n_+)\,, \tag{3.31}$$

Here $\alpha(a)$ is the capture efficiency and a is the particle radius. Of course, α depends on the mass accommodation coefficient S_p. The latter is defined as the probability for an A molecule to stick to the particle. For completely sticking particles, $S_\mathrm{p} = 1$.

The interface and in-particle processes fix the value of n_+. In the simplest case of the first-order chemical reactions, n_+ is a linear function of J, $n_+ = J\psi(a)$ and thus

$$J = \frac{\alpha(a) n_\infty}{1 + \alpha(a)\psi(a)}, \tag{3.32}$$

Here $\psi(a)$ is a function depending on the nature of the chemical process and independent of J. An example of such function is given below. If the chemical process inside the particle is nonlinear, then the function $\psi(a)$ depends on J and J is then a solution to the transcendent equation Eq. 3.32.

The central problem is thus to find $\alpha(a)$. Equations 3.31 and 3.32 allow also for the consideration of normal condensation and evaporation. In this case A molecules are the same as the molecules of the host particle and $\alpha(a)$ is referred to as the condensational efficiency.

3.3.1.2 Flux Matching for Condensation

Next, we extend the flux-matching theory to the case of condensation of neutral molecules onto the particle surface with $n_+ \neq 0$ and $S_\mathrm{p} \leq 1$. To this end we generalize Eq. 3.31 as follows:

$$J = \alpha\,(a, R)\,(n_R - n_+)\,, \tag{3.33}$$

where n_R is the vapor concentration at a distance R from the particle center. Indeed, the total flux J is independent of R, and we have the right to consider the condensation from any finite distance. It is important to emphasize that n_R is (still) *an arbitrary value* introduced as a boundary condition at the distance R (also arbitrary) to a kinetic equation that is necessary to solve for defining the generalized condensational efficiency $\alpha\,(a, R)$. The value of $\alpha\,(a, R)$ does not depend on $n_R - n_+$ because of the linearity of the problem.

Assuming that we know the exact vapor concentration profile $n_\mathrm{exact}(r)$ corresponding to the given flux J from infinity, we can express J in terms of n_exact as follows:

$$J = \alpha\,(a, R)\,(n_\mathrm{exact}(R) - n_+)\,. \tag{3.34}$$

If we choose R as sufficiently large, then the diffusion approximation reproduces the exact vapor concentration profile:

$$n_\mathrm{exact}(R) = n_\mathrm{c}(R) = -\frac{J}{4\pi DR} + n_\infty, \tag{3.35}$$

with $n_\mathrm{c}(r)$ being the steady-state vapor concentration profile corresponding to a given total molecular flux J.

Combining Eqs. 3.33, 3.34, and 3.35 gives

$$J = \alpha(a, R)\left(n_\infty - n_+ - \frac{J}{4\pi DR}\right). \tag{3.36}$$

We solve this equation with respect to J and obtain the expression for $\alpha(a)$:

$$\alpha(a) = \frac{\alpha\,(a, R)}{1 + \frac{\alpha(a,R)}{4\pi DR}}. \tag{3.37}$$

Equation 3.37 is exact if $R \gg l$, where l is the mean free path of condensing molecules in the carrier gas. To find $\alpha\,(a, R)$ and R we must call on the approximations.

- The free–molecule expression approximates $\alpha\,(a, R)$.

$$\alpha\,(a, R) \approx \alpha_{\mathrm{fm}}\,(a, R)\,, \tag{3.38}$$

  where $\alpha_{\mathrm{fm}}\,(a, R)$ is the trapping efficiency in the free molecule zone.
- The radius R of the limiting sphere is found from the condition: "the diffusion flux from the diffusion zone is equal to the diffusion flux from the free molecule zone" The diffusion flux is defined from Fick's law. Hence,

$$\left.\frac{\mathrm{d}n_{\mathrm{fm}}(r)}{\mathrm{d}r}\right|_{r=R} = \left.\frac{\mathrm{d}n_{\mathrm{c}}(r)}{\mathrm{d}r}\right|_{r=R}, \tag{3.39}$$

  where $n_{\mathrm{fm}}(r)$ is the vapor concentration profile found in the free–molecule zone for $a < r < R$ and $n_{\mathrm{c}}(r)$ is the concentration profile in the diffusion zone. The distance R separates the zones of the free–molecule and the continuous regimes.
- The total flux of A in the free-molecule zone is equal to the total flux in the diffusion zone.

3.3.2 Solving the Kinetic Equation

Now we will solve the kinetic equation

$$sv_r \frac{\partial f_s}{\partial r} = 0 \tag{3.40}$$

For the following it is convenient to introduce the notation,

$$\theta_r = \theta\left(L_r^2 - L^2\right), \quad \theta_+ = \theta\left(L^2 - L_a^2\right) \quad \theta_- = 1 - \theta_+ = \theta\left(L_a^2 - L^2\right) \tag{3.41}$$

Here $\theta(x)$ is the Heaviside step function ($\theta(x) = 1$ at $x \geq 1$ and 0 otherwise). The factor θ_- cuts off the molecules flying past by the target particle. Then the Maxwell boundary condition has the form:

$$f_1\,(a, E, L) = \left[\left(1 - S_{\mathrm{p}}\right) f_{-1} + \frac{1}{2} S_{\mathrm{p}} n_+\right] \theta_-. \tag{3.42}$$

Here S_p is referred to as the mass accommodation coefficient. The left–hand side of this equation gives the distribution function of the molecules moving outward from the particle surface. The part $1 - S_\mathrm{p}$ of inward moving molecules specularly rebounds from the particle surface (the first term on the right-hand side). The second term describes the emission of the reactant molecules from the particle.

In the particular case when the reactant molecules do not experience chemical transformations inside the particles, $n_+ = n_\mathrm{e}$ (equilibrium number concentration over the particle surface), which means that all guest molecules trapped by the particle thermalize and escape from it having the Maxwell distribution over energies.

Let us write down the solution to Eq. 3.40:

$$f_s = \frac{1}{2} M(E)\theta_r \left\{\tilde{n}_\infty\, \theta_+ + \tilde{n}_\infty\, \theta_{-}\delta_{s,-1} + \left[(1 - S_\mathrm{p})\, \tilde{n}_\infty + S_\mathrm{p} n_+\right] \theta_{-}\delta_{s,1}\right\}. \quad (3.43)$$

The first term describes all molecules flying past by the particles. They fly in both radial directions, $s = +1$ and $s = -1$. The second term describes the molecules flying from infinity and hitting the particle. The third term describes the motion of the molecules that flew from infinity and recoiled from the particle surface and the molecules evaporated from the particle. Here we introduced $\tilde{n}_\infty$. The point is that free molecule concentration $\tilde{n}_\infty$ does not correspond to that of the reactant in the diffusion zone and serves as a fitting parameter allowing us to make the concentration $n_\mathrm{fm}(R)$ equal to $n_\mathrm{c}(R)$. Equation 3.43 can be cast into the form:

$$f_s = \frac{1}{2} M(E)\theta_r \left[\tilde{n}_\infty - S_\mathrm{p}(\tilde{n}_\infty - n_+)\theta_{-}\delta_{s,1}\right], \quad (3.44)$$

where $\delta_{q,s}$ stands for the Kroneker delta and

$$M(E) = 2\pi(\pi k T)^{-3/2}\sqrt{E}\mathrm{e}^{-E/kT} \quad (3.45)$$

is the Maxwellian. In deriving Eq. 3.44 the evident identities

$$\delta_{s,1} + \delta_{s,-1} = 1 \quad \text{and} \quad \theta_+ + \theta_- = 1 \quad (3.46)$$

were used.

Equations 3.26 and 3.44 yield:

$$n_\mathrm{fm}(r) = \tilde{n}_\infty - \frac{1}{2} S_\mathrm{p}\,(\tilde{n}_\infty - n_+)\left(1 - \sqrt{1 - \frac{a^2}{r^2}}\right) = \tilde{n}_\infty - (\tilde{n}_\infty - n_+)\, b_-(r). \quad (3.47)$$

The following chain of equalities gives $\alpha\,(a, R)$.

$$\begin{aligned} J &= \alpha_{\text{fm}}\,(\tilde{n}_\infty - n_+) = \alpha_{\text{fm}}\,(a, R)\,(n_R - n_+) \\ &= \alpha_{\text{fm}}\,(a, R)\,[\tilde{n}_\infty - (\tilde{n}_\infty - n_+)\,b_-(R) - n_+] \\ &= \alpha_{\text{fm}}\,(a, R)\,(\tilde{n}_\infty - n_+)\,[1 - b_-(R)] \end{aligned}$$

or

$$\alpha_{\text{fm}}\,(a, R) = \frac{\alpha_{\text{fm}}}{b_+(R)} \tag{3.48}$$

From Eqs. 3.28 and 3.44 we find:

$$\alpha_{\text{fm}} = S_{\text{p}} \pi a^2 v_T, \tag{3.49}$$

Now we must express $n(r)$ via n_R instead of $\tilde{n}_\infty$. We have

$$n_{\text{fm}}(r) = \tilde{n}_\infty\, b_+(r) + n_+ b_-(r). \tag{3.50}$$

From Eq. 3.50 we have

$$n_{\text{fm}}(R) = \tilde{n}_\infty\, b_+(R) + n_a b_-(R). \tag{3.51}$$

We solve this equation with respect to $\tilde{n}_\infty$ and find

$$\tilde{n}_\infty = \frac{n_R - n_a b_-(R)}{b_+(R)} \tag{3.52}$$

Now

$$n(r) = \frac{n_R - n_+ b_-(R)}{b_+(R)} b_+(r) + n_+ b_-(r). \tag{3.53}$$

Next,

$$\frac{n_R - n_+ b_-(R)}{b_+(R)} = \frac{n_R - n_+ + n_+ - n_a b_-(R)}{b_+(R)} = \frac{n_R - n_+}{b_+(R)} + n_+. \tag{3.54}$$

And finally,

$$n(r) = \frac{n_R - n_+}{b_+(R)} b_+(r) + n_+. \tag{3.55}$$

In deriving this equation we used the identity $b_+(r) + b_-(r) = 1$.

3.3.3 *Flux Matching for $S_p \neq 1$*

Now we find R from the condition Eq. 3.39

$$\frac{\mathrm{d}n_{\mathrm{fm}}}{\mathrm{d}r} = \frac{n_a - S_p n_R}{1 - S_p b(R)} \frac{db}{\mathrm{d}r} \tag{3.56}$$

$$\left.\frac{\mathrm{d}b}{\mathrm{d}r}\right|_R = \frac{a^2}{R^3\sqrt{1 - a^2/R^2}} \tag{3.57}$$

The equation for R is

$$\frac{\alpha_{\mathrm{fm}}}{2\pi DR} = \frac{a^2}{R\sqrt{R^2 - a^2}} \tag{3.58}$$

or

$$\frac{v_T}{2D} = \frac{1}{\sqrt{R^2 - a^2}} \tag{3.59}$$

From here we have

$$R = \sqrt{a^2 + R_o^2} \tag{3.60}$$

with

$$R_o = \frac{2D}{v_T} \tag{3.61}$$

We had already

$$\alpha = \frac{\alpha\,(a, R)}{1 + \frac{S_p \alpha(a,R)}{4\pi DR}} \tag{3.62}$$

On substituting thus $\alpha\,(a, R)$ and R we find

$$\alpha = \frac{\alpha_{\mathrm{fm}}}{1 - S_p b(R) + \frac{S_p \alpha_{\mathrm{fm}}}{4\pi DR}} \tag{3.63}$$

After some transformation one finally gets

$$\alpha(a) = \frac{\alpha_{\mathrm{fm}}}{1 + \frac{S_p}{2}\left(\sqrt{1 + \left(\frac{a v_T}{2D}\right)^2} - 1\right)} \tag{3.64}$$

3.3.4 First-Order Chemical Reaction Inside the Particle

Here we give an example of the function $\psi(a)$ appearing in Eq. 3.32. To this end we consider a steady-state diffusion–reaction kinetics inside the particle. The respective equation has the form:

$$D_L \Delta n_L(r) - \kappa n_L(r) = 0 \tag{3.65}$$

Here D_L is the diffusivity of the reactant inside the particle, $n_L(r)$ is the reactant radial profile inside the particle, and κ is the reaction constant. We use

$$J = -D_L \left.\frac{\partial n_L}{\partial r}\right|_{r=a} \tag{3.66}$$

as the boundary condition to Eq. 3.65. This condition provides the independence of n_L of time. The solution to this equation can be found elsewhere. The result is

$$n(a) = n_- = \frac{J}{4\pi D_L a\,(\lambda a \coth \lambda a - 1)}. \tag{3.67}$$

Next, $n_- = H n_+$ (the Henri law) with H being the dimensionless Henri constant. Finally we find

$$\psi(a) = \frac{1}{4\pi D_L a H\,(\lambda a \coth \lambda a - 1)}. \tag{3.68}$$

Here $\lambda = \sqrt{\kappa / D_L}$.

3.3.5 Results

Here we list the results of the present consideration.

- The total flux J is given by Eq. 3.32:

$$J = \frac{\alpha(a) n_\infty}{1 + \alpha(a)\psi(a)}.$$

This result is exact and thus does not depend on the approximations done in calculating the trapping efficiency $\alpha(a)$. The function $\psi(a)$ is independent of J in the case of the first-order physicochemical processes at the surface and inside the particle. In more complicated cases this function depends on J and the total flux is no longer a linear function of n_∞

- The total flux of A toward the particle is given by Eq. 3.31 with

$$\alpha(a) = \frac{S_\mathrm{p}\pi a^2 v_T}{1 + \frac{S_\mathrm{p}}{2}\left[\sqrt{1 + \left(\frac{av_T}{2D}\right)^2} - 1\right]}, \tag{3.69}$$

  where S_p is the sticking probability of A–molecules
- The radius of the limiting sphere is

$$R = \sqrt{a^2 + \left(\frac{2D}{v_T}\right)^2}. \tag{3.70}$$

  It is independent of S_p.
- The trapping efficiency in the free molecule zone is

$$\alpha_\mathrm{fm}(a, R) = \frac{\alpha_\mathrm{fm}}{b_+(R)}, \tag{3.71}$$

  where

$$\alpha_\mathrm{fm} = S_\mathrm{p}\pi a^2 v_T, \tag{3.72}$$

  is the free molecule condensational efficiency,

$$v_T = \sqrt{8kT/\pi m_a} \tag{3.73}$$

  is the thermal velocity of condensing molecules, m_a is the molecular mass, and

$$b_-(r) = \frac{S_\mathrm{p}}{2}\left(1 - \sqrt{1 - \frac{a^2}{r^2}}\right) \tag{3.74}$$

$$b_+(r) = 1 - b_-(r) = 1 - \frac{S_\mathrm{p}}{2}\left(1 - \sqrt{1 - \frac{a^2}{r^2}}\right) \tag{3.75}$$

- The reactant concentration profile $n(r)$ is

$$n(r) = \frac{n_R - n_+}{b_+(R)} b_+(r) + n_+ \tag{3.76}$$

  inside the limiting sphere (at $r < R$) and

$$n(r) = n_\infty - \frac{R}{r}(n_\infty - n_R) \tag{3.77}$$

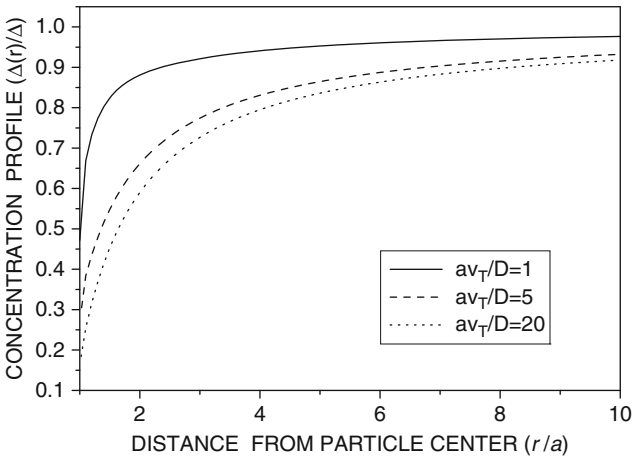

Fig. 3.2 The concentration profiles of A at different particle sizes $av_T/D = 1, 5, 20$. Here $\Delta(r) = n(r) - n_+$ and $\Delta = n_\infty - n_+$)

outside the limiting sphere (at $r \geq R$). Here

$$n_R = n(R) = n_\infty - \frac{\alpha(a)\,(n_\infty - n_+)}{4\pi DR}. \tag{3.78}$$

The function $n(r)$ is continuous at $r = R$ together with its first derivative. Excluding n_R from Eqs. 3.77 and 3.78 yields the profile in the form:

$$\frac{n_r - n_+}{n_\infty - n_+} = \left(1 - \frac{\alpha(a)}{4\pi DR}\right)\frac{b_+(r)}{b_+(R)} \tag{3.79}$$

at $r < R$ and

$$\frac{n_r - n_+}{n_\infty - n_+} = 1 - \frac{\alpha(a)}{4\pi Dr} \tag{3.80}$$

at $r \geq R$. Figure 3.2 displays the profile at three different dimensionless particle sizes.

3.3.6 Discussion

3.3.6.1 Trapping Efficiency

Although Eq. 3.31 is widely used in the aerosol literature, I never met its derivation for the transition regime. This equation is known to hold in the continuous limit,

where it is readily derived on solving the diffusion equation or in the free molecule regime, where it is a consequence of the balance of in- and out-fluxes $J = J_{\text{in}} - J_{\text{out}}$. Here $J_{\text{in}} = \pi a^2 v_T n_\infty$ and $J_{\text{out}} = \pi a^2 v_T n_+$.

To derive Eq. 3.31 in the transition regime, let us split the distribution function into two terms, $f = f_0 + J f_J$, where f_0 is the part of the distribution independent of the reactant flux J and the second term is linear in J because of the linearity of the transport equation with respect to f. We rewrite this equation in the integral form:

$$f = f_{\text{fm}} + D^{-1} R[f], \tag{3.81}$$

where D^{-1} is the inversion of the differential operator standing on the left-hand side of the transport equation, $R[f]$ is the collision integral, and f_{fm} is the solution to the collisionless transport equation with Maxwell's boundary condition. Let then the triangle brackets $< \cdot >$ stand for the operation that produces the flux from f, $< f >= J$. Let us apply this operator to both sides of Eq. 3.81. On introducing $B =< D^{-1} R f_J >$ gives

$$J = \pi a^2 v_T \left(n_\infty - n_+\right) + BJ \tag{3.82}$$

or

$$J = \frac{\pi a^2 v_T \left(n_\infty - n_+\right)}{1 - B}. \tag{3.83}$$

This is exactly Eq. 3.31.

The efficiency $\alpha(a)$ has dimension $\left[l^3/t\right]$. Very simple dimension considerations allow us to establish a general form of the condensational efficiency. Three parameters govern the condensation kinetics: the particle radius a, the thermal velocity of the condensable gas molecules $v_T = \sqrt{8kT/\pi m}$, and their diffusivity D. Their dimensions are $a = [\text{cm}]$, $v_T = [\text{cm/s}]$, and $D = \left[\text{cm}^2/\text{s}\right]$. Because $\alpha(a) = \left[\text{cm}^3/\text{s}\right]$, we can write

$$\alpha(a) = S_p \pi a^2 v_T \phi\left(a v_T / D\right). \tag{3.84}$$

The multiplier π normalizes $\phi(0)$ to unity, $\phi(0) = 1$ (see Eq. 3.72). The function $\phi(x)$ is not yet known. To find this function one should solve the Boltzmann kinetic equation that describes the time evolution of the coordinate–velocity distribution of the condensing molecules, then find the flux of the condensing molecules toward the particle, and then extract $\alpha(a)$. This is not easy to do in general form. However, the limiting situations are well analyzable (see Seinfeld and Pandis 2006): $\phi(x) = 1$ at small x and $\phi(x) = 4/x$ as $x \to \infty$.

It is remarkable that all existing approaches give similar dependence on the sticking probability:

$$\phi(x) = \frac{1}{1 + S_{\text{p}} F(x)} \tag{3.85}$$

Three approximate expressions for $F(x)$ are considered below.

1. The Lushnikov–Kulmala (LK) approximation (Lushnikov and Kulmala 2004a) (see Eq. 3.69):

$$F_{\mathrm{LK}}(x) = \frac{1}{2}\left(\sqrt{1+\frac{x^2}{4}} - 1\right). \tag{3.86}$$

The ideas on the derivation of this equation are given below

2. The Fuchs–Sutugin (FS) approximation (Fuchs and Sutugin 1971): in deriving this equation these authors divided the space into two parts: the free molecule zone and the diffusion zone. They then used the principle of constancy of the total flux. The radius of the limiting sphere (the spherical surface dividing the space into free molecular and diffusion zones) is found from the numerical solution of the BGK (Bhatnagar et al. 1954) kinetic equation obtained by Sahni (1966). In addition, they replaced $\alpha(a, R)$ by α_{fm}. Their final result is widely known:

$$F_{\mathrm{FS}}(x) = \frac{x\,(x+1.13)}{4\,(x+3)}. \tag{3.87}$$

3. Dahneke's (D) approximation (Dahnecke 1983):

$$F_{\mathrm{D}}(x) = \frac{x^2}{4\,(x+2)}. \tag{3.88}$$

The last two approximations are discussed by Seinfield and Pandis (2006).

Figure 3.3 compares these three approximation. It is seen that the difference is minor.

3.3.6.2 Concentration Jump

Let us write down the concentration profile in the free molecule regime (Eq. 3.47):

$$n_{\mathrm{fm}}(r) = n_\infty - (n_\infty - n_+)\, b_-(r). \tag{3.89}$$

The concentration profiles are presented in Fig. 3.2. Figure 3.4 shows the dependence of the reduced concentration jump Δ_a/Δ on a. Figure 3.5 displays the size dependence of the trapping efficiency. Here we compare our results with the numerical results of Loylaka et al. (1989) and two semiempirical formulas. The difference between these results does not exceed 10%.

The synthetic concentration profile obtained by sewing the free–molecular and diffusion profiles (Fig. 3.6) is compared to the results of calculations obtained by Williams and Loylaka (1991) and by Loylaka et al. (1989), where the Boltzmann equation was solved numerically. Both these curves reproduce identical fluxes but display a different behavior at small particle sizes.

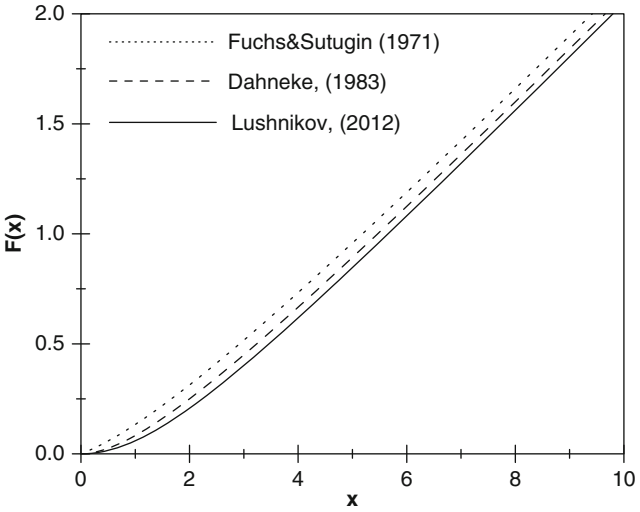

Fig. 3.3 The universal function F entering the expression for the trapping efficiency (see Eqs. 3.84 and 3.85). It is seen that three different approximations give very close results

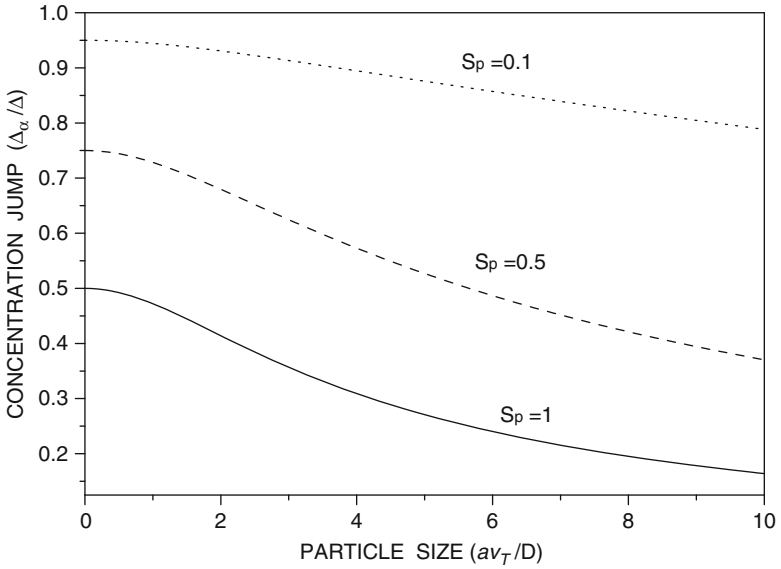

Fig. 3.4 Reduced concentration jump (Eq. 3.93) versus reduced particle size: it drops to zero as the particle size grows

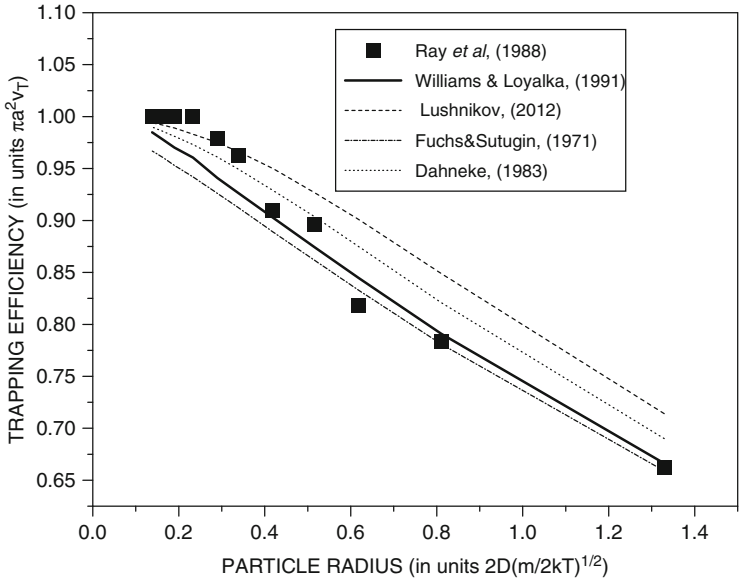

Fig. 3.5 Trapping efficiency versus particle size. Shown are the experimental results of Ray et al. (1988), the semi-empirical curves from Fuchs and Sutugin (1971) and from Dahnecke (1983), and the present chapter. The *solid line* is the result of a numerical solution to the kinetic equation (Williams and Loyalka 1991; Loyalka et al. 1989)

This spectrum possesses two remarkable features: it depends on (1) the radial coordinate (the function $b_+(r)$ is given by Eq. 3.74) and (2) $n_{\rm fm}(a) \neq n_+$. From Eq. 3.89 one finds

$$n_{\rm fm}(a) = \frac{S_{\rm p}}{2} n_+ + \left(1 - \frac{S_{\rm p}}{2}\right) n_\infty . \tag{3.90}$$

If we define the concentration jump as $\Delta_a = n(a) - n_+$ then in the free molecule regime we find

$$\Delta_a^{\rm fm} = \left(1 - \frac{S_{\rm p}}{2}\right)(n_\infty - n_+)\,. \tag{3.91}$$

Combining Eqs. 3.76 and 3.78 yields the concentration jump in the general case:

$$\Delta_a = n_a - n_+ = (n_\infty - n_+)\left(1 - \frac{\alpha(a)}{4\pi DR}\right)\frac{b_+(a)}{b_+(R)}. \tag{3.92}$$

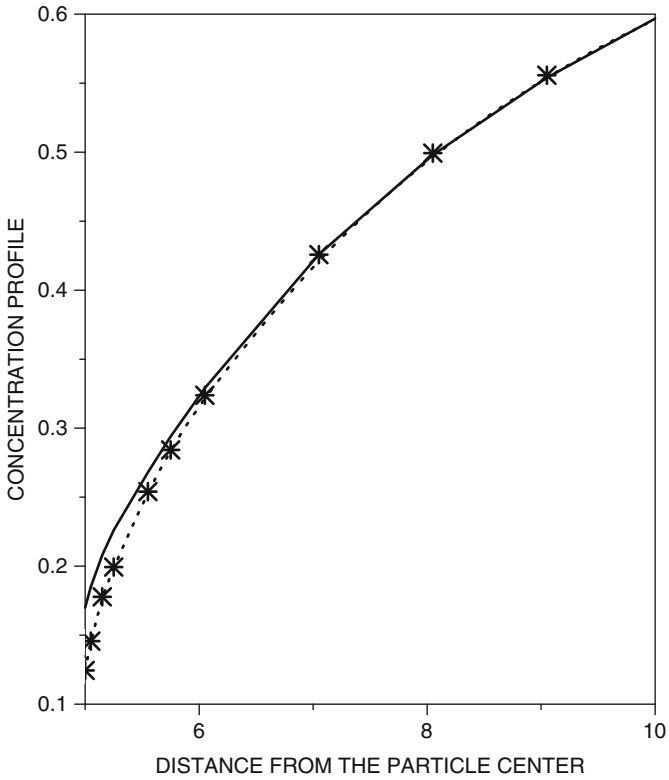

Fig. 3.6 Concentration profile versus distance from the particle center. *Solid curve* shows results from the numerical solution of the Boltzmann equation (Williams and Loyalka 1991; Loyalka et al. 1989). The *second curve* is the analytical result (Eqs. 3.79 and 3.80)

or

$$\frac{\Delta_a}{\Delta} = \frac{2 - S_\mathrm{p}}{2 + S_\mathrm{p}\left[\sqrt{1 + \left(\frac{av_T}{2D}\right)^2} - 1\right]}, \tag{3.93}$$

where $\Delta = n_\infty - n_+$.

3.4 Evaporation

The evaporation process demands some more attention, because now we must consider the motion of the evaporating molecule inside the particle, then crossing the interface and then the diffusion in the gas phase. The latter stage can be considered

to be very similar to condensation. The only problem is how to find the pressure of the evaporating substance over the particle surface. There are two sorts of problem: the evaporation of an admixed molecule and the evaporation of the molecules of the particle host material. The commonly accepted approach to the latter problem assumes that the pressure of the host material over the particle surface is equal to its equilibrium pressure over the curved surface. The effects related to the curvature of the particle surface are of importance for nanoparticles. We discuss this issue at the end of this section and begin with the evaporation of an alien molecule.

The diffusion of the alien molecule inside the particle is described by the diffusion equation

$$\frac{\partial c}{\partial t} = D\Delta c \tag{3.94}$$

with the boundary condition

$$J(t) = -4\pi a^2 D \nabla c|_a \tag{3.95}$$

and the initial condition

$$c(r, 0) = c_0(r) \tag{3.96}$$

In what follows we assume that c_0 is independent of r. Next, the characteristic diffusion time $\tau_{\text{diff}} = a^2/D$ is much shorter than the evaporation time $\tau_{\text{ev}} = 1/\alpha n(a)$, where $n(a)$ is the vapor concentration over the particle surface; this means that the concentration profile inside the particle is always almost flat. Hence, we can find the concentration beneath the particle surface:

$$c_-(a, t) = \frac{N(t)}{4\pi a^2} \tag{3.97}$$

The concentration over the particle surface is

$$c_+(a, t) = Hc_-, \tag{3.98}$$

where H is the dimensionless Henri constant. The conservation of the flux demands

$$\frac{\mathrm{d}N}{\mathrm{d}t} = -\alpha(a)c_-(a, t) = -\alpha\frac{3N(t)}{4\pi} \tag{3.99}$$

Finally we have

$$N(t) = N_0 \exp\left(-3\alpha(a)t/4\pi\right) \tag{3.100}$$

A less primitive consideration may be seen in Ford and Harris (2004).

In the case of evaporation of the host molecules, the consideration does not change except that in this case we must take into account the changes of the particle size and the dependence of the equilibrium pressure over the particle surface on the particle size (see Friedlander 2000, p. 257):

$$c_e(a) = c_\infty exp\,(2\sigma v_m/akT) \tag{3.101}$$

Here v_m is the volume per a molecule in the gas phase and σ is the surface tension.

3.5 Particle Charging in the Free Molecule Regime

Charging of small neutral and charged particles suspended in a weakly ionized plasma is investigated under the assumption that the Coulomb + image forces affect the ion transport in the carrier plasma and define the rate of charging processes. Our approach is based on a solution of the collisionless kinetic equation describing the ion transport in the presence of force fields created by the particle charge and the image force. The exact free molecule ion distribution over coordinates and velocities is used for calculating the rate of ion deposition onto neutral and charged dielectric particles. Our approach easily reproduces well-known results for metallic particles and allows us to derive rather simple expressions for the charging efficiencies of dielectric particles. Our theory is applicable either for particles whose sizes are much smaller than the ion mean free path (the charging of neutral particles) or when the ion mean free path much exceeds the Coulomb length (the distance at which the ion thermal and Coulomb's energy become comparable) (ion–particle recombination).

3.5.1 Introduction

The problem of particle charging is not new and its importance is beyond any doubt. Charged aerosol particles are met almost everywhere. The reason for this is apparent: the energy excess of a charged aerosol particle becomes comparable to the thermal energy kT already at particle size of the order of the Coulomb length $l_c = e^2/kT$. Here e is the electron charge, T is the temperature in K, and k is the Boltzmann constant. At ambient condition this length is about 60 nm (for a singly charged particle) and comparable to the mean free path l of air molecules (Seinfeld and Pandis 2006). On the other hand, there exist many sources of particle charging: natural and artificial radioactivity, short-wave electromagnetic radiation, cosmic rays, intra-atmospheric chemical reactions producing ions (Hodges 1969; Marlow and Brock 1975; Marlow 1980; Hussin et al. 1983; Jensen and Thomas 1991; Beig and Brasseur 2000). Cosmic rays generate ions deep within the troposphere and control its electrical state down to the Earth's surface. The ions produced by

cosmic rays give rise to the formation of aerosol particles and change the rate of the aerosol processes such as nucleation, coagulation, and condensation (Castelman 1982; Kulmala et al. 2004; Harrison and Carslaw 2003).

Recent modeling work by Yu and Turko (2001) indicates that small ions can provide a source of atmospheric cloud condensation nuclei (CCN). The cloud processes actively exerting the weather condition and climate occur within a weak ionic plasma, susceptible to changes on all spatial and temporal scales. Coagulation rates and the scavenging of aerosol particles from the atmosphere can be generally affected by electric charging of aerosols. Many studies (Havnes et al. 1990, 1992, 1996; Rapp 2000; Rapp and Lübken 1999; Yu and Turko 1998a, b; Sorokin and Mirabel 2001; Sorokin et al. 2003) have suggested that the charging processes in the atmosphere play a key role in the formation of the aerosol state of the atmosphere and especially its upper layers (Rapp 2000; Rapp and Lübken 1999). Such important effects, such as the reduction in electron density in the mesosphere, can be caused by positively charged aerosol particles that appear consequent to the aerosol photoeffect (Rapp and Lübken 1999).

The particle charging is of key importance in the processes of formation of aerosols from aircraft exhaust plumes. The dispersed and chemical content of aerosols appearing in the atmosphere as a result of increasing air flight activity strongly depends on the dynamics of charged particle formation in high-temperature processes in aircraft motors (Yu and Turko 1998a, b; Sorokin and Mirabel 2001; Sorokin et al. 2003).

Of course, the significance of charged aerosol particles is not exhausted with their atmospheric implications. Modern aerosol technologies of nanoparticle production (Wen et al. 1984; Adachi 1985; Wiedenscholer and Fissan 1991; Romay and Pui 1992; Matsoukas 1997; Smith et al. 1999) widely apply charged aerosol particles for modification of the particle-size distributions or for the regulation of the particle content.

Aerosol electrification modifies aerosol deposition in the lungs (Hashish and Bailey 1991), including deposition of therapeutic aerosols. Domestic ionizers are designed to release large quantities of negative ions, causing unipolar aerosol charging. There are known biological effects of small ions. Harmful bacteria can be killed or their growth inhibited by ions of both signs (Krueger and Reed 1976).

The charging of aerosol particles is widely used for detecting fine aerosol particles with sizes less than 0.1 μm (Liu 1976).

All kinetic models used for treating the effects just outlined demand knowledge of the rates of elementary charging processes. Many authors addressed their efforts to deriving the expressions for charging efficiencies of an aerosol particle by ions. It is not difficult to resolve this problem for the continuous limit, where ion transport is described by the diffusion equation (Reist 1984; Smirnov 2000a, b).

In the free molecule regime the charging efficiency can be easily found only when the ion–particle interaction is described by the Coulomb potential alone. Attempts to take into account the image forces make the analysis much more difficult. Especially this concerns the dielectric particles, in which case the ion–particle interaction is described by an infinite and slowly convergent series (Landau and Lifshits 1969).

The first successful attempt to apply the free molecule approximation for calculating the charging efficiencies of small aerosol particles was undertaken by Natanson (1959, 1960). Later this problem was considered by many authors (Marlow and Brock 1975; Natanson 1959, 1960; Gentry and Brock 1967; Keefe et al. 1968; Hahn 1997; Huang et al. 1991). None of these works could avoid the difficulty related to the very inconvenient expression for the ion–dielectric particle potential. The latter has been replaced by the ion–metal particle potential modified by the multiplier $(\varepsilon - 1)/(\varepsilon + 1)$, with ε being the dielectric permeability of the particle material.

Attempts to consider the transition regime using as the zero approximation the solution of the collisionless kinetic equation have been done (Smith et al. 1999; Huang et al. 1990, 1991; Hoppel and Frick 1986) and also fairly recently (Lushnikov and Kulmala 2004a, b, 2005). The analysis of these authors clearly demonstrated the significance of the ion–carrier gas interaction in calculating the efficiency of the particle–ion recombination. The point is that the ion can be captured by the charge particle from the bound states with negative energies. This effect has been considered (Hoppel and Frick 1990) by taking into account a single ion–molecular collision in the Coulomb field created by the charged particle. A new version of flux-matching theory (Natanson 1959, 1960) has been applied by Lushnikov and Kulmala (2004a) to take this effect into account explicitly.

Commonly accepted theories (Reist 1984; Hidy and Brock 1971) of particle charging apply a purely mechanical approach and include two steps:

- First, one calculates the dependence of the impact parameter of the ion capture on the ion velocity.
- Second, one averages the cross section thus found over the Maxwell distribution of ions and finds the charging efficiency.

Of course, there is nothing wrong in this approach, and it gives right results. Still, it has some disadvantages compared to an alternative, kinetic approach that we apply below. This approach also includes two (very different) steps:

- First, one solves the collisionless Boltzmann equation in the external field created by the charged particle or by the image forces and finds the ion distribution over coordinates and velocities.
- Second, the ion distribution thus found is used for calculating the ion fluxes toward the target particle.

There are strong arguments in favor of the second approach. Any attempts to consider the correction from ion–carrier gas interaction demand a solution (approximate, of course) of the Boltzmann equation. The second approach gives a good starting platform for this, whereas the mechanical approach gives nothing in this respect. Next, the kinetic approach allows one to find the ion concentration profiles for different boundary conditions at the particle surface. And finally, the kinetic approach is simpler than the mechanical one. We thus apply the second route for deriving rather simple and well observable *exact* expressions for charging

efficiencies of small metallic and dielectric particles. To this end we use the method developed by Lushnikov and Kulmala (2004a) for studying the charging efficiencies of metallic particles in the transition regime. The decisive step allowing for a consideration of dielectric particles is found in (Lushnikov and Kulmala 2005) where a simple integral representation of the image potential is derived that immediately solves the problem. We repeat this derivation here.

Our final goal is to find the ion flux $J(a)$ as a function of the particle size, its charge, and dielectric permeability. Actually, we look for the enhancement factor $\varepsilon(a)$ defined as

$$\varepsilon(a) = \frac{J(a)}{J_0(a)}. \tag{3.102}$$

Here $J_0(a)$ is the ion flux when the ion–particle interaction is switched off (e.g., the condensation of neutral molecules on a neutral particle).

Below we use the free molecule approximation, which normally assumes the smallness of the particle size as compared to the ion mean free path. If, however, the particle charge exerts the charge transport, an additional parameter characterizing the kinetic process appears: the ratio of the ion Coulomb energy to its thermal energy. Then, the free molecule approximation also assumes the smallness of this parameter, which is of the order of unity at the Coulomb distance, $l_c = e^2/kT \approx 0.6 \cdot 10^{-5}$cm, comparable to the mean free path at normal pressure; this means that the free molecule limit correctly describes the ion–particle recombination only at very low pressure of the carrier gas.

3.5.2 *Solution of the Kinetic Equation*

Below we solve the kinetic equation assuming that no ions escape from the particle surface:

$$f_1(a, E, L) = 0. \tag{3.103}$$

Because the total flux J is independent of r, Eq. 3.29 can be rewritten as

$$J = \frac{4\pi^2}{m^3} \int \mathrm{d}E \int \mathrm{d}L^2 f_{-1}(a, E, L). \tag{3.104}$$

3.5.2.1 Free Molecule Distribution

In what follows we consider the free molecule regime, which means that we ignore the collisions of the incident ions with the carrier gas molecules. The solution to Eq. 3.23 is constructed as follows: the function f_s is a non-zero constant (as the

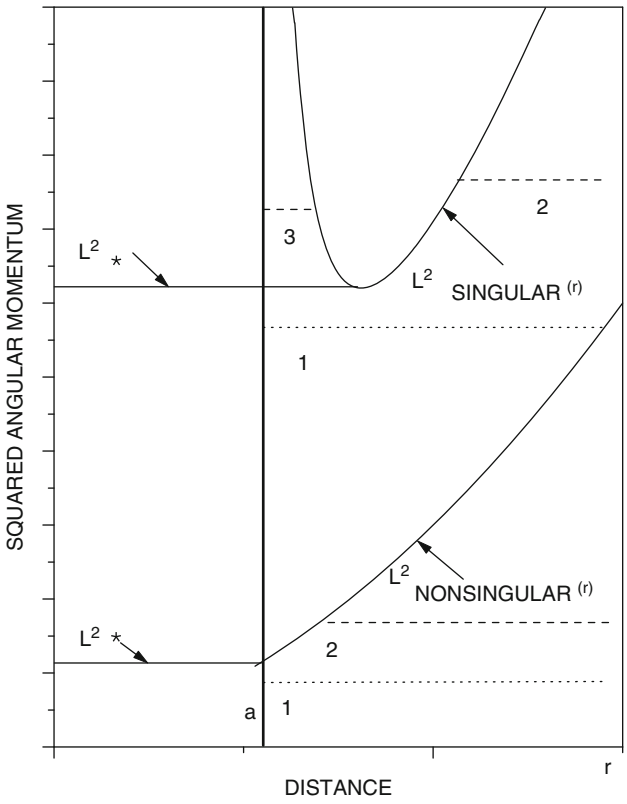

Fig. 3.7 Nonsingular and singular ion–particle interactions. Shown are the maximal admissible angular momenta $L^2(r)$ as the functions of r. Ions with the trajectories *1* can reach the particle surface and be captured by the particle. Ions of trajectories *2* pass aside from the particle. The finite trajectory *3* cannot be populated in the free molecule regime and thus does not contribute to the particle charging efficiency

function of r) in the admissible interval of L. The latter is defined by two conditions: (1) $0 < L^2 < L^2(r)$ (this condition provides the existence of the square root on the right-hand side of Eq. 3.23), and (2) the finite ion trajectories do not contribute to the ion distribution. These trajectories can appear as the bound states of attractive potentials at negative E or at $E > 0$ if the function $L^2(r)$ has a minimum at $r = r_* > a$ as it takes place, for example, in the case of attractive potentials (see Fig. 3.7). Hence,

$$f_s\left(r, E, L\right) = B_s\left(E, L\right)\theta\left(L_{\mathrm{m}}^2(r) - L^2\right) \tag{3.105}$$

with $\theta(x)$ being the Heaviside step function. The function $B_s\left(E, L\right)$ is still arbitrary. Its dependence on E is defined by the condition that $f_s \propto e^{-\beta E}\theta(E)$ as $r \to \infty$. Here, $\beta = 1/kT$. The factor $\theta(E)$ excludes the bound states of ions, for they do

not present far away from the particle. The function $L^2_{\mathrm{m}}(r)$ is defined as

$$L^2_{\mathrm{m}}(r) = L^2(r)\theta\left(r - r_*\right) + L^2_*\theta\left(r_* - r\right) \tag{3.106}$$

Here $L^2_* = \min\left(L^2(r)\right)$.

The dependence on L follows from the boundary condition (Eq. 3.105):

$$\begin{aligned} B_s\left(E, L\right) &= C e^{-\beta E}\theta(E)\left[\theta\left(L - L_*\right) + \delta_{s,-1}\theta\left(L_* - L\right)\right] \\ &= C e^{-\beta E}\theta(E)\left[\delta_{s,1}\theta\left(L - L_*\right) + \delta_{s,-1}\right], \end{aligned} \tag{3.107}$$

where C is the normalization constant of the Maxwell distribution, $C = n_\infty \left(\beta m/2\pi\right)^{3/2}$, $\beta = 1/kT$, and $\delta_{i,k}$ is the Kroneker delta. The angular momentum L_* separates the ion trajectories crossing the particle surface ($L < L_*$) from those passing aside the particle ($L > L_*$). It is easy to see that the distribution in this form contains no outgoing ions at $r = a$, because the factor $\theta\left(L - L_*\right)$ in the first term does not permit for the trajectories crossing the point $r = a$. Hence, $f_1(a) = 0$.

3.5.2.2 Free Molecule Flux

The integration over L^2 in Eq. 3.29 is readily performed to give:

$$J(a) = C\frac{4\pi^2}{m^3}\int L^2_* \mathrm{e}^{-\beta E}\mathrm{d}E. \tag{3.108}$$

In most practically important cases the angular momentum $L(r)$ reaches its minimum at $r_* > a$, i.e. $L_* = L\left(r_*\right)$. The condition $\partial_r L^2(r) = 0$ rewritten as

$$r_*\left.\frac{\partial U}{\partial r}\right|_{r=r_*} = \frac{L^2\left(r_*\right)}{m r_*^2} \tag{3.109}$$

or

$$\frac{1}{2}r_* U'\left(r_*\right) + U\left(r_*\right) = E \tag{3.110}$$

defines r_* as a function of a and E.

Let us introduce $x = \beta E$ and

$$\Psi = \frac{\beta L^2_*}{2ma^2} = \frac{r_*^2}{a^2}\left(x - \beta U\left(r_*\right)\right). \tag{3.111}$$

The factor Ψ is seen to depend on x and a via r_* and explicitly.

The free molecule flux is now expressed in terms of Ψ as follows:

$$J(a) = \pi a^2 n_\infty v_T \int\limits_0^\infty \mathrm{e}^{-x} \Psi(x) \theta\left(\Psi(x)\right) \mathrm{d}x, \tag{3.112}$$

where $v_T = \sqrt{8kT/\pi m}$ is the thermal velocity. From Eq. 3.112 we can find the enhancement factor:

$$\varepsilon(a) = \int\limits_0^\infty \mathrm{e}^{-x} \Psi(x) \theta\left(\Psi(x)\right) \mathrm{d}x, \tag{3.113}$$

because the multiplier before the integral on the right-hand side of Eq. 3.112 is equal to the free molecule flux of neutral molecules on a neutral particle (see following).

Now we prove that

$$\frac{\mathrm{d}\Psi}{\mathrm{d}x} = \frac{r_*^2}{a^2}. \tag{3.114}$$

Indeed, differentiating both sides of Eq. 3.112 over x gives

$$\frac{\mathrm{d}\Psi}{\mathrm{d}x} = \frac{r_*^2}{a^2} + \frac{2r\, r'_x}{a^2}\left[x - \beta U\left(r_*\right) - \frac{1}{2} r_* U'\left(r_*\right)\right].$$

The expression in the parentheses on the right-hand side of this equation is zero because of Eq. 3.110.

Integrating by parts in Eq. 3.113 and using Eq. 3.114 leads to the final result:

$$J(a) = \pi n_\infty v_T \left(a^2 \Psi_0 + \int\limits_0^\infty \mathrm{e}^{-x} r_*^2(x) \theta\left(\Psi(x)\right) \mathrm{d}x\right), \tag{3.115}$$

where $\Psi_0 = \Psi(x = 0)$ if $\Psi(x) > 0$ at $x > 0$ and $\Psi_0 = 0$ otherwise.

3.5.2.3 Ion Density Profile

Equations 3.27, 3.105, and 3.107 allow us to find the ion density profile $n(r)$

$$n(r) = n_\infty \left[F(r) + G(r)\right], \tag{3.116}$$

where n_∞ is the ion density far away from the particle,

$$F(r) = A(r) \int\limits_{E_0 \theta(E_0)}^\infty \mathrm{e}^{-\beta E} \mathrm{d}E \int\limits_0^{L_\mathrm{m}^2(r)} \frac{\mathrm{d}L^2}{\sqrt{L_\mathrm{m}^2(r) - L^2}}, \tag{3.117}$$

and

$$G(r) = A(r) \int\limits_{E_0\theta(E_0)}^{\infty} \mathrm{e}^{-\beta E}\mathrm{d}E \int\limits_{L_*^2}^{L_\mathrm{m}^2(r)} \frac{\mathrm{d}L^2}{\sqrt{L_\mathrm{m}^2(r) - L^2}}. \tag{3.118}$$

Here the energy E_0 is defined by the condition $L_*^2 \geq 0$ and

$$A(r) = \frac{\pi}{m^2 r}\left(\frac{\beta m}{2\pi}\right)^{3/2}.$$

On integrating over L^2 in Eqs. 3.117 and 3.118 gives

$$F(r) = \frac{1}{\sqrt{\pi}} \int\limits_{E_0\theta(E_0)}^{\infty} \mathrm{d}x \cdot \mathrm{e}^{-\beta x}\left[\sqrt{x - \beta U(r)} \cdot \theta\left(r_* - r\right) + \frac{a}{r}\sqrt{\Psi(x)} \cdot \theta\left(r_* - r\right)\right] \tag{3.119}$$

and

$$G(r) = \frac{1}{\sqrt{\pi}} \int\limits_{\beta E_0\theta(E_0)}^{\infty} \mathrm{d}x \cdot \mathrm{e}^{-x}\left[\sqrt{x - \frac{a^2}{r^2}\Psi - \beta U(r)} \cdot \theta\left(r - r_*\right)\right] \tag{3.120}$$

We must remember that r_* depends on x.

3.5.3 Nonsingular Potentials

In this section we consider the molecular fluxes onto the particle surface assuming that the interaction potentials are nonsingular, that is, they remain finite at $r = a$. Most widespread potentials are nonsingular, for example, the Coulomb potential or the interaction of polar molecules with a charged particle. The common feature of these potentials is their monotonic behavior that provides the minimum of $L(r)$ to locate at $r = a$. The consideration of nonsingular potentials is much simpler than singular ones having a singularity at the particle surface. Examples of such potentials are also well known, for example, the potential of image force which, as we see next, plays an important role in considering the particle charging.

Two simplest examples illustrate our approach: the free condensation of molecules onto the particle surface (see Sect. 3.3) and the capture of polar molecules by charged particles.

3.5.3.1 Potential Driven Condensation

If the potential $U(r)$ does not have a singularity at $r = a$ and behaves monotonously, then the expressions for J and $F(r)$ can be considerably simplified. In this case the angular momentum $L(r)$ reaches the minimum at the particle surface, $r_* = a$. The function Ψ is $\Psi(x) = x - \beta U(a)$. Equations 3.119, 3.120, and 3.115 then reduce to

- Repulsion ($U(r) > 0$)

$$F(r) = \mathrm{e}^{-\beta U(r)}, \tag{3.121}$$

$$G(r) = \frac{1}{\sqrt{\pi}}\mathrm{e}^{-\beta U(r)}\Gamma\left(\frac{3}{2}, \beta\frac{(U(a) - U(r))\, r^2}{r^2 - a^2}\right)\sqrt{1 - \frac{a^2}{r^2}} \tag{3.122}$$

Here $\Gamma(\alpha, x) = \int\limits_x^\infty s^{\alpha-1}\mathrm{e}^{-s}\mathrm{d}s$ is the incomplete gamma function.

$$\varepsilon(a) = J(a)/J_0(a) = \mathrm{e}^{-\beta U(a)} \tag{3.123}$$

- Attraction $U(r) < 0$

$$F(r) = \frac{1}{\sqrt{\pi}}\mathrm{e}^{\beta|U(r)|}\Gamma\left(3/2, \beta|U(r)|\right) \tag{3.124}$$

$$G(r) = \frac{1}{\sqrt{\pi}}\mathrm{e}^{-\beta U(r)}\Gamma\left(\frac{3}{2}, \beta\frac{U(r)r^2 - U(a)a^2}{r^2 - a^2}\right)\sqrt{1 - \frac{a^2}{r^2}} \tag{3.125}$$

and

$$\varepsilon(a) = 1 + \beta\,|U(a)| \tag{3.126}$$

3.5.3.2 Condensation of Polar Molecules

The foregoing theory can be readily applied for calculating the flux of polar molecules toward a charged particle. Although the interaction potential depends on the orientation of the polar molecule, we can ignore this dependence and consider the dipoles directed to the particle center. In this case the interaction potential is

$$U(r) = -\frac{d\, e^2}{r^2}, \tag{3.127}$$

where d is the distance between the opposite charges of the polar molecule. There are strong grounds for using Eq. 3.127. The point is that the dipole reorientation time τ_r is much shorter than the time of flight, the distance of the order of the particle size $\tau_a \propto a/v_T$. Indeed, the dynamics of the dipole rotation is governed by the equation of motion $I\ddot{\phi} = F$, where $I \propto md^2$ is the moment of inertia of the molecule, m is its mass, and the rotating moment is $F \propto e^2d^2/a^3$. The angular acceleration is $\ddot{\phi} \propto 1/\tau_r^2$. Hence, $\tau_r^2 \propto a^3m/e^2$ and $\tau_r^2/\tau_a^2 \propto amv_T^2/e^2 \propto akT/e^2 \propto a/l_c \ll 1$. Here, $l_c = \beta e^2$ is the Coulomb length. Hence,

$$\varepsilon(a) = 1 + \frac{\beta e^2 d}{a^2}, \tag{3.128}$$

Equations 3.116, 3.124, and 3.125 define the concentration profile of the condensing molecules

$$n(r) = \frac{n_\infty}{2}\left(\sqrt{1-\frac{a^2}{r^2}} + \frac{2}{\sqrt{\pi}}\mathrm{e}^{\beta d e^2/r^2}\Gamma\left(3/2, \beta d e^2/r^2\right)\right) \tag{3.129}$$

3.5.4 Charging of Particles

Here we consider the charging of dielectric particles consisting of a material with the dielectric permeability ε. In this case the image potential is not given by a simple analytical formula. Still, the situation is not hopeless.

3.5.4.1 Image Potential

The expression for the potential of the image force can be found in Stratton (1941):

$$U_{\text{image}}(r) = -\frac{q^2e^2}{2}(\varepsilon - 1)\sum_{n=1}^{\infty}\frac{n}{n(\varepsilon-1)+1}\frac{a^{2n+1}}{r^{2n+2}}P_n(0), \tag{3.130}$$

where e is the electron charge, q is the ion charge in units of e, ε is the dielectric permeability of the particle material, and $P_n(\cos\theta)$ are the Legendre polynomials of the n–th order. At $\theta = 0$, all $P_n(0) = 1$. This fact allows for the summation in Eq. 3.130:

$$U_{\text{image}}(r) = -\frac{q^2e^2}{2a}\cdot\frac{\varepsilon-1}{\varepsilon+1}\cdot S\left(r/a\right), \tag{3.131}$$

where

$$S(x) = \frac{1}{x^2}\Phi\left(\frac{1}{x^2}\right) \tag{3.132}$$

and $\Phi(x)$ is the solution to the differential equation

$$x\Phi' + \frac{1}{\varepsilon+1}\Phi = \frac{x}{(1-x)^2} \tag{3.133}$$

with the initial condition $\Phi(0) = 0$. This solution has the form:

$$\Phi(x) = x^{-1/(\varepsilon+1)} \int_0^x \frac{y^{1/(\varepsilon+1)}}{(1-y)^2}\mathrm{d}y \tag{3.134}$$

or, on integrating twice by parts,

$$\Phi(x) = \frac{x}{x-1} - \frac{1}{\varepsilon+1}\ln\frac{1}{1-x} + \frac{1}{(\varepsilon+1)^2}x^{-1/(\varepsilon+1)} \int_0^x y^{-\varepsilon/(\varepsilon+1)} ln\frac{1}{1-y}\mathrm{d}y \tag{3.135}$$

The last term in this equation is nonsingular at the particle surface. The approximation

$$\Phi_a(x) \approx \frac{x}{x-1} - \frac{1}{\varepsilon+1}\ln\frac{1}{1-x} + \frac{x}{(\varepsilon+1)(\varepsilon+2)} \tag{3.136}$$

reproduces the asymptotic behavior of $\Phi(x)$ as $x \to 0$ and $x \to 1$.

The function $S(x)$ obeys the differential equation

$$xS' = -2\left[\frac{1}{(x^2-1)^2} + \frac{\varepsilon}{\varepsilon+1}S\right] \tag{3.137}$$

which follows from Eq. 3.133.

At $\varepsilon = \infty$ the function $\Phi(x) = x/(1-x)$ and we come to the quite familiar expression for the image potential of a metallic particle:

$$U_{\text{image}}(r) = -\frac{q^2e^2}{2a} \cdot \frac{a^4}{r^2(r^2-a^2)}. \tag{3.138}$$

Equation 3.137 plays a key role in our further consideration.

3.5.4.2 General Considerations

Let us consider the ion flux toward a charge particle. The incident ion and the target particle interact via the Coulomb and the image potentials:

$$U(r) = \pm\frac{qQe^2}{r} - \frac{q^2e^2}{2a}\cdot\frac{\varepsilon-1}{\varepsilon+1}\cdot S\left(r/a\right), \tag{3.139}$$

where Q and q are the charges of the particles and the ion in units of e [Q and q are nonnegative integers; the upper sign (here "+") refers to the Coulomb repulsion]. Introducing

$$\frac{r}{a} = \rho, \quad \zeta = \frac{Q}{q}\cdot\frac{\varepsilon+1}{\varepsilon-1}, \quad \gamma = \frac{\beta q^2e^2}{2a}\cdot\frac{\varepsilon-1}{\varepsilon+1}, \quad \text{and} \quad u = \frac{\beta E}{\gamma} \tag{3.140}$$

allows Eq. 3.139 to be rewritten as follows:

$$\beta U\left(\rho\right) = \gamma\left(\pm\frac{2\zeta}{\rho} - S\left(\rho\right)\right), \tag{3.141}$$

where $S(\rho)$ is introduced by Eq. 3.137. We also introduce

$$u\left(\rho\right) = \frac{1}{\left(\rho^2-1\right)^2} \pm \frac{\zeta}{\rho} - \frac{1}{\varepsilon+1}\cdot S\left(\rho\right). \tag{3.142}$$

Then $\rho_* = \rho_*(u)$ (see Eq. 3.111) is the solution to the equation

$$u = u\left(\rho\right). \tag{3.143}$$

Equation 3.112 now looks as follows:

$$\Psi(u) = \gamma\psi\left(\rho_*(u)\right), \tag{3.144}$$

where

$$\psi\left(\rho\right) = \rho^2\left[u\left(\rho\right) \mp \frac{2\zeta}{\rho} + S\left(\rho\right)\right]. \tag{3.145}$$

For calculating the ion flux we use Eq. 3.115. Let us replace there the integration variable x with ρ:

$$\int \mathrm{e}^{-x} r_*^2(x)\mathrm{d}x = -a^2\gamma\int \mathrm{e}^{-\gamma u(\rho)}\rho^2\frac{\mathrm{d}u}{\mathrm{d}\rho}\mathrm{d}\rho.$$

The integration limits are introduced by the product of Heaviside's step functions $\theta\left(u\left(\rho\right)\right)\theta\left(\psi\left(u\left(\rho\right)\right)\right)$. We have

$$\varepsilon(a)=\gamma\psi\left(\rho_u\right)-\gamma\int\limits_1^\infty \mathrm{e}^{-\gamma u(\rho)}\rho^2\frac{\mathrm{d}u}{\mathrm{d}\rho}\theta\left(u\left(\rho\right)\right)\theta\left(\psi\left(u\left(\rho\right)\right)\right)\mathrm{d}\rho, \tag{3.146}$$

where $u\left(\rho\right)$ is given by Eq. 3.142, ρ_u is the positive zero of this function, and

$$\rho^2\frac{\mathrm{d}u}{\mathrm{d}\rho}=-\frac{4\rho^3}{\left(\rho^2-1\right)^3}\mp\zeta+\frac{2\rho}{\varepsilon+1}\left[\frac{1}{\left(\rho^2-1\right)^2}+\frac{\varepsilon}{\varepsilon+1}S\left(\rho\right)\right]. \tag{3.147}$$

3.5.5 *Charging of Metallic and Small Dielectric Particles*

Less general and more observable results can be obtained for metallic particles $\varepsilon=\infty$ and small dielectric particles $a\ll\beta e^2$.

3.5.5.1 Neutral Particle + Ion

A neutral particle interacts with ions via image forces whose potential is always attractive ($Q=0$ and $\zeta=0$ in Eqs. 3.139, 3.140, 3.141, 3.142, 3.143, 3.144, 3.145, 3.146, 3.147, 3.148, 3.149, 3.150, 3.151, 3.152, 3.153, 3.154, 3.155, 3.156, 3.157, 3.158, 3.159).

We begin by considering a metallic particle ($\varepsilon\to\infty$, $S\left(\rho\right)=1/\rho^2\left(\rho^2-1\right)$). Equation 3.115 reduces to $u=\left(\rho_*^2-1\right)^{-2}$ and can be solved analytically to give

$$\rho_*^2(u)=1+\frac{1}{\sqrt{u}}. \tag{3.148}$$

From Eq. 3.145 we can find ψ:

$$\psi\left(\rho_*(u)\right)=u+2\sqrt{u}. \tag{3.149}$$

Equation 3.115 immediately leads to the familiar result (Natanson 1960):

$$\varepsilon(a)=\gamma\int\limits_0^\infty \mathrm{e}^{-\gamma u}\cdot\left(1+1/\sqrt{u}\right)\mathrm{d}u=1+\sqrt{\frac{\pi\beta q^2e^2}{2a}}. \tag{3.150}$$

For dielectric particles we must use the general result, Eqs. 3.146 and 3.147 with $\zeta=0$. However, some analytical results can be found in the limit of small particles $a\ll\beta e^2$. We will derive a two-term (approximate) formula similar to Eq. 3.148.

As a starting point, we use Eq. 3.115 rewritten in terms of the dimensionless variables:

$$\varepsilon(a) = \gamma \int_0^\infty \mathrm{e}^{-\gamma u} \cdot \rho_*^2(u)\mathrm{d}u. \tag{3.151}$$

It is possible to prove that $\psi\,(\rho_*(u))$ has no zeros at $u > 0$ and $\psi\,(\rho_*(0)) = 0$. Equation 3.149 confirms this statement.

At small a (large γ), small $u \propto 1/\gamma$ contributes to the integral on the right-hand side of Eq. 3.151. We thus must seek the roots of Eq. 3.143 in the limit of small u. As is seen from Eq. 3.148, small u corresponds to large ρ. The following approximations are used:

$$\frac{1}{\varepsilon+1} S\,(\rho) \approx \frac{1}{\varepsilon+2}\frac{1}{\rho^4} + \frac{2}{2\varepsilon+3}\frac{1}{\rho^6}$$

and

$$\frac{1}{(\rho^2-1)^2} \approx \frac{1}{\rho^4} + \frac{2}{\rho^6}.$$

Now we get

$$u = \frac{\varepsilon+1}{\varepsilon+2}\cdot\frac{1}{\rho^4} + 4\cdot\frac{\varepsilon+1}{2\varepsilon+3}\cdot\frac{1}{\rho^6} \tag{3.152}$$

In the lowest approximation we have

$$\rho_*^2(u) \approx \sqrt{\frac{\varepsilon+1}{(\varepsilon+2)\,u}}$$

To find the next approximation, we rearrange Eq. 3.152:

$$\rho^2 = \sqrt{\frac{\varepsilon+1}{(\varepsilon+2)\,u}}\cdot\sqrt{1+4\cdot\frac{\varepsilon+2}{2\varepsilon+3}\cdot\frac{1}{\rho^2}}$$

The last term under the square root on the right-hand side of this equation is small. Expanding the square root and replacing ρ^2 with its lowest approximation give

$$\rho_*^2(u) = 2\cdot\frac{\varepsilon+2}{2\varepsilon+3} + \sqrt{\frac{\varepsilon+1}{(\varepsilon+2)\,u}}$$

Table 3.1 The values of ρ_ε^2, $\psi\,(\rho_\varepsilon)$ (Eq. 3.125), u_ε, and $\rho_*^2\,(u_\varepsilon)$ (the set of Eqs. 3.158 at different dielectric permeability ε) and the ratio of particle-to-ion charges Q/q

ε	Q/q	ρ_ε^2	$\psi\,(\rho_\varepsilon)$	u_ε	$\rho_*^2\,(u_\varepsilon)$
2	1	1.615	8.994	3.902	1.737
3	1	1.777	6.447	2.402	1.959
5	1	1.926	5.136	0.1.684	2.174
∞	1	2.22	3.8	1.002	2.615
2	2	1.427	16.351	8.661	1.492
3	2	1.535	11.56	5.415	1.633
5	2	1.633	9.107	3.846	1.767
∞	2	1.821	6.617	2.331	2.037
2	1/2	1.894	5.05	1.718	2.117
3	1/2	2.139	3.673	1.041	2.47
5	1/2	2.369	2.96	0.721	2.817
∞	1/2	2.833	2.229	0.421	3.54

Now we come to the result similar to that for metallic particles (Eq. 3.150):

$$\varepsilon(a) \approx 2 \cdot \frac{\varepsilon+2}{2\varepsilon+3} + \sqrt{\frac{\pi\beta q^2 e^2}{2a} \cdot \frac{\varepsilon-1}{\varepsilon+2}}. \tag{3.153}$$

3.5.5.2 Opposite Polarities

No noticeable simplifications comes up at $\varepsilon = \infty$ (metallic particles).

The analytical results for arbitrary ε can be found for small particles. We again return to Eq. 3.115, rewritten in the dimensionless variables:

$$\varepsilon(a) = \psi\,(\rho_\varepsilon) + \gamma \int_0^\infty \mathrm{e}^{-\gamma u} \cdot \rho_*^2(u)\mathrm{d}u, \tag{3.154}$$

where ρ_ε is the zero of $u\,(\rho)$ at arbitrary ε. The first term is

$$\psi\,(\rho_\varepsilon) = \frac{2\zeta}{\rho_\varepsilon} + S\,(\rho_\varepsilon)\,. \tag{3.155}$$

At large γ, the integral on the right-hand side of Eq. 3.154 can be easily estimated, for again, small $u \propto 1/\gamma$ contributes to the integral. We have

$$\varepsilon(a) \approx \psi\,(\rho_\varepsilon)\,\gamma + \rho_\varepsilon^2 \ldots \tag{3.156}$$

The values of ρ_ε^2 and $\psi\,(\rho_\varepsilon)$ are collected in Table 3.1 for a number of values of the dielectric permeability ε.

3.5.5.3 Similar Polarities

For dielectric particles and the repulsive Coulomb potential, Eq. 3.113 gives

$$\varepsilon(a) = \gamma \int_0^\infty \mathrm{e}^{-\gamma u} \cdot \rho_*^2(u)\mathrm{d}u, \tag{3.157}$$

where u_ε and $\rho\,(u_\varepsilon)$ are the roots of the set of two simultaneous equations,

$$u - \frac{2\zeta}{\rho} + S\,(\rho) = 0$$

$$u = \frac{1}{(\rho^2-1)^2} + \frac{\zeta}{\rho} - \frac{1}{\varepsilon+1} \cdot S\,(\rho)\,. \tag{3.158}$$

At large γ, Eq. 3.157 gives

$$\varepsilon(a) \approx \mathrm{e}^{-\gamma u_\varepsilon} \cdot \rho_*^2\,(u_\varepsilon)\,. \tag{3.159}$$

So the problem is just to find u_ε and $\rho_*^2\,(u_\varepsilon)$. It is easy to do. The results are presented in Table 3.1.

3.5.6 Results and Discussion

We have proposed a comprehensive kinetic approach for studying the charging of dielectric aerosol particles in the free molecule regime. A compact exact expression is derived for the enhancement factor $\varepsilon(a)$ that shows how strong is the influence of the particle and ion charges on the efficiency of particle charging. In addition to the exact result (Eq. 3.146), we derived simplified asymptotic expressions for the enhancement factor. Our numerical analysis has shown that these expressions can be used up to particle sizes of the order of the Coulomb length $l_\mathrm{c} = \beta e^2$ with precision better than 5%. The most simple result has been obtained for charging a neutral particle. In this case the asymptotic result looks as follows (Eq. 3.153):

$$\varepsilon(a) \approx 2 \cdot \frac{\varepsilon+2}{2\varepsilon+3} + \sqrt{\frac{\pi\beta q^2 e^2}{2a} \cdot \frac{\varepsilon-1}{\varepsilon+2}}.$$

The dependencies of $\varepsilon(a)$ on the particle size at different dielectric permeabilities ε are displayed in Fig. 3.8. It is seen that the smaller the particle, the stronger the influence of the dielectric permeability.

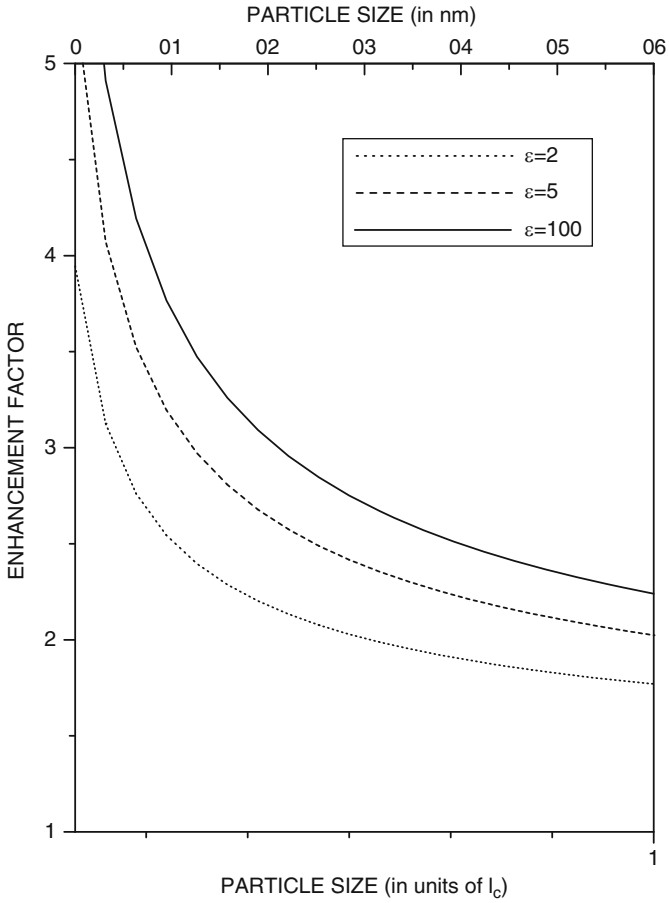

Fig. 3.8 Enhancement factor $\varepsilon(a)$ as the function of particle size for charging a neutral particle. *Lower horizontal axis* shows particle size in units of the Coulomb length $l_c = \beta e^2$

The particle–ion recombination is again described by Eq. 3.146. This formula can be used directly for the estimations, but for many practical purposes it is enough to use the simplified asymptotic result (Lushnikov and Kulmala 2004a):

$$\varepsilon(a) \approx \psi\left(\rho_u\right) \frac{\varepsilon - 1}{\varepsilon + 1} \cdot \frac{\beta e^2}{2a} + \rho_u^2 \ldots$$

Although this equation is derived for small particles $a \ll l_c$, the numerical analysis shows that it well reproduces the exact expression up to the sizes $a = l_c$. The dependence of the enhancement factor on the particle size is presented in Fig. 3.9 for a number of values of the dielectric permeability and equal values of

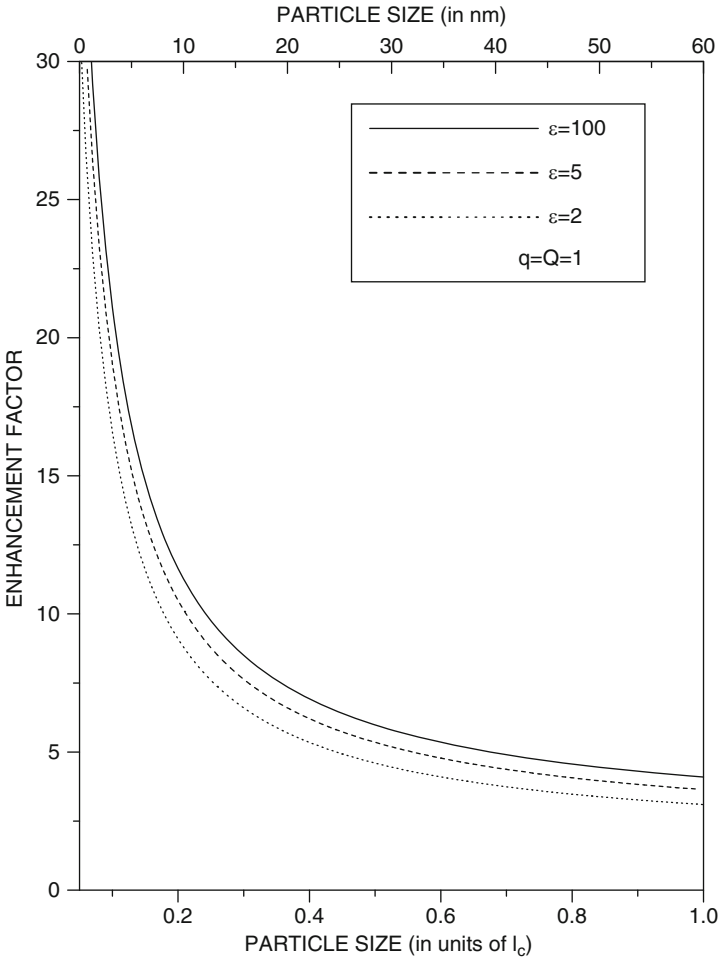

Fig. 3.9 Enhancement factor $\varepsilon(a)$ as the function of particle size for recombination of oppositely charged ion and particle. *Lower horizontal axis* shows particle size in units of the Coulomb length $l_c = \beta e^2$

charges $q = Q = 1$. It is seen that in this case the enhancement factor is less sensitive to the value of ε. Another factor, the ratio of charges, strongly affects the ion flux. This effect is shown in Fig. 3.10.

Similarly charged particles and ions are repelled, and the process of double charging is suppressed by the charge repulsion. This effect is shown in Figs. 3.11 and 3.12 for the same sets of ε and ζ as in Figs. 3.9 and 3.10. A single-term approximate formula describes this process:

$$\varepsilon(a) \approx \mathrm{e}^{-u_0\gamma} \cdot \rho_*^2\,(u_0)$$

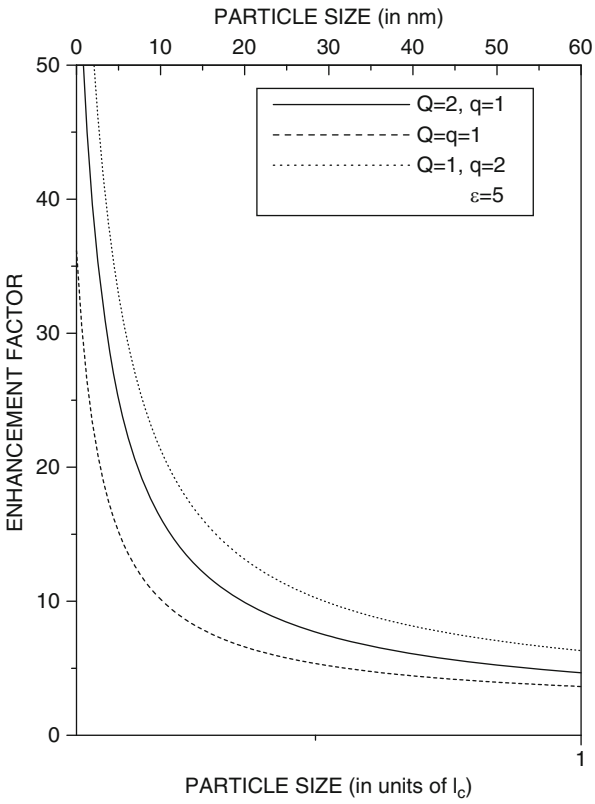

Fig. 3.10 Influence of particle (ion) charge on recombination efficiency. Shown are the enhancement factors $\varepsilon(a)$ as the function of the particle size at different particle and ion charges Q and q. *Lower horizontal axis* shows particle size in units of the Coulomb length $l_c = \beta e^2$

We have also obtained the analytical expression for the image potential (Eq. 3.131). The integral on the right-hand side of this expression can be expressed in terms of the hypergeometric function. At $\varepsilon = 1$ this integral is expressed in terms of elementary functions. The approximation Eq. 3.136 is very efficient. The numerical study shows that this approximation reproduces exact results with the precision 1% within $2 < \varepsilon < \infty$.

3.6 Particle Charging in the Transition Regime

Charging of small neutral and charged particles suspended in a weakly ionized plasma is investigated under the assumption that the Coulomb + image forces and diffusion contribute to the ion transport in the carrier plasma and define the rate of charging processes (Brock 1970; Burtcher and Schmidt-Ott 1985; Khachatourian and Wistrom 2001). Our approach is based on the flux-matching theory already described. The collisionless kinetic equation is solved, and the ion concentration profile in the free molecule zone (at distances less than the ion mean free path)

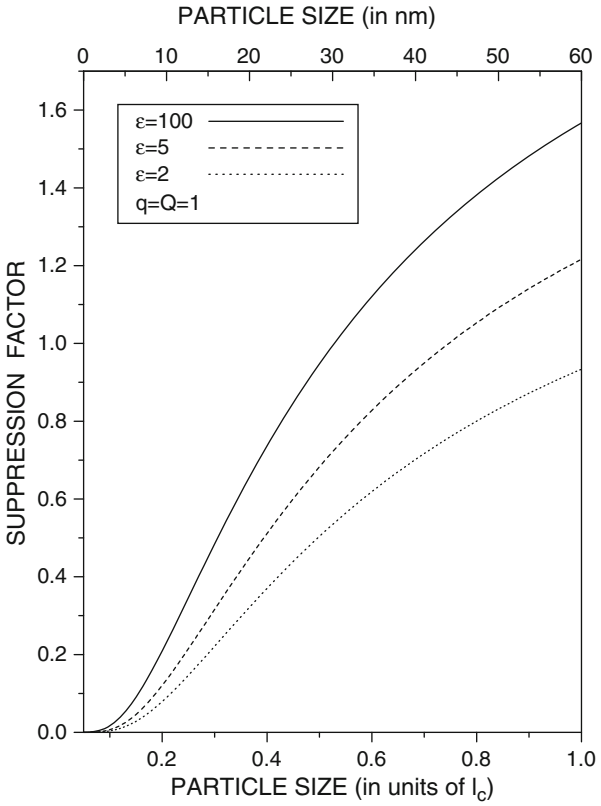

Fig. 3.11 Suppression factor $\varepsilon(a)$ as the function of particle size for double charging of similarly charged particles. *Lower horizontal axis* shows particle size in units of the Coulomb length $l_c = \beta e^2$

is found and then matched to that found in the diffusion limit. We introduce three matching parameters: the ion flux, the matching distance, and the ion density at the particle surface. Three conditions are formulated for fixing these parameters: (1) the constancy of the total ion flux, (2) the continuity of the ion concentration profile, and (3) the continuity of the derivative of the ion concentration profile. This approach is applied for calculating the efficiencies of particle charging in the transition regime (the particle size is comparable to the ion mean free path and the Coulomb distance $l_c = e^2/kT$).

3.6.1 Free Molecule Ion Distribution

Before constructing the general solution to the kinetic equation describing the motion of ions in the free molecule regime, we find first the interval of angular

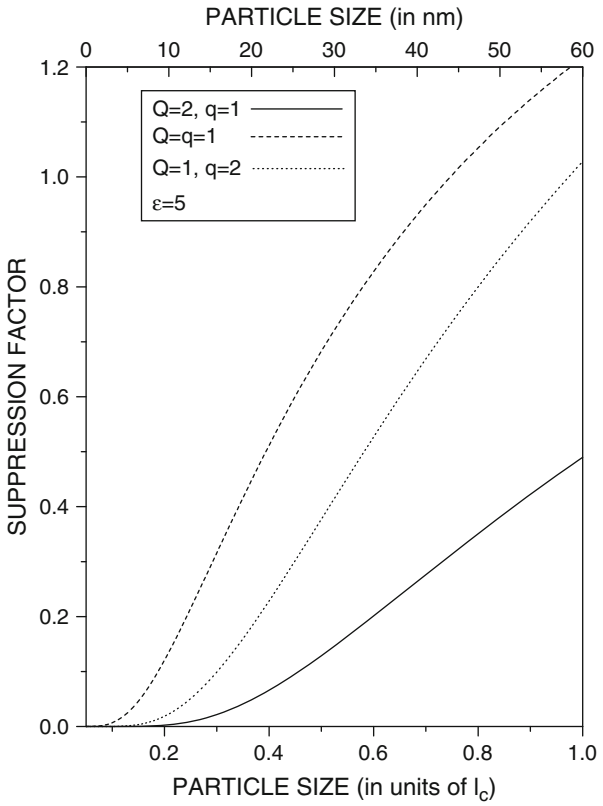

Fig. 3.12 Influence of particle (ion) charge on double charging efficiency. Shown are the suppression factors $\varepsilon(a)$ as the function of particle size at different particle and ion charges Q and q. *Lower horizontal axis* shows particle size in units of the Coulomb length $l_c = \beta e^2$

momenta corresponding to the ion trajectories intersecting the particle surface. The analysis becomes somewhat nontrivial because we consider the flux from a sphere of *finite* radius R. In what follows we introduce the notation L_a for the separating angular momentum (its value depends on the ion energy).

3.6.1.1 Nonsingular Attraction

Let us begin by considering attractive nonsingular potentials $|U(r)| \propto r^{-\alpha}$, $\alpha < 2$. The function $L^2(r) = 2mr^2\,(E - U(r))$ is shown schematically in Figs. 3.13 and 3.14 for $E > 0$ and $E < 0$. It is seen that ions with $L^2 < 2m(E - U(a))$ are able to reach the particle surface. At $E < 0$ the situation changes; if $2mR^2\,(-|E| + |U(R)|) < 2ma^2\,(-|E| + |U(a)|)$, then the trajectories with

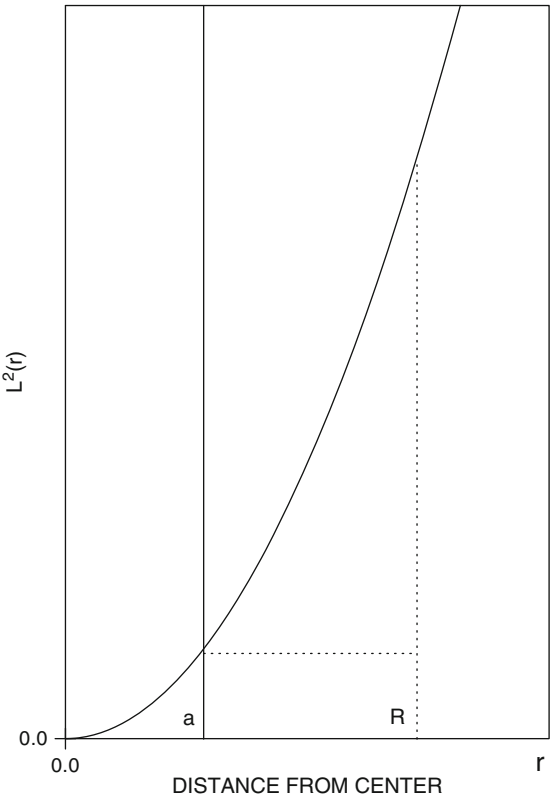

Fig. 3.13 Angular momentum $L^2(r)$ versus ion distance r from the center. At positive energies, $E > 0$, ions with $L < L(a)$ can reach the particle surface

$L^2 < 2mR^2\,(-|E| + |U(R)|)$ will cross the particle surface (see Fig. 3.14). Otherwise the restriction $L^2 < 2ma^2\,(-|E| + |U(a)|)$ works. Hence,

$$L_a^2 = min\left(L^2(a), L^2(R)\right)$$

for the attractive nonsingular potentials. The notation L_a stands for the angular momentum separating the trajectories crossing the particle surface from those passing aside.

It is easy to find that $L_a^2 = L^2(R)$ in the interval of energies ($E < 0$):

$$|U(R)| < |E| < E_0 = \frac{R^2|U(R)| - a^2|U(a)|}{R^2 - a^2}.$$

In the case of the Coulomb attraction, this interval is narrow:

$$\frac{e^2}{R} < |E| < \frac{e^2}{R + a}$$

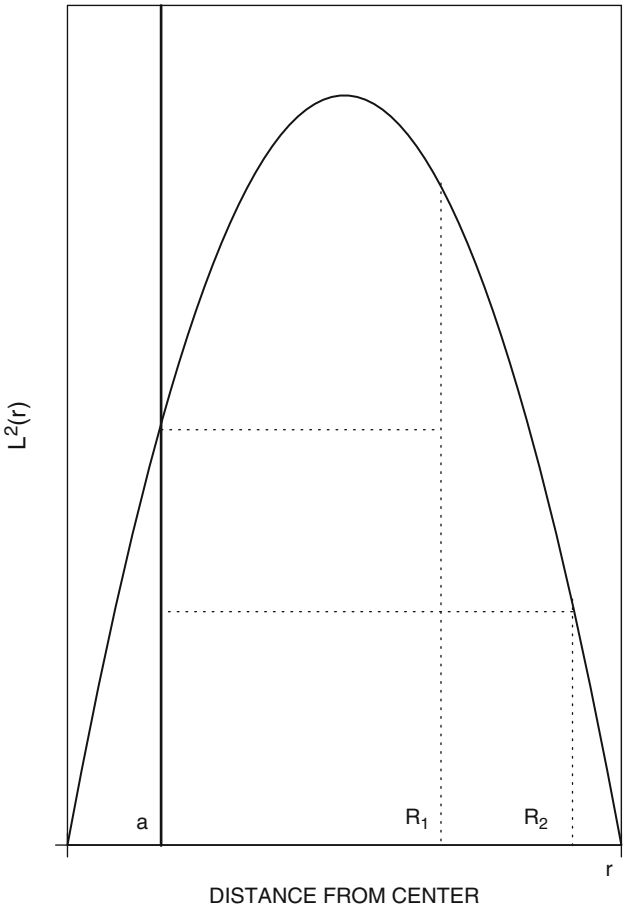

Fig. 3.14 Same as in Fig. 3.13. The energy is negative, $E < 0$. Now if $L(R) < L(a)$, the ions with $L < L(R)$ reach the particle surface

3.6.1.2 Singular Attraction

Let the interaction potential have a singularity at $r = a$ resembling the potential of image force. Figures 3.15 and 3.16 show schematically the situation in this case. When energy E is positive, function $L^2(r)$ has a minimum at $r = r_*$ located at $r > a$ and $L_a^2 = L^2(r_*)$. At negative E (see Fig. 3.16)

$$L_a^2 = min\left(L^2(r_*), L^2(R)\right)$$

where r_* is the solution to the equation

$$L(r_*) = L_a = min(L(r)), \quad r \geq a. \tag{3.160}$$

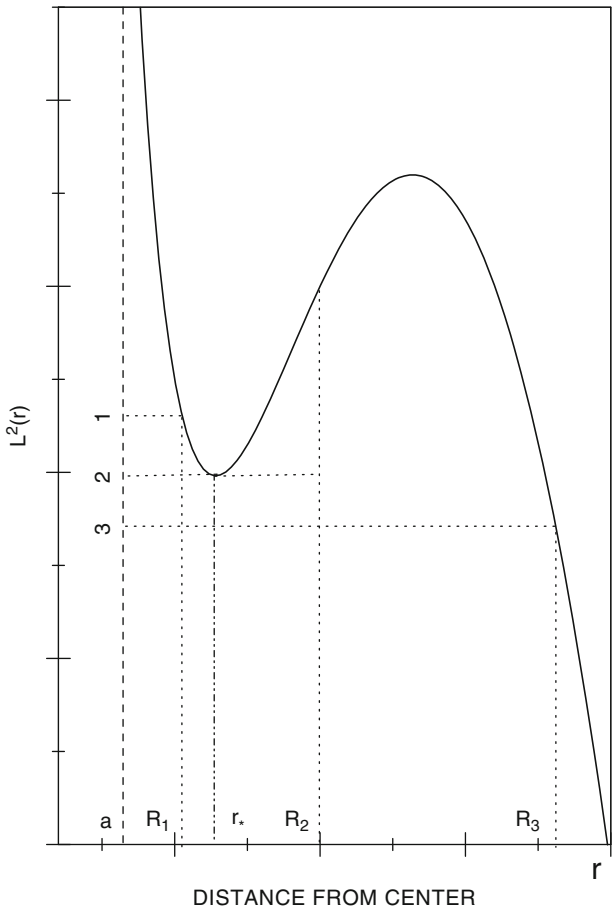

Fig. 3.15 Same as in Fig. 3.13. The energy is positive, $E > 0$. The ions with $L < L(r_*)$ reach the particle surface

Now the energy $E_0(E)$ depends on E

$$E_0(E) = \frac{R^2\,|U(R)| - r_*^2\,|U\,(r_*)|}{R^2 - r_*^2}$$

3.6.1.3 Repulsion + Singular Attraction

An example is the Coulomb repulsion + image potential (always attractive). Figure 3.15 explains what is happening. In this case the ions can reach the particle

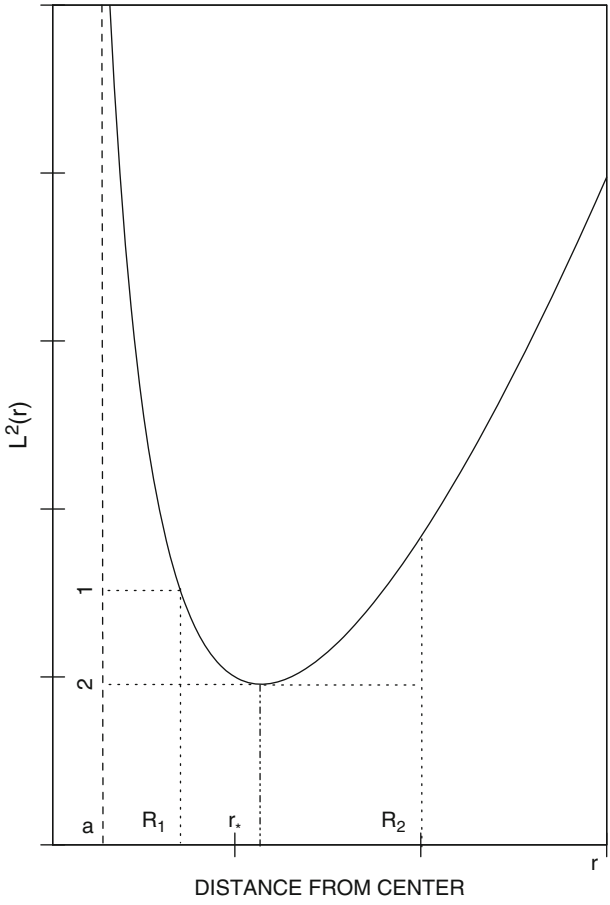

Fig. 3.16 Same as in Fig. 3.13. At negative energies, $E<0$, the situation is knottier. Ions with $L < L(r_*)$ reach the particle surface if $L(r_*) < L(R)$. Otherwise, only ions with $L < L(R)$ can reach the particle surface

surface only if the energy E exceeds the value defined by the conditions

$$\frac{\partial L^2(r)}{\partial r} = 0, \quad L^2(r) = 0$$

The energy is always positive at $E>0$, but the ion reaches the particle surface if E exceeds the threshold energy. Then the ions with $L < L(r_*)$ reach the particle surface.

No problem comes up for monotonous repulsion alone. In this case

$$L_a^2 = L^2(a) = 2ma^2\,(E - U(a))$$

The lower integration limit over E is always $U(r)$.

3.6.2 Solving the Kinetic Equation

The most general solution to Eq. 3.23 is

$$f_s(r, E, L) = B_s(E, L, R)\,\theta\left(L_{\mathrm{m}}^2(r) - L^2\right)\theta\left(L_{\mathrm{m}}^2(r)\right) \tag{3.161}$$

with $\theta(x)$ being the Heaviside step function and L_m the maximal admissible angular momentum. It is

$$L_{\mathrm{m}}^2(r) = L^2(r)$$

for repulsive and nonsingular attractive potentials at $E > 0$. At $E < 0$ (attractive potentials), the ions cannot occur in the states with $L > L_a$ at r, r_* (see Fig. 3.16). Then

$$L_{\mathrm{m}}(r) = L(r)\theta(r - r_*) + L_a\theta(r_* - r), \tag{3.162}$$

If, however, R, r_*, then a part of the trajectories that are able to reach the particle surface (with $L < L_a$) is populated as a result of ion diffusion. In this case (Fig. 3.17),

$$L_{\mathrm{m}}(r) = L(R).$$

The function $B_s(E, L, R)$ is defined by the boundary conditions $f_{-1}(a) = 0$ and has the form

$$B_s(E, L, R) = C(R)\mathrm{e}^{-\beta(E-U(R))}\theta(E - U(R))\left[\theta(L - L_a) + \delta_{s,-1}\theta(L_a - L)\right], \tag{3.163}$$

where the constant $C(R)$ is defined by the boundary condition at $r = Rn_{\mathrm{fm}}(R) = n_c(R)$ and $\delta_{i,k}$ is the Kroneker delta.

It is easy to see that the distribution in this form contains no outgoing ions at $r = a$, because the factor $\theta(L - L_a)$ in the first term does not permit trajectories crossing the point $r = a$. Hence, $f_1(a) = 0$. The factor $\theta(E - U(R))$ reflects the fact that no ions with the lower energy $U(R)$ can appear in the free molecule zone (such ions could appear only as a result of collisions with the carrier gas molecules). The structure of the expression in the square braces on the right-hand side of Eq. 3.163 provides the independence of the $s = -1$ component of the distribution on L_a, which means that all ions with $L < L(r)$ can move toward the particle center (but not all can reach the particle surface). The outgoing component f_1 does not contain the contribution from the trajectories crossing the particle surface.

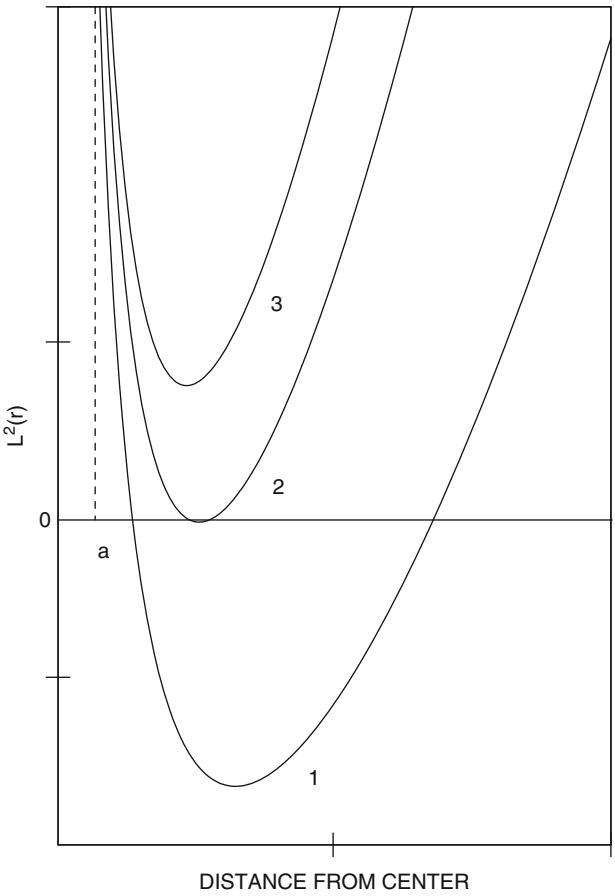

Fig. 3.17 Same as in Fig. 3.13. Energy is always positive, $E > 0$, but the ion reaches the particle surface if E exceeds the threshold energy. Then the ions with $L < L(r_*)$ reach the particle surface

It is of interest to have the solution corresponding to the ion sticking $\eta(E)$ depending on the ion energy.

$$B_s\left(E, L, R\right) = C(R)\mathrm{e}^{-\beta(E-U(R))}\theta\left(E - U(R)\right) \times \left[\theta\left(L - L_a\right) + \eta(E)\delta_{s,1}\theta\left(L_a - L\right) + \bar{\eta}(E)\delta_{s,-1}\theta\left(L_a - L\right)\right],$$

where

$$\eta(E) + \bar{\eta}(E) = 1$$

For example, we can put $\eta(E) = \theta\left(E - E_t\right)$, with E_t being a threshold energy. Then all collisions with the ion energies exceeding E_t will be ineffective. If $E_t = 0$, the ion capture goes only from bound states of the potential well. This solution allows us to find the efficiency of the ion recombination.

3.6.2.1 Ion Density Profile

Let us find the expression for the ion concentration profile $n(r)$ in the free molecule zone.

We begin by considering the attractive potentials. Equation 3.28 gives

$$n(r) = \frac{\pi C(R)}{m^2 r} \int\limits_{U(R)}^{\infty} \mathrm{d}E \cdot \mathrm{e}^{-\beta(E-U(R))} \int\limits_{0}^{L_{\mathrm{m}}^2} \frac{\mathrm{d}L^2}{\sqrt{L_{\mathrm{m}}^2(r) - L^2}} \left[1 + \theta\left(L - L_a\right)\right]$$

$$= \frac{2\pi C(R)}{m^2 r} \int\limits_{-|U(R)|}^{\infty} \mathrm{d}E \cdot \mathrm{e}^{-\beta(E+|U(R)|)} \left(L_{\mathrm{m}} + \sqrt{L_{\mathrm{m}}^2(r) - L_a^2}\right)$$

$$= \frac{2\pi\sqrt{2m}C(R)}{m^2} \int\limits_{-|U(R)|}^{\infty} \mathrm{d}E \cdot \mathrm{e}^{-\beta(E+|U(R)|)}$$

$$\times \left(\sqrt{E + |U(r)|} + \theta\left(r - r_*(E)\right)\theta\left(E + E_0(E)\right)\sqrt{E + |U(r)| - \frac{L_a^2}{2mr^2}}\right)$$

In what follows we omit $\theta\left(r - r_*(E)\right)$. It can be easily restored where it is needed. We thus have

$$n(r) = \left(\frac{2\pi}{m\beta}\right)^{3/2} C(R)\mathrm{e}^{-\beta|U(R)|} \cdot \frac{1}{\sqrt{\pi}} \int\limits_{-\beta|U(R)|}^{\infty} \mathrm{d}x \cdot \mathrm{e}^{-x} \left[\sqrt{x + \beta\,|U(r)|}\right.$$

$$\left. + \theta\left(E + |E_0(E)|\right)\sqrt{x + \beta\,|U(r)| - \left(x + \beta\,|U\left(r_*\right)|\right)\frac{r_*^2}{r^2}}\right], \tag{3.164}$$

where

$$C(R) = n(R)\left(\frac{m\beta}{2\pi}\right)^{3/2} \frac{2}{1 + \mathrm{e}^{-\beta|U(R)|}F(R)}, \tag{3.165}$$

with

$$F(R) = \frac{2}{\sqrt{\pi}} \int\limits_{-\beta|U(R)|}^{\infty} \mathrm{d}x \cdot \mathrm{e}^{-x}\theta\left(x + x_0\right)\sqrt{x + \beta\,|U(R)| - \left(x + \beta\,|U\left(r_*\right)|\right)\frac{r_*^2}{R^2}}, \tag{3.166}$$

where $x_0 = \beta|E_0|$.

For further needs we also introduce the functions $G_o(r,R)$ and $G_a(r,R)$ defined as

$$G_{\mathrm{o}}(r,R)=\frac{2}{\sqrt{\pi}}\int\limits_{-\beta|U(R)|}^{\infty}\mathrm{d}x\cdot\mathrm{e}^{-x}\sqrt{x+\beta\,|U(r)|}.$$

$$G_a(r,R)=\frac{2}{\sqrt{\pi}}\int\limits_{-\beta|U(R)|}^{\infty}dx\cdot e^{-x}\theta\left(r-r_*\right)\theta\left(x+x_0\right)\times\sqrt{x+\beta\,|U(r)|-\left(x+\beta\,|U\left(r_*\right)|\right)\frac{r_*^2}{r^2}}.$$

Using the identities $F(R)=G_a(R,R)$ and $G_{\mathrm{o}}(R,R)=\mathrm{e}^{\beta|U(R)||}$ yields

$$n(r)=\frac{n(R)}{1+e^{-\beta|U(R)|}F(R)}e^{-\beta|U(R)|}\left[G_o(r,R)+G_a(r,R)\right]. \tag{3.167}$$

In the case of repulsion, the conditions $L^2(r)>0$ and $L^2(a)>0$ determine the lower limits of integration in the expression for $n(r)$. Following the route of derivation of Eq. 3.164 we obtain

$$n(r)=\left(\frac{2\pi}{m\beta}\right)^{3/2}C(R)\mathrm{e}^{\beta U(R)}\cdot\frac{1}{\sqrt{\pi}}\left[\int\limits_{\beta U(r)}^{\infty}\mathrm{d}x\cdot e^{-x}\sqrt{x-\beta U(r)}+\int\limits_{\beta U(a)}^{\infty}\mathrm{d}x\cdot e^{-x}\sqrt{x-\beta U(r)-\left(x-\beta U(a)\right)\frac{a^2}{r^2}}\right],$$

where, again, $C(R)$ is given by Eq. 3.165. The definitions of $F(R)$, G_o, and G_a change. Instead of Eq. 3.166 we have

$$F_{\mathrm{rep}}(R)=\frac{2}{\sqrt{\pi}}\int\limits_{\beta U(a)}^{\infty}dx\cdot\mathrm{e}^{-x}\sqrt{x-\beta U(R)-\left(x-\beta U(a)\right)\frac{a^2}{R^2}}.$$

Next,

$$G_{\mathrm{o}}(r,R)=\frac{2}{\sqrt{\pi}}\int\limits_{\beta U(r)}^{\infty}\mathrm{d}x\cdot\mathrm{e}^{-x}\sqrt{x-\beta U(r)}=e^{-\beta U(r)},$$

$$G_a(r,R) = \frac{2}{\sqrt{\pi}} \int\limits_{\beta U(a)}^{\infty} \mathrm{d}x \cdot \mathrm{e}^{-x} \sqrt{x - \beta U(r) - (x - \beta U(a))\,\frac{a^2}{r^2}}.$$

Using the identities $F(R) = G_a(R,R)$ and $G_o(R,R) = e^{-\beta U(R)}$ yields again

$$n(r) = \frac{n(R)}{1 + \mathrm{e}^{\beta U(R)} F(R)} \mathrm{e}^{\beta U(R)} \left[\mathrm{e}^{-\beta U(r)} + G_a(r,R)\right].$$

3.6.3 Flux and Charging Efficiency

The expression for the flux follows from Eq. 3.29:

$$J(a,R,n_R) = \frac{4\pi^2}{m^3} C(R) \int\limits_{-|U(R)|}^{\infty} \mathrm{e}^{-\beta(E+|U(R)|)} L_a^2 dE. \tag{3.168}$$

Hence,

$$\begin{aligned}\alpha_{\mathrm{fm}}(a,R) &= \frac{8\pi^2}{m^3} \cdot \left(\frac{m\beta}{2\pi}\right)^{3/2} \frac{1}{1 + \mathrm{e}^{-\beta|U(R)|} F(R)} \int\limits_{-\beta|U(R)|}^{\infty} \mathrm{e}^{-\beta(E+\beta|U(R)|)} L_a^2 \mathrm{d}E \\ &= \frac{2\alpha_o}{1 + \mathrm{e}^{-\beta|U(R)|} F(R)}. \end{aligned} \tag{3.169}$$

Dependence on the matching distance R is clearly seen. It enters via the multiplier $1/(1 + F(R))$ and in the lower limit of the integral. The latter fact means that the bound states of ions in the potential $U(r)$ are taken into account. The value α_o differs from α_{fm} by the lower limit of integration over E ($-|U(R)|$ instead of 0).

In the case of nonsingular repulsion, the result looks as follows:

$$\begin{aligned}\alpha_{\mathrm{fm}}(a,R) &= \frac{8\pi^2}{m^3} \cdot \left(\frac{m\beta}{2\pi}\right)^{3/2} \frac{1}{1 + \mathrm{e}^{\beta U(R)} F_{\mathrm{rep}}(R)} \int\limits_{-\beta U(R)}^{\infty} \mathrm{e}^{-\beta(E-U(R))} L_a^2 \mathrm{d}E \\ &= \frac{2\mathrm{e}^{\beta U(a)} \alpha_{\mathrm{fm}}(a)}{1 + \mathrm{e}^{\beta U(R)} F_{\mathrm{rep}}(R)}. \end{aligned}$$

3.6.3.1 Matching Distance

Here we use Eq. 3.12 for deriving the equation defining the matching distance R. Substituting Eq. 3.164 into Eq. 3.12 yields

$$\left.\frac{\partial \ln n_J}{\partial r}\right|_R = \frac{\mathrm{e}^{-\beta|U(R)|}}{1+\mathrm{e}^{-\beta|U(R)|}F(R)}\frac{\partial}{\partial r}\left[G_o\left(r,R\right)+G_a\left(r,R\right)\right]\Big|_{r=R} \tag{3.170}$$

From Eqs. 3.12 and 3.169 it is not difficult to find that

$$\left.\frac{\partial \ln n_J}{\partial r}\right|_R = \beta|U(R)|' + \frac{\alpha_o(a)}{2\pi D R^2}\cdot\frac{1}{1+\mathrm{e}^{-\beta|U(R)|}F(R)} \tag{3.171}$$

In deriving Eq. 3.171 we used the inversion of Eq. 3.9:

$$\alpha\left(a,R\right) = \frac{\alpha(a)\mathrm{e}^{\beta U(R)}}{1-\frac{\alpha(a)}{4\pi D}\int\limits_R^\infty \frac{\mathrm{e}^{\beta U(r')}\mathrm{d}r'}{r'^2}}$$

Now we must find the derivatives of G_o and G_a. We will do this first for a nonsingular attractive potential. From the definition of G_o we find

$$\left.\frac{\partial G_\mathrm{o}\left(r,R\right)}{\partial r}\right|_{r=R} = \mathrm{e}^{\beta|U(R)|}\beta|U(R)|'$$

Next (see the definition of E_o),

$$\left.\frac{\partial G_a(r,R)}{\partial r}\right|_{r=R} = \beta|U(R)|'\frac{1}{\sqrt{\pi}}\int\limits_{-\beta|U(R)|}^\infty \frac{\mathrm{d}x\cdot\mathrm{e}^{-x}\theta\left(x+x_0\right)}{\sqrt{x+x_0}\cdot\sqrt{1-\frac{r_*^2}{R^2}}}$$

$$+\frac{2}{\sqrt{\pi}}\int\limits_{-\beta|U(R)|}^\infty \frac{\mathrm{d}x\cdot\mathrm{e}^{-x}\left(x+\beta\left|U\left(r_*\right)\right|\right)\frac{r_*^2}{R^3}\theta\left(x+x_0\right)}{\sqrt{x+x_0}\cdot\sqrt{1-\frac{r_*^2}{R^2}}}$$

$$F(R) = \frac{2}{\sqrt{\pi}}\int\limits_{-\beta|U(R)|}^\infty \mathrm{d}x\cdot\mathrm{e}^{-x}\theta\left(x+x_0\right)\sqrt{x+x_0}\cdot\sqrt{1-\frac{r_*^2}{R^2}}$$

For nonsingular potentials this expression simplifies

$$\left.\frac{\partial G_a\left(r,R\right)}{\partial r}\right|_{r=R} = \frac{\mathrm{e}^{\beta|E_0|}}{\sqrt{1-\frac{a^2}{R^2}}}\left[\beta|U(R)|' + \frac{a^2}{R^3}\left(1+2\left(\beta\left|U(a)\right|-\beta\left|E_0\right|\right)\right)\right]$$

$$F(R) = \mathrm{e}^{\beta E_0}\sqrt{1-\frac{a^2}{R^2}}$$

The equation for determining R takes the form (nonsingular case)

$$\frac{\alpha_{\mathrm{o}}(a,R)}{2\pi DR} = \frac{1}{\sqrt{1-\frac{a^2}{R^2}}}\mathrm{e}^{-\beta\Delta}\frac{a^2}{R^2}\left[\beta|U(R)|'R + (1+2\beta(|U(a)|-|E_0|)\right], \tag{3.172}$$

where

$$\Delta = |U(R)-E_0| = \frac{a^2}{R^2-a^2}(|U(a)|-|U(R)|).$$

Now our task is to find α_o. A trivial but tedious algebra yields

$$\alpha_o(a,R) = \pi a^2 v_T \mathrm{e}^{-\beta\Delta}\left[1+\beta|U(a)|+\beta|E_0|+\frac{R^2}{a^2}\left(\mathrm{e}^{\beta\Delta}-1-\beta\Delta\right)\right]$$

Once the matching distance is known as a function of the particle size, it is easy to find the charging efficiencies for any potential. We therefore begin with the analysis of the dependencies of $R = R(a)$ and then present the results on the dependence of the charging efficiencies on particle sizes for the potentials given by Eq. 3.102.

The equation describing the dependence of the matching distance on the particle size for $U(r) = 0$ has the structure,

$$R(a) = \sqrt{R_o^2(a)+a^2}, \tag{3.173}$$

with

$$R_0(a) = \frac{2D}{v_T}. \tag{3.174}$$

The value of $R_o(a)$ is independent of a, so at very small particle size the matching distance is of the order of the molecular mean free path, as has been expected. At large particle size $a \gg l$ the difference $R(a) - a \propto l$.

When the ion–particle interaction is turned on, the analysis becomes more complex. It can be done only numerically, but first we analyze the behavior of the function $R(a)$ at small $a \ll l, l_c$. In our analysis we assume that $U(a) \to \infty$ as $a \to 0$.

Let us begin with the attractive potentials. At small particle size, $\alpha_0 \approx \pi a^2 v_T$ $\beta|U(a)|$ (the leading term in $U(a)$ is retained). The term of the same order of magnitude on the right-hand side of Eq. 3.172 is $2\beta|U(a)|\left(a^2/R^2\right)$. Equation 3.172 then gives

$$R(a) \approx \frac{4D}{v_T}. \tag{3.175}$$

Again, in the limit of small a the matching distance is of the order of the ion mean free parts and independent of the particle size. Moreover, it is independent of the ion–particle potential.

In the limit of large particles $a \gg l$ the left-hand side of Eq. 3.172 becomes large, which can happen because of the growth of the expression under the square root on the right-hand side of this equation when R approaches a. Our numerical analysis showed that the solution to Eq. 3.172 can be well approximated by the formula of the type of Eq. 3.173, with

$$R_0(a) = \frac{2D}{v_T} \cdot \frac{1 + 2\beta\,|U(a)|}{1 + \beta\,|U(a)|}. \tag{3.176}$$

Let us now analyze the repulsive potentials. In the limit of small a the leading term on the right-hand side of the equation for R is small as $1|\sqrt{\delta} \propto 1|\sqrt{\beta U(a)}$. Then at small a ($q = Q = 1$),

$$R \approx \pi^{-1/4}(2D/v_T)^{1/2} l_c^{1/4} a^{1/4} \left[\frac{2\,(\varepsilon + 2)}{\varepsilon + 5}\right]^{1/4}. \tag{3.177}$$

The dependence of the matching distance $R(a)$ on the particle size is shown in Fig. 3.18 for the potentials given by Eq. 3.102 with $\varepsilon = 4$ and $q = Q = 1$.

In contrast to zero or attractive potentials, where the matching distance has the order of the ion mean free path and does not depend on the particle size, ion–particle repulsion leads to the matching distances decreasing with diminishing particle size. From first sight this fact is very unpleasant, for the diffusion approximation cannot work at distances much smaller than the ion mean free path. On the other hand, the dependence of $R(a)$ is very weak, and even for $a = 1nm$ R is comparable with the ion mean free path.

3.6.3.2 Very Small Particles

Let us first analyze Eq. 3.172 in the limit of small a for the Coulomb attraction, $\beta\,|U(r)| = l_c/r$, where $l_c = \beta e^2$ is the Coulomb distance ($l_c \propto l$). As is seen from Eq. 3.172

$$\alpha_o \approx \pi a l_c.$$

Hence,

$$\frac{\pi a l_c v_T}{2\pi D R} = 2\frac{a l_c}{R^2}$$

or

$$R = \frac{4D}{v_T}$$

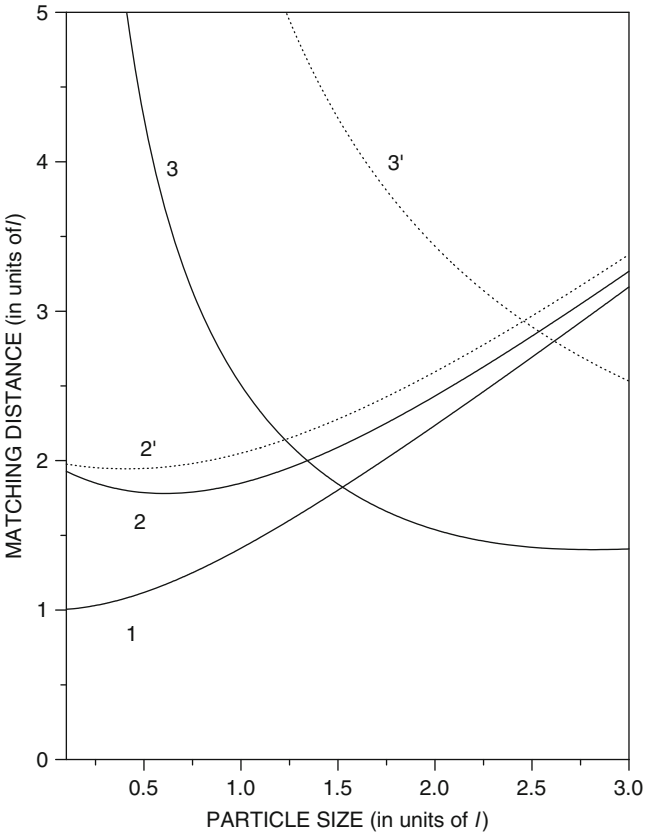

Fig. 3.18 Dependence of matching distance $R(a)$ on particle radius a. The scale of both axes is $l = 2D/v_T$, the ion mean free path. *Curve 1* shows the function $R(a)$ for the potential-free condensation. *Curves 2 and 2′* are the matching distances for the attractive potential at different Coulomb lengths, $l_c = l$ (*solid line*) and $l_c = 3$ (*dotted line*). *Curves 3 and 3′* display the same for the repulsive potential

This consideration shows that the value of R is of the order of the mean free path l. If we assume that the interaction contains a long-range potential, such as the Coulomb potential, which is sufficiently strong at distances of the order of l or more, and is short range potential effective at shorter distances (of the order of a), then it is possible to find a general expression for R. The behavior of the short-range potential at short distances is of no importance for the derivation described next. It can be even singular at $r = a$.

It is clear what to do. We introduce an effective particle radius a_* that is defined from a specially formulated asymptotic condition imposed on $n(r)$.

Let us introduce $G_{a*}(r, R)$,

$$G_{a*}(r, R) = \frac{2}{\sqrt{\pi}} \int\limits_{-\beta|U(R)|}^{\infty} \mathrm{d}x \cdot \mathrm{e}^{-x} \theta(x + x_0) \sqrt{x + \beta |U(r)| - (x + \beta |U(a_*)|) \frac{a_*^2}{r^2}},$$

where a_* is independent of E. Next, we present $G_a(r, R)$ in the form

$$G_a(r, R) = [G_a(r, R) - G_{a*}(r, R)] + G_{a*}(r, R)$$

We define a_* from the condition that the expansion of the difference in the square braces would not contain the term $\propto a^2/r^2$.

Now it is easy to find that

$$[G_a(r, R) - G_{a*}(r, R)] = \frac{2}{\sqrt{\pi}} \frac{1}{r^2} \int\limits_{-\beta|U(R)|}^{\infty} \mathrm{d}x \cdot \mathrm{e}^{-x} \theta(x + x_0)$$

$$\frac{r_*^2 (x + |U(r_*)|) - a_*^2 (x + |U(a_*)|)}{\sqrt{x + \beta |U(r)| - (x + \beta |U(r_*)|) \frac{r_*^2}{r^2}} + \sqrt{x + \beta |U(r)| - (x + \beta |U(a_*)|) \frac{a_*^2}{r^2}}}$$

Now we neglect all terms contributing additional negative powers of r or R. We thus neglect the contribution of the bound states (the lower limit of integration is replaced by 0), and we neglect the terms containing the ratio a^2/r^2 in the denominator. We find then

$$[G_a(r, R) - G_{a*}(r, R)(r, R)] = \frac{1}{\sqrt{\pi}} \frac{1}{r^2} \int\limits_{-\beta|U(R)|}^{\infty} \mathrm{d}x \cdot \mathrm{e}^{-x} \theta(x + x_0)$$

$$\times \frac{r_*^2 (x + |U(r_*)|) - a_*^2 (x + |U(a_*)|)}{\sqrt{x + \beta |U(r)|}}$$

We can also neglect all terms containing $U(r)$ and $U(R)$, for they also introduce additional negative powers of R. We finally find

$$\frac{1}{\sqrt{\pi}} \int\limits_0^{\infty} \frac{r_*^2 U(r_*) \mathrm{e}^{-x}}{\sqrt{x}} \mathrm{d}x = a_*^2 U(a_*)$$

3.6.3.3 Short-Range Potentials

The consideration remains simple for the weak potentials such that $\beta U(R) \ll 1$. In this case the function $F(r)$ at large $r \gg a$ behaves as in the case of free condensation with the particle radius replaced by ηa, where the modifier η depends on the details of the potential and

$$F(R) = \sqrt{1 - \frac{\zeta^2 a^2}{R^2}}. \tag{3.178}$$

Let us introduce $z(a)$, the free molecule enhancement factor

$$z(a) = \frac{\alpha_{\text{fm}}(a)}{\pi a^2 v_T}. \tag{3.179}$$

We obtain,

$$\frac{z(a) v_T a^2}{2DR^2} = \frac{\zeta^2 a^2}{2R^3 \sqrt{1 - \frac{\zeta^2 a^2}{R^2}}} \tag{3.180}$$

On solving Eq. 3.180 gives

$$R = \sqrt{\left(\frac{2D\zeta^2}{z(a) v_T}\right)^2 + \zeta^2 a^2}. \tag{3.181}$$

and

$$\alpha(a) = \frac{2\pi a^2 v_T z(a)}{1 + \sqrt{1 + \left(\frac{a v_T z(a)}{2D\zeta^2}\right)^2}} \tag{3.182}$$

It is possible to find $\zeta(a)$. To this end we simplify $F(R)$ by ignoring $U(R)$ and replacing the lower limit of integration by 0. After these simplifications we find

$$F(R) = \frac{2}{\sqrt{\pi}} \int_0^\infty \mathrm{d}x \cdot \mathrm{e}^{-x} \sqrt{x - (x + \beta \left| U\left(r_*\right)\right|) \frac{r_*^2}{R^2}}$$

$$\approx \frac{2}{\sqrt{\pi}} \int_0^\infty \mathrm{d}x \cdot \mathrm{e}^{-x} \sqrt{x} \left(1 - \frac{1}{2}\left(1 + \frac{\beta \left| U\left(r_*\right)\right|}{x}\right) \cdot \frac{r_*^2}{R^2}\right)$$

Comparing this expression with the expansion of the square root on the right-hand side of Eq. 3.178 gives

$$\zeta^2 = \frac{2}{\sqrt{\pi}} \int_0^\infty \mathrm{d}x \cdot \mathrm{e}^{-x} \sqrt{x} \left(1 + \frac{\beta \left|U\left(r_*\right)\right|}{x}\right) \frac{r_*^2}{a^2}$$

For nonsingular attractive potentials ($r_* = a$), this equation permits us to obtain the rather general result

$$\zeta^2 = 1 + 2\beta \left|U(a)\right|$$

3.6.3.4 Charging of Neutral Particles

Let us consider the ion flux toward a neutral metallic particle. The incident ions interact with the particle via the image potential

$$U(r) = -\frac{e^2}{2a} \cdot \frac{a^4}{r^2\left(r^2 - a^2\right)} \tag{3.183}$$

It is seen that at $a \propto l$ the potential is very weak, $\beta U(l) \propto \beta e^2 a^3/l^4 \propto l_\mathrm{c} a^3/l^4$, where $l_\mathrm{c} = e^2/kT$ is the Coulomb length. Normally $l_\mathrm{c} \propto l$. Hence, we can use Eq. 3.182 for calculating the charging efficiency.

The function $z(a)$ is known:

$$z(a) = 1 + \sqrt{\frac{\pi\beta e^2}{2a}}, \tag{3.184}$$

For metallic particles, ζ^2 is

$$\frac{r_*^2}{a^2} = 1 + \sqrt{\frac{\beta e^2}{ax}}$$

Substituting this expression into Eq. 3.183 gives

$$\zeta^2 = 1 + \sqrt{\frac{2\beta e^2}{\pi a}}$$

3.6.3.5 Charging Efficiencies

For charged particles the general result, Eq. 3.10, should be used. The approximations Eqs. 3.11 and 3.12 allow us to express $\alpha(a)$ in terms of the charging efficiency $\alpha_\mathrm{fm}(a, R)$ found in the free molecule limit and the matching distance R.

$$\alpha(a) = \frac{\alpha_{\rm fm}\,(a, R)\,{\rm e}^{-\beta U(R)}}{1 + \frac{\alpha_{\rm fm}(a,R){\rm e}^{-\beta U(R)}}{4\pi D} \int\limits_{R}^{\infty} {\rm e}^{\beta U(r')} \frac{dr'}{r'^2}}, \tag{3.185}$$

The numerical calculations were performed for the potential from Lushnikov and Kulmala (2004a) that includes Coulomb + image forces with $q = Q = 1$ and $l_{\rm c} = l$ or $l_{\rm c} = 3l$.

The results are presented in Figs. 3.19 and 3.20 in terms of the correction factors $\xi(a)$, the ratios of the charging efficiencies found from Eq. 3.176 to their values in the free molecule regime.

$$\xi(a) = \frac{\alpha(a)}{\alpha_{fm}(a)}, \tag{3.186}$$

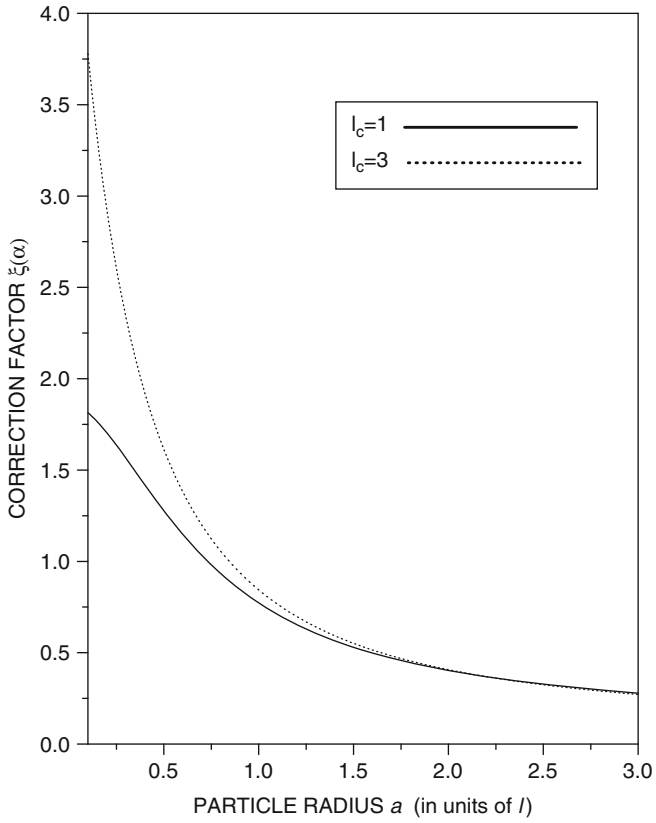

Fig. 3.19 Correction factor $\xi(a) = \alpha(a)/\alpha_{fm(a)}$ for ion–particle recombination as a function of particle radius (in units of $l = 2D/v_T$). *Solid and dotted curves* display $R(a)$ for $l_c = 1$ and $l_c = 3$, respectively. It is seen that even at small particle sizes these curves deviate from unity; i.e., the free molecule approximation is noticeably corrected by ion–carrier gas interaction $l_c \propto l$

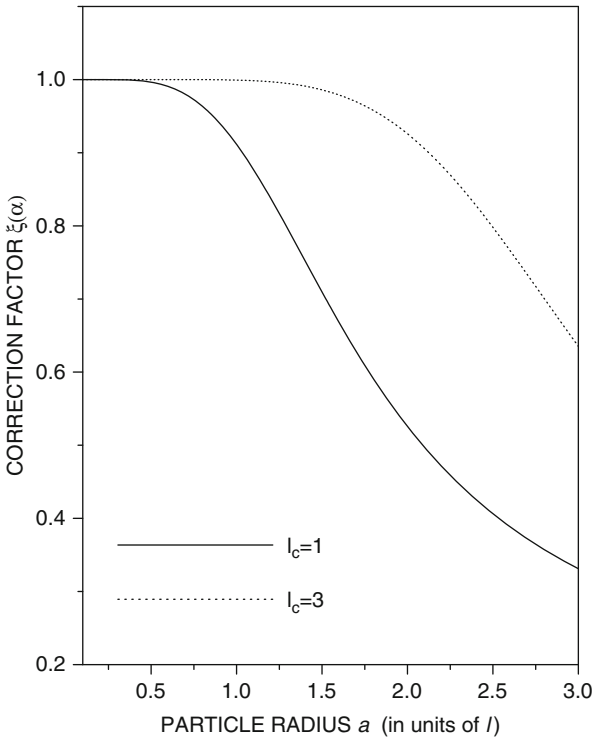

Fig. 3.20 Same as in Fig. 3.19, but for repulsive potential. In contrast to attraction, in this case the free molecule limit works even when the particle size is comparable to the ion mean free path

where $\alpha_{\rm fm}(a) = \alpha_{\rm fm}(a, R = \infty)$.

Let us analyze the expression for charging efficiency (Eq. 3.185) in the free molecule limit $a \ll l$. First, we notice that at $a \ll l$ the denominator in Eq. 3.185 can be always replaced by unity. Then for the recombination rate Eq. 3.175 gives

$$\alpha(a) \approx \pi a^2 v_T \left[1 + \beta |U(a)| + \beta |U(4D/v_T)|\right] \mathrm{e}^{\beta |U(4D/v_T)|} \tag{3.187}$$

To obtain the widely cited free molecule limit $\alpha(a) = \pi a^2 v_T [1 + \beta U(a)]$, the term $\beta U(4D/v_T)$ should be small compared to 1. The inequality $\beta U(4D/v_T) \ll 1$ does not hold for the Coulomb potential at ambient conditions. Indeed, $l_c = \beta e^2 \approx 6 \cdot 10^{-6}$cm $\approx l$. For the attractive potential given by Eq. 3.1 one finds

$$\alpha(a) \approx \pi a^2 v_T \times \left[1 + qQ\frac{l_c}{a}\left(1 + \frac{q}{2Q} \cdot \frac{\varepsilon - 1}{\varepsilon + 2}\right) + qQ\frac{l_c v_T}{4D}\right] \mathrm{e}^{qQl_c v_T/4D}. \tag{3.188}$$

Figure 3.19 clearly demonstrates the role of the Coulomb distance in the case of the Coulomb attraction. It is seen that even at small particle sizes $a \ll l$ the

free molecule expression for the ion–particle recombination does not work. On the other hand, no modifications related to the Coulomb interaction appear in the case of repulsive potential. The free molecule formula works for small particles ($a \ll l_c$) and only when the particle size becomes comparable to the Coulomb distance do the corrections become perceptible.

In the case of repulsion nothing interesting appears. Equation 3.185 reproduces the well-known free molecule limit

$$\alpha(a) \approx \pi a^2 v_T \mathrm{e}^{-\beta U(a)}. \tag{3.189}$$

Indeed, at small particle sizes α_{fm} has the form

$$\alpha_{\mathrm{fm}}(a) \approx \pi a^2 v_T \mathrm{e}^{-\beta U(a)} \mathrm{e}^{\beta U(R)}. \tag{3.190}$$

On substituting this expression into Eq. 3.185, one comes to Eq. 3.189.

At large a, Eq. 3.185 always reproduces the diffusion limit

$$\alpha_{\mathrm{diff}}(a) = \frac{4\pi D}{\int\limits_a^\infty r^{-2} \mathrm{e}^{\beta U(r)} \mathrm{d}r}. \tag{3.191}$$

3.6.4 Recombination

The important role of charging processes in aerodisperse systems had been recognized long ago (Natanson 1959, 1960). More or less reliable expressions for particle charging efficiencies had been found only for neutral particles. The case of particle–ion recombination remained, and still remains, open for further theoretical attacks. The nature of the difficulty is the necessity for the incident ion to loose a part of its kinetic energy. This process goes only in the presence of a third body (normally a carrier gas molecule). The respective expression for the recombination efficiency should thus depend on the density of the carrier gas. It is quite clear that the recombination process goes at the distances not exceeding the ion mean free path. Next, on colliding with a third body the ion should occupy sufficiently deep energy levels; otherwise, the lifetime of a loosely bounded dipole (ion + particle) with respect to the collisions with the molecules of the carrier gas becomes very short. So far the parameters, the recombination distance, and energy have been introduced by hand. The goal of this subsection is to demonstrate how this arbitrariness can be removed. The flux-matching theory allows one to introduce and to define the radius of the limiting sphere, which in the limit of very small particle sizes depends only on the ion diffusivity in the carrier gas. This radius has the order of the ion mean free path. Next, this theory allows for taking into account the contribution of the ion

bound states. However, the contribution of these states is dependent on the particle size. The reason for this lies in the fact that in the free molecule zone the incident ion is assumed not to experience any collisions with the carrier gas molecules and thus eventually returns back to the diffusion zone. Hence, according to this theory only the trajectories intersecting the particle surface are able to contribute to the recombination efficiency. Meanwhile, ion states lying deeper in the Coulomb energy at the separation distance should contribute to recombination efficiency independent of particle size. The chance for the ion to return to the state with higher energies is negligibly small. Here we report on an attempt to apply this flux-matching theory for determining the efficiency of ion–particle recombination. We assume that the three-body trapping becomes efficient only inside the limiting sphere. We thus solve the kinetic equation in the free molecule zone assuming that the ion can loose a part of its energy and thus be trapped by the particle. The rate of the losses is introduced and is considered to be known. In principle, its value can be found from the solution of the Boltzmann equation for the ion moving in the Coulomb field. Here we estimate this constant from the data on the ion–ion recombination. Hence, our theory includes three steps. We first solve the diffusion equation for the ion moving in the Coulomb field created by the particle. Instead of the boundary condition to this diffusion equation, we introduce the value of the ion flux toward the target particle. Then, we solve the Boltzmann equation that takes into account only the losses of ions caused by the three-body trapping. Their returns to states with higher energies are ignored. The next step assumes the calculations of the ion profiles in the diffusion and free molecule zones and their first derivatives. The conditions of continuity of the ion profile and its derivative at the surface of the limiting sphere give a set of two equations for determining the radius of the free molecule zone and ion flux onto the aerosol particle. The final expression for the recombination efficiency thus consists of two parts. The first term contains the geometric particle cross section times the Coulomb enhancement factor. This part depends on the particle size as its first power. The second part is proportional to the area of the limiting sphere times a factor linearly dependent on the rate of the ion energy losses in the free molecule zone. This term is independent of the particle size in the limit of very small particles. The ideology of our approach reminds us of that adopted in the theory of nuclear reactions, where the optical potential is introduced whose imaginary part is responsible for capturing the incident nucleons by atomic nuclei. This imaginary part of the optical potential is also an empirical constant, although it can be calculated once the rates of doorway inelastic channels can be properly accounted.

However, under some reasonable approximation it is possible to derive a simple expression for recombination efficiency. Namely, we assume that at the border of the limiting sphere all ions disappear; that is, the recombination process inside the limiting sphere goes so fast that diffusion transport in the diffusion zone is not able to deliver enough ions to restore the non-zero ion concentration at $r = R(a)$. Then the efficiency of recombination is given by the formula

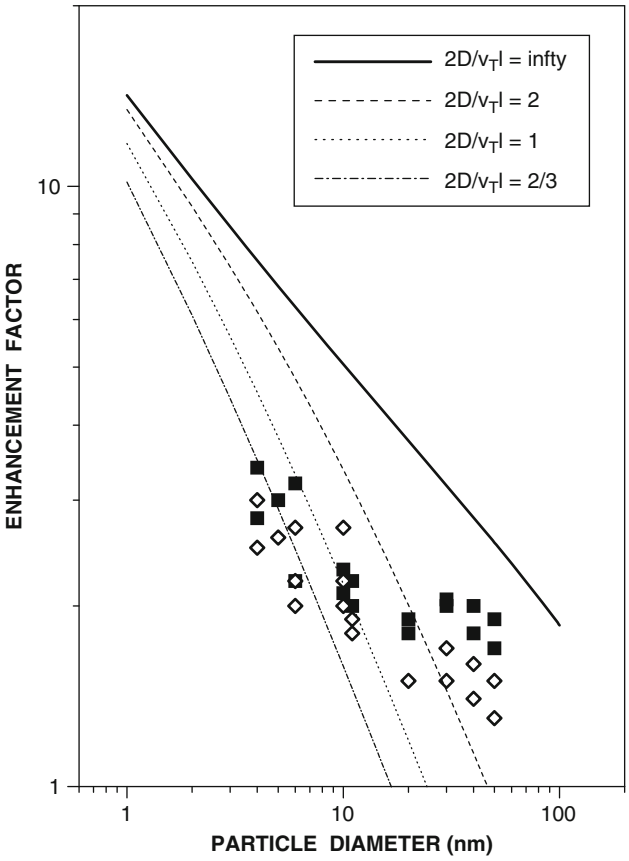

Fig. 3.21 Good agreement is illustrated between the theory and experiment. Shown is the enhancement factor versus particle size for four ratios of $2D/v_T l_c$

$$\alpha(a) = \frac{4\pi D l_c}{1 - \exp\left(-l_c/R(a)\right)} \tag{3.192}$$

where $R(a) = 4D/v_T$ for small particles. Because all ion–carrier gas collisions lead to the loss of ion energy and are thus responsible for ion capture happening inside the free molecule zone, then this consideration takes them into account.

We compared the charging efficiency of a neutral metallic particle with the experimental data of Pui et al. (1988) (Fig. 3.21). We calculated the enhancement factor (charging efficiency/condensation efficiency). The enhancement is related to the action of the image forces between the particle and the ion. The calculations were done for the ratios $2D/v_T$ from Pui's paper (Pui et al. 1988). The last value,

2/3, corresponds to the BGK theory. $D/v_T = \infty$ means infinite mean free path (free molecule regime). One clearly sees that the agreement of the theoretical and the experimental data is fairly good.

3.7 Heat Transfer

A new flux-matching theory is formulated and applied to the study of heat transfer from (or to) aerosol particles whose size is comparable to the molecular mean free path in the carrier gas. The collisionless kinetic equation is solved, and the temperature profile in the free molecule zone (at distances less than the molecular mean free path) is found. This profile is then matched to that derived from the solution of the thermoconductivity equation, which describes heat transport outside the free molecule zone. The final output of this section is the expression for particle heat transfer efficiency, which contains its free molecule value (also derived here), the thermoconductivity of the carrier gas, and the thermal velocity of the carrier gas molecules.

3.7.1 Introduction

In this section we outline the derivation of the formula for the particle heat transfer efficiency $\gamma(a)$ defined as the proportionality coefficient between the temperature difference of the particle and the carrier gas and the energy flux from (to) the particle. This formula is valid throughout the whole interval of particle sizes and contains *no free parameters*. This problem received attention at the very beginning of this century by Filippov and Rosner (2000), who applied a Monte Carlo method for studying heat transfer from the particle to the surrounding gas. Some earlier references can be found in this paper. This problem was studied experimentally: the authors (Winkler et al. 2004, 2006) compared their results to a modification of the Fuchs–Sutugin formula and found satisfactory agreement between theoretical and experimental data (Lee et al. 1985).

We again introduce a limiting sphere outside of which the temperature profile can be described by the thermoconductivity equation. Inside the limiting sphere we solve the collisionless Boltzmann equation subject to a given boundary condition at the particle surface and put additional conditions: (1) total heat flux does not change in crossing the border of the limiting sphere, (2) carrier gas density is a continuous function of the radial coordinate, and (3) its radial derivative at the surface of the limiting sphere coincides with that found from the solution of the thermoconductivity equation. These three conditions determine three matching parameters: heat flux, matching distance, and temperature at the matching distance.

Below we demonstrate the details of the derivation of the expression for the heat transfer efficiency.

3.7.2 Free Molecule Solution

As we already saw, in spherically symmetrical systems the set of variables r, E, L, is of extreme convenience, with L being the angular momentum of the carrier gas molecule. In these variables the Boltzmann equation takes an especially simple form:

$$v_r \frac{\partial f_s}{\partial r} = 0, \tag{3.193}$$

where $v_r = (mr)^{-1}\sqrt{L^2(r) - L^2}$ is the radial ion velocity, and $L^2(r) = 2mEr$, $s = \pm 1$ is an auxiliary variable defining the direction of ion motion along the radial coordinate ($s = -1$ corresponds to the direction toward the particle).

In the free molecule zone we operate with the mean kinetic energy $q(r)$, which is proportional to the temperature of the carrier gas. Now we give the exact definition of the values $q(r)$, the energy flux $\mathcal{Q}(r)$, and the number density $n(r)$:

$$\begin{aligned} n(r) &= \frac{\pi}{m^2 r}\sum_s \int \mathrm{d}E \int \frac{\mathrm{d}L^2}{\sqrt{L^2(r) - L^2}} f_s(r, E, L) \\ q(r) &= \frac{\pi}{m^2 r}\sum_s \int E\mathrm{d}E \int \frac{\mathrm{d}L^2}{\sqrt{L^2(r) - L^2}} f_s(r, E, L) \\ Q(r) &= \frac{4\pi^2}{m^3}\sum_s s \int E\mathrm{d}E \int \mathrm{d}L^2 f_s(r, E, L) \end{aligned} \tag{3.194}$$

Here m is the mass of a carrier gas molecule.

The boundary condition

$$f_1(a, E, L) = \left[(1-\alpha) f_{-1}(a, E, L) + \eta M^*(E) n(a)\right] \theta\left(L^2(a) - L^2\right). \tag{3.195}$$

couples f_1 and f_{-1} on the particle surface. Here, $n(a)$ is given by Eq. 3.194 at $r = a$, α is the energy accommodation coefficient, and the asterisk (*) refers to the particle surface:

$$M(E) = (m/2\pi kT)^{3/2} \mathrm{e}^{-E/kT}$$

is the Boltzmann distribution normalized to unity, η is a factor providing the equality of the inward and outward molecular fluxes (will be determined later on), and $\theta(x)$ is the Heaviside step function. This boundary condition claims that part $1 - \alpha$ of molecules experiences the mirror reflection from the particle surface whereas part α sticks to the particle surface, acquires its temperature T_*, and then isotropically leaves the particle surface. Two points should be emphasized:

1. This boundary condition is *linear* in f.
2. The function f_1 appears on the right-hand side of the boundary condition.

The latter circumstance is not convenient, and we eliminate $n(a)$ by the following trick. We find the product $\eta n(a)$ from the condition that the mass flux of the carrier gas molecules is equal to zero. This condition gives:

$$\eta n(a) = \alpha n_\infty \xi \tag{3.196}$$

where $\xi = \sqrt{T_\infty / T_*}$

Substituting Eq. 3.196 into Eq. 3.195 allows for presenting the distribution f_s in the form

$$f_s = f_s^{(0)} + f_s^{(1)},$$

where

$$f_s^{(0)} = n_\infty M_\infty \theta \left(L^2(r) - L^2 \right). \tag{3.197}$$

This function describes the unperturbed distribution, that is, the carrier gas molecules distributed in the empty space (no particle or a particle with $\alpha = 0$). The function

$$f_s^{(1)} = \alpha n_\infty \left(\xi M_* - M_\infty \right) \theta \left(L^2(r) - L^2 \right) \theta \left(L^2(a) - L^2 \right) \delta_{s,1} \tag{3.198}$$

describes the perturbation generated by the heated particle. Here δ_{ik} is the Kroneker delta and $\theta(x)$ is the Heaviside step function.

The contribution from $f^{(1)}$ to the mass flux should be zero in the steady state. This condition is seen to be fulfilled. The function $f_s^{(1)}$ contains only outgoing molecular trajectories.

Now let us find the free molecule heat transfer efficiency. Equation 3.195 gives

$$\mathcal{Q} = 2\pi \alpha a^2 v_\infty k n_\infty \left(T_* - T_\infty \right) \tag{3.199}$$

and

$$\gamma_{\text{fm}}(a) = 2\pi \alpha a^2 v_\infty k n_\infty. \tag{3.200}$$

Here $v_\infty = \sqrt{8kT_\infty / \pi m}$ is the thermal velocity of the carrier gas molecules.

To calculate the q- and n profiles we use the equation

$$\int_0^{L^2(a)} \frac{dL^2}{\sqrt{L^2(r) - L^2}} = 2L(r) D(r), \tag{3.201}$$

where

$$D(r) = 1 - \sqrt{1 - \frac{a^2}{r^2}} \tag{3.202}$$

The q-profile found from Eq. 3.194 is then

$$q(r) = q_\infty \left[1 + \frac{\alpha}{2} \left(\frac{T_*}{T_\infty} - 1 \right) D(r) \right] \tag{3.203}$$

The density profile can also be found:

$$n(r) = n_\infty \left[1 - \frac{\alpha}{2} \left(1 - \frac{T_\infty}{T_*} \right) D(r) \right] \tag{3.204}$$

It is important to notice that $n(a)$ found from Eq. 3.204 coincides with n_* from Eq. 3.195.

The temperature at $r = a$ differs from T_*:

$$n_* T(a) = n_\infty T_\infty \left[1 + \frac{\alpha}{2} \left(\sqrt{\frac{T^*}{T_\infty}} - 1 \right) \right] \tag{3.205}$$

The temperature jump at the particle surface is then

$$T_* - T(a) = T_* - \sqrt{T_* T_\infty} \left[1 - \frac{\alpha}{2} \left(\sqrt{\frac{T_*}{T_\infty}} - 1 \right) \right] \tag{3.206}$$

3.7.3 *Limiting Sphere*

Now let the temperature at $r = R$ be fixed. Then, to satisfy the boundary condition of Eq. 3.20, we should modify the distribution by introducing the multiplier $C(R)$ and replacing $q_\infty \to q_R$:

$$q(r) = q_R C(R) \left[1 + \frac{\alpha}{2} \left(\sqrt{\frac{T_*}{T_R}} - 1 \right) \left(1 - \sqrt{1 - \frac{a^2}{r^2}} \right) \right] \tag{3.207}$$

This step is possible because of the linearity and homogeneity of the boundary conditions for f. From the condition $q(R) = q_R$ we have

$$C(R) = \left[1 + \frac{\alpha}{2} \left(\sqrt{\frac{T_*}{T_R}} - 1 \right) \left(1 - \sqrt{1 - \frac{a^2}{R^2}} \right) \right]^{-1} \tag{3.208}$$

Similarly we find $n(r)$

$$n(r) = n_\infty C(R)\left[1 - \frac{\alpha}{2}\left(1 - \sqrt{\frac{T_R}{T_*}}\right) D(r)\right] \tag{3.209}$$

Because $q_R = 1.5kT_R n_R$ (continuous approximation), we can express n_R in terms T_R

$$n(R) = n_\infty \frac{T_\infty}{T_R} \tag{3.210}$$

From the condition $n(R) = n_R$ and Eqs. 3.209 and 3.210 we have

$$\frac{T_\infty}{T_R} = C(R)\left[1 - \frac{\alpha}{2}\left(1 - \sqrt{\frac{T_R}{T_*}}\right) D(R)\right] \tag{3.211}$$

This is the equation linking R and T_R. Another equation for these unknowns follows from the condition that the derivative of n is continuous. To derive this equation we need to find $\gamma\,(a, R)$,

The radius R of the free molecule zone can be now determined from the condition of the continuity $d_r n(R)$. The contribution of the free molecule zone is

$$n' = n_\infty C(R)\frac{\alpha}{2}\left(1 - \sqrt{\frac{T_R}{T_*}}\right)\frac{a^2}{R^2\sqrt{R^2 - a^2}}$$

To find the contribution of the continuous zone we use the equation

$$\gamma\,(a, R) = C(R)\sqrt{\frac{T_R}{T_\infty}}\frac{n_R}{n_\infty}\gamma_{\mathrm{fm}}(a) \tag{3.212}$$

and

$$n(r) = n_\infty \frac{T_\infty}{T(r)}$$

Then

$$n' = -\frac{n_\infty T_\infty}{T_R^2} T'(R)$$

Next,

$$T'(R) = -\frac{Q}{4\pi\Lambda R^2} = -\frac{\gamma\,(a, R)\,(T_* - T_R)}{4\pi\Lambda R^2}$$

From the condition $n' = n'$ we have some subsequent simplifications:

$$\frac{\xi^3 (1+\tau)}{\tau^5} = \frac{R_0}{\sqrt{R^2 - a^2}} \tag{3.213}$$

where $\tau = \sqrt{T_R/T_*}$ and $\xi = \sqrt{T_\infty/T_*}$ and $R_0 = \Lambda/v_\infty$. This equation is readily solved to give

$$R = \sqrt{R_\tau^2 + a^2} \tag{3.214}$$

where

$$R_\tau = R_0 \frac{\tau^5}{\xi^3 (1+\tau)}$$

From Eq. 3.211 we derive the equation for $\tau = \tau(\xi)$:

$$\frac{\xi^2}{\tau^2} = \frac{1 - 0.5\alpha (1-\tau) D(R_\tau)}{1 + 0.5\alpha (\tau^{-1} - 1) D(R_\tau)} \tag{3.215}$$

For technical work it is convenient to note that

$$D(R) = 1 - \frac{R_\tau}{R}$$

It is seen that at $Kn \gg 1$ $\tau = \xi$, i.e., $T_R \approx T_\infty$ (not surprising). In the opposite limit, $D(R_\tau) = 1$ and

$$\frac{\xi^2}{\tau^2} = \frac{1 - 0.5\alpha (1-\tau)}{1 + 0.5\alpha (\tau^{-1} - 1)} \tag{3.216}$$

3.7.4 Results and Discussion

The final expression for the heat transfer efficiency is

$$\gamma(a) = \frac{2\pi\alpha a^2 v_\infty (\xi/\tau)}{1 + 0.5\alpha (1-\tau) D(R) + \alpha (\xi/\tau) a^2/(2R_0 R)} \tag{3.217}$$

Let us introduce the modifier

$$\gamma(a) = Z(a, \xi)\, \gamma_{\text{fm}}(a) \tag{3.218}$$

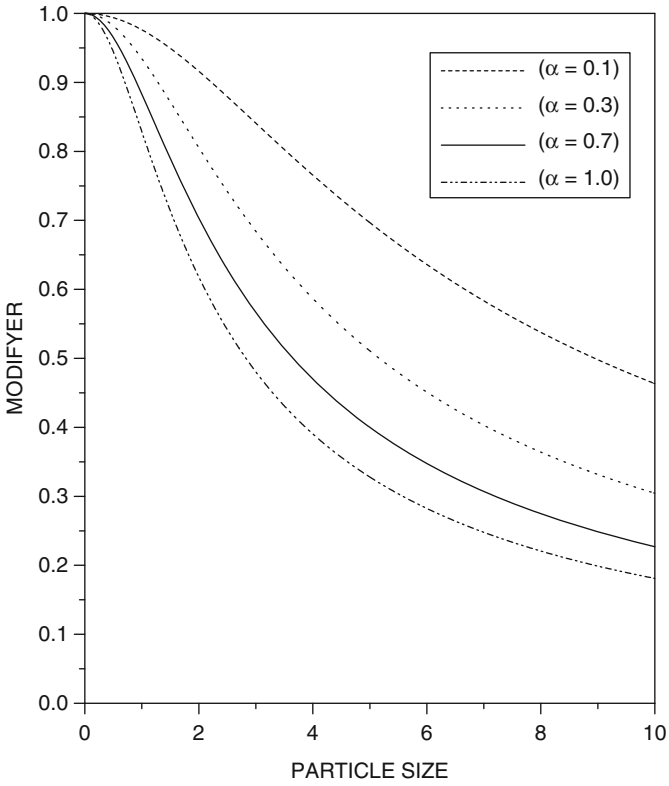

Fig. 3.22 Size dependence of the modifier $Z = \gamma(a)/\gamma_{fm}(a)$ (see Eq. 3.219) on reduced particle size av_∞/Λ at different values of the thermal accommodation coefficient α

We find then

$$Z\,(a,\xi) = \frac{(\xi/\tau)}{1 + 0.5\alpha\,(1-\tau)\,D(R) + \alpha\,(\xi/\tau)\,a^2/\,(2R_0R)} \tag{3.219}$$

Figures 3.22 and 3.23 demonstrate the dependencies of the modifier γ on the particle size and the temperature ratio T_∞/T_*.

3.8 Conclusion

The most important feature of all atmospheric processes is their stochasticity. Even if we know all conditions with the highest possible precision, it is impossible to predict the scenarios of atmospheric processes, because respective dynamic equations are unstable and admit very different scenarios under even the tiniest

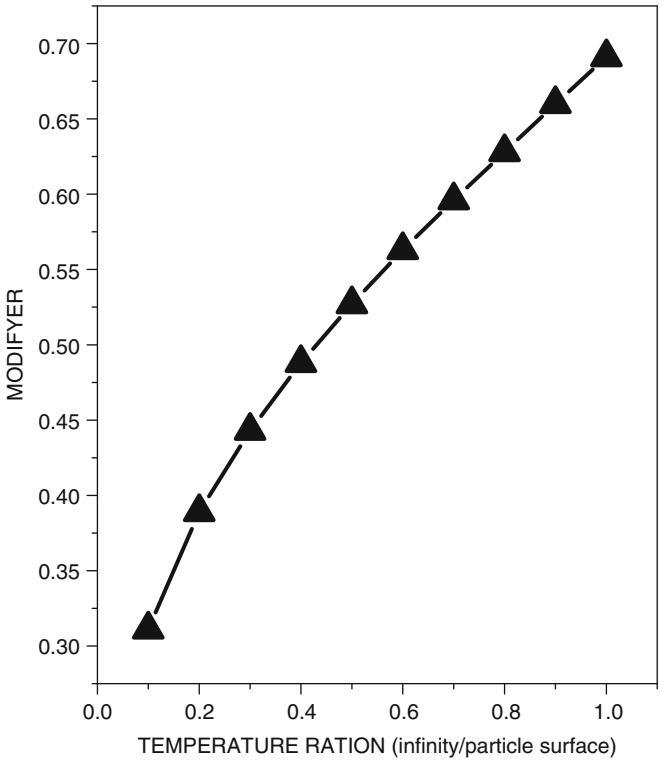

Fig. 3.23 Dependence of the modifier at the reduced size *1* on the temperature ratio T_∞/T_*

changes to the initial and boundary conditions. The question thus arises: whether is it necessary to have accurate expressions for the rate of elementary atmospheric processes such as those considered here? The answer is still positive. The point is that respective deterministic equations can be replaced by the stochastic analogues, where the respective rates will enter the expressions for the rates of transitions between different states. In this case, the analytical expressions for the respective rates are absolutely irreplaceable.

In this chapter, I tried to demonstrate a simple trick (flux-matching procedure) allowing one to operate in a very difficult situation: I mean the transition regime, where it is necessary to solve the Boltzmann equation. Although in principle it is possible to do numerically, the problem is how to apply these numerical results to concrete atmospheric situations. The most striking example is the rate of particle charging. If one needs to average over a group of boundary conditions, it would be necessary to solve the Boltzmann equation many times.

In principle, the problem can be resolved by applying semi-empirical formulas. But, undoubtedly, it is much better to handle the expressions derived from some known and readily controllable principles, as has been done in this chapter.

I demonstrated in detail how to use the flux-matching theory for deriving the expressions for the efficiencies of condensation, particle charging, and heat transfer. It is very likely that this approach is applicable to other aerosol microprocesses.

References

Aalto P, Hammeri K, Becker S, Weber R, Salm J, Mäkelä JM, Hoell C, O'Dowd C, Karlsson H, Hansson H-C, Väkevä M, Buzorius G, Kulmala M (2001) Physical characterization of aerosol particles during nucleation events. Tellus 53B:344

Adachi M (1985) Unipolar and bipolar diffusion charging of ultrafine aerosol particles. J Aerosol Sci 16:109–123

Ammann M, Pöschl U (2007) Kinetic model framework for aerosol and cloud surface chemistry and gas–particle interactions – part 2: exemplary practical applications and numerical simulations. Atmos Chem Phys 7:6025–6045

Anttila T, Kerminen V-M, Kulmala M, Laaksonen A, O'Dowd C (2004) Modeling the formation of organic particles in the atmosphere. Atmos Chem Phys 4:1071–1083

Arey J, Atkinson R, Aschmann SM (1990) Product study of gas-phase reactions of monoterpenes with the OH radical in the presence of NO_x. J Geophys Res 96:18539

Beig G, Brasseur GP (2000) Model of tropospheric ion composition: a first attempt. J Geophys Res 105:22671–22684

Bhatnagar PL, Gross EP, Krook M (1954) A model for collision processes in gases. I. Small amplitude processes in charge and neutral one–component systems. Phys Rev 94:511–525

Boy M, Kulmala M (2002) Nucleation events on the continental boundary layer: influence of physical and meteorological parameters. Atmos Chem Phys 2:1–16

Boy M, Rannik U, Lehtinen KE, Tarvainen V, Hakola H, Kulmala M (2003) Nucleation events in the continental boundary layer: long-term statistical analysis of aerosol relevant characteristics. J Geophys Res 108(D21):4667–4675

Brock JR (1970) Aerosol charging: the role of the image force. J Appl Phys 41:843–844

Burtcher H, Schmidt-Ott A (1985) Experiments on small particles in gas suspension. Surface Sci 156:735–740

Castelman AV (1982) Experimental studies of ion clustering relationship to aerosol formation processes and some atmospheric implications. J Aerosol Sci 13:73–85

Cercignani C (1975) Theory and application of the Boltzmann equation. Scottish Academic Press, Edinburgh/London

Charlson RJ, Heitzenberg RL (1995) Aerosol forcing of climate. Wiley, New York

Clement CF (2007) Mass transfer to aerosols. In: Colbeck I (ed) Environmental chemistry of aerosols. Wiley Interscience, New York, pp 49–89

Clement CF, Kulmala M, Vesala T (1996) Theoretical consideration on sticking probabilities. J Aerosol Sci 27:869–882

Dahnecke B (1983) Simple kinetic theory of Brownian diffusion in vapors and aerosols. In: Meyer E (ed) Theory of dispersed multiphase flows. Academic, New York, pp 97–133

Dal Maso M, Kulmala M, Rippinen I, Hussein T, Wagner R, Aalto PP, Lehtinen KEJ (2005) Formation and growth of fresh atmospheric aerosols: eight years of aerosol size distribution data from SMEAR II, Hyytiala, Finland. Boreal Environ Res 10:3232–3336

Davidovits P, Jaine JT, Duan SX, Worsnop DR, Zahniser MS, Kolb CE (1991) Uptake of gas molecules by liquids. A model. J Phys Chem 95:6337–6340

Davidovits P, Hu JH, Worsnop DR, Zahnister MS, Colb CE (1995) Entry of gas molecules into liquids. Faraday Discuss 100:65–81

Davis EJ (1983) Transport phenomena with single aerosol particle. Aerosol Sci Technol 2:121

Farman JC, Gardiner PG, Shanklin JD (1985) Large losses of total ozone in Antarctica reveal seasonal ClO_x/NO_x interaction. Nature 315:207–210
Feng X, Bogan MJ, Chuah E, Agnes GR (2001) Micro–heterogeneous catalysis at the surface of electrodynamically levitated particles. J Aerosol Sci 32:1147–1159
Filippov AV, Rosner DE (2000) Energy transfer between an aerosol particle and gas at high temperature ratios in the Knudsen transition regime. Int J Heat Mass Transfer 43:127–137
Finlayson-Pitts BJ, Pitts JN Jr (2000) Chemistry of the upper and lower atmosphere. Academic, San Diego
Ford IJ, Harris SA (2004) Molecular cluster decay viewed as escape from a potential of mean force. J Chem Phys 120:4428–4437
Friedlander SK (1983) Dynamics of aerosol formation by chemical reactions. Ann N Y Acad Sci 404:354–363
Friedlander SK (2000) Smoke, dust, and haze. Wiley, New York/London
Fuchs NA (1964) The mechanics of aerosols. MacMillan, New York
Fuchs NA, Sutugin AG (1971) High–dispersed aerosols. In: Hidy GM, Brock JR (eds) Topics in current aerosol research, vol 2. Pergamon, Oxford, pp 1–60
Gentry JW, Brock JR (1967) Unipolar diffusion charging of small aerosol particles. J Chem Phys 47:64–67
Grini A, Korhonen H, Lehtinen K, Isaksen I, Kulmala M (2005) A combined photochemistry/aerosol dynamics model: model development and a study of new particle formation. Boreal Environ Res 10:525–541
Hahn Y (1997) Electron–ion recombination processes. Rep Prog Phys 60:691–759
Harrison RG, Carslaw KS (2003) Ion–aerosol–cloud processes in the lower atmosphere. Rev Geophys 41:1–25
Hashish AH, Bailey AG (1991) Electrostatic enhancement of particle deposition in the lung when using jet and ultrasonic nebulisers. In: O'Neil BC (ed) Electrostatic 1991: invited and contributed papers from the eighth international conference, held at the University of Oxford, 10–12 April 1991. Inst Phys Conf Ser 118:45–50
Havnes O, de Angelis U, Bingham R, Goetz CK, Morfill GE, Tsytovich V (1990) On the role of dust in the summer mesopause. J Atmos Terr Phys 52:637–643
Havnes O, Melandso F, La Hoz C, Aslaksen TK, Harquist T (1992) Charged dust in the earth's mesopause: effect on radar backscatter. Phys Scr 45:535–544
Havnes O, Troim J, Blix T, Mortensen W, Naesheim LI, Thrain E, Tonnesen T (1996) First detection of charged dust particles in the earth's mesosphere. J Geophys Res 101:10839–10847
Hidy JM, Brock JR (1971) The dynamics of aerocolloidal systems. Pergamon, Oxford
Hodges RR Jr (1969) Ion pair annihilation by aerosols in the lower ionosphere. J Geophys Res 74:2223–2228
Hoppel WA, Frick GM (1986) Ion–aerosol attachment coefficients and the steady–state charge distribution on aerosols in a bipolar ion environment. J Aerosol Sci Technol 5:1–21
Hoppel WA, Frick GM (1990) The nonequilibrium character of the aerosol charge distribution produced by neutralizers. Aerosol Sci Technol 12:471–496
Huang DD, Seinfeld JH, Marlow WH (1990) BGK equation solution for large Knudsen number aerosol with a singular attractive contact potential. J Colloid Interface Sci 140:258–276
Huang DD, Seinfeld JH, Okuyama K (1991) Image potential between a charged particle and an uncharged particle in aerosol coagulation–enhancement in all size regimes and interplay with van der Waals forces. J Colloid Interface Sci 141:191–198
Hussin A, Scheibel HG, Becker KH, Porstendorfer J (1983) Bipolar diffusion charging of aerosol particles – I. Experimental results within the diameter range 4 – 30 nm. J Aerosol Sci 14:671–677
Janson R, Rozman K, Karlsson S, Hansson HC (2001) Biogenic emission and gaseous precursor to forest aerosols. Tellus B53:423–440
Jensen EJ, Thomas GE (1991) Charging of mesospheric particles: implication for electron density and particle coagulation. J Geophys Res 96:18603–18615

Juozaitis A, Trakumas S, Girgzdiene D, Girgzdis A, Sopauskiene D, Ulevicius V (1996) Investigation of gas–to–particle conversion in the atmosphere. Atmos Res 41:445
Keefe D, Nolan PJA, MRI, Scott JA (1968) Influence of Coulomb and image forces on combination in aerosols. Proc R Ir Acad 66A:17–29
Kerminen V-M, Lehtinen K, Anttila T, Kulmala M (2004) Dynamics of atmospheric nucleation mode particles: timescale analysis. Tellus 56B:135–146
Khachatourian AV, Wistrom AO (2001) Size effect in aerosol electrostatic interactions. J Colloid Interface Sci 242:52–58
Korhonen H, Lehtinen KEJ, Pirjola L, Napari I, Vehkamäki H, Noppel M, Kulmala M (2003) Simulation of atmospheric nucleation mode: a comparison of nucleation models and size distribution representations. J Geophys Res 108(D15):4471. doi:10.1029/2002JD003305
Korhonen H, Lehtinen KEJ, Kulmala M (2004) Multicomponent aerosol dynamic model UHMA: model development and validation. Atmos Chem Phys Discuss 4:471–506
Krueger AP, Reed EJ (1976) Biological impact of small air ions. Science 193:1209–1213
Kulmala M, Wagner PE (2001) Mass accommodation and uptake coefficients – a quantitative comparison. J Aerosol Sci 32:833–841
Kulmala M, Vehkamäki H, Petäjä T, Dal Maso M, Lauri A, Kerminen V-M, Birmili W, McMurry PH (2004) Formation and growth rates of ultrafine atmospheric particles: a review of observations. J Aerosol Sci 35:143–176
Laaksonen A, Vesala T, Kulmala M, Winkler PM, Wagner PE (2005) Commentary on cloud modeling and mass accommodation coefficient of water. Atmos Chem Phys 5:461–464
Landau LD, Lifshits EM (1969) Electrodynamics of continuous media. Nauka, Moscow
Lee YC, Chyou YP, Pfender E (1985) Particle dynamics and particle heat and mass transfer in thermal plasmas. Part II. Particle heat and mass transfer in thermal plasmas. Plasma Chem Plasma Process 5:391
Lehtinen KEJ, Kulmala M (2003) A model for particle formation and growth in the atmosphere with molecular resolution in size. Atmos Chem Phys 3:251–257
Li W, Davis EJ (1995) Aerosol evaporation in the transition regime. Aerosol Sci Technol 25:11–19
Li YQ, Davidovits P, Shi Q, Jayne JT, Kolb CE, Worsnop DR (2001) Mass and thermal accommodation coefficients of $H_2O(g)$ on liquid water as a function of temperature. J Phys Chem A105:10627–10634
Liu BYH (1976) Fine particles, aerosol generation, measurement, sampling, and analysis. Academic, New York
Lohman U, Feichter J (2005) Global indirect aerosol effects: a review. Atmos Chem Phys 5:715–737
Loyalka SK, Hamodi SA, Tompson RV (1989) Isothermal condensation on a spherical droplet. Phys Fluids A1:358–362
Lushnikov AA (2010a) Introduction to aerosols. In: Agranovski I (ed) Aerosols – science and technology. WILEI – VCH Verlag GmbH&Co KGaA, Weinheim, pp 1–42
Lushnikov AA (2010b) Condensation, evaporation, nucleation. In: Agranovski I (ed) Aerosols – science and technology. WILEI – VCH Verlag GmbH&Co KGaA, Weinheim, pp 91–126
Lushnikov AA, Kulmala M (1998a) Nucleation controlled formation and growth of disperse particles. Phys Rev Lett 8:23
Lushnikov AA, Kulmala M (1998b) Dimers in nucleating vapors. Phys Rev E58:3157
Lushnikov AA, Kulmala M (2000) Nucleation burst in a coagulating system. Phys Rev E62:4932
Lushnikov AA, Kulmala M (2001) Kinetics of nucleation controlled formation and condensational growth of disperse particles. Phys Rev E63:061109
Lushnikov AA, Kulmala M (2004a) Flux–matching theory of particle charging. Phys Rev E70:046413
Lushnikov AA, Kulmala M (2004b) Charging of aerosol particles in the near free–molecule regime. Eur Phys J D29:345–355
Lushnikov AA, Kulmala M (2005) A kinetic theory of particle charging in the free–molecule regime. J Aerosol Sci 39:1069–1088

Lushnikov AA, Lyubovtseva YuS, Kulmala M (2008) A model of nucleation bursts. Russ J Earth Sci 10(ES1005). doi:10.2205/2007ES000275
Lushnikov AA, Zagaynov VA, Lyubovtseva YuS (2010) Formation of aerosols in the atmosphere. In: Bychkov VL, Golubkov GV, Nikitin AI (eds) Atmosphere and ionosphere. Dynamics, processes, and monitoring. Springer, New York, pp 69–96
Lyubovtseva YuS, Sogacheva L, Dal Maso M, Bonn B, Keronen P, Kulmala M (2005) Seasonal variations of trace gases, meteorological parameters, and formation of aerosols in boreal forests. Boreal Environ Res 10:493–510
Lyubovtseva YuS, Zagaynov VA, Khodzher TV, Kulmala M, Boy M, Dal Maso M, Junninen H, Obolkin VA, Potyomkin VL, Biryukov YuG, Lushnikov AA (2010) Comparison of formation conditions of secondary aerosol particles in boreal forests of Southern Finland and Siberia. Russ J Earth Sci 11:4002. doi:10.2205/2009ES000410
Marlow WH (1980) Derivation of the collision rates for singular attractive contact potentials. J Chem Phys 73:6284–6287
Marlow WH, Brock JR (1975) Unipolar charging of small aerosol particles. J Colloid Interface Sci 50:32–38
Matsoukas T (1997) The coagulation rate of charged aerosols in ionized gases. J Colloid Interface Sci 178:474–483
Natanson GL (1959) On the theory of volume ion recombination. Sov Phys Tech Phys Engl Transl 29:1373–1380
Natanson GL (1960) On the theory of the charging of amicroscopic aerosol particles as a result of capture of gas ions. Sov Phys Tech Phys Engl Transl 30:573–588
Natanson GM, Davidovits P, Worsnop DR, Kolb CE (1996) Dynamics and kinetics at the gas-liquid interface. J Phys Chem 100:13007
Pöschl U, Rudich Y, Ammann M (2007) Kinetic model framework for aerosol and cloud surface chemistry and gas–particle interactions – part 1: general equations, parameters, and terminology. Atmos Chem Phys 7:5989–6023
Pui DYH, Fruin S, McMurry PH (1988) Unipolar diffusion charging of ultrafine aerosols. J Aerosol Sci Technol 8:173–187
Qu X, Davis EJ (2001) Droplet evaporation and condensation in the near continuum regime. J Aerosol Sci 32:861–875
Rapp M (2000) Capture rates of electrons and positive ions by mesospheric aerosol particles. J Aerosol Sci 31:1367–1369
Rapp M, Lübken FJ (1999) Modelling of positively charged aerosols in the polar summer mesopause region. Earth Planet Space 51:799–807
Ray AK, Lee AJ, Tilley HL (1988) Direct measurements of evaporation rates of single droplets at large Knudsen numbers. Langmuir 4:631–639
Reist PC (1984) Introduction to aerosol science. Macmillan, New York
Romay FJ, Pui DYH (1992) On the combination coefficient of positive ions with ultrafine neutral particles in the transition and free–molecule regimes. J Aerosol Sci Technol 17:134–137
Sahni DC (1966) The effect of black sphere on the flux distribution of an infinite moderator. J Nucl Energy 20:915–920
Seinfeld JH, Pandis SP (2006) Atmospheric chemistry and physics. Wiley, New York
Shi B, Seinfeld JH (1991) On mass transport limitation to the rate of reaction of gases in liquid droplets. Atmos Environ 25A:2371
Smirnov BM (2000a) Clusters and small particles in gases. Springer, New York
Smirnov BM (2000b) Cluster plasma. Phys Usp 170:495–534
Smith M, Lee K, Matsoukas T (1999) Coagulation of charged aerosols. J Nanopart Res 1:185–195
Smith GD, Woods E, Baer T, Miller RE (2003) Aerosol uptake described by numerical solution of the diffusion–reaction equation in the particle. J Phys Chem A107(45):9582–9587
Sorokin A, Mirabel P (2001) Ion recombimation in aircraft exhaust plumes. Geophys Res Lett 14:955–958
Sorokin A, Vancassel X, Mirabel P (2003) Emission of ions and charged soot particles by aircraft engines. Atmos Chem Phys 3:325–334

Stolzenburg MR, McMurry PH, Sakurai H, Smith JN, Mauldin RL, Eisele FL, Clement CF (2005) Growth rates of freshly nucleated atmospheric particles in Atlanta. J Geophys Res 110:D22S05
Stratton JA (1941) Electromagnetic theory. McGraw, New York/London
Tsang TH, Rao A (1988) Comparison of different numerical schemes for condensational growth of aerosols. Aerosol Sci Technol 9:133
Wagner PE (1982) Aerosol growth by condensation. In: Marlow WH (ed) Aerosol microphysics, vol II. Springer, Heidelberg, pp 129–178
Weber AP, Seipenbusch M, Christoph T, Kasper G (1999) Aerosol catalysis on nickel nanoparticles. J Nanopart Res 1:253–265
Wen HY, Reischl GP, Kasper G (1984) Bipolar diffusion charging of fibrous aerosol particles. I. J Aerosol Sci 15:103–122
Widmann JF, Davis EJ (1997) Mathematical models of the uptake of $ClONO_2$ and other gases by atmospheric aerosols. J Aerosol Sci 28:87–106
Wiedenscholer A, Fissan HJ (1991) Bipolar charge distributions of aerosol particles in high–purity argon and nitrogen. J Aerosol Sci Technol 14:358–364
Williams MMR, Loyalka SK (1991) Aerosol science, theory & practice. Pergamon Press, Oxford
Winkler PM, Vrtala A, Wagner PE, Kulmala M, Lehtinen KEJ, Vesala T (2004) Mass and thermal accomodation during gas–liquid condensation of water. Phys Rev Lett 93:07501
Winkler PM, Vrtala A, Rudolf R, Wagner PE, Riipinen I, Vesala T, Lehtinen KEJ, Viisanen Y, Kulmala M (2006) Condensation of water vapor: experimental determination of mass and thermal accommodation coefficients. J Geophys Res 111:D19202
Yu F, Turko RP (1998a) The formation and evolution of aerosols in atmospheric aircraft plumes: numerical simulation and comparison with observations. J Geophys Res 103:25119–25934
Yu F, Turko RP (1998b) The role of ions in the formation and evolution of particles in aircraft plumes. Geophys Res Lett 24:1927–1930
Yu F, Turko RP (2001) From molecular clusters to nanoparticles: role of ambient ionization in tropospheric aerosol formation. J Geophys Res 106:4797–4814
Zagaynov VA, Sutugin AG, Petryanov-Sokolov IV, Lushnikov AA (1976) Sticking probability of molecular clusters to solid surfaces. J Aerosol Sci 7:389–395

Chapter 4
Electromagnetic Drivers in the Upper Atmosphere: Observations and Modeling

A.A. Namgaladze, M. Förster, B.E. Prokhorov, and O.V. Zolotov

Abstract This chapter presents and discusses some of the most recent measurements obtained by the Electron Drift Instrument (EDI) on "Cluster", the accelerometer on board the low-Earth-orbiting satellite CHAMP, and global maps of total electron content (TEC) gathered by the fleet of GPS satellites. It aims at a better understanding of the globally interconnected complex plasma physical and electrodynamic processes of the Earth's upper atmosphere by means of first-principle numerical modeling using the Upper Atmosphere Model (UAM). The study results show ionospheric electric fields, generated by magnetospheric and seismogenic sources, and reveal their influence on the thermospheric dynamics and the TEC pattern. UAM simulations of the thermospheric neutral wind at high latitudes are compared with CHAMP observations for varying interplanetary magnetic field (IMF) conditions on 28 October 2003, the day before the famous Halloween superstorm of the previous solar cycle. The simulations show the immediate response of the upper atmosphere and its high sensitivity to IMF changes in strength and orientation. Investigation of the 'lithosphere–atmosphere–ionosphere' coupling problem allowed statistically describing GPS-measured TEC variations treated as precursors to earthquakes as (1) anomalous strong (30–90% and more) TEC-positive or -negative deviations relative to the quiet conditions before the forthcoming seismic event, not less than M5 by magnitude, linked to the near-

A.A. Namgaladze (✉) • O.V. Zolotov
Physics Department, Murmansk State Technical University, 183010 Murmansk, Russia
e-mail: Namgaladze@yandex.ru; NamgaladzeAA@mstu.edu.ru; ZolotovO@gmail.com

M. Förster • B.E. Prokhorov
Helmholtz Centre Potsdam, GFZ German Research Centre for Geosciences, Telegrafenberg, 14473 Potsdam, Germany

B.E. Prokhorov
Applied Mathematics, Interdisciplinary Center for Dynamics of Complex Systems (DYCOS), University Potsdam, 14476 Potsdam, Germany
e-mail: boris@gfz-potsdam.de; BorisProkhorov@yandex.ru

V. Bychkov et al. (eds.), *The Atmosphere and Ionosphere*, Physics of Earth and Space Environments, DOI 10.1007/978-94-007-2914-8_4,

epicenter area. (2) The typical zone of the anomaly maximum manifestation extends more than 1,500 km in latitude and 3,500–4,000 km in longitude. (3) Anomaly living time is from several hours or days to couple of weeks before the earthquake release moment. (4) Analogous effects at the magnetically conjugated area are often reported. (5) In the case of strong low-latitudinal earthquakes, there are effects related to the modification of the ionospheric F2-region equatorial anomaly. From the analysis of the TEC deviations before a few strong recent seismic events (12 January 2010, Haiti; 1 and 2 January 2011, Argentina and Chile; 11 March 2011, Japan), these pre-earthquake TEC signatures are extended with terminator and 'ban'-time effects. We strongly believe that the main reason for the appearance of these TEC anomalies is the vertical drift of F2-region ionospheric plasma under the influence of a zonal electric field of seismic origin. Increase of the atmospheric radioactivity level during earthquake preparation leads to enlargement of the ionization and electric conductivity of the near-ground atmosphere. Another (and possibly more effective) ionization mechanism proposed is the so-called positive holes effect. Changes of resistance of the underlying atmosphere lead to the generation of an external electric current flowing between the Earth and the ionosphere and to the corresponding disturbances of the ionospheric electric field and TEC. These disturbances were modeled by UAM and compared with the GPS TEC observations. Comparison shows satisfactory agreement between the model and observations. Methodical recommendations for detection of ionospheric earthquake precursors are given.

Keywords High-latitude ionospheric convection • Thermospheric neutral wind • Magnetosphere-ionosphere-thermosphere (MIT) coupling • Upper Atmosphere Model (UAM) • Solar wind and IMF influence • Ionospheric currents • Global total electron content (TEC) pattern • Seismogenic ionospheric effects • Earthquake precursors

4.1 Introduction

The weather, climate, and space weather (processes related to solar and geomagnetic activity) and their forecasting are extremely important for mankind. Observations and mathematical modeling used together are the modern ways for solving the forecasting needs. Modern first-principle numerical models are time dependent, three dimensional (3D), and global. Until recent years these models were being developed for the lower atmosphere (responsible for the weather and climate; heights <100 km) and upper atmosphere (responsible for space weather; heights >100 km) separately, despite the lack of any boundary between these two atmospheric regions. Their principal physical difference consists of the amount of the charged particles, the ions and electrons, that is, in their concentration (number density), which is high in the upper atmosphere and low in the lower. Therefore, electrodynamic processes are very important in the upper atmosphere (thermosphere, ionosphere, and magnetosphere).

However, electrodynamic processes are important in the lower and middle atmosphere (troposphere, stratosphere, and mesosphere) as well because of the existence of such lower atmosphere electricity sources as cosmic rays, thunderstorms, soil radioactivity, and seismodynamic effects. The lower atmosphere electric currents are connected with the ionospheric electric currents so that they are closely related to the magnetospheric currents, creating a common global electric circuit. This circuit consists of currents flowing upward from thunderstorm current generators, through the ionosphere, and down to the Earth's surface as fair-weather currents. The vertical fair-weather current between the ionosphere and the Earth is about 2–3 pA/m^2 and the total global current is about 1 kA, producing a potential difference of about 250–300 kV between the ionosphere and the Earth.

The horizontal potential difference in the ionosphere may reach 100–150 kV (usually 30–50 kV) between the morning and evening sides of the polar cap boundaries at the polar edges of the auroral zones (at about 75° magnetic latitude) in both Northern and Southern Hemispheres. The cross-polar cap potential difference (or drop) is the commonly used characteristic of the high-latitude ionospheric electric fields. Its dependences on solar and geomagnetic activity have been investigated by many authors and used as input in electric field calculations of the model.

This potential difference is generated at the magnetopause under the solar wind–magnetosphere interaction and transported into the polar ionosphere along the geomagnetic field lines via so-called field-aligned currents (FACs) of Region-1. They flow down into the ionosphere at the dawn side and up from the ionosphere at the dusk side, creating electric fields of several tens or even hundreds of mV/m in the polar caps directed from dawn to dusk. FACs of opposite signs flow at the equatorial edges of the auroral zones (Region-2 FACs). These currents shield the inner magnetosphere and the mid-latitude ionosphere from penetrating magnetospheric electric fields. This shielding and the presence of internal atmospheric dynamo processes results in smaller mid-latitude electric fields (of about several mV/m) in comparison with the high-latitude and subauroral ones.

Region-0 FACs are found during intervals of a strictly positive B_z-component of the interplanetary magnetic field (IMF). They may exist in the vicinities of the cusps. The IMF B_y-component is responsible for the asymmetry of the morning and evening cells of the ionospheric convection (plasma drift trajectories). The intensity of the FACs and the corresponding cross-polar cap potential drops (or the electric field strength) are well correlated with the southward IMF B_z-component, which can trigger magnetospheric substorm and storm generation processes.

Another source of ionospheric electric fields is the dynamo action of the thermospheric winds pushing ions across the geomagnetic field lines at ionospheric E- and F1-region heights (100–170 km), where electrons are magnetized (electron-neutral collision frequency $\nu_{en} \ll \Omega_e$ – electron cyclotron frequency) but ions are not (ion-neutral collision frequency $\nu_{in} \gg \Omega_i$ – ion cyclotron frequency). For this reason, this height region is referred to as the dynamo region. Horizontal ionospheric currents of the upper atmosphere flow predominantly in this height range.

In the ionospheric F2-region and above it (heights >170 km), both electrons and ions are magnetized (ν_{en}, $\nu_{in} \ll \Omega_e$,Ω_i) and electric currents flow first and foremost

along the geomagnetic field lines (FACs), which conduct well; exceptions are plasma drift processes in the magnetosphere, like pressure gradient-driven currents.

Because of the high electrical conductivity of the geomagnetic field lines, they can be assumed to be electrical equipotentials, so that electric fields along these lines are zero or very small. Electric fields at heights >170 km are therefore almost always perpendicular to the geomagnetic field lines. These mutually perpendicular electric ($\boldsymbol{E}$) and magnetic ($\boldsymbol{B}$) fields force the ionospheric plasma to move with the so-called $\boldsymbol{E} \times \boldsymbol{B}$ plasma drift velocity (equal to $\boldsymbol{E} \times \boldsymbol{B}/B^2$), that is, in the direction perpendicular to both. In this drift motion, ions and electrons move together with the same velocity; that is, there is no charge separation and they do not create electric currents.

Furthermore, there exists the so-called co-rotation electric field induced by the rotation of the Earth and its atmosphere around the geodetic axis. In the equatorial plane, this electric field is directed toward the Earth's center and causes the magnetized ionospheric plasma to rotate together with the Earth (to drift with the Earth's rotation velocity).

Global electric field patterns obtained mainly from satellite measurements are usually presented as polar maps of electric potential distributions for different magnetic activity levels and/or different IMF orientations. We show and discuss some of the recent data in Sect. 4.3 of this chapter.

Ionospheric $\boldsymbol{E} \times \boldsymbol{B}$ plasma drifts cause many important peculiarities of the spatial and time variations of the ionospheric plasma, such as the formation of the equatorial anomaly, the main ionospheric trough, the plasmasphere, and ionospheric disturbances related to magnetic storms and substorms.

At high and subauroral latitudes (where the geomagnetic field inclination I is near 90°–60°), the ionospheric plasma drifts affect electron density mainly because of the divergence/convergence of the horizontal plasma flows. The daytime plasma, having high density, can thus flow across the polar caps to the night side, increasing the density there. Plasma motion will stagnate where the magnetospheric convection and the co-rotation are oppositely directed with about the same velocity magnitudes. If this occurs outside the sunlit region, the plasma will be lost because of recombination processes to very low density values, forming the so-called main ionospheric trough in the dark winter ionosphere at subauroral latitudes.

At middle to low latitudes, the plasma co-rotation with the Earth leads to the formation of the plasmasphere. At these latitudes (where inclination I is small) the vertical plasma drifts also become important. Close to the equator, they cause the so-called fountain effect, forming the equatorial anomaly. At middle latitudes, they can create increases or decreases of electron density by lifting the plasma up or down the geomagnetic field lines to heights where the ion loss rate is lower or higher, respectively.

Both the ionospheric plasma drifts and the electric currents influence ion and neutral temperatures (Joule heating) via ion-neutral collisions. Thermospheric wind circulation changes the thermospheric gas composition, which in turn influences the ionospheric ion composition and electron density and so forth. The plasma physical processes within the near-Earth space environment as well as the interactions

between the various regions appear to be highly complex. To understand the dynamics of the whole system with all its interrelationships at various levels of complexity is one of the most important reasons to use first-principle models for their description. They allow us to perform "numerical experiments" and to interpret different measurements on a common basis, which may be obtained at various places far from each other by both ground-based observations and remote or in situ data gathering with satellites.

This chapter presents and discusses some of the most recent measurements of the near-Earth environment obtained by Cluster, CHAMP, and the global positioning system (GPS) satellites and their modeling in the framework of the Upper Atmosphere Model (UAM). The results concern ionospheric electric fields, generated by magnetospheric and seismogenic sources, and show their influence on the thermospheric dynamics and the ionospheric total electron content (TEC).

4.2 UAM: The Upper Atmosphere Model

The global numerical model of the Earth's upper atmosphere has been constructed at the Kaliningrad Observatory (now West Department) of the Institute of Terrestrial Magnetism, Ionosphere and Radiowave Propagation of the Russian Academy of Sciences (IZMIRAN) (Namgaladze et al. 1988, 1990, 1991, 1994) and modified at the Polar Geophysical Institute and Murmansk State Technical University (Hall et al. 1997; Namgaladze et al. 1995a, b; Volkov and Namgaladze 1996). The model describes the thermosphere, ionosphere, plasmasphere, and inner magnetosphere of the Earth as a single system by means of numerical integration of the corresponding time-dependent three-dimensional continuity, momentum, and heat balance equations for neutral, ion, and electron gases as well as the equation for the electric field potential. It covers the height range from 60 (sometimes 80) km up to 15 Earth radii of geocentric distance and takes into account the offset between the geomagnetic and geographic axes of the Earth. It consists of four main blocks:

1. The neutral atmosphere and lower ionosphere block, which calculates neutral atmosphere temperature, mass density, neutral gas composition, and winds as well as ion and electron temperatures, molecular ion density, and velocity at heights from 60 to 520 km
2. The ionospheric F2-region and protonospheric block, which calculates atomic ion O^+ and H^+ densities, velocities, and temperatures as well as electron temperature at heights from 175 km to $15R_E$ of geocentric distance
3. The electric field block, which calculates the electric field potential of magnetospheric, thermospheric (dynamo), and lower atmosphere origin, assuming that geomagnetic field lines are equipotential at heights above 175 km
4. The magnetospheric block, which calculates magnetospheric plasma sheet ion density, velocity, pressure, and field-aligned currents at the same heights as in the second block

In these blocks the corresponding continuity, momentum, and heat balance equations for the neutral, electron, and ion gases, as well as the equation for the electric field potential, are solved numerically by the use of the finite-difference methods, using different coordinate systems and different spatial grids of numerical integration. The height steps of numerical integration are variable, from 1–3 km at heights below 100 km to 30 km and more at heights above 400 km. A spherical geomagnetic coordinate system is used in the neutral atmosphere and lower ionosphere block and a geomagnetic dipole coordinate system is used in the other blocks. The exchange of information between the blocks is carried out at every time step of the numerical integration of the modeling equations.

4.2.1 Neutral Atmosphere and Lower Ionosphere Block

4.2.1.1 Neutral Atmosphere

In the neutral atmosphere section of this block, the neutral gas temperature T_n, mass density ρ, thermospheric wind velocity vector $\boldsymbol{V}$, and number densities n_n of the main neutral gas components N_2, O_2, and O are calculated for the height range from 60 to 520 km using the spherical geomagnetic coordinate system. We can perform our calculations either by solving the full system of hydrodynamic equations for the neutral gas or by using empirical thermospheric models such as MSISE-90 (Hedin et al. 1991) and its later modifications NRLMSISE-00 (Picone et al. 2002) to calculate the temperature and number densities of the main neutral gas components. In all cases the three-dimensional thermospheric circulation is calculated from the solution of the momentum and continuity equations.

The following system of the continuity, momentum, and energy balance equations for the neutral gases is solved in the fully self-consistent variant:

$$\partial n_n/\partial t + \nabla\left[n_n\left(\boldsymbol{V} + \boldsymbol{V}_{dn}\right)\right] = Q_n - L_n \tag{4.1}$$

$$\begin{aligned}&\rho[\partial \boldsymbol{V}/\partial t + (\boldsymbol{V}, \nabla)\,\boldsymbol{V} + 2\boldsymbol{\Omega} \times \boldsymbol{V}]_{\text{hor}} \\ &= -(\nabla p)_{\text{hor}} - \sum_i \sum_n \mu_{\text{ni}} \nu_{\text{ni}} n_n (\boldsymbol{V} - \boldsymbol{V}_i)_{\text{hor}} + \eta(\nabla^2 \boldsymbol{V})_{\text{hor}},\end{aligned} \tag{4.2}$$

$$\rho g = -\partial p/\partial r \tag{4.3}$$

$$\partial \rho/\partial t + \nabla(\rho \boldsymbol{V}) = 0 \tag{4.4}$$

$$\rho = \sum_n n_n m_n \tag{4.5}$$

$$p = \sum_n n_n k T \tag{4.6}$$

$$\rho c_v \left[\partial T/\partial t + (\boldsymbol{V}, \nabla) T\right] + p \nabla \boldsymbol{V} = \nabla \left(\lambda_{\mathrm{n}} \nabla T\right) + P_{\mathrm{n}Q}^{UV} + P_{\mathrm{n}Q}^{J} + P_{\mathrm{n}Q}^{C} - P_{\mathrm{n}L} \tag{4.7}$$

In these equations, n_n is the concentration of the n-th neutral component; $\boldsymbol{V}$ is the neutral wind velocity vector; $\boldsymbol{V}_{\mathrm{d}n}$ is the diffusion velocity vector, which has only a vertical component equal to the sum of molecular and eddy diffusion velocities; Q_n, L_n are the production and loss rates of the n-th neutral component taking into account the dissociation of O_2 and the reactions of recombination for O and O_2; the index "hor" stands for horizontal vector components; ρ, p are the mean mass density and pressure of the neutral gas; $\boldsymbol{\Omega}$ is the Earth's angular velocity vector; μ_{ni}, ν_{ni} are the reduced mass and frequency of collisions between the neutral and ion components of the atmosphere; $\boldsymbol{V}_{\mathrm{i}}$ is the ion velocity vector; η is the coefficient of viscosity; g is the sum of gravity and centrifugal accelerations; r is the geocentric distance; m_n is the mass of the n-th neutral component; k is the Boltzmann's constant; T is the temperature of the neutral gas; c_{v} is the specific heat at constant volume; λ_{n} is the thermal conductivity coefficient of the neutral gas; $P_{\mathrm{n}Q}^{\mathrm{UV}}$, $P_{\mathrm{n}Q}^{\mathrm{J}}$, and $P_{\mathrm{n}Q}^{\mathrm{C}}$ are the rates of heating of the neutral gas by ultraviolet (UV) and extra-ultraviolet (EUV) solar radiation, Joule heating, and heating by precipitating energetic particles; and $P_{\mathrm{n}L}$ is the rate of heat loss of the neutral gas resulting from radiation. The detailed expressions for all coefficients and terms of Eqs. 4.1, 4.2, 4.3, 4.4, 4.5, 4.6, and 4.7 and their form in a spherical geomagnetic coordinate system can be found in Namgaladze et al. (1988) and in Brunelli and Namgaladze (1988).

We use Eq. 4.1 to compute the O and O_2 concentrations; the total mass density ρ is calculated from the hydrostatic equilibrium equation, Eq. 4.3. As for the N_2 concentration, the barometric law for the molecular nitrogen density is used to calculate it above the turbopause level instead of calculating it as difference between the total mass density and mass density of molecular and atomic oxygen (Eq. 4.5) because of great errors that arise when this difference is small. Equations 4.2 are used to calculate the horizontal meridional (V_x) and zonal (V_y) components of the neutral wind velocity. To obtain the vertical wind velocity we use the continuity equation, Eq. 4.4, because the vertical component of the momentum equation for the neutral gas is reduced to Eq. 4.3, which does not contain the vertical component of the neutral wind velocity. At last, the heat balance equation (Eq. 4.7) is used to compute the neutral temperature T.

The system of Eqs. 4.1, 4.2, 4.3, 4.4, 4.5, 4.6, and 4.7 is completed by initial and boundary conditions. At the upper boundary ($h = 520$ km) we assume that

$$\partial \boldsymbol{V}/\partial r = \partial T/\partial r = 0$$

and all neutral components are in the diffusion equilibrium there. At the lower boundary ($h = 60$ km) the wind velocity is taken according to the geostrophic

approximation (or tides can be assumed alternatively), and the temperature and concentrations of the neutral components are taken from the empirical thermospheric models (see foregoing). We also use these models to obtain the initial spatial distribution of the neutral concentrations and temperature. As for wind, we use zero velocity as the initial condition. To obtain a stationary solution we need to integrate the modeling equation system until the results of integration remain practically unchanged when containing the integration. Usually, to reach it, several days (geophysical but not computing time) of integration are required.

4.2.1.2 Lower Ionosphere (D, E, and F1 Ionospheric Regions)

In this section the following parameters of D, E, and F1 ionospheric regions are calculated: the total concentration of the molecular ions $n(XY^+) = n(NO^+) + n(O_2{}^+) + n(N_2{}^+)$, ion and electron temperatures T_i and T_e and the molecular ion velocity $\boldsymbol{V}(XY^+)$ for the height range from 60 to 175 km (for T_i and T_e) or 520 km (for $n(XY^+)$ and $\boldsymbol{V}(XY^+)$). The following equations are solved:

$$\partial n\left(XY^+\right)/\partial t = Q\left(XY^+\right) - L\left(XY^+\right) \tag{4.8}$$

$$(3n_i k/2)\,\partial T_i/\partial t = P_{iQ}^{J} + P_{iT}^{e} + P_{iT}^{n} \tag{4.9}$$

$$(3n_e k/2)\,\partial T_e/\partial t = P_{eQ}^{p} + P_{eQ}^{c} + P_{eT}^{i} + P_{eT}^{n} \tag{4.10}$$

$$n_i m_i \boldsymbol{g} - \nabla\left(n_i k T_i\right) - \sum_n \mu_{in}\nu_{in} n\left(\boldsymbol{V}_i - \boldsymbol{V}\right) + e n_i(\boldsymbol{E} + \boldsymbol{V}_i \times \boldsymbol{B}) = 0 \tag{4.11}$$

$$\nabla\left(n_e k T_e\right) + e n_e(\boldsymbol{E} + \boldsymbol{V}_e \times \boldsymbol{B}) = 0 \tag{4.12}$$

$$n_e = n_i = n\left(XY^+\right) \tag{4.13}$$

In these equations $Q(XY^+)$, $L(XY^+)$ are the production and loss rates of the molecular ions taking into account ionization by solar EUV direct and scattered radiation, ionization by precipitating electrons, ion molecular reactions and dissociative recombination; P_{iQ}^{J} is the rate of the Joule heating of the ion gas; P_{iT}^{e} and P_{iT}^{n} are the rates of the heat exchange between ion and electron and neutral gases; n_e is the electron concentration; P_{eQ}^{p} and P_{eQ}^{c} are the rates of heating of the electron gas by photoelectrons and by precipitating magnetospheric electrons, respectively; $P_{eT}^{i} = -P_{iT}^{e}$; P_{eT}^{n} is the rate of the elastic and inelastic exchange of heat between electron and neutral gases; m_i is ion mass; $\boldsymbol{g}$ is the vector of gravity acceleration; $\nu_{in} n_i = \nu_{ni} n_n$; e is the electron charge; and $\boldsymbol{E}$, $\boldsymbol{B}$ are the electric and magnetic fields. More information about the terms of Eqs. 4.8, 4.9, 4.10, 4.11, and 4.12 can be found in Namgaladze et al. (1988) and Brunelli and Namgaladze (1988).

As one can see from Eqs. 5.8, 5.9, and 5.10, we neglect the heat and charge particle transport processes in the D, E, and F1 ionospheric regions because of the dominating photochemical, local heating, and heat exchange processes in these ionospheric regions. Equations 4.11 and 4.12 are used to obtain the components of the ion velocity vector, which are needed to calculate the thermospheric wind and temperature, taking into account ion drag and Joule heating.

4.2.2 Ionospheric F2-Region and Protonosphere Block

In this block, parameters of the ionospheric F2-region and the protonosphere (plasmasphere and inner magnetosphere cold plasma) are calculated, namely, the atomic oxygen and hydrogen ion number densities $n(O^+)$ and $n(H^+)$ as well as ion and electron temperatures T_i and T_e and ion velocities $\boldsymbol{V}(O^+)$ and $\boldsymbol{V}(H^+)$ for the height range from 175 km to the radial distance of $15R_E$. We consider that all charged components of the upper atmosphere are fully magnetized above 175 km because $\nu_{in} \ll \Omega_i$ at these heights (where Ω_i is ion gyrofrequency) so that the geomagnetic field has a very strong influence on the behavior of the ion and electron gases. For this reason, we use the magnetic dipole coordinate system in this block and perform the integration of modeling equations along dipole geomagnetic field lines simultaneously, taking into account electromagnetic plasma drift perpendicular to geomagnetic field lines. The following continuity, momentum, and heat balance equations are solved in this block:

$$\mathrm{D}n_\mathrm{i}/\mathrm{D}t + \nabla^{\mathrm{par}}\left(n_\mathrm{i}V_\mathrm{i}^{\mathrm{par}}\right) = Q_\mathrm{i} - L_\mathrm{i} - n_\mathrm{i}\nabla^{\mathrm{per}}\boldsymbol{V}^{\mathrm{per}} \tag{4.14}$$

$$\begin{aligned} 2m_\mathrm{i}n_\mathrm{i}(\boldsymbol{\Omega}\times\boldsymbol{V}_\mathrm{i})^{\mathrm{par}} &= m_\mathrm{i}n\boldsymbol{g}^{\mathrm{par}} - \nabla^{\mathrm{par}}\left(n_\mathrm{i}kT_\mathrm{i}\right) - \left(n_\mathrm{i}/n_\mathrm{e}\right)\nabla^{\mathrm{par}}\left(n_\mathrm{e}kT_\mathrm{e}\right) \\ &- \sum_n \mu_{\mathrm{in}}\nu_{\mathrm{in}}n_\mathrm{i}\left(\boldsymbol{V}_\mathrm{i}^{\mathrm{par}} - \boldsymbol{V}^{\mathrm{par}}\right) - \sum_\mathrm{j}\mu_{\mathrm{ij}}\nu_{\mathrm{ij}}n_\mathrm{i}\left(\boldsymbol{V}_\mathrm{i}^{\mathrm{par}} - \boldsymbol{V}_\mathrm{j}^{\mathrm{par}}\right) \end{aligned} \tag{4.15}$$

$$\boldsymbol{V}_\mathrm{i}^{\mathrm{per}} = \boldsymbol{V}_\mathrm{e}^{\mathrm{per}} = \boldsymbol{E}\times\boldsymbol{B}/B^2 \tag{4.16}$$

$$\boldsymbol{V}_\mathrm{e}^{\mathrm{per}} = \sum_\mathrm{i} n_\mathrm{i}\boldsymbol{V}_\mathrm{i}^{\mathrm{per}}/n_\mathrm{e} \tag{4.17}$$

$$\begin{aligned} &(3n_\mathrm{i}k/2)\left(DT_\mathrm{i}/Dt + \boldsymbol{V}_\mathrm{i}^{\mathrm{par}}\nabla^{\mathrm{par}}T_\mathrm{i}\right) + \left(n_\mathrm{i}kT_\mathrm{i}\right)\nabla\boldsymbol{V}_\mathrm{i}^{\mathrm{par}} - \nabla^{\mathrm{par}}(\kappa_\mathrm{i}\nabla^{\mathrm{par}}T_\mathrm{i}) \\ &= P_{\mathrm{i}Q}^{\mathrm{J}} + P_{\mathrm{i}T}^{\mathrm{e}} + P_{\mathrm{i}T}^{\mathrm{j}} + P_{\mathrm{i}T}^{\mathrm{n}} \end{aligned} \tag{4.18}$$

$$\begin{aligned} &(3n_\mathrm{e}k/2)\left(DT_\mathrm{e}/Dt + \boldsymbol{V}_\mathrm{e}^{\mathrm{par}}\nabla^{\mathrm{par}}T_\mathrm{e}\right) + \left(n_\mathrm{e}kT_\mathrm{e}\right)\nabla\boldsymbol{V}_\mathrm{e}^{\mathrm{par}} - \nabla^{\mathrm{par}}\left(\kappa_\mathrm{e}\nabla^{\mathrm{par}}T_\mathrm{e}\right) \\ &= P_{\mathrm{e}Q}^{\mathrm{p}} + P_{\mathrm{e}Q}^{\mathrm{c}} + P_{\mathrm{e}T}^{\mathrm{i}} + P_{\mathrm{e}T}^{\mathrm{j}} + P_{\mathrm{e}T}^{\mathrm{n}} \end{aligned} \tag{4.19}$$

In these equations the subscripts i, j, and e refer to ions O^+, H^+, and electrons, respectively. The symbols par and per refer to the directions parallel and perpendicular to the geomagnetic field. The operator $D/Dt = \partial/\partial t + (\boldsymbol{V}_{\text{per}}, \nabla)$ gives the Langrangian temporal derivatives along the electromagnetic drift trajectory determined by Eq. 4.16. Q_i, L_i are the production and loss rates of O^+ and H^+ ions, which take into account the photo- and corpuscular ionization, ion molecular reactions between O^+ and O_2 and N_2, charge exchange processes between O^+ and H and between H^+ and O; $\boldsymbol{g}^{\text{par}}$ is a geomagnetic field-aligned component of the sum of gravity and centrifugal accelerations; $P^{\text{J}}_{\text{i}Q}$ is the rate of the Joule heating of the ion gas; $P^{\text{e}}_{\text{i}T}$, $P^{\text{j}}_{\text{i}T}$, $P^{\text{n}}_{\text{i}T}$ are the ion heat exchange rates; $P^{\text{p}}_{\text{e}Q}$, $P^{\text{c}}_{\text{e}Q}$ are the rates of local and nonlocal heating of the electron gas by photoelectrons and by precipitating magnetospheric electrons; and $P^{\text{i}}_{\text{e}T}$, $P^{\text{j}}_{\text{e}T}$, $P^{\text{n}}_{\text{e}T}$ are the electron heat exchange rates.

For the densities of neutral hydrogen we use the barometric law with a boundary condition at 500-km altitude from the neutral atmosphere model of Jacchia (1977). Detailed description of the terms of Eqs. 4.14, 4.15, 4.16, 4.17, 4.18, and 4.19 has been given by Namgaladze et al. (1988) and Brunelli and Namgaladze (1988).

The integration of Eqs. 4.14, 4.15, 4.16, 4.17, 4.18, and 4.19 is done along lines of a dipole geomagnetic field drifting with the speed of Eq. 4.16. The boundary conditions are given near the bases of the field lines in Northern and Southern Hemispheres at a height of 175 km. The atomic ion concentrations at this boundary are obtained from photochemical equilibrium conditions. The values of the ion and electron temperatures at this boundary are calculated from Eqs. 4.9 and 4.10 of heat balance. We assume that geomagnetic field lines with $L \geq 15$ (L parameter of McIlwain) are open and ion concentrations and heat fluxes are set equal to 0 at $r = 15\ R_E$.

Zero ion concentrations, and ion and electron temperatures equal to the temperature of the neutral gas, or, alternatively, the results of preceding calculations of the modeled parameters or input values from empirical ionospheric models, may be chosen as initial conditions.

4.2.3 Electric Field Computation Block

The next block of our model is the electric field computation block. The equation for the potential φ of the electrostatic field $-\nabla\varphi$ is solved numerically in this block, taking into account the dynamo action of the thermospheric winds:

$$\text{div}\,\boldsymbol{j} = \text{div}\,(\boldsymbol{j}_\text{i} + \boldsymbol{j}_m + \boldsymbol{j}_\text{l}) = \nabla\left[\sigma^\text{T}\,(-\nabla\varphi + \boldsymbol{V} \times \boldsymbol{B}) + \boldsymbol{j}_m + \boldsymbol{j}_\text{l}\right] = 0 \quad (4.20)$$

where σ^T is the ionospheric conductivity tensor and $\boldsymbol{j}_\text{i}$, $\boldsymbol{j}_\text{m}$, and $\boldsymbol{j}_\text{l}$ are the ionospheric, magnetospheric, and lower atmosphere current densities, respectively. The last two are used as input parameters at the upper (175 km) and lower (60 km) boundaries of the electric field computation block.

The ionospheric conductivity is a tensor, and Ohm's law for the ionospheric current can be written as

$$\boldsymbol{j}_{\mathrm{i}} = \sigma_{\mathrm{par}} \boldsymbol{E}_{\mathrm{par}} + \sigma_{\mathrm{p}} \boldsymbol{E}_{\mathrm{per}} + \sigma_{\mathrm{h}} \left[\boldsymbol{b} \times \boldsymbol{E}_{\mathrm{par}}\right] \tag{4.21}$$

$$\boldsymbol{E}_{\mathrm{par}} = B\,(B, \boldsymbol{E})\,/B^2, \quad \boldsymbol{E}_{\mathrm{per}} = B \times [\boldsymbol{E} \times B]\,/B^2$$

where σ_{h}, σ_{p}, and σ_{par} are the Hall, Pedersen, and along $\boldsymbol{B}$ conductivities, correspondingly.

$$\sigma_{\mathrm{h}} = e^2 n_{\mathrm{e}} \left[\Omega_{\mathrm{e}}/m_{\mathrm{e}} \left(\Omega_{\mathrm{e}}^2 + \nu_{\mathrm{en}}^2\right) - \Omega_{\mathrm{i}}/m_{\mathrm{i}} \left(\Omega_{\mathrm{i}}^2 + \nu_{\mathrm{in}}^2\right)\right]$$

$$\sigma_{\mathrm{p}} = e^2 n_{\mathrm{e}} \left[\nu_{\mathrm{in}}/m_{\mathrm{i}} \left(\Omega_{\mathrm{i}}^2 + \nu_{\mathrm{in}}^2\right) + \nu_{\mathrm{en}}/m_{\mathrm{e}} \left(\Omega_{\mathrm{e}}^2 + \nu_{\mathrm{en}}^2\right)\right]$$

$$\sigma_{\mathrm{par}} = e^2 n_{\mathrm{e}} \left[1/m_{\mathrm{i}}\nu_{\mathrm{in}} + 1/m_{\mathrm{e}}\nu_{\mathrm{en}}\right]$$

where m_{i}, m_{e} are ion and electron masses, Ω_{i}, Ω_{e} are ion and electron cyclotron frequencies, and ν_{in}, ν_{en} are ion-neutral and electron-neutral collision frequencies.

$\boldsymbol{E} = -\nabla\varphi + \boldsymbol{V} \times \boldsymbol{B}$, where φ is electrostatic potential, $\boldsymbol{V} \times \boldsymbol{B}$ is the so-called induction dynamo field, and $\boldsymbol{V}$ is neutral gas velocity vector.

After integrating of Eq. 4.20 over the height of the current-carrying layer with neglect of the height dependence of the electric field components in this layer, the problem to define the electric potential becomes two dimensional and is solved by an iterative technique in the geomagnetic coordinate system. The ionospheric conductivities needed to solve Eq. 4.20 are calculated using the standard formulae with parameter values of the ionosphere and thermosphere taken from the thermospheric and ionospheric-protonospheric blocks of the model. The 3D patterns of the electric potential and electric field vector components are calculated using the solution of Eq. 4.20 together with the condition of the electrical equipotentiality of the geomagnetic field lines above 175 km.

4.2.4 Magnetospheric Block

The magnetospheric block (Volkov and Namgaladze 1996) contains the following equations for the magnetospheric plasma:

$$\partial n_{\mathrm{i}}/\partial \mathrm{t} + \nabla\,(n_{\mathrm{i}} \boldsymbol{V}_{\mathrm{i}}) = 0 \tag{4.22}$$

$$n_{\mathrm{i}} e(\boldsymbol{E} + \boldsymbol{V}_{\mathrm{i}} \times \boldsymbol{B}) = \nabla p_{\mathrm{i}} \tag{4.23}$$

$$\mathrm{d}\,(p_{\mathrm{i}} V^{\gamma})\,/\mathrm{d}t = 0, \quad \gamma = 5/3 \tag{4.24}$$

$$j_{//} = \boldsymbol{e}_z \left[\nabla V, \nabla p_\mathrm{i}\right] / B, \quad V = B \int_0^l B^{-1} \mathrm{d}z, \tag{4.25}$$

where $j_{//}$ is the field-aligned current density, $\boldsymbol{E}$ and $\boldsymbol{B}$ are the electric and geomagnetic fields, $\boldsymbol{e}_z$ is the field-aligned (along $\boldsymbol{B}$) unit vector, V is a half-volume of the geomagnetic field tube, z is a distance along the geomagnetic field line, l is the value of z at the top of the geomagnetic field line, p_i is the magnetospheric ion gas pressure considered isotropic and constant along the geomagnetic field line, n_i is the magnetospheric ion concentration, $\boldsymbol{V}_\mathrm{i}$ is the magnetospheric ion drift velocity, and e is the electron charge. The magnetospheric electrons are considered to be cold, and their pressure is neglected in comparison with that of the magnetospheric ions. The geomagnetic field is considered as a dipole at latitudes equatorward of the polar cap boundary ($\Phi = 75°$) and having the field lines opened inside the polar cap areas.

4.2.5 Inputs of the Model

The input parameters of the model are (1) solar UV and EUV spectra; (2) precipitating particle fluxes; (3) field-aligned currents connecting the ionosphere with the magnetosphere and/or the electric field potential distribution at the polar cap boundaries; and (4) vertical currents at the lower ionospheric boundary flowing from the lower atmosphere. For the solar UV and EUV fluxes and their dependencies on solar activity we use the data from Ivanov-Kholodny and Nusinov (1987). Intensities of night sky scattered radiation are chosen equal to 5 kR for $\lambda = 121.6$ nm and 5 R for each of the other emission lines ($\lambda\lambda = 102.6$ nm, 58.4 nm, and 30.4 nm).

Spatial distributions of the precipitating electron fluxes are taken at the upper boundary of the thermosphere ($h = 520$ km) in a simple form:

$$I\left(\Phi, \Lambda, E\right) = I_\mathrm{m}(E) \exp\left[-\left(\Phi - \Phi_\mathrm{m}(E)\right)^2 \Big/ \left(\Delta\Phi(E)\right)^2 - \left(\Lambda - \Lambda_\mathrm{m}(E)\right)^2 \Big/ \left(\Delta\Lambda(E)\right)^2\right] \tag{4.26}$$

$$\Phi_\mathrm{m} = \left(\Phi_\mathrm{md} + \Phi_\mathrm{mn}\right)/2 + \left(\cos\Lambda\right)\left(\Phi_\mathrm{md} - \Phi_\mathrm{mn}\right)/2 \tag{4.27}$$

where Φ, Λ are geomagnetic latitude and longitude, $\Lambda = 0$ corresponds to the midday magnetic meridian, $I_\mathrm{m}(E)$ is the maximum intensity of the precipitating electron flux, E is the energy of the precipitating electrons, and Φ_md, Φ_mn are the geomagnetic latitudes of the maximum precipitation at the midday and midnight magnetic meridians. All precipitation parameters (I_m, Φ_md, Φ_mn, $\Delta\Phi$, Λ_m, $\Delta\Lambda$) can vary depending on geophysical conditions.

The magnetospheric sources of the electric field are field-aligned currents in Region-1 and -2 and in the cusp region (Iijima and Potemra 1976). The Region-1 field-aligned currents, flowing into the ionosphere on the dawn side and out on the

dusk side, are at the polar cap boundary (±75° magnetic latitude). The Region-2 field-aligned currents flowing opposite to the Region-1 currents are located equatorward of them. The spatial distributions of the current intensities in all zones vary in dependence on the geophysical conditions. If we do not use the magnetospheric block, we either take all FAC regions as inputs of the model or we take the electric potential distribution at the polar cap boundary and the cusp and Region-2 FACs as inputs. When we use the magnetospheric block, we take the electric potential distribution at the polar cap boundary and the cusp FACs as inputs. In this case, the Region-2 FACs are calculated self-consistently in the magnetospheric block, and the precipitating electron fluxes are taken in proportion to the magnetospheric plasma-sheet ion number density, being normalized to empirical models such as that given by Hardy et al. (1985) and others.

4.2.6 Numerical Grids

In the neutral atmosphere and lower ionosphere block, Eqs. 4.1, 4.2, 4.3, 4.4, 4.5, 4.6, 4.7, 4.8, 4.9, 4.10, 4.11, 4.12, and 4.13 are solved by finite-difference numerical methods in a spherical geomagnetic coordinate system. In the preceding calculations (Namgaladze et al. 1988, 1990, 1991, 1994) the steps of the numerical integration were 10° in geomagnetic latitude, 15° in geomagnetic longitude, variable in altitude (3 km near the lower boundary at $h = 80$ km, 5 km near $h = 115$ km, 15 km near $h = 220$ km, 25 km near $h = 330$ km, and 40 km near $h = 500$ km, resulting in 30 levels for the altitude range from 80 to 520 km) and 5 min in time. For the present calculations of this study we choose mostly higher resolutions, depending on the simulation task.

The neutral atmosphere parameters calculated in the spherical geomagnetic coordinate system are interpolated to the nodes of the finite-difference magnetic dipole coordinate grid to calculate the parameters of the ionospheric F2-region and the protonosphere. Previously, we had used the following steps of this grid: 5° or 8° in latitude near the bases of the geomagnetic field lines at 175 km altitude, and 15° in longitude and variable in distance along the geomagnetic field lines. The number of the nodes of the grid along $\boldsymbol{B}$ varies from 9 on the innermost equatorial field line to a maximum value of 140 on the field line with $L = 15$. In turn, the necessary parameters of the ion and electron gases are put into the neutral atmosphere block from the ionospheric F2 region and protonosphere block, which uses the electric field values obtained from the electric field computation block. In this latter block a two-dimensional grid was used with 5° latitude and 15° longitude steps.

Later, the following main alterations have been done (Namgaladze et al. 1995a, b). In all blocks the constant latitudinal steps of the numerical integration of the modelling equations have been replaced by the differences $\Phi_i - \Phi_k$, which are not constant but depend on latitude, that is, they depend on the numbers of the i-th and k-th latitudinal nodes of the grid, which, in turn, depend on latitude. So, in each block the kind of the grid is determined by its own law of the dependence of the latitudinal step on latitude.

4.3 High-Latitude Thermospheric Winds: CHAMP Satellite Observations and UAM Modeling

4.3.1 Magnetosphere–Ionosphere Coupling Under External Forcings

The largest magnitudes of neutral wind speed anywhere on the globe were found to occur within the high-latitude upper thermosphere. Long-term observations with ground-based Fabry-Perot interferometers (FPI) located at Thule and Søndre Strømfjord, Greenland, for example, showed typical wind speeds of about 200 m/s at solar minimum, rising to about 800 m/s at solar maximum, depending on the geomagnetic activity level (Killeen et al. 1995).

The high-latitude upper atmosphere and its embedded ionized layers are known to be controlled by both solar EUV radiation and magnetospheric processes, as precipitations of energetic particles and plasma convection, driven mainly by reconnection processes at the magnetopause and in the magnetospheric tail. Thermospheric winds respond rather directly via ion drag to plasma motions in the ionosphere that are imposed by the solar wind–magnetosphere interaction and the resulting large-scale magnetospheric plasma drift at high latitudes. The thermospheric drag mode is particularly efficient with respect to the main outer magnetospheric generator processes, mediated primarily via the Region-1 current system of Iijima and Potemra. Vasyliūnas (2007) talks in this context about the mechanical advantage of the magnetosphere: the Lorentz force in the outer magnetosphere is coupled with a Lorentz force in the ionosphere in such a way that it becomes amplified by a factor given approximately by the square root of the magnetic field magnitude ratio. The electromagnetic forces are very effective, as has been shown, for example, with the energy input estimation by Siscoe and Siebert (2006), concerning the strong neutral air accelerations during a particular superstorm event, the so-called Bastille storm of mid-July (by accident, during this day the CHAMP satellite was launched).

Relative motions of the neutral gas and ionized components result in Joule heating of the ionosphere and thermosphere, being proportional to the square of the velocity difference. A recent study showed mesoscale structures and variations of the thermosphere on the scales of tens of kilometers and minutes that indicate a very dynamic response to ionospheric forcing (Aruliah et al. 2004).

Coupling between the ionized layers of the upper atmosphere and the thermospheric neutral gas is mediated through magnetic field changes and both field-aligned and ionospheric currents. This electrodynamic system is driven by processes of momentum and energy transfer, mainly reconnection, between the highly variable solar wind and its inherent interplanetary magnetic field with the magnetosphere and by inner magnetospheric plasma processes. These processes are particularly important at high latitudes, and they constitute a vital driving force for the transpolar thermospheric wind circulation.

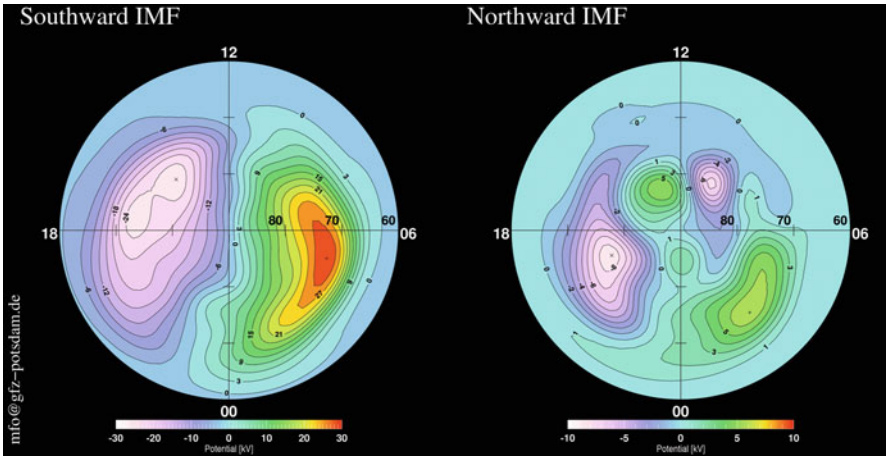

Fig. 4.1 Electric potential patterns for the Northern Hemisphere, as a function of the interplanetary magnetic field (IMF) orientation, derived from measurements of the Electron Drift Instrument (EDI) on board the Cluster S/C (Förster et al. 2007; Haaland et al. 2007). Patterns represent statistical averages of the large-scale magnetospheric circulation, mapped into the polar ionosphere, for (**a**) southward and (**b**) northward IMF conditions. Note the different color scale ranges: three times larger for the *left panel*

Figure 4.1 illustrates the results obtained by this kind of studies, showing the high variability of the plasma drift pattern in dependence on the IMF orientation. The left panel is a statistical average of strict southward IMF (large negative IMF B_z values in Geocentric Solar Magnetospheric (GSM) coordinates), where the energy and momentum transfer from the solar wind by front-side reconnection is most effective, and the right panel shows a four-cell pattern that develops under strict northward IMF conditions (positive IMF B_z). The contrast between these two patterns of different IMF orientation illustrates the 'bandwidth' of possible forcings.

On the other hand, the motion of the thermospheric neutral air across geomagnetic field lines within the so-called ionospheric dynamo region (∼80 to ∼175 km) or in the F-layer dynamo region leads to the generation of internal electric fields. The inertia of the thermospheric neutral winds can therefore help to maintain the ionospheric-magnetospheric convection independently of the magnetospheric driver processes; this has been known for long time as the flywheel effect (Banks 1972; Coroniti and Kennel 1973). The contribution of this thermosphere–ionosphere interaction was already implied in Fig. 4.1 as part of the statistical average patterns.

4.3.2 The Climatological View: Statistically Averaged Patterns

The CHAllenging Minisatellite Payload (CHAMP) mission was launched in July 2000 into a circular near-polar orbit with 87.3° inclination, initially at an altitude of

460 km, and it is managed by the GFZ German Research Centre for Geosciences, Helmholtz Centre Potsdam. This mission was designed to perform detailed studies of the Earth's gravitational and geomagnetic field with unprecedented accuracies and space–time resolutions as well as GPS atmosphere and ionosphere profiling (Reigber et al. 2002). One key scientific instrument on board CHAMP was a triaxial accelerometer for in situ measurements at F-layer heights (∼300–450 km). Located at the spacecraft's center of mass, it effectively probed the in situ acceleration with an accuracy of $\sim 3 \times 10^{-9}$ m s^{-2} (Doornbos et al. 2010). Accelerometers carried by satellites provide valuable data for improving our understanding of the thermospheric density and neutral winds at upper atmosphere altitudes (>∼250 km).

From the air drag observations, thermospheric mass density and cross-track neutral wind have been obtained using a first set of calibrations and, as far as it concerns the wind measurements, a simplified methodology (Liu et al. 2006a). This method neglects lift and sideways forces on the spacecraft or requires that these forces were modeled and removed from the acceleration beforehand, as was done later by Sutton et al. (2007), who named it a "dual-axis method." Using these first cross-track wind estimations, a preliminary study on the algorithm to deduce statistical pattern of the high-latitude thermospheric wind circulations for 1 year of moderate to high solar activity (2003) and its dependence on the IMF orientation has been performed by Förster et al. (2008). This analysis has been repeated here in Fig. 4.2 (cf. also Förster et al. 2011) with a newly calibrated CHAMP data set, performed recently within an European Space Agency (ESA) project study, where an improved methodology of neutral wind determination was implemented. The new method employs a sophisticated iterative algorithm for determining density and the crosswind component simultaneously from multi-axis accelerometer measurements. It makes use of detailed numerical models of the spacecraft's surface interaction with various radiation sources and aerodynamic forces (Doornbos et al. 2010).

Figure 4.2 shows the average circulation at the Northern Hemisphere for moderate to high solar activity conditions of the full year 2003 without sorting for any IMF dependence as measured by the CHAMP accelerometer (for the south polar cap see, e.g., Förster et al. 2011). The method for deriving full vector plots from the single-component (cross-track) measurements was explained by Förster et al. (2008). Some peculiarities, which are the result of the tight coupling to the plasma drift and the specific high-latitude electrodynamics, are already obvious in the average circulation pattern. Among them are the large-amplitude anti-solar cross-polar streaming over the central polar cap with the occurrence of an extended clockwise vortex in the dusk sector, a stream stagnation region equatorward of the cusp position, and some deflection in the counterclockwise sense on the dawn side. The large dusk side circulation cell is nearly co-located with the position of the plasma drift dusk cell for southward IMF (see Fig. 4.1, left panel). Vorticity studies of the high-latitude neutral wind confirm the circulation cell structure with opposite vorticity orientations at the dawn and dusk sides, some prevalence in magnitude of the dusk over the dawn side vortex, and the strong dependence of the circulation pattern on IMF B_z and B_y (Förster et al. 2011).

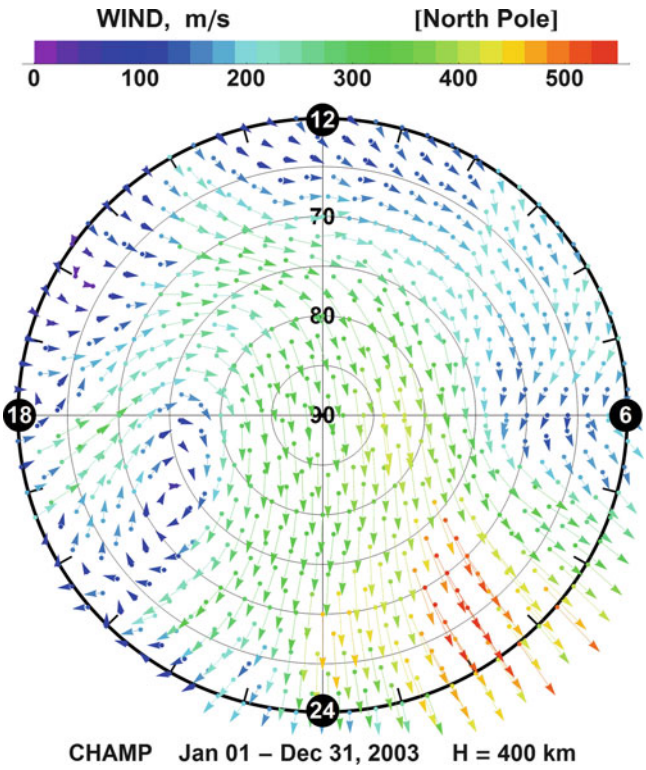

Fig. 4.2 Average North Hemisphere thermospheric wind pattern given in polar geomagnetic coordinates (>60° magnetic latitude) at F-layer heights (∼400 km) using cross-track CHAMP accelerometer data of the full year 2003 as obtained from a recent European Space Agency (ESA) study (Doornbos et al. 2010). The sun's position of the dial is at top of the figure, with dawn side at *right* and dusk to the *left*. The wind direction is shown by small vectors with the origin in the dots at the bin's position; their length and color coding indicates the wind vector magnitude with the scale given on *top*

As already shown by earlier theoretical work and numerical modeling (e.g., Killeen and Roble 1984; Killeen et al. 1995; Rees et al. 1986; Thayer and Killeen 1993), the dusk side vorticity as driven by the plasma component is preferably sustained by a favorable action of the Coriolis force. Any detailed analysis of high-latitude dynamics and energetics requires numerical methods and modelings because of the complexity of these processes (thermodynamic, electrodynamic, gas kinetic, etc.).

To obtain information about the external driving forces from IMF and solar wind interactions with the magnetosphere, we consider patterns of magnetospheric convection drift velocities, which map into the upper ionosphere at high latitudes, provided the characteristic time scales are large enough to be considered as quasi-static. There are numerous measurement methods, both ground based (e.g., radars

such as the SuperDARN network; Ruohoniemi and Greenwald 2005) and based on in situ measurements at ionospheric heights by satellites (e.g., Weimer 1995, 2005), but we use here statistical data obtained in the spacious area of the whole magnetosphere by the Cluster satellites during the same time interval as the CHAMP data acquisition.

The Cluster mission is an European Space Agency (ESA) project, launched in 2000, comprising four identical satellites flying in close formation around the Earth. Cluster has a nearly 90° inclination elliptical polar orbit, with initial perigee at around 4 RE and apogee around 19 RE geocentric distance, and an orbital period of approximately 57 h (Escoubet and Schmidt 1997). Measurements of the plasma convection (or drift) velocity have been obtained with the Electron Drift Instrument (EDI) on board Cluster. The basis of the electron drift technique is the injection of 2 weak beams of electrons and their detection after one or more gyrations in the ambient magnetic field. Because of their cycloidal motion, beam electrons can return to the associated detectors only when fired in directions uniquely determined by the magnitude and direction of the plasma drift velocity. The drift velocity is computed either from the direction of the beams (via triangulation) or from the difference in their times-of-flight. An important advantage of EDI for high-latitude convection measurements is its immunity from wake effects that can interfere with the double-probe measurements under conditions of low plasma density that often occur over the polar cap. Furthermore, the EDI measures the entire vector drift velocity, which is equivalent to the transverse electric field when gradient drift effects are small, as it is the case over the polar cap (for more details, see, e.g., Paschmann et al. 2001).

Vector measurements of the EDI instrument, available for several years, have been used to derive statistical maps of the high-latitude plasma convection, as shown here in Fig. 4.3 for the Southern Hemisphere. The EDI measurements, obtained at geocentric distances between 4 and 15 RE over both hemispheres, are mapped into the polar ionosphere and sorted according to the clock angle of the IMF as measured at ACE upstream in the solar wind (Förster et al. 2007, 2009; Haaland et al. 2007). The IMF clock angle considers the orientation of the IMF in the GSM yz-plane, with zero angle for purely northward IMF and then counted clockwise in this plane, so that we have $+90°$ for sector 2, $\pm 180°$ for sector 4 (purely southward IMF), and so on.

Comparison with published statistical results based on Super Dual Auroral Radar Network (SuperDARN) radar (e.g., Ruohoniemi and Greenwald 2005) and low-altitude satellite measurements (e.g., Weimer 2005) shows excellent agreement of the average convection patterns, and in particular the incomplete mirror symmetry between the effects of positive and negative IMF B_y, the appearance of a duskward flow component for strongly southward IMF, and the general weakening of the flows and potentials for northward IMF orientations (sector 0). This agreement lends credence to the validity of the assumption underlying the mapping of the EDI data, namely, that magnetic field lines are equipotentials.

Figure 4.4 gives an impression about the influence of the IMF orientation and the differences between the hemispheres. The wind amplitudes are smallest

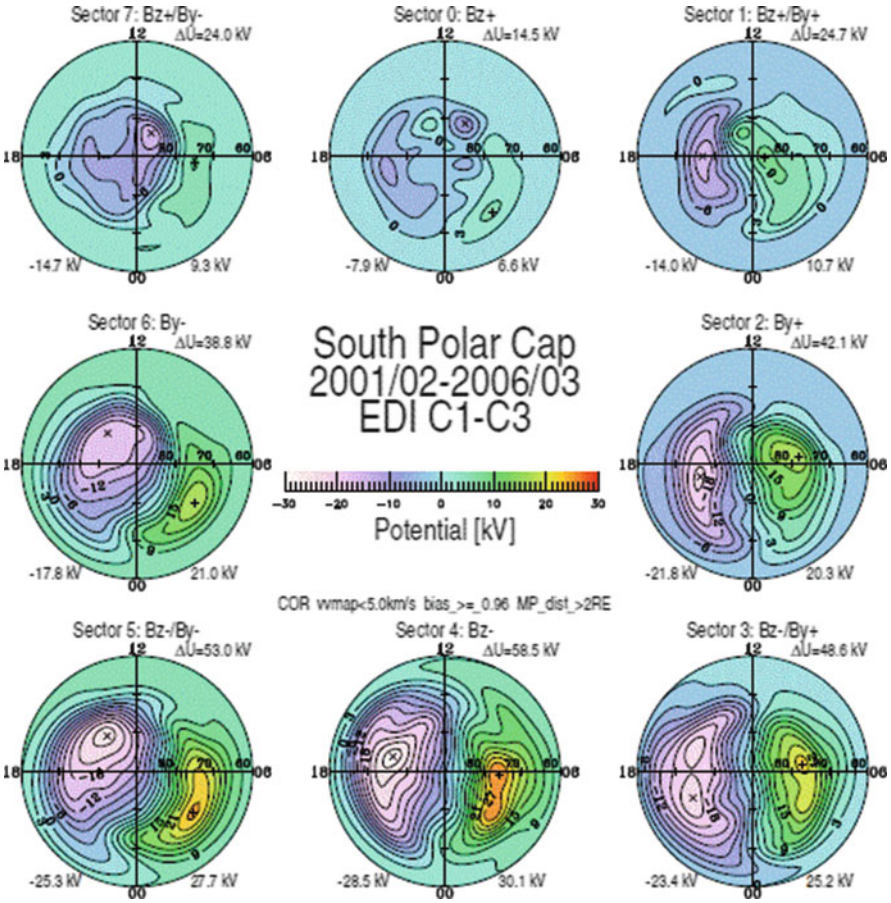

Fig. 4.3 Electric potentials obtained from Cluster EDI measurements that were mapped into the Southern Hemisphere. The potentials are shown as a function of magnetic latitude (outer circle at 60°) and magnetic local time for 8 clock-angle orientations (45°-wide sectors) of the IMF. The background color shows the potential value, according to the color bar in the center; the lines are drawn at fixed potential values with a 3-kV spacing. The minimum and maximum potentials are listed at the *bottom*, and the total cross-polar potential drop is given at the *upper right* of each dial from *Annales Geophysicae* by Copernicus GmbH Copyright 2012 (Reproduced with permission of European Geosciences Union)

for northward IMF and increase steadily with southward-turning IMF B_z. In the Northern Hemisphere, the maximum amplitude is achieved for sector 5 $\left(B_z-/B_y-\right)$, whereas at the Southern Hemisphere this is the case for sector 3 $\left(B_z-/B_{y+}\right)$. Moreover, for all three sectors with IMF B_{y+} (sectors 1–3), the average neutral wind amplitudes of the Southern Hemisphere are significantly (10–20%) larger than of the Northern Hemisphere, whereas the opposite is true for IMF B_{y-} in sectors 5–7. The total average of the wind amplitudes is about the same in the Northern Hemisphere

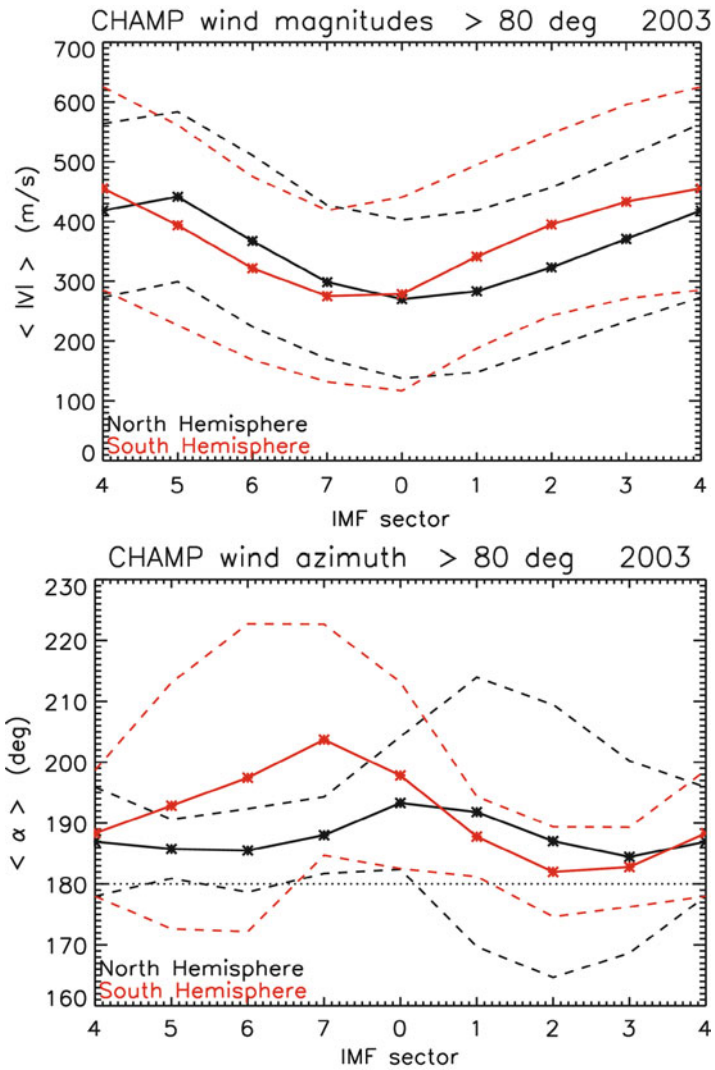

Fig. 4.4 Statistical averages of the thermospheric neutral wind velocity magnitude above 80° magnetic latitude (*upper panel*) and its orientation (wind vector azimuth, counted from high noon clockwise; *lower panel*) in dependence of the IMF orientation. The *horizontal dotted line* in the *lower panel* stands for purely anti-sunward wind direction. The abscissa specifies here, as in Fig. 4.3, the IMF orientation, sorted into eight separate sectors of 45° width, i.e., Sector 0 stands for purely northward-directed IMF, Sector 2 for B_{y+}, and Sector 4 is equivalent to southward-directed IMF, and so forth. *Dashed curves* indicate the variances. Northern (*black line*) and southern (*red line*) neutral wind responses to the solar wind and IMF forcing show a different behavior (see also tables 1 and 2 in Förster et al. 2008)

compared with the Southern, although the variances differ significantly. Expressed as standard deviation, they have about one-fourth (between 20% and 40%) larger values at South with respect to North (cf. Förster et al. 2008).

The standard deviation of the flow direction (Fig. 4.4, lower panel) shows remarkable differences between IMF B_{y+} and IMF B_{y-} conditions for both hemispheres. In the Northern Hemisphere, the flow is much more aligned for the latter, with a minimum value for sector 5, where the wind amplitude maximizes. In the Southern Hemisphere, there is a clear tendency for the opposite IMF B_y behavior with smaller standard deviations for IMF B_{y+}, coinciding with the maximum wind amplitudes. The formation of the large round-shaped plasma convection cell that is present under IMF B_{y+} $\left(B_{y-}\right)$ conditions at the Northern (Southern) Hemisphere at the dusk side traces in the thermospheric wind pattern. It acts apparently as an obstacle for the neutral wind flow across the polar region at high latitudes. The curl-free noon–midnight aligned plasma flow seems on the contrary to operate as a "pressure valve", allowing the largest cross-polar thermospheric wind amplitudes for IMF angle ranges corresponding to sector 5 at North and sector 3 at South.

4.3.3 *Electric Fields and Thermospheric Winds from UAM Modeling*

We performed model calculations for both geomagnetically quiet and moderately perturbed days during medium to high solar activity conditions near the fall equinox on 12 and 28 October 2003, respectively. The latter (28 October) coincides with our case study example day (see Fig. 4.7, below), which is discussed in the next section and compared there with direct observations of CHAMP during overflights over the polar regions. This day has directly preceded the huge famous superpower magnetic storm of 29–30 October 2003, the so-called Halloween superstorm, the global complex modeling of which is a big challenge for solar-terrestrial research (see, e.g., Toth et al. 2007).

In our view, it represents mean geomagnetic conditions of 2003, although the solar radiation conditions were somehow exceptional on this day. Some of the most intense solar flares in recent history (measured in the X-ray range 0.1–0.8 nm) occurred near the end of 2003. The solar flare event of 28 October 2003 at ~11 UT was the fourth most intense (X17), launching a coronal mass ejection (CME) that arrived Earth's environment on the subsequent day (~06 UT) causing the huge geomagnetic storm (Tsurutani et al. 2005). The mean EUV radiation level at that time was moderate. Expressed with the 10.7-cm wavelength radio radiation fluxes as proxy index, the 81-day average was about 140, while its daily value reached ~271. The X17 flare of 28 October 2003 determined a remarkable increase in the EUV bands and X-ray bands and caused increased photoionization effects in the dayside ionosphere, particularly in the lower ionospheric layers (Villante and Regi 2008).

Most global-scale modeling of the Earth's upper atmosphere environment makes use of global input parameters of both solar and geomagnetic indices. This work concerns both first-principle models like the UAM of this chapter, which describe the complex interaction of the various geospace "spheres" from a full-scale physical-theoretical point of view, as well as empirical models, which merely generalize large observational data sets in terms of more or less sophisticated parametrized simulation tools to obtain a best-fit description of observable physical quantities such as density or neutral wind vector patterns. All these global-scale models are, first of all, climatological in nature, that is, they reproduce the large-scale general trends in dependence of a few parameters such as the planetary 3-h-range magnetic index K_p, the geomagnetic A_p, or the solar EUV radiation proxy index $F_{10.7}$ already mentioned.

Most global empirical models for the description of the Earth's upper atmosphere environment such as the International Reference Ionosphere (IRI), the NRLMSISE-00 empirical model of the atmosphere (Picone et al. 2002), which is also used here as boundary condition, and upper atmosphere neutral wind models such as the HWM (Hedin et al. 1991) or its recently renewed version HWM07 (Drob et al. 2008), and its companion paper with the disturbance wind DWM07 model (Emmert et al. 2008), describe the average geospace storm-induced perturbations of the upper thermospheric neutral wind. All these models make use of global-scale input parameters to describe accordingly the actual solar and geomagnetic activity status as climatological descriptions of the atmospheric and plasma environment state. The empirical models are also used as initial or boundary conditions for simulation runs of the first-principle models or are enquired for comparison purposes.

Such large-scale model designs are good for global studies of low- to mid-latitude phenomena, but fail for the study of highly dynamic and mesoscale processes, which are typical particularly at auroral and polar latitudes. There are no empirical high-latitude upper atmosphere neutral wind models with input parameters that describe typically high-latitude forcing such as the auroral electrojet index AE, solar wind parameters, and the IMF magnitude and orientation.

Seeking for better representation of the high-latitude energy and momentum input, we tried to find adequate formulations for Region-1 FAC and high-energy precipitations at auroral and polar latitudes. We made use of the IMF-dependent empirical model of FACs of Papitashvili et al. (2002), as shown in Fig. 4.5 for Southern Hemisphere conditions and an average IMF magnitude of 5 nT. The pattern shows the spiral structure of Region-0, Region-1, and Region-2 currents, discovered first by the famous work of Iijima and Potemra in the 1970s, with current sheet pairs of opposite direction at the dawn and dusk side. Further related input (or boundary) conditions comprise the auroral high-energy particle precipitations, including the cusp region as the most important and intense energy input and mesoscale thermospheric upwelling region, which has recently been shown by CHAMP observations as a regular mass density anomaly near noon at high latitudes (cf., e.g., Rentz and Lühr 2008). The precipitation pattern must be chosen in accordance with the FAC input regions.

A complication of the physical model formulation consist also in an optimal choice of temporal and spatial discretization steps. The usual spatial steps are $\sim$1–2°

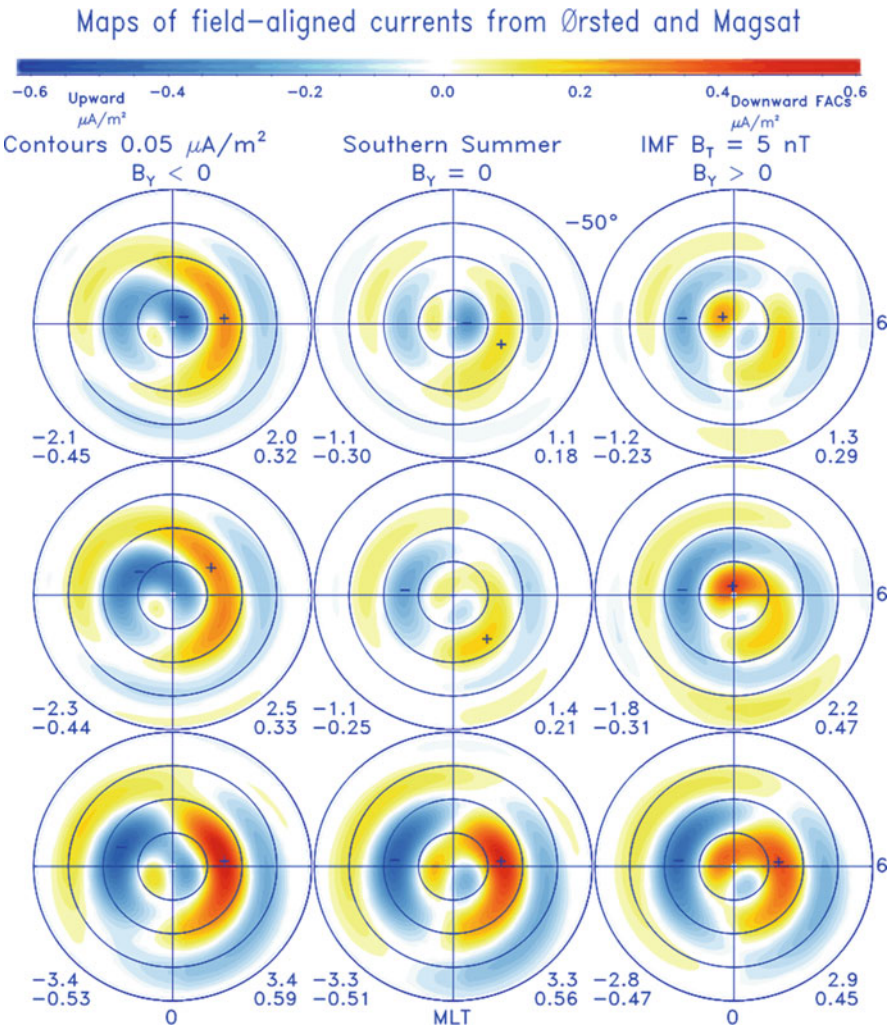

Fig. 4.5 Statistical field-aligned current (FAC) pattern obtained from magnetometer measurements on board the Earth-orbiting satellites Ørsted and Magsat for summer conditions at the southern polar area sorted for the same 8 clock-angle orientations as the convection potentials in Fig. 4.3 according to the study of Papitashvili et al. (2002). These model patterns are parametrized for an IMF magnitude value of 5 nT. The *central panel* shows the FAC distribution for a vanishing IMF vector, the so-called zero-state magnetosphere without any reconnection processes with the IMF, but persisting interaction with the solar wind streaming past the magnetopause. From *Geophysical Research Letters* by American Geophysical Union Copyright 2012 Reproduced with permission of American Geophysical Union

in latitude and ∼5–15° in longitude, but at high latitude, in particular for mesoscale phenomena, other choices might be appropriate for a best-fit formulation of the physical phenomena under study. Using the FAC density of Papitashvili et al. (2002) as (time-varying) input values of Fig. 4.5 for the equinox conditions of our study interval, we obtained the IMF-dependent electric field potential distributions shown

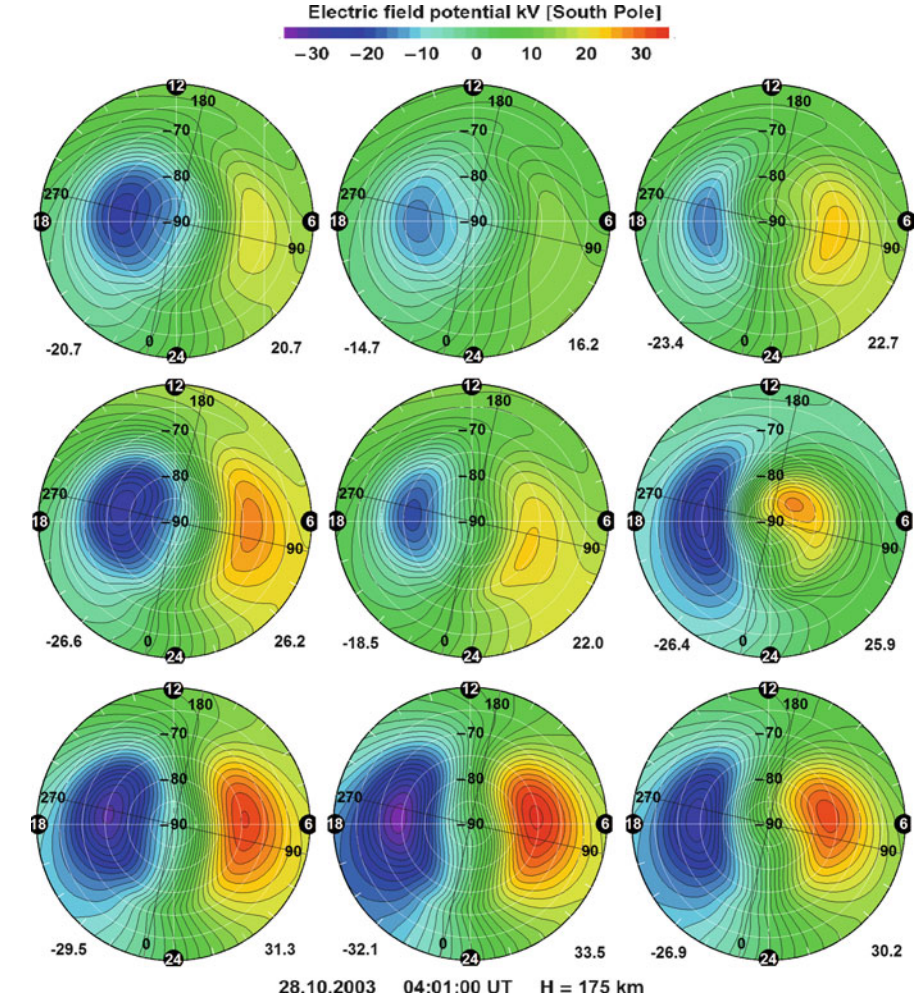

Fig. 4.6 Electric potential distributions for various IMF orientations as in Fig. 4.3 obtained from UAM simulations using the input FAC patterns as shown in Fig. 4.5. The potential pattern shows the characteristic two-cell structure with stronger anti-sunward convection over the pole for southward IMF and a clear IMF B_y dependence similar to the statistical observational pattern shown in Fig. 4.3. In contrast to the observations, the four-cell pattern for northward IMF (Sector 0 in Fig. 4.3) is not obtained

in Fig. 4.6. They reproduce mostly the average climatological pattern as obtained, for example, with the Cluster/EDI observations (see Fig. 4.3) in dependence of IMF strength and orientation, except the four-cell pattern for purely northward IMF (sector 0).

In the following, specified values of time-varying input parameters have to be used for the modeling of concrete case study situations.

4.3.4 Case Study Results of 28 October 2003 Compared with CHAMP Data

One of the most intense activity periods in recent history occurred during the past 23rd solar cycle with a series of extreme solar eruptive events in October–November 2003 that had serious consequences felt in the entire heliosphere, in particular throughout the geospheres. These events have already been analyzed thoroughly in numerous studies; the American Geophysical Union (AGU) *Journals of Geophysical Research Letters* (Vol. 32, Nos. 3 and 12, 2005) and the *Journal of Geophysical Research* (*Space Physics*, Vol. 110, No. A9, 2005) have devoted special issues to these particular space weather events entitled "Violent Sun–Earth Connection Events of October–November 2003." Some of these publications have direct relevance to key points of the present study (for instance, see Lin et al. 2005; Liu and Lühr 2005; Sutton et al. 2005; Thuillier et al. 2005; Tsurutani et al. 2005).

On 28 October 2003, ∼11 UT, an extreme solar flare with significant increases in EUV and X-ray flux caused increased photo-ionization effects in the dayside ionosphere and determined a remarkable solar flare effect (SFE) manifestation that preceded the Halloween superstorm. Some evidence was found for a highly confined counter electrojet in the dawn sector. Additionally, there are elements, at higher latitudes, that might suggest in these regions a more significant role of the X-ray flux and the onset of additional currents below the normal dynamo current region (Villante and Regi 2008).

Figure 4.7 shows the variation of the solar wind IMF B_y and B_z components together with some geomagnetic indices (K_p, AE, D_{st}) on October 28, 2003, the day preceding the Halloween superstorm of end October 2003. This particular day we have chosen as a case study period for a closer inspection of model–observation comparisons during several CHAMP satellite overflights of the northern and southern polar regions. The day is characterized by strong changes of IMF orientation and magnitude. The first half of the day is dominated by conditions of negative IMF B_y with a step-like change between two magnitude levels of this IMF component: ∼−5 nT until ∼03:00 UT and ∼ −15 nT until ∼09:30 UT. The IMF B_z component is mostly near zero or negative during this time, and positive during the subsequent hours until ∼14:00 UT. Later on, both IMF components are highly variable throughout the remaining hours of the day.

Liu et al. (2007) reexamined the 28 October event and showed that neutral and plasma perturbations during the first phase of the disturbance period contrasted each other remarkably. They found a decoupling of the neutral and plasma disturbances during this stage. About 2–3 h after the burst, plasma-neutral coupling via ion drag was found to become important at low- to mid-latitudes. They concluded that electrodynamics related to the equatorial fountain dominated the photochemistry in controlling the plasma density disturbances.

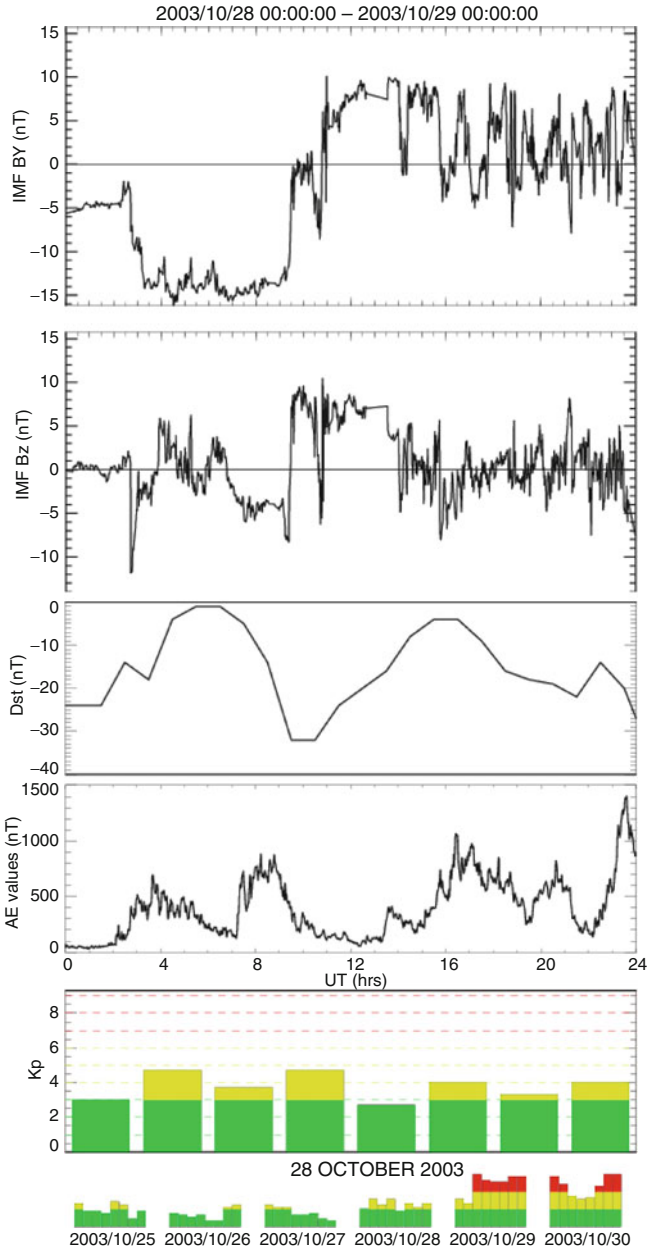

Fig. 4.7 The B_y and B_z (in nT) components of the interplanetary magnetic field (IMF) in the GSM *yz*-plane near the frontside magnetopause, deduced from time-shifted IMF and solar wind plasma measurements of the Advanced Composition Explorer (ACE) spacecraft, using the phase front propagation technique of Weimer et al. (2003), in a slightly modified version, that is based on a constrained minimum variance analysis of the IMF (Haaland et al. 2006), together with the hourly Dst, 1-min AE, and 3-h Kp index values for the modeled day, 28 October 2003, the day before one of the strongest space weather storm events of solar cycle 23, the so-called Halloween superstorm (see Toth et al. 2007) of end October 2003

Based on global first-principle modeling, Lin et al. (2005) performed various numerical experiments to identify the relative importance of storm-time ionospheric drivers, primarily for mid- and low-latitude regions, and with respect to the equatorial ionization anomaly. Lei et al. (2011) analyzed thermospheric density observations of the CHAMP and GRACE satellites to study the recovery of the thermosphere during the October 2003 storm. They found that neither the empirical models such as NRL-MSISE00 nor the global theoretical modeling with TIEGCM reproduced the observed rapid thermosphere relaxation times adequately. Comparing the CHAMP observations with model predictions, Sutton et al. (2005) had also demonstrated some empirical model shortcomings of the NRL-MSISE00 thermospheric density and HWM-93 neutral wind predictions in the course of this disturbance event. As global simulation tasks, one has to keep in mind the complexity and the global interrelations of the described phenomena, although the focus of our studies is on the high-latitude upper atmosphere physics and its relationship to external drivers. UAM performs calculations of the neutral and ionized components of the upper atmosphere self-consistently and starts the simulations at a quasi-equilibrium state obtained beforehand.

Figures 4.8 and 4.9 show UAM model results for the same four time moments (06, 12, 18, and 24 UT) of the case study day 28 October 2003, at high latitudes of the Northern Hemisphere. Figure 4.8 presents the calculated horizontal electric potential distributions, and Fig. 4.9 shows the corresponding results for the dynamic response of the thermospheric neutral wind with snapshots at the same time moments. Note that the isolines of the electric potential distributions in Fig. 4.8 correspond practically to the almost horizontal electromagnetic drift trajectories of the F-layer plasma at high latitudes.

Figure 4.8 clearly shows a strengthening of the potential difference across the polar cap at 18 and 24 UT. These increased plasma drift velocities come along with accordingly enhanced horizontal thermospheric wind speeds in Fig. 4.9. The comparison of the neutral wind patterns in Fig. 4.9 with the statistical average of 2003 in Fig. 4.2 corroborates the similarity of the modeled thermospheric circulations during moderate geomagnetic disturbances with the mean pattern and the approximate coincidence of the characteristic speed values. They exceed the statistical average pattern somehow during the more active periods (18 and 24 UT), and the peak values are at different places compared with the mean pattern (see Fig. 4.2); this is indicative for the mutual dynamic reactions between the neutrals and the plasma motion. At 18 UT we find the maximum neutral wind speed in the afternoon sector at about 70° magnetic latitude, whereas at 24 UT the neutral wind velocities maximize over the central polar cap.

The calculated vector plots of the thermospheric circulation at a 400-km altitude as shown in Fig. 4.9 for four different UT moments are related both to the characteristic disturbance effects (i.e., essential the IMF dependencies, cf. Haaland et al. 2007; Weimer 2005) and also to a regular (background) variation, which is the result of the offset between geographic and geomagnetic coordinates. This offset causes a regular variation of the solar luminosity with respect to its coverage of

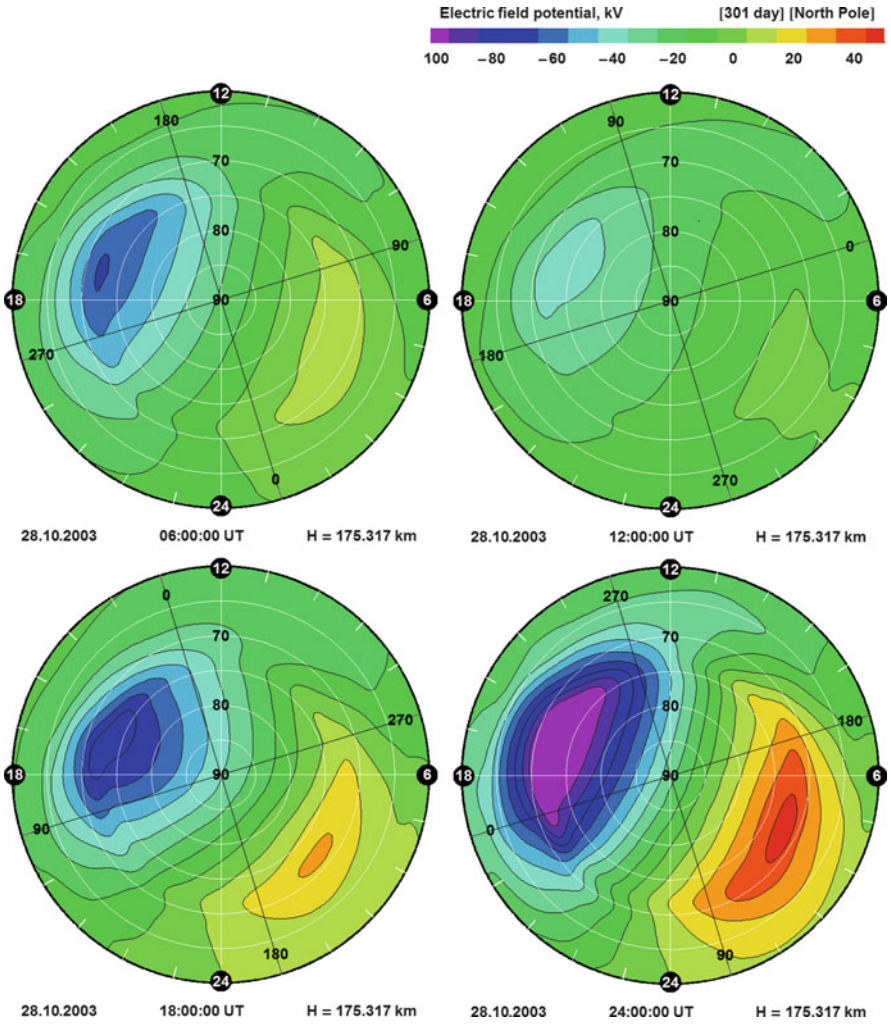

Fig. 4.8 Electric field potential distributions in polar geomagnetic coordinates at latitudes higher than 60° (Northern Hemisphere) calculated using the UAM model at various universal time (UT) moments (06, 12, 18, and 24 UT) on 28 October 2003. The simulation run uses solar and geomagnetic input parameters (partly shown in Fig. 4.7) and the parametrized FAC pattern of Papitashvili et al. (2002) (cf. Fig. 4.5)

auroral and polar regions and hence of the ionospheric conductivity. Lukianova and Christiansen (2008) found a rather complicated dependence of the convection patterns on the combination of UT and IMF clock-angle variation.

Finally, to estimate the degree of quantitative agreement between model calculations and the CHAMP satellite observations, we compared the respective thermospheric cross-track wind components during particular polar region crossings

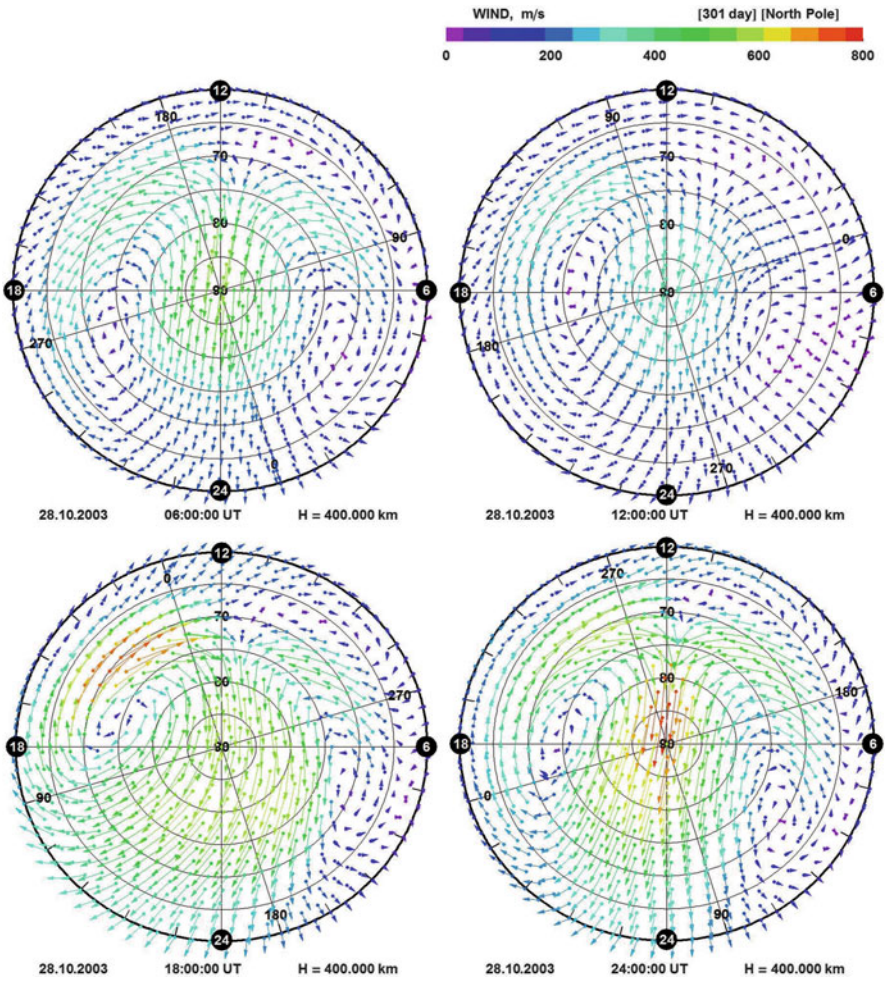

Fig. 4.9 Model calculations of the high-latitude thermospheric neutral wind circulation at 400-km altitude, presented here in the same format as in Fig. 4.2 as wind vector pattern in polar geomagnetic coordinates at latitudes higher than 60° (Northern Hemisphere). The four panels show the wind pattern at four UT moments (06, 12, 18, and 24 UT) on 28 October 2003 as obtained with the theoretical upper atmosphere model, UAM. Maximum wind speed is 700 m/s in the dusk sector at 18 UT and within the polar cap area at 24 UT

of CHAMP on 28 October 2003. This comparison revealed a close agreement between them during certain overflights and discrepancies during others. One characteristic example of a Northern Hemisphere crossing is shown in Fig. 4.10. The dotted line symbolizes the CHAMP satellite trace over the polar region with the triangle indicating the actual position at the given time moment (17:12 UT). The projection of the modeled 2-D thermospheric wind vector on the cross-track

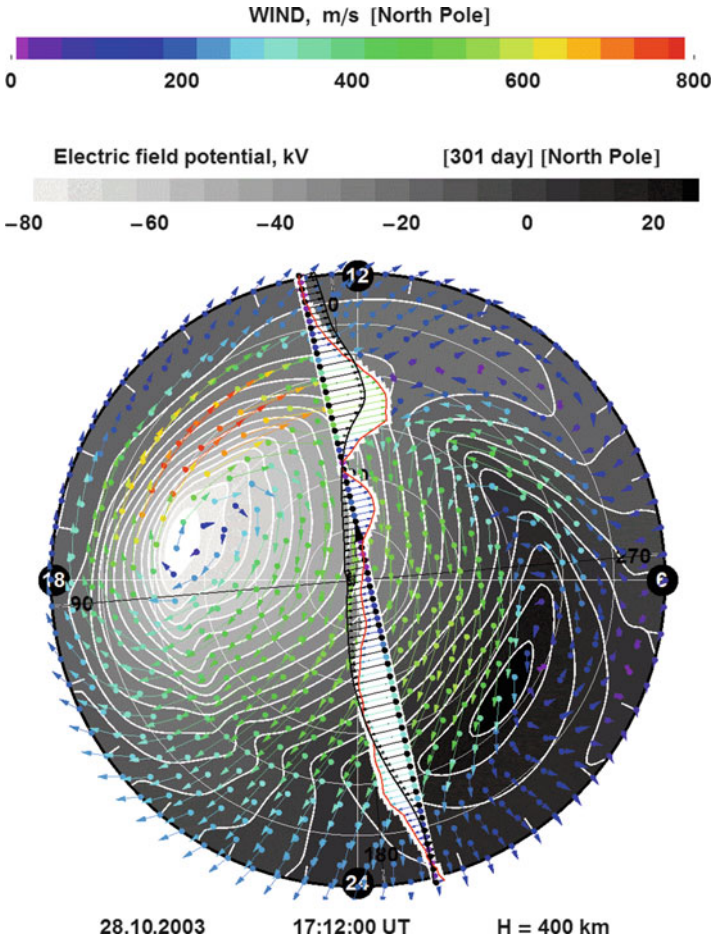

Fig. 4.10 UAM model results compared with cross-track accelerometer measurements of the CHAMP satellite for one overflight over the Northern Hemisphere in polar geomagnetic coordinates at latitudes higher than 60°. The dial shows 12 MLT on *top*, dusk side (18 MLT) to the *left*, and dawn (06 MLT) to the *right*, respectively. Magnetic longitude coordinates are indicated with the *black crosslines*. The *dotted line* follows along the orbital track from ∼01 MLT to ∼13 MLT with a *larger arrow* at the actual spacecraft position at 17:12:00 UT. The cross-track *fine black arrows* correspond to the calculated UAM crosswind speed; the *colored arrows* show a cross-track wind component as measured by CHAMP. The background wind vector pattern (*colored arrows* according to the scale on *top*) and the electric potential (*b/w color scale*) is calculated by the UAM for this time moment

direction (as shown by black arrows) compares quite well with the accelerometer measurements of CHAMP (as shown by the collinear colored arrows). The observations show slightly more variations in form of mesoscale structures, but the general shape and position of the dusk circulation cell and the wind amplitudes are well reproduced.

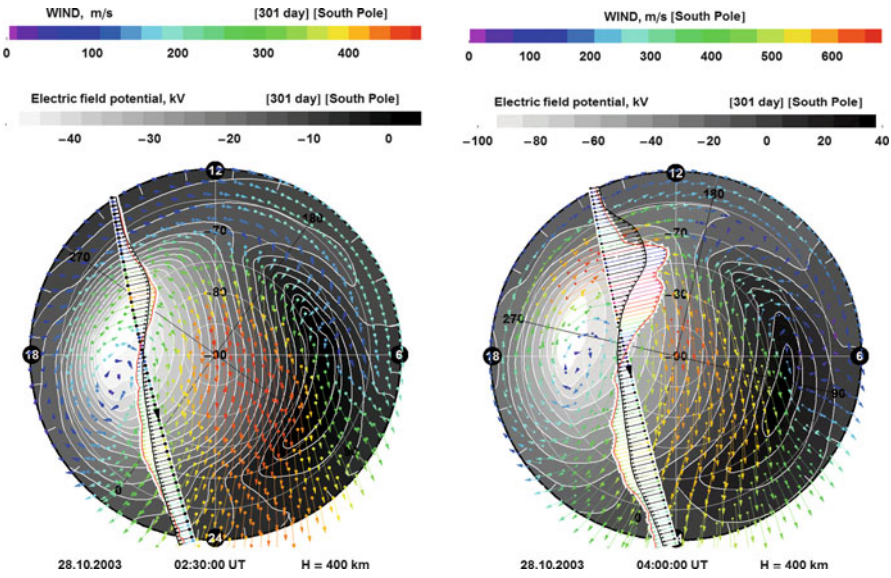

Fig. 4.11 UAM model results of two further time moments, 02:30 UT (*left*) and 04:00 UT (*right*), during CHAMP overflights over the southern polar region from afternoon hours (∼14 MLT) to midnight (24 MLT), presented in the same manner as in Fig. 4.10. The actual solar wind and IMF condition differ: in both cases we have predominantly negative IMF B_y-, but the B_y component is much more intense for the later moment (cf. Fig. 4.7). Please note the different scales for the wind vector and electric potential presentations, being considerably larger for the *right panel*

The mentioned discrepancies during other example orbits were likely related to the initial neglect of the IMF dependence of the convection electric field, in particular on its B_y component. The behavior of this component during 28 October 2003 is shown in Fig. 4.7. We performed a series of numerical experiments to improve the model's boundary conditions of the Region-1 FACs as one of the primary sources of energy and momentum input at high latitudes, which had to accompany a corresponding adjustment of the high-energy precipitations at auroral and polar latitudes.

Figure 4.11 shows the comparison of two consecutive CHAMP overflights over the southern polar region, displaced by the orbital period of ∼90 min. Both periods were characterized by near-zero IMF B_z and a negative IMF B_y component, which carried out a jump-like intensification from ∼5 nT to ∼15 nT between the two orbits (see Fig. 4.7). The more correct description of the IMF dependence of the Region-1 FACs, particularly of its strong pattern-shaping by the IMF B_y component (larger round-shaped dusk convection cell for negative B_y- at the Southern Hemisphere; see Fig. 4.3), resulted in much better agreement between model values and observations. The strong increase of the neutral wind component velocities for the later time moment (note that the scales for electric potential and wind amplitudes are different for the two panels of Fig. 4.11) is obviously the result

of the stronger negative IMF B_y component and of the increase of the IMF amplitude in general. The position of the modeled dusk circulation cell at 74° geomagnetic latitude near 18:30 MLT did not change very much, but the area occupied by both the plasma convection and the neutral wind circulation increased during the transition toward more intense IMF values. The approximate coincidence of the modeled and observed phase of this neutral wind circulation cell as well as the agreement of the corresponding amplitudes along the track lends credit to the correctness of the simulations.

Future model runs and comparisons with more abundant, independent concurrent measurements of both ground-based and in situ observations opens the way to detailed analyses of the high-latitude upper atmosphere dynamics and to the understanding of mesoscale structures of the highly dynamic and complex system. With new upcoming missions such as the Swarm ionospheric multisatellite project, or the EISCAT 3-D project, the time has come to take into account variations in all three dimensions simultaneously, as they occur in the real ionosphere (Amm et al. 2008). Global numerical first-principle modelings such as the UAM presented here or more specified numerical tools (e.g., Song et al. 2009) allow a much more comprehensive analysis of the physical processes involved, provided they are suited with, among others, their temporal and spatial resolutions and their boundary condition formulations, etc., to the subject of the investigation, which here is the upper atmosphere dynamics at high latitudes in the global context of solar radiation and solar wind-driven external forcings.

4.3.5 Seismogenic Electric Fields and Their Ionospheric Effects

4.3.5.1 Introduction

Seismogenic electric fields generated near the tectonic faults are important elements of the global electric circuit (e.g., Harrison et al. 2010; Pulinets and Boyarchuk 2004, and references therein; Freund 2011; Pulinets and Ouzounov 2011; Sorokin and Chmyrev 1999; Sorokin et al. 2007). We consider next their ionospheric effects mainly in the total electron content (TEC) variations as possible ionospheric precursors of earthquakes.

The statistically distinguished TEC pre-earthquake signatures are often described (Liu et al. 2006b; Pulinets and Boyarchuk 2004; Zakharenkova et al. 2007a) as (1) anomalous strong (30–90% and more deviations relative to the quiet conditions) TEC-positive or -negative modifications (increases or reductions) before the forthcoming seismic event not less than M5 by magnitude linked to the near-epicenter area. According to I.E. Zakharenkova, positive ones are more often reported. The typical zone of the anomaly maximum manifestation extends greater than 1,500 km in latitude and 3,500–4,000 km in longitude. The shapes and dimensions of the disturbed areas are kept rather stable. (2) Local long-living anomaly formation

(deviation from background conditions) is often reported from several days or hours to a couple of weeks before the earthquake release moment. TEC precursor evolution might be in form of sign change to opposite ones. Before the earthquake release moment or a few hours earlier, the anomaly depression up to its full decay could take place. The lifetime of the seismo-induced deviations of the same sense is from about 4–6 h up to 12 h in case of very strong earthquakes. (3) The vertical projection of the epicenter position does not mandatorily coincide with the maximum phenomenon's manifestation location. (4) Similar effects are often reported at the magnetically conjugated area. (5) In the case of strong low-latitudinal earthquakes, there are effects related to the modification of the ionospheric F2-region equatorial anomaly: increase or decrease of the equatorial (Appleton) anomaly with trough deepening or filling (Depueva and Ruzhin 1995; Depueva et al. 2007).

Many authors (e.g., (Pulinets 1998; Sorokin and Chmyrev 1999; Sorokin et al. 2005a, b, 2006, 2007) strongly rely on the hypothesis of a seismogenic electric field related to the vertical turbulent transportation of injected aerosols and radioactive particles (radon isotopes). The increase of the atmospheric radioactivity level during the earthquake formation leads to the enlargement of the ionization and electric conductivity of the near-ground atmosphere. The joint action of these processes leads to an intensification of an electric field in the ionosphere up to the value of units of tens of mV/m (Chmyrev et al. 1989). Freund (2011) proposed another mechanism of the near-ground atmosphere layer ionization based on so-called positive holes. Most crustal rocks contain dormant electronic charge carriers in the form of peroxy defects; when rocks are stressed, peroxy links break, releasing electronic charge carriers, known as positive holes. The positive holes are highly mobile and can flow out of the stressed subvolume. Freund expects this mechanism to be significantly more efficient than the aforementioned radon-related ones.

Total electron content (TEC) is formed mainly by the F2-layer plasma density. NmF2 and TEC disturbances related with magnetic activity are created by the neutral atmosphere (neutral gas composition, internal gravity waves, and winds) and electric field variations. However, it is impossible to localize neutral atmosphere disturbances at a limited area as they will propagate away from the source. Therefore, there are strong arguments in favor of the idea of an electric field of seismic origin as the main cause for the TEC anomalies observed before earthquakes: (a) the geomagnetically conjugate ionospheric precursors (Pulinets et al. 2003); (b) effects related to the ionospheric F2-region equatorial (Appleton) anomaly controlled by the zonal electric field (Depueva and Ruzhin 1995; Pulinets and Legen'ka 2002); and (c) "ban-time" at the near-noon hours (Namgaladze et al. 2011).

It was proposed (Namgaladze et al. 2007) that the main reason for the appearance of local TEC anomalies in the form of an increased (decreased) total electron content of the ionosphere, observed on the base of GPS (Global Positioning System) signal measurements, is the vertical drift of F2-region ionospheric plasma upward (or downward) under the influence of a zonal electric field of seismogenic origin directed to the east (or west). At middle latitudes the vertical upward component of the electromagnetic drift, created by an eastward electric field, leads to an

increase of the F2 region electron concentration maximum (NmF2) and TEC as a result of the plasma transport up to regions with lower concentration of the neutral molecules O_2 and N_2 and, consequently, with lower loss rate of the dominating ions O^+ in the ion molecular reactions (Brunelli and Namgaladze 1988). An electric field of the opposite direction (westward) creates the opposite—negative—effect in NmF2 and TEC. In the low-latitude regions (near the geomagnetic equator) an increased eastward electric field leads to a deepening of the Appleton anomaly minimum ("trough" over the magnetic equator in the latitudinal distribution of electron concentration) from the intensification of the fountain effect.

To check this hypothesis of the zonal electric field as the most probable cause for the observed TEC disturbances before earthquakes, model calculations were carried out with the UAM, the global numerical model of the Earth's upper atmosphere (Namgaladze et al. 1988, 1990, 1991, 1998a, b). The aims to be solved were (1) to check in principle the ability to set additional electric potentials of seismic origin to create the required zonal electric field at the near-epicenter area; (2) to calculate this electric field and the corresponding TEC disturbances; and (3) to estimate the efficiency of the proposed mechanism and to compare simulated TEC deviations with those, which are usually treated as precursors at low- and mid-latitudinal sectors.

First, the upper atmosphere state, presumably foregoing a strong earthquake, was modeled (Namgaladze et al. 2009a, b, 2008a) by means of switching on additional sources of electric field in the UAM electric potential equation, which was solved numerically jointly with all other UAM equations (continuity, momentum, and heat balance) for neutral and ionized gases. These sources were switched on and maintained permanently for 24 h in the form of additional positive and negative potentials with values of 2 and 5 kV (in case of the low-latitudinal sources) and of 10 kV (in case of the mid-latitudinal source) on the western and eastern boundaries of near-epicenter areas, respectively.

We investigated two near-epicenter areas (Namgaladze et al. 2009b) with sizes of 10° in latitude and 30° in longitude. The epicenters were situated at these points with the following magnetic coordinates: (1) (45°N, 90); (2) (15°S, 210). These sizes approximately correspond to the horizontal sizes of those regions of increased TEC values, which were found by Pulinets et al. 2003 and Zakharenkova et al. (2007b), for example. The first region is a typical mid-latitude ionosphere, and the second region is a near-equatorial ionosphere, for which the electric field effects are more essential than at middle latitudes. For the simulations we chose a magnetically quiet day of the June solstice at high solar activity.

In Fig. 4.12 the numerical grid of geomagnetic coordinates used in the model calculations is shown; its mesh points, in which additional potentials were set, are marked by circles (dark circles correspond to the positive potential, light circles correspond to the negative potential).

The calculated electric potential pattern and horizontal electric field vectors for the sources of 5 and 10 kV per mesh point are shown in Fig. 4.13 for the quiet and seismo-disturbed conditions. The figure illustrates the regions where an eastward electric field above the prospective epicenters of the future earthquakes

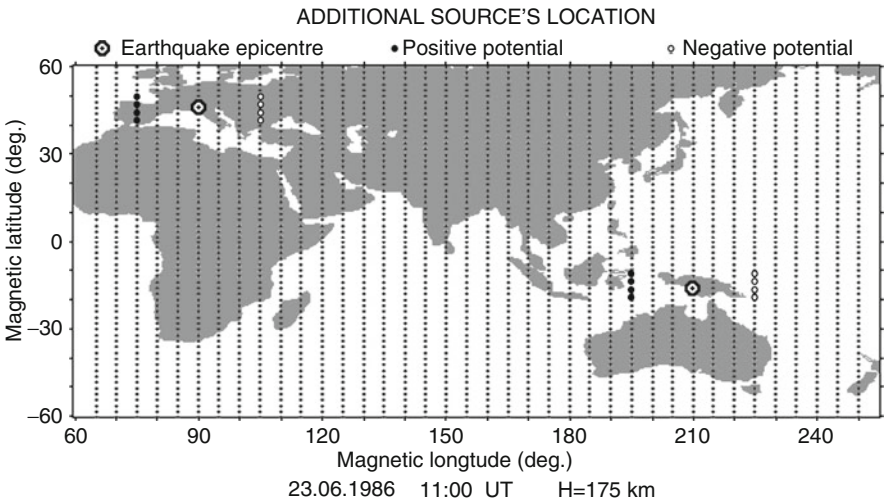

Fig. 4.12 The numerical grid of geomagnetic coordinates used in the model calculations and its mesh points in which the additional potentials were set noted by the circles (*dark circles* correspond to the positive potential; *light circles* correspond to the negative potential)

appeared when imposing (switching on) additional potentials. The appearance of similar magneto-conjugated regions in the opposite hemisphere is visible. The symmetry of the potential and electric field relative to the geomagnetic equator results from the ideal electric conductivity of the plasma along the geomagnetic field lines and, accordingly, their electric equipotentiality. The amplitudes of the additional eastward electric fields are about 2–4 mV/m in the low-latitude source and 4–10 mV/m the mid-latitude source. They exceed the background quiet fields (of about 0.2 and 1 mV/m, correspondingly), but they are noticeably smaller than the quiet high-latitude electric fields of magnetospheric origin (15–25 mV/m) obtained in the model calculations.

The calculated ionospheric effects in TEC and foF2 (F2-layer critical frequency) created by the additional electric field sources are shown in Figs. 4.14 and 4.15. The action of the near-equatorial source intensifies the equatorial anomaly of the F2-layer in the near-epicentral area of the ionosphere by deepening the minimum of foF2 over the magnetic equator and displacing the anomaly crests from the equator to the middle latitudes. This behavior agrees very well with the Alouette-1 and -2 observations (Depueva and Ruzhin 1995; Depueva et al. 2007; Ruzhin and Depueva 1996).

The action of the mid-latitudinal source leads to an increase of foF2 and TEC in the near-epicentral and in the magnetically conjugated areas. The amplitude of the enhancements and its spatial sizes are in good agreement with the corresponding characteristics of precursors in the TEC observations. Although the electric field magnitudes in case of the mid-latitudinal source in our calculations are two to five times larger than in the low-latitudinal case, the evoked effects are weaker than in the near-equatorial regions.

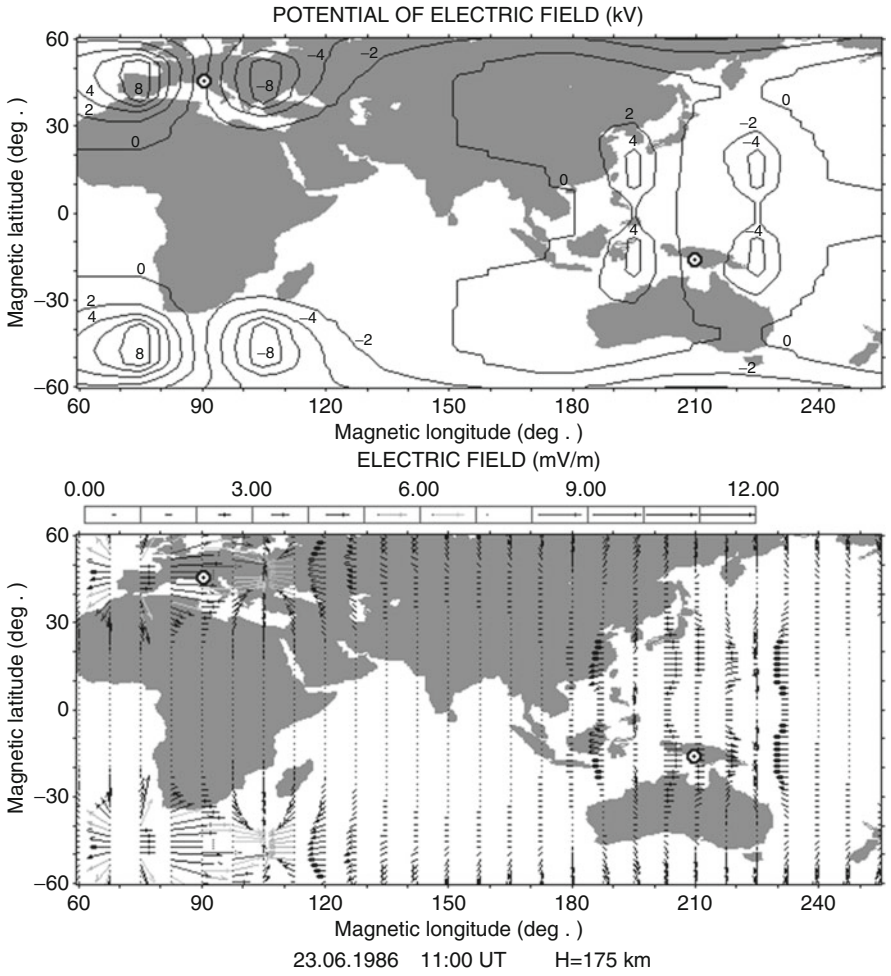

Fig. 4.13 Model-calculated electric field potential (*top*) and horizontal electric field vectors (*bottom*) generated by the background and additional (seismogenic) sources for two earthquake epicenters indicated by the markers

Namgaladze et al. (2009a, b) presented simulations in first approximation proving that NmF2 and TEC disturbances observed before earthquakes can be generated by the vertical drift of the F2-region ionospheric plasma under the influence of a zonal electric field of seismogenic origin. In case of TEC enhancements in mid-latitudes and deepening of the equatorial anomaly trough, this field is directed to the east and induces an electromagnetic drift of the plasma across the geomagnetic field with velocity directed straight upward over the magnetic equator and upward and poleward at mid-latitudes. The pattern of spatial distribution of the seismogenic

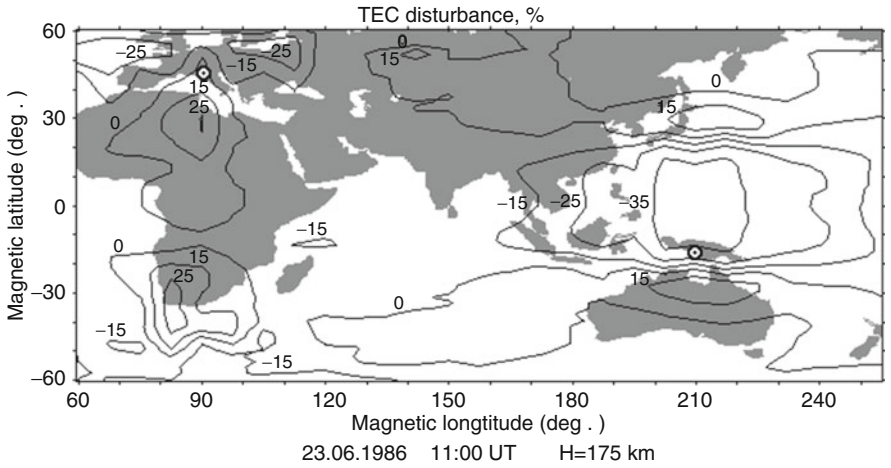

Fig. 4.14 Model-calculated relative total electron content (TEC) disturbances (%) induced by the additional (seismogenic) sources for two earthquake epicenters indicated by the markers

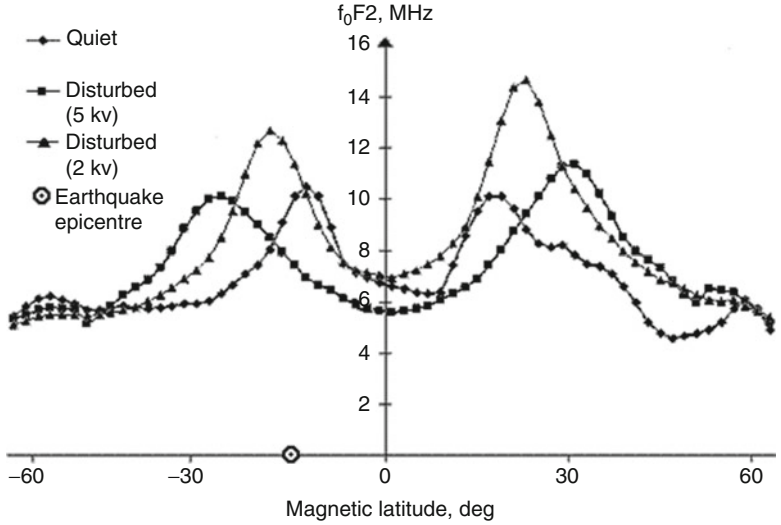

Fig. 4.15 Model calculated latitudinal variations of the F2 layer critical frequencies along the magnetic meridian of the equatorial earthquake epicenter located at 15° magnetic latitude for quiet and disturbed conditions

origin electric field potential has been proposed. For the existence of an eastward electric field in the near-epicentral area, it is necessary to dispose positive electric charges on the western boundary and negative charges on the eastern boundary of this area. However, we did not discuss the mechanism of the generation of a seismogenic electric field, and we did not explain why the positive charges should

accumulate on the western boundary of the near-epicentral region, and negative charges on its eastern boundary, or vice versa. We showed only what kinds of electric field were able to produce TEC and NmF2 disturbances observed before strong earthquakes.

The next step was to reproduce TEC variations before concrete earthquake events instead of synthetic model cases and to investigate other types of electric field sources (dipole-like, positive, and negative) and their spatial configurations. Numerical simulations were carried out for (1) the 26 September 2005 earthquake in Peru (Zolotov et al. 2008b) and (2) the Kythira seismic event on 8 January 2006 in Greece, at mid-latitudes (Zakharenkova et al. 2008; Zolotov et al. 2008a).

It was shown that in case of the Kythira earthquake that a simulated dipole-like source agreed better with the experimental GPS TEC data than in cases of monopole (positive) additional sources. Variations of the TEC disturbances for the low-latitude region (Peru earthquake) had the form and the structure of the equatorial anomaly ("trough"). The increase of the eastward electric field leads to the deepening of the equatorial anomaly minimum ("trough" over the magnetic equator in the latitudinal distribution of electron density) from an intensification of the fountain effect. The dipole-like and single sign (positive) additional electric field sources generate similar disturbances in ionospheric TEC (in contrast to the mid-latitudinal cases). A noticeable difference appears in the magnitude of these variations: the dipole-like sources generate a deeper equatorial trough. The amplitudes of the peaks (the "camel case" maxima) remain nearly at the same level or are slightly larger. That behavior agrees well (at least qualitatively) with the observed Peru pre-earthquake TEC variations.

Thus, both cases reveal a good agreement with the observations; the dipole-like and monopole sources have fewer differences in their manifestation at low latitudes.

It should be noticed that the applied "manually fixing" technique has two drawbacks: (1) it is hard to explain the nature of the "manually set" electric potential sources (which should be charges) on the borders of the near-epicenter area, especially their accumulation; and (2) the approaching sunrise terminator and its corresponding changes of the ionospheric conductivity caused by the well-conducting sunlit ionosphere should depress the additional electric potential and the corresponding disturbances up to full disappearance down to zero.

A more physical approach was realized by Sorokin et al. (2005a, 2006, 2007) by setting vertical electric currents flowing between the Earth and ionosphere at the considered region. This 'electric current technique' was used for the case of the Haiti earthquake of 12 January.

4.3.5.2 TEC Disturbances Before the Haiti Earthquake of 12 January 2010: GPS Observations and UAM Modeling

This section is aimed at (1) the determination of pre-earthquake TEC modifications and their description for the case of the 12 January 2010, 21:53 UT (16:53 LT) Haiti

shock event (18.46°N, 72.5°W) magnitude (M) 7.0 and (2) the numerical simulation of the ionosphere TEC response on electric fields generated by external seismo-related electric currents.

The upper atmosphere is very sensitive to influences of solar activity changes and to the impacts from outer space. Thus, changes in geomagnetic activity such as magnetic storms and substorms can lead to the generation of different positive and negative ionospheric disturbances at mid- to low latitudes (increases or decreases of the NmF2 and TEC) that may mask pre-earthquake disturbances, triggered possibly by seismo-ionosphere coupling processes, because the magnetic activity effects are of similar or even stronger magnitudes.

The geomagnetic situation was relatively quiet for the considered period: the Kp index was in general less than 2 during 1–12 January 2010, reaching distinct maxima values less than 3 for a short period. The Ap index took values of about 5 nT and did not exceed 10 nT for the considered period. The D_{st} index variations were in the range from −15 nT up to 15 nT. Therefore, the observed TEC disturbances could not be explained by solar and geomagnetic activity; they must be caused by processes originating from the underlying near-Earth atmosphere impact.

To estimate pre-earthquake TEC variations we have built differential (%) TEC maps relative to the quiet background conditions. We used global ionospheric maps (GIM) of the TEC (Dow et al. 2009) provided by NASA in IONEX format as the initial data for the analysis (ftp://cddisa.gsfc.nasa.gov/pub/gps/products/ionex/). The spatial resolution of those TEC data is 5° in longitude and 2.5° in latitude. Corresponding time resolution is 2 h. In contrast to other ground-based and satellite systems, GNSS-based networks provide almost global coverage and near-permanent (i.e., almost without time gaps) data.

We defined and calculated background TEC values (i.e., undisturbed conditions) as 7-day UT-grouped running observation medians before the current calculation moment. The resulting TEC difference (%) maps are presented in Fig. 4.16.

Anomalous TEC enhancements were observed during 06 UT–14 UT of 9 January 2010, 12 UT–14 UT of 10 January 2010, 08 UT–16 UT of 11 January 2010, and 04 UT–10 UT of 12 January 2010, reaching more than 50% by magnitude relative to the background values (Zolotov et al. 2011a, b). The amplitudes of the positive anomalies were significantly larger at the magnetically conjugated region. They were strongly fixed at the near-epicenter area. Their lifetime was limited to the nighttime hours. The terminator and subsolar point positions (indicated by continuous lines and circle symbols, respectively) have apparently some influence on the behavior of the observed positive structures. Approaching of the sunlit ionosphere is correlated with a disappearance of the anomalies. Such a behavior of the positive TEC disturbances could be explained by the corresponding disappearance (from increased conductivity) of the external electric field generated by the external electric current. Therefore, we consider positive structures as evidence of the "lithosphere–atmosphere–ionosphere" coupling via an electric current system. It should be noticed that there exist also negative TEC disturbances around the positive ones but with smaller magnitudes (about 15%).

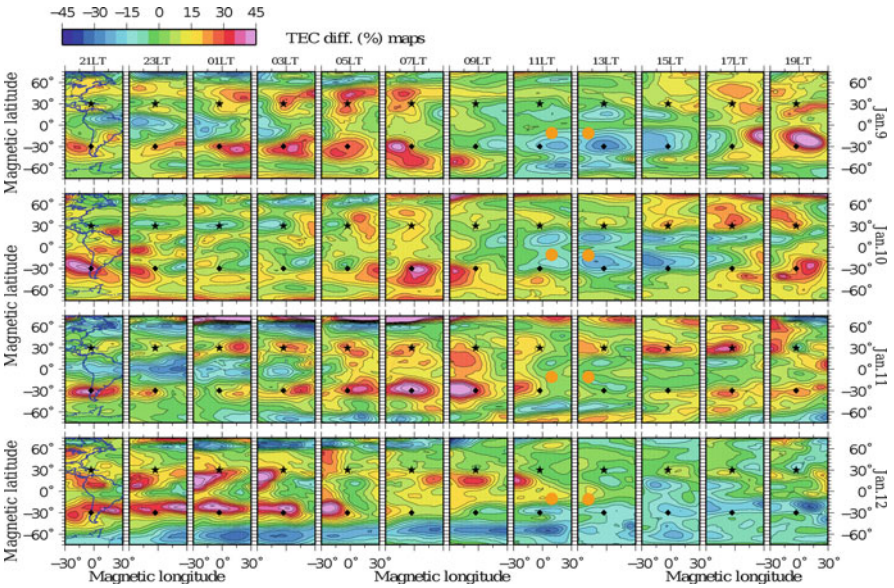

Fig. 4.16 TEC disturbance (%) maps for 9–12 January 2010 (from *top* to *bottom*) before the Haiti earthquake of 12 January 2010 (21:53UT). *Star*, epicenter position; *diamond*, magnetically conjugated point; *orange circle*, subsolar point; *black curve*, the terminator

In the electric current technique the upper atmosphere state, presumably preceding a strong earthquake, is modeled by means of switching on additional external electric current sources (and not electric potential sources at 175 km as in the electric potential technique described in the previous case) at the lower boundary (80 km) in the UAM electric potential equation, which was solved numerically jointly with all other UAM equations (continuity, momentum, and heat balance) for neutral and ionized gases.

To estimate an upper limit for the magnitudes of the vertical electric current applied, we looked through the publications available. Sorokin et al. (2005a, 2006, 2007) calculated the ionospheric electric field related to external electric current variations in the lower atmosphere. This current is formed presumably by the convective upward transport of charged aerosols and their gravitational sedimentation in the lower atmosphere. This effect is related to the occurrence of ionization sources from seismic-related emanation of radon and other radioactive elements into the lower atmosphere. Freund (2011) proposed other sources of the near-ground atmosphere layer ionization, the so-called positive holes, which he expected to be significantly more efficient then the named radon-related ones. According to Sorokin et al. (2005a, b, 2007), an external current density of about 10^{-6} A/m^2 within an area about 200 km in radius (approximately 130,000 km^2) is required to create an electric field of several mV/m in the ionosphere.

To build model difference maps (of the electric potential, zonal, and meridional electric field and TEC) we first performed a regular calculation without any additional electric current sources (set as lower boundary condition) to use the results as quiet background values. Then, an external electric current flowing between the lower atmosphere and the ionosphere over the Haiti earthquake (12 January 2010, 21:53 UT, M7.0) epicenter area was used as model input for the calculations of the ionospheric electric field and the corresponding TEC variations. Several spatial configurations and magnitudes of these currents have been taken into consideration: (1) "point" current (equivalent to one cell) sources of different signs and magnitudes, given in a single node of the numerical grid and (2) "line" sources.

According to UAM simulations, point current sources with magnitudes of about 10^{-5} and 10^{-6} A/m^2 given in a single grid node (corresponding to one grid cell of 5×2 or approximately 500 km $\times$ 200 km, and averaged vertical electric current densities of 5×10^{-6} A/m^2 and 5×10^{-7} A/m^2, respectively) induced extremely strong and unrealistic TEC disturbances and very intense vertical drift motions. Point sources of 10^{-9} A/m^2 and 5×10^{-9} A/m^2 triggered TEC disturbances not exceeding 15% in magnitude.

The "line" kind sources have been simulated as vertical external currents with a magnitude of 4×10^{-8} A/m^2 directed from the ionosphere to the Earth set centric at nine numerical grid nodes with 5° longitudinal steps along the magnetic parallel of the earthquake epicenter. It corresponds to an external electric current density of 2×10^{-8} A/m^2 set on the region of approximately $\sim$200 km $\times$ $\sim$4,000 km (2° along the meridian and 40° along the parallel). The generated TEC disturbances have reached $\sim$20–50% by magnitude depending on the current's spatial distribution and lifetime. Simulation results are presented in Figs. 4.17 and 4.18.

As one can see, the additional electric potential generated by the external current reduces down to zero when approaching the terminator in both (the modelled and the observed) cases. Corresponding TEC disturbances disappear later than the electric potential with a time lag of about 4–6 h. The simulations underestimate the observed magnitude of anomalous TEC increase in the Northern Hemisphere and overestimate it in the Southern Hemisphere. Both (modeled and observed) cases show stronger TEC magnitudes at the magnetically conjugated region in comparison with the near-earthquake epicenter area.

The calculated latitude-altitude variations of the electron density for 08 UT on 11 January 2010 along the –20°, 0°, and +20° longitudes are presented in Fig. 4.19. As follows from this, the effects in comparison to nondisturbed conditions (i.e., without seismic electric current sources) are an electron density 'trough' filling at the geomagnetic equator and formation of inhomogeneities. At –20° longitude, a mid-latitude maximum stratification took place with a trough formation in the latitude range of $\sim$30–40°; at +20° longitude we see an electron concentration increase at 300-km height and a depletion of the magnetic tubes higher up. Main changes took place at the $\sim$200–600 km altitude range.

Summarizing the numerical simulation results with external electric currents flowing between the lower atmosphere and ionosphere caused by seismo-induced conductivity changes of the underlying atmosphere column, one can state that they

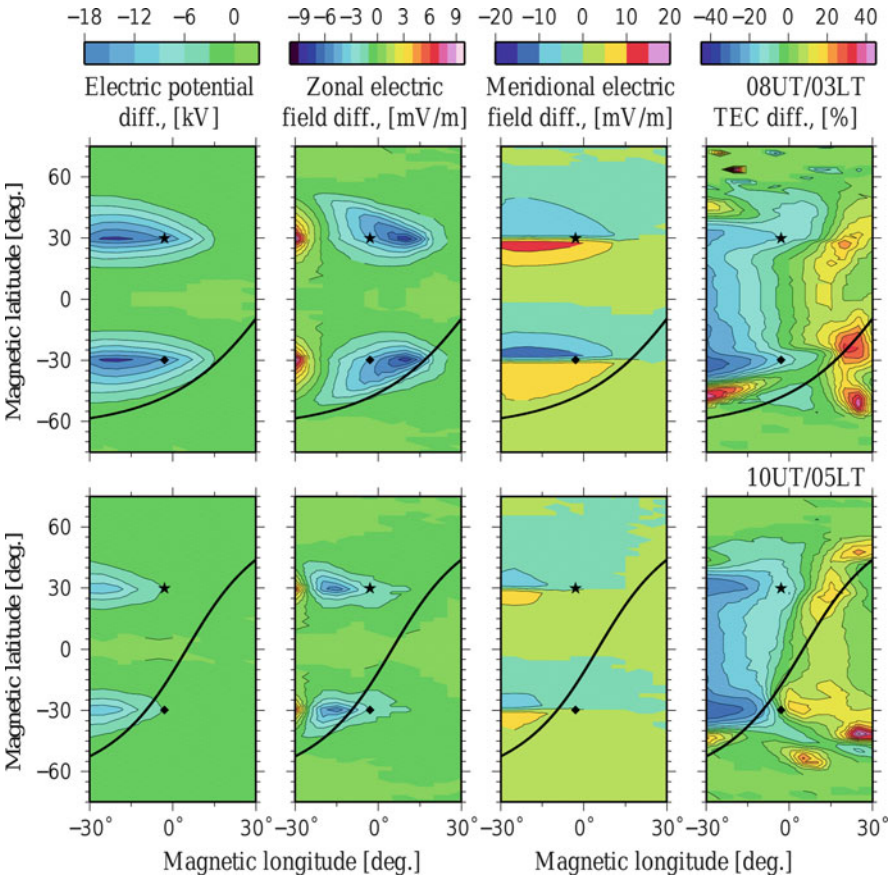

Fig. 4.17 Modeled (from *left* to *right*): (*1*) electric potential difference map; (*2*) zonal and (*3*) meridional components of the electric field generated by external electric current flowing between the Earth and the ionosphere; and (*4*) regional map of the TEC deviations relative to the nondisturbed conditions for 08 UT/03 LT (*top panel*) and 10 UT/05 LT (*bottom panel*). *Star*, earthquake epicenter position (Haiti); *diamond*, magnetically conjugated point; *black curve*, terminator

reproduce the main features of the TEC variations. In both the GPS observations and the model cases we have (1) areas of increased TEC exist and are localized in the near-epicenter area; (2) magnetic conjugation took place; (3) TEC disturbances at the magnetically conjugated area were stronger by magnitude than in the near-epicenter region; (4) the amplitude of TEC enhancements reached 50% and more; (5) negative structures (areas of the TEC reduction) existed westward and equatorward relative to the positive ones; (6) approaching the sunrise terminator with the well-conducting sunlit ionosphere triggered a shift of the anomaly to the night side and caused the subsequent suppression of the TEC variations, both at the epicenter and in the magnetically conjugated regions; and (7) the anomalies did

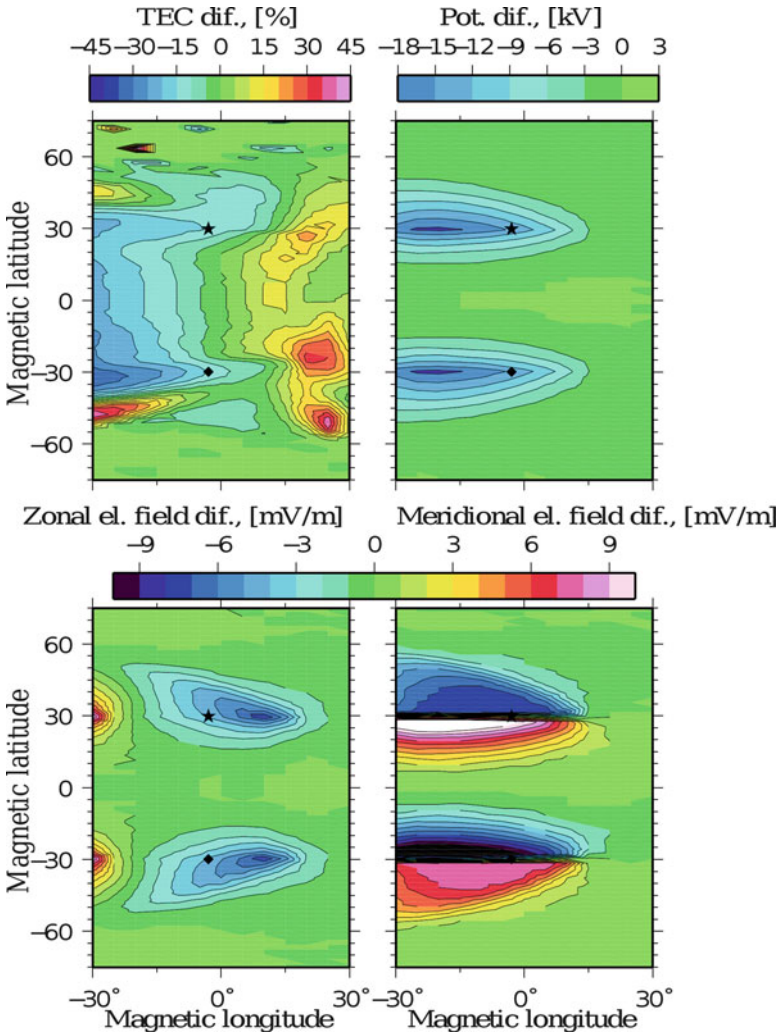

Fig. 4.18 Modeled regional difference maps from quiet background conditions: (*1*) TEC (*top left*); (*2*) electric potential (*top right*); (*3*) zonal and (*4*) meridional electric field for 08 UT (03 LT) of 11 January 2010. *Star*, earthquake epicenter position (Haiti); *diamond*, magnetically conjugated point (lg[Ne, m^{-3}])

not exist during the near-noon hours. Such behavior and the lifetime agreed with the results of Akhoondzadeh and Saradjian (2011). The obtained morphological features also agreed with Pulinets and Tsybulya (2010).

We should notice that a few discrepancies persist between the observations and the model results. (1) The simulations underestimate the amplitudes of the TEC anomaly at the Northern Hemisphere and overestimate them at the Southern Hemisphere in comparison with the observations. (2) Negative structures are

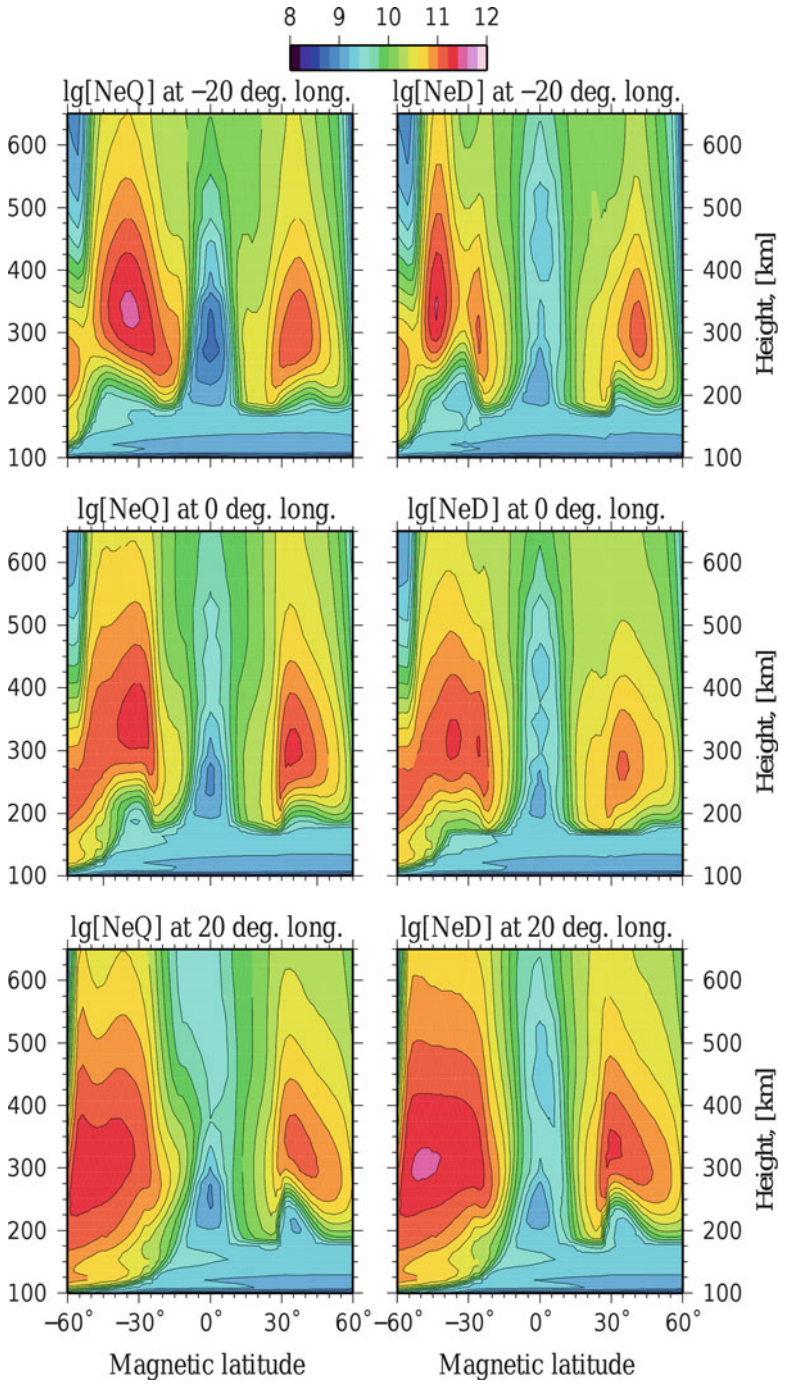

Fig. 4.19 Latitude-altitude variations of electron density along the geomagnetic meridians: −20° (*upper row*); 0° (*middle row*); +20° (*lower row*) calculated for 11 January 2010, 08 UT (03 LT). At *left*, the quiet variations; at *right*, variations disturbed by the seismogenic electric field

stronger than the observed ones by magnitude in the model case. (3) The increased TEC area occupies a smaller region in the model case. (4) The isoline patterns and the magnitudes differ from the observed ones but not drastically. The discrepancies between the simulation results and the GPS observations could be caused by the rather simplified assumptions about the external electric field sources, their density distribution, and acting regime.

Night domination effects, the existence of a "ban-time," and the terminator-driven TEC anomaly suppression should be caused by the changes of the conductivity of the ionosphere. It is related to the crossing of the sunrise terminator, where the well-conducting sunlit ionosphere leads to a depression of the electric potential disturbances and to a reduction of the electric field, generated by the externally driven electric current.

4.3.5.3 Case Study of the TEC Disturbances Before the Earthquakes of 1 January 2011, Argentina, M7.0, and 2 January 2011, Chile, M7.1

We considered the earthquakes of 1 January 2011, 09:56 UT/06:56 LT, Argentina, M7.0 (26.794°S, 63.079°W), D 576.8 km, and 2 January 2011, 20:20 UT/17:20 LT, Chile, M7.1 (38.354°S, 73.275°W), D 25.1 km as one single (or united) case. The Chile earthquake took place 1 day after the Argentina earthquake. The positions of the epicenters are close to each other and can be considered as situated within one and the same 'traditional' seismic phenomena manifestation area. Therefore, relying on the traditional pre-earthquake TEC modification signature (spatial and temporal features), it is impossible to distinguish separately each of the different sources that impact the ionospheric TEC. On the one hand, the depth of the Argentina earthquake epicenter was 576.8 km whereas the traditional TEC signatures are statistically defined only for earthquakes with less than 80–150 km depth; that is, ionospheric manifestations of such phenomena have not been investigated at all up to now. On the other hand, the TEC disturbances triggered by this earthquake should, if ever there are any, be masked or merged with Chile's earthquake effects. The TEC difference maps for 30.12.2010–02.01.2011 are presented in Fig. 4.20.

The geomagnetic situation was quiet to moderate for the considered period. During 22 December 2010–3 January 2011 (except 28–30 December 2010), the K_p index was less than 3, A_p mostly about 5 nT, and D_{st} was primarily in the range between −20 nT and +10 nT. A moderate magnetic storm occurred during 28–30 December 2010: on 28 December, the K_p index reached values to 4, A_p to 27 nT, and the D_{st} index changed from +13 nT at 10 UT down to −43 nT at 17 UT on 28 December 2010. As the moderate magnetic storm generated, in 28–30 December 2010, TEC disturbances of considerable magnitude that are able to mask the seismo-related variations, we excluded the TEC difference maps of this period from the analysis. Therefore, the considered long-living TEC disturbances linked to the near-epicenter position were expected to be caused by going through the underlying atmosphere impact.

In the case of the earthquakes of 1 January 2011, Argentina, M7.0 and 2 January 2011, Chile, M7.1, significant TEC enhancements took place 1 January 2011,

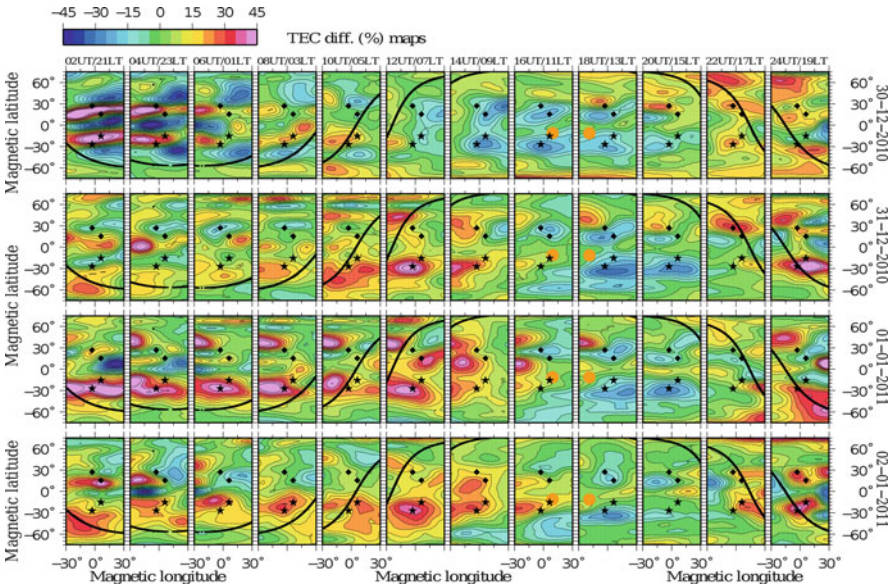

Fig. 4.20 Regional TEC difference maps for 30.12.2010–02.01.2011 (*top to bottom*), 02 UT-24 UT (*left to right*) before the earthquakes of Argentina, 1 January 2011, 09:56 UT and Chile, 2 January 2011, 20:20 UT. *Stars*, epicenter position for Argentina (*right star*) and Chile (*left star*) earthquakes; *diamond*, corresponding magnetically conjugated point; *orange circle*, subsolar point; *black curve*, terminator line

02 UT-14 UT, in both Northern and Southern Hemispheres. After the passage of the sunrise terminator, positive structures were also observed at the Southern Hemisphere during 08–12 UT of January 2002. Disturbances at the magnetically conjugated region were insignificant or absent. After the shock of the seismic event realization and the terminator crossing, as well as the passage of the subsolar point, we still observe positive disturbances, possibly as post-effects of the earthquake. The sunlit conditions lead to TEC enhancement modifications up to their full suppression close to the subsolar point sector.

4.3.5.4 Case Study of the TEC Disturbances Before the Earthquake of 11 March 2011, M9.0, in Japan

Although the case of the Haiti earthquake was an example of a ‘clear’ phenomenon manifestation undisturbed by geomagnetic or other seismic events, the Japan earthquake is a case of disturbed events. The aim of this section is to check the conformance of the foregoing scheme and to contrast it with real pre-earthquake TEC modifications.

In case of the 11 March 2011 earthquake in Japan, M9.0 (38.322°N, 142.369°E), D 32 km, a sequence of strong seismic events took place close to and associated

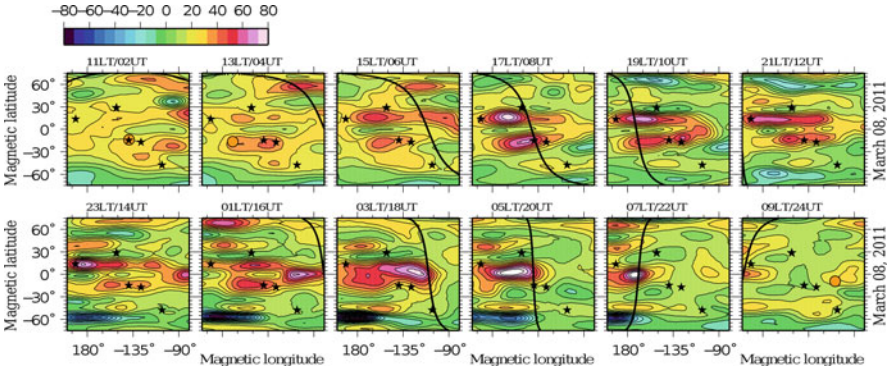

Fig. 4.21 Regional TEC difference maps for 02 UT–24 UT, 8 March 2011. *Star*, epicenter position; *orange circle*, subsolar point; *black curve*, the terminator line. Local time is for the 11 March 2011 epicenter position in Japan

with the epicenter area and time interval before and after the M9.0 event. An M7.2 earthquake 9 March 2011 (38.424°N, 142.836°E), D 32 km, 02:45 UT/11:45 LT, took place at almost exactly the same epicenter position as the 11 March event. Also on 9 March, a second earthquake, M6.5, (6.022°S, 149.659°E), 21:24 UT, happened. Thus, we have to look at the TEC variations as triggered by a united source of a spatially distributed cluster of earthquakes. The geomagnetic activity was quiet to moderate with episodic periods of moderate to strong disturbances. During 6–10 March 2011, the D_{st} index was within the interval of -22 nT $+ 4$ nT without any significant disturbances. On 10 March, a moderate magnetic storm took place: D_{st} index varied from -7 nT down to -82 nT on 11 March.

The selected set of seismic events allows us to successively investigate from the 'clear' case of a seismic impact on the neutral atmosphere to 'disturbed' ones with combined actions of geomagnetic and seismic activities. In spite of the differences between geomagnetic activity and seismic sources, common features derived from these cases should be caused by the same physical nature of lithosphere–ionosphere coupling processes.

As for the previous cases, we defined and calculated the background TEC values (i.e., undisturbed conditions) as 7-day UT-grouped running observation medians before the current calculation moment. The resulting TEC difference (%) maps are presented in Fig. 4.21.

In the 11 March 2011, Japan, M9.0 (38.322°N, 142.369°E), D 32 km and associated earthquakes, the following TEC disturbances took place. On 8 March 2011, TEC enhancements up to 80% were observed from 06 UT until 20 UT; they first were formed at the near-epicenter areas, then their magnitude increased. During 08 UT–12 UT, the anomalies spread out along the parallel at both hemispheres, occupying a larger region. From 12 UT onward there was a tendency to replenish the Appleton's anomaly. The TEC anomaly comprised an ellipse-like region with the earthquake on its border. At 18 UT-20 UT, we see a single increased TEC spot.

The passages of the sunrise terminator and later of the subsolar point degraded the anomaly and led to its full decay in the course of the whole day of 9 March, that is, no significant TEC disturbances were observed on the day of the M7.2 earthquake 9 March, 02:45 UT (which happened at nearly the same exact positions as the earthquakes of M9, 11 March and the M6.5, 6.022°S, 149.659°E, 21:24 UT). The equatorial anomaly modifications described above are expected to be the TEC response on this equatorial earthquake. We also see some moving positive structures on 10 March, but they are likely caused by activity-driven disturbances.

All the features revealed for the clear case of the Haiti 2010 earthquake were also shown for both the activity-disturbed (Chile and Argentina, 2011) and multiple-earthquake (Japan, 11 March 2011) periods. Those features comprise the terminator and subsolar point-related effects: anomaly depression and 'ban' time at the near-noon hours, and modification of the shapes of the anomalies under influence of the terminator approach. In case of the Japan "cluster" earthquakes, the afore-described features also happened, and the conjugated action of equatorial and mid-latitudinal earthquakes could be extracted or unambiguously separated. The equatorial one makes the main impact in Appleton's anomaly modification. Unfortunately, basing only on the spatial or time interval criteria, it is impossible to distinguish the 9 March from the M9.0, 11 March, Japan earthquakes. Also, it should be mentioned that the magnitude of the TEC anomaly is larger than in Haiti (M7.0) or Chile (M7.1) and Argentina (M7.0) cases. We expect this is the result of the stronger magnitude of the 11 March Japan (M9) earthquake. The warning criteria in this case are applicable only for region- or country-wide areas, but not for smaller ones. We expect that 'traditional' signatures should be extended with the terminator and subsolar point related effects.

Sequential consideration of quiet-to-moderate cases showed that solar and geomagnetic activities can create similar TEC disturbances, but they are not linked to a fixed geoposition. Their lifetime corresponds to the duration of the activity disturbances (characterized by the indices of D_{st}, K_p, etc.) with some time lag from the inertness of the ionosphere. They usually originate from the aurora zone and may penetrate down to middle latitudes. Therefore, the applied technique for the TEC disturbance discrimination should be very carefully used at high latitudes ($>60°$), especially during moderate-to-strong disturbance conditions.

There were no statistical investigations of TEC anomalies related to the deep earthquakes, so that no precursory schemes exist. Nevertheless, the widely accepted spatial scale of TEC precursors did not allow us to separate both (Chile and Argentina) earthquakes from each other. Such combined action, if any, may be expressed as some shift of the anomalously enhanced region.

4.4 Discussion and Conclusions

We have considered some recent results concerning the modeling of ionospheric electric fields and their effects on thermospheric dynamics and total electron content (TEC) variations. The global numerical model of the Earth's upper atmosphere

(UAM, Upper Atmosphere Model) was used for the presented investigations. Ionospheric electric field patterns were calculated by solving numerically Eq. 4.20, taking into account both the dynamo action of neutral winds and the external current drivers at the lower and upper boundaries of the ionospheric dynamo region. These currents transfer electric charges from the magnetosphere to the dynamo region upper boundary and from the near-Earth's lower atmosphere to the lower boundary. We should keep in mind, however, that the original sources of both kinds of electric fields (of magnetospheric and seismogenic origin) are motion: the solar wind plasma generator flow across the magnetopause and the displacement of tectonic plates.

Electric fields generated by the interaction of the solar wind and its embedded interplanetary magnetic field with the geomagnetic field, as well as geomagnetic field-aligned currents, have already been studied for many years; their existence is beyond doubt. Very high electrical conductivity along the geomagnetic field lines ensures reliable electrical coupling between the magnetosphere and the ionosphere. Another situation takes place with the seismogenic electric fields because of the very low (in comparison with the ionized layers above ~ 80 km) conductivity of the neutral air between the Earth and the ionosphere. Nevertheless, it is not zero, and varies significantly from place to place, for example, from "good weather" regions to thunderstorm areas. The average vertical electric current density between the Earth and the ionosphere is about 2–3 pA/m^2, and the corresponding average electric potential difference amounts to about 250–300 kV. In thunderstorm areas, the vertical electric current density increases by several orders in magnitude. The same takes place, presumably, near tectonic fault regions before earthquakes as a consequence of the motion of (or accumulated stresses between) tectonic plates.

Some of the recent results presented here on TEC variations before earthquakes, which were obtained using GPS data, give strong evidence in favor of the hypothesis on seismogenic electric fields as the main cause for these variations. The persistence of the near-epicenter disturbance regions, their geomagnetically conjugate occurrence, and their tendency to avoid sunlit time periods constitute these evidences. The UAM calculations presented above show that a vertical electric current of about 10^{-8} A/m^2 at an area of about 1,000 km $\times$ 4,000 km can create electric fields of several mV/m in the nighttime ionosphere, which in turn can produce the TEC variations of up to 50%, which turns out to be very similar to those observed.

The electric coupling between the tectonic faults and the ionosphere requires the presence of emerging electric charges (or ionization sources) near the faults. Two mechanisms were considered in recent years: ionization by radioactive radon emission and the "positive hole" mechanism by Freund. Possibly, they are not competing but both acting. The detailed physics and chemistry of the lower (near the Earth surface) atmosphere in presence of these ionization sources should be developed in the future.

Electric fields of magnetospheric origin, on the other hand, have proved to be very important for the "space weather" tasks. One should necessarily notice their strong dependence on the solar wind parameters, primarily on the interplanetary magnetic field strength and orientation. The coupling of the magnetosphere with the ionosphere via field-aligned currents and their use in electric field modeling should

be carefully monitored. Thermosphere-ionosphere models such as the present UAM should be combined with global MHD models of the magnetosphere, taking into account the plasma sheet not frozen in ions. And last, in the near future both the "space weather" and the usual weather and climate models should be combined in some way. Nowadays, computer techniques and technology permit us to realize these tasks.

Acknowledgments Work at GFZ Potsdam (M.F. and B.P.) was supported by Deutsche Forschungsgemeinschaft (DFG). We thank the ACE SWEPAM and MAG instrument teams and the ACE Science Center for providing the data, and the World Data Center for Geomagnetism, Kyoto, for the D_{st}, ASYM, and AE indices. The CHAMP mission is sponsored by the Space Agency of the German Aerospace Center (DLR) through funds of the Federal Ministry of Economics and Technology, following a decision of the German Federal Parliament (grant code 50EE0944). The data retrieval and operation of the CHAMP satellite by the German Space Operations Center (GSOC) of DLR is acknowledged.

The authors (A.N. and O.Z.) acknowledge (1) NOAA National Geophysical Data Center/NGDC and the World Data Center for Geomagnetism, Kyoto, for the Ap, Kp, and D_{st} indexes data (http://spidr.ngdc.noaa.gov/spidr/); (2) U.S. Geological Survey and National Earthquake Information Center for the earthquake data, URL: http://earthquake.usgs.gov/earthquakes/; (3) IGS community and Crustal Dynamics Data Information System (CDDIS) for the TEC Global Ionosphere Maps (Noll et al. 2009; Noll 2010); and (4) University of Hawaii for Generic Mapping Tools (Wessel and Smith 1998).

References

Akhoondzadeh M, Saradjian MR (2011) TEC variations analysis concerning Haiti (January 12, 2010) and Samoa (September 29, 2009) earthquakes. Adv Space Res 47(1):94–104

Amm O, Aruliah A, Buchert SC, Fujii R, Gjerloev JW, Ieda A, Matsuo T, Stolle C, Vanhamäki H, Yoshikawa A (2008) Towards understanding the electrodynamics of the 3-dimensional high-latitude ionosphere: present and future. Ann Geophys 26:3913–3932. doi:10.5194/angeo-26-3913-2008

Aruliah AL, Griffins EM, McWhirter I et al (2004) First tristatic studies of meso-scale ion-neutral dynamics and energetics in the high-latitude upper atmosphere using collocated FPIs and EISCAT radar ionosphere. Geophys Res Lett 31(L03802):1–4. doi:10.1029/2003GL018469

Banks PM (1972) Magnetospheric processes and the behavior of the neutral atmosphere. Space Res 12:1051–1067

Brunelli BE, Namgaladze AA (1988) Fizika ionosfery. Nauka, Moscow, 527 p (in Russian)

Chmyrev VM, Isaev NV, Bilichenko SV, Stanev GA (1989) Observation by space-borne detectors of electric fields and hydromagnetic waves in the ionosphere over on earthquake center. Phys Earth Planet Interiors 57:110–114

Coroniti FV, Kennel CF (1973) Can the ionosphere regulate magnetospheric convection? J Geophys Res 78:2837–2851

Depueva AKh, Ruzhin YuYa (1995) Seismoionospheric fountain-effect as analogue of active space experiment. Adv Space Res 15(N 12):151–154

Depueva AKh, Mikhailov AV, Devi M, Barbara AK (2007) Spatial and time variations in critical frequencies of the ionospheric F region above the zone of equatorial earthquake preparation. Geomagn Aeron 47(N. 1):129–133. doi:10.1134/S0016793207010197

Doornbos E, IJssel J, van den Lühr H, Förster M, Koppenwallner G (2010) Neutral density and crosswind determination from arbitrarily oriented multi-axis accelerometers on satellites. J Spacecraft Rockets 47:580–589. doi:10.2514/1.48114

Dow JM, Neilan RE, Rizos C (2009) The international GNSS service in a changing landscape of global navigation satellite systems. J Geodesy 83:191–198. doi:10.1007/s00190-008-0300-3

Drob DP, Emmert JT, Crowley G, Picone JM, Shepherd GG, Skinner W, Hays P, Niciejewski RJ, Larsen M, She CY, Meriwether JW, Hernandez G, Jarvis MJ, Sipler DP, Tepley CA, O'Brien MS, Bowman JR, Wu Q, Murayama Y, Kawamura S, Reid IM, Vincent RA (2008) An empirical model of the earth's horizontal wind fields: HWM07. J Geophys Res 113:A12304. doi:10.1029/2008JA013668

Emmert JT, Drob DP, Shepherd GG, Hernandez G, Jarvis MJ, Meriwether JW, Niciejewski RJ, Sipler DP, Tepley CA (2008) DWM07 global empirical model of upper thermospheric storm-induced disturbance winds. J Geophys Res 113:A11319. doi:10.1029/2008JA013541

Escoubet CP, Schmidt R (1997) Goldstein ML0 cluster – science and mission overview. Space Sci Rev 79:11–32

Förster M, Paschmann G, Haaland SE, Quinn JM, Torbert RB, McIlwain CE, Vaith H, Puhl-Quinn PA, Kletzing CA (2007) High-latitude plasma convection from cluster EDI: variances and solar wind correlations. Ann Geophys 25(N. 7):1691–1707

Förster M, Rentz S, Köhler W, Liu H, Haaland SE (2008) IMF dependence of high-latitude thermospheric wind pattern derived from CHAMP cross-track measurements. Ann Geophys 26(N. 6):1581–1595

Förster M, Feldstein YI, Haaland SE, Dremukhina LA, Gromova LI, Levitin AE (2009) Magnetospheric convection from cluster EDI measurements compared with the ground-based ionospheric convection model IZMEM. Ann Geophys 27(N. 8):3077–3087

Förster M, Haaland SE, Doornbos E (2011) Thermospheric vorticity at high geomagnetic latitudes from CHAMP data and its IMF dependence. Ann Geophys 29(N. 1):181–186

Freund F (2011) Pre-earthquake signals: underlying physical processes. J Asian Earth Sci. doi:10.1016/j.jseaes.2010.03.009

Haaland SE, Paschmann G, Sonnerup BUÖ (2006) Comment on "A new interpretation of Weimer et al.'s solar wind propagation delay technique" by Bargatze et al. J Geophys Res 111:A06102. doi:10.1029/2005JA011376

Haaland SE, Paschmann G, Förster M, Quinn JM, Torbert RB, McIlwain CE, Vaith H, Puhl-Quinn PA, Kletzing CA (2007) High-latitude plasma convection from cluster EDI measurements: method and IMF-dependence. Ann Geophys 25(N. 1):239–253

Hall CM, Brekke A, Martynenko OV, Namgaladze AA (1997) EISCAT measurements and model calculations of the turbulent energy dissipation in the high-latitude mesosphere. In: Abstracts of the VIII international EISCAT workshop, Leicester, p 6

Hardy DA, Gussenhoven MS, Holeman E (1985) A statistical model of auroral electron precipitation. J Geophys Res 90:4229–4248

Harrison RG, Aplin KL, Rycroft MJ (2010) Atmospheric electricity coupling between earthquake regions and the ionosphere. J Atmos Solar-Terr Phys 72(N. 5–6):376–381

Hedin AE, Biondi MA, Burnside RG, Hernandez G, Johnson RM, Killeen TL, Mazaudier C, Meriwether JW, Salah JE, Sica RJ, Smith RW, Spencer NW, Wickwar VB, Virdi TS (1991) Revised global model of thermospheric winds using satellite and ground-based observations. J Geophys Res 96:7657–7688

Iijima T, Potemra TA (1976) The amplitude distribution of field-aligned currents at northern high latitudes observed by Triad. J Geophys Res 81:2165–2174

Ivanov-Kholodny GS Nusinov AA (1987) Korotkovolnovoe izluchenie Solntza i ego vozdeistvie na verchnyuu atmospheru i ionospheru. Issledovaniya cosmicheskogo prostranstva (Investigations of Outer Space), vol 26. VINITI Press, Moscow (in Russian)

Jacchia LG (1977) Thermospheric temperature, density and composition: New models. SAO special report, N. 375, p 106

Killeen TL, Roble RG (1984) An analysis of the high-latitude thermospheric wind pattern calculated by a thermospheric general circulation model 1. Momentum forcing. J Geophys Res 89:7509–7522

Killeen TL, Won Y-I, Niciejewski RJ, Burns AG (1995) Upper thermosphere winds and temperatures in the geomagnetic polar cap: solar cycle, geomagnetic activity, and interplanetary magnetic field dependencies. J Geophys Res 100(N. A11):21327–21342

Lei J, Thayer JP, Lu G, Burns AG, Wang W, Sutton EK, Emery BA (2011) Rapid recovery of thermosphere density during the October 2003 geomagnetic storms. J Geophys Res 116:A03306. doi:10.1029/2010JA016164

Lin CH, Richmond AD, Heelis RA, Bailey GJ, Lu G, Liu JY, Yeh HC, Su S-Y (2005) Theoretical study of the low- and mid-latitude ionospheric electron density enhancement during the October 2003 superstorm: relative importance of the neutral wind and the electric field. J Geophys Res 110:A12312. doi:10.1029/2005JA011304

Liu H, Lühr H (2005) Strong disturbance of the upper thermospheric density due to magnetic storms: CHAMP observations. J Geophys Res 110:A09S29

Liu H, Lühr H, Watanabe S, Köhler W, Henize V, Visser P (2006a) Zonal winds in the equatorial upper thermosphere: decomposing the solar flux, geomagnetic activity, and seasonal dependencies. J Geophys Res 111:A07307. doi:10.1029/2005JA011415

Liu JY, Chen YI, Chuo YJ, Chen CS (2006b) A statistical investigation of preearthquake ionospheric anomaly. J Geophys Res 111:A05304. doi:10.1029/2005JA011333

Liu H, Lühr H, Watanabe S, Köhler W, Manoj C (2007) Contrasting behavior of the thermosphere and ionosphere in response to the 28 October 2003 solar flare. J Geophys Res 112:A07305. doi:10.1029/2007JA012313

Lukianova R, Christiansen F (2008) Modeling the UT effect in global distribution of ionospheric electric fields. J Atmos Solar-Terr Phys 70(N. 2–4):637–645

Namgaladze AA, Korenkov YuN, Klimenko VV, Karpov IV, Bessarab FS, Surotkin VA, Glushchenko TA, Naumova NM (1988) Global model of the thermosphere-ionosphere-protonosphere system. Pure Appl Geophys 127(N. 2/3):219–254. doi:10.1007/BF00879812

Namgaladze AA, Korenkov YuN, Klimenko VV, Karpov IV, Bessarab FS, Surotkin VA, Glushchenko TA, Naumova NM (1990) Global numerical model of the thermosphere, ionosphere, and protonosphere of the earth. Geomagn Aeron 30:612–619 (in Russian)

Namgaladze AA, Korenkov YuN, Klimenko VV, Karpov IV, Surotkin VA, Naumova NM (1991) Numerical modeling of the thermosphere-ionosphere-protonosphere system. J Atmos Terr Phys 53(N. 11/12):1113–1124. doi:10.1016/0021-9169(91)90060-K

Namgaladze AA, Korenkov YuN, Klimenko VV, Karpov IV, Surotkin VA, Bessarab FS, Smertin VM (1994) Numerical modelling of the global coupling processes in the near-earth space environment. COSPAR Coll Ser 5:807–811

Namgaladze AA, Martynenko OV, Namgaladze AN (1995a) Numerical simulation of substorm ionospheric variations observed by EISCAT by the use of the self-consistent ionosphere-thermosphere model including electric field calculations. In: Abstracts of the VII international EISCAT workshop, Cargese, p 114

Namgaladze AA, Martynenko OV, Namgaladze AN (1995b) Global model of the upper atmosphere with variable latitudinal steps of numerical integration. In: Abstracts of the IUGG XXI general assemb1ly, Boulder, GAB41F-6. B150; (1996) Geomagn Aeron 36:89–95 (in Russian)

Namgaladze AA, Martynenko OV, Namgaladze AN (1998a) Global model of the upper atmosphere with variable latitudinal integration step. Int J Geomagn Aeron 1(N. 1):53–58

Namgaladze AA, Martynenko OV, Volkov MA, Namgaladze AN, Yurik RYu (1998b) High-latitude version of the global numeric model of the Earth's upper atmosphere. Proc MSTU 1(N. 2): 23–84. http://goo.gl/8x9f2

Namgaladze AA, Shagimuratov II, Zakharenkova IE, Zolotov OV, Martynenko OV (2007) Possible mechanism of the TEC enhancements observed before earthquakes. In: Proceedings of the XXIV IUGG general assembly, Perugia, Italy

Namgaladze AA, Klimenko MV, Klimenko VV, Zakharenkova IE (2009a) Physical mechanism and mathematical modeling of earthquake ionospheric precursors registered in total electron content. Geomagn Aeron 49(N. 2):252–262. doi:10.1134/S0016793209020169

Namgaladze AA, Zolotov OV, Zakharenkova IE, Shagimuratov II, Martynenko OV (2009b) Ionospheric total electron content variations observed before earthquakes: possible physical mechanism and modeling. Proc MSTU 12(N. 2):308–315. http://goo.gl/A8cLx

Namgaladze AA, Zolotov OV, Prokhorov BE (2011) The TEC signatures as strong seismic event precursors. In: Proceedings of the XXX general assembly of URSI, Istanbul, Turkey

Noll C (2010) The crustal dynamics data information system: a resource to support scientific analysis using space geodesy. Adv Space Res 45(N. 12):1421–1440

Noll C, Bock Y, Habrich H, Moore A (2009) Development of data infrastructure to support scientific analysis for the international GNSS service. J Geodesy 83:309–325

Papitashvili VO, Christiansen F, Neubert T (2002) A new model of field-aligned currents derived from high-precision satellite magnetic field data. Geophys Res Lett 29(N. 14). eid: 1683. doi: 10.1029/2001GL014207

Paschmann G, Quinn JM, Torbert RB, Vaith H, McIlwain CE, Haerendel G, Bauer OH, Bauer TM, Baumjohann W, Cornilleau-Wehrlin N, Fillius W, Förster M, Frey S, Georgescu E, Kerr SS, Kletzing CA, Matsui H, Puhl-Quinn P, Whipple EC (2001) The electron drift instrument on cluster: overview of first results. Ann Geophys 19:1273–1288

Picone JM, Hedin AE, Drob DP, Aikin AC (2002) NRLMSISE-00 empirical model of the atmosphere: statistical comparisons and scientific issues. J Geophys Res A 107:1468. doi:10.1029/2002JA009430

Pulinets SA (1998) Seismic activity as a source of the ionospheric variability. Adv Space Res 22(N. 6):903–906

Pulinets SA, Boyarchuk K (2004) Ionospheric precursors of earthquakes. Springer, Berlin, 315 p

Pulinets SA, Legen'ka AD (2002) Dynamics of equatorial ionosphere during the preparation of strong earthquakes. Geomagn Aeron 42(N. 2):239–244 (in Russian)

Pulinets S, Ouzounov D (2011) Lithosphere–atmosphere–ionosphere coupling (LAIC) model – an unified concept for earthquake precursors validation. J Asian Earth Sci 41(4–5):371–382. doi:10.1016/j.jseaes.2010.03.005

Pulinets SA, Tsybulya KG (2010) Unique variations of the total electron content in the preparation period of Haitian earthquake (M7.9) on January 12, 2010. Geomagn Aeron 50(N. 5):686–689. doi:10.1134/S0016793210050166

Pulinets SA, Legen'ka AD, Gaivoronskaya TV, Depuev VKh (2003) Main phenomenological features of ionospheric precursors of strong earthquakes. J Atmos Solar-Terr Phys 65:1337–1347

Rees D, Fuller-Rowell TJ, Gordon R, Smith MF, Maynard NC, Heppner JP, Spencer NW, Wharton L, Hays PB, Killeen TL (1986) A theoretical and empirical study of the response of the high latitude thermosphere to the sense of the "Y" component of the interplanetary magnetic field. Planet Space Sci 34(N. 1):1–40

Reigber Ch, Lühr H, Schwintzer P (2002) CHAMP mission status. Adv Space Res 30:129–134

Rentz S, Lühr H (2008) Climatology of the cusp-related thermospheric mass density anomaly, as derived from CHAMP observations. Ann Geophys 26(N. 9):2807–2823

Ruohoniemi JM, Greenwald RA (2005) Dependencies of high-latitude plasma convection: consideration of interplanetary magnetic field, seasonal, and universal time factors in statistical patterns. J Geophys Res 110:A09204. doi:10.1029/2004JA010815

Ruzhin YuYa, Depueva AKh (1996) Seismoprecursors in space as plasma and wave anomalies. J Atmos Electr 16(N. 3):251–288

Siscoe GL, Siebert KD (2006) Bimodal nature of solar wind-ionosphere-thermosphere coupling. J Atmos Solar-Terr Phys 68(N. 8):911–920

Song P, Vasyliūnas VM, Zhou X-Z (2009) Magnetosphere-ionosphere/thermosphere coupling: self-consistent solutions for a one-dimensional stratified ionosphere in three-fluid theory. J Geophys Res 114:A08213. doi:10.1029/2008JA013629

Sorokin VM, Chmyrev VM (1999) Modification of the ionosphere by seismic related electric field. In: Hayakawa M (ed) Atmospheric and ionospheric electromagnetic phenomena associated with earthquakes. Terra Scientific Publishing Company (TERRAPUB), Tokyo, pp 805–818

Sorokin VM, Chmyrev VM, Yaschenko AK (2005a) Theoretical model of DC electric field formation in the ionosphere stimulated by seismic activity. J Atmos Solar-Terr Phys 67: 1259–1268

Sorokin VM, Yaschenko AK, Chmyrev VM, Hayakawa M (2005b) DC electric field amplification in the mid-latitude ionosphere over seismically active faults. Nat Hazards Earth Syst Sci 5: 661–666

Sorokin VM, Yaschenko AK, Hayakawa M (2006) Formation mechanism of the lower-ionosphere disturbances by the atmosphere electric current over a seismic region. J Atmos Solr-Terr Phys 68:1260–1268

Sorokin VM, Yaschenko AK, Hayakawa M (2007) A perturbation of DC electric field caused by light ion adhesion to aerosols during the growth in seismic-related atmospheric radioactivity. Nat Hazards Earth Syst Sci 7:155–163

Sutton EK, Forbes JM, Nerem RS (2005) Global thermospheric neutral density and wind response to the severe 2003 geomagnetic storms from CHAMP accelerometer data. J Geophys Res 110:A09S40. doi:10.1029/2004JA010985

Sutton EK, Nerem RS, Forbes JM (2007) Density and winds in the thermosphere deduced from accelerometer data. J Spacecraft Rockets 44(N. 6):1210–1219

Thayer JP, Killeen TL (1993) A kinematic analysis of the high-latitude thermospheric neutral circulation pattern. J Geophys Res 98(N. A7):11549–11565

Thuillier G, Perrin J-M, Lathuillère C, Hersé M, Fuller-Rowell T, Codrescu M, Huppert F, Fehrenbach M (2005) Dynamics in the polar thermosphere after the coronal mass ejection of 28 October 2003 observed with the EPIS interferometer at Svalbard. J Geophys Res 110:A09S37. doi:10.1029/2004JA010966

Toth G, De Zeeuw DL, Gombosi TI, Manchester WB, Ridley AJ, Sokolov IV, Roussev II (2007) Sun-to-thermosphere simulation of the 28–30 October 2003 storm with the space weather modeling framework. Space Weather 5:S06003. doi:10.1029/2006SW000272

Tsurutani BT et al (2005) The October 28, 2003 extreme EUV solar flare and resultant extreme ionospheric effects: comparison to other Halloween events and the Bastille Day event. Geophys Res Lett 32:L03S09. doi:10.1029/2004GL021475

Vasyliūnas VM (2007) The mechanical advantage of the magnetosphere: solar-wind-related forces in the magnetosphere-ionosphere-earth system. Ann Geophys 25:255–269. doi:10.5194/angeo-25-255-2007

Villante U, Regi M (2008) Solar flare effect preceding Halloween storm (28 October 2003): results of a worldwide analysis. J Geophys Res 113:A00A05. doi:10.1029/2008JA013132

Volkov MA, Namgaladze AA (1996) Model calculations of the field-aligned currents and electric fields during the substorm expansion phase. Geomagn Aeron 36:438–444 (in Russian)

Weimer DR (1995) Models of high-latitude electric potentials derived with a least error fit of spherical harmonic coefficients. J Geophys Res 100(N. A10):19595–19607

Weimer DR (2005) Improved ionospheric electrodynamic models and application to calculating Joule heating rates. J Geophys Res 110(N. A5):A05306. doi:10.1029/2004JA010884

Weimer DR, Ober DM, Maynard NC, Collier MR, McComas DJ, Ness NF, Smith CW, Watermann J (2003) Predicting interplanetary magnetic field (IMF) propagation delay times using the minimum variance technique. J Geophys Res 108:1026. doi:10.1029/2002JA009405

Wessel P, Smith WHF (1998) New, improved version of generic mapping tools released. EOS Trans 79:579–1998

Zakharenkova IE, Shagimuratov II, Krankowski A, Lagovsky AF (2007a) Precursory phenomena observed in the total electron content measurements before great Hokkaido earthquake of September 25, 2003 (M = 8.3). Stud Geophys Geod 51(N. 2):267–278

Zakharenkova IE, Shagimuratov II, Krankowski A (2007b) Features of the ionosphere behavior before Kythira 2006 earthquake. Acta Geophysica 55(N. 4):524–534

Zakharenkova IE, Zolotov OV, Namgaladze AA, Shagimuratov II, Martynenko OV (2008) Pre-seismic modification of the ionosphere for Greece 2006 earthquake: GPS TEC measurements and modeling results. In: Proceedings of the international conference "Fundamental Space Research", Sunny Beach, Bulgaria, pp 371–374

Zolotov OV, Namgaladze AA, Zakharenkova IE, Shagimuratov II, Martynenko OV (2008a) Modeling of the ionospheric earthquake precursors generated by various electric field sources. In: Proceedings of the XXIX general assembly of URSI, Chicago, HP-HGE.21

Zolotov OV, Namgaladze AA, Zakharenkova IE, Shagimuratov II, Martynenko OV (2008b) Simulations of the equatorial ionosphere response to the seismic electric field sources. In: Abstracts of the 7th international conference "Problems of Geocosmos", St. Peterburg, Petrodvorets, p 294

Zolotov OV, Prokhorov BE, Namgaladze AA, Martynenko OV (2011a) Variatsii polnogo electronnogo soderjanija ionosferi v period podgotovki zemletrjasenii. Khimicheskaja Fizika 30(N. 5):84–87 (in Russian)

Zolotov OV, Prokhorov BE, Namgaladze AA, Martynenko OV (2011b) Variationsof the ionosphere total electron content before earthquakes. Russ J Phys Chem B5(3): 435–438. doi: 10.1134/S1990793111030146

Chapter 5
Discharge Processes in a Stratosphere and Mesosphere During a Thunderstorm

K.V. Khodataev

Abstract This work is devoted to the theory development of the discharge phenomena called elves and sprites in the stratosphere and mesosphere initiated by tropospheric storm processes. The process of redistribution of charges in an atmosphere at altitudes up to 150 km during charging and discharging of a storm cloud is investigated at a quantitative level. An important role of the small electric conductivity of the stratosphere and mesosphere is shown. At the lightning discharge of a storm cloud, the area of the overcritical field appears under the ionosphere in which the avalanche ionization arises (elf). The avalanche ionization front instability causes the growth of large-scale perturbances, developing into an area of a subcritical field and initiating the system of subcritical streamer discharges. The account of the small electric conductivity of the atmosphere between the troposphere and the ionosphere has allowed explaining the long duration of discharge processes developing under the ionosphere, basically in the residual electrostatic polarization field.

Keywords Plasma • Ionosphere • Mesosphere • Discharge • Streamer • Elves • Sprites • Ionization avalanche • Thunderstorm • Clouds • Lightning

5.1 Introduction

Pioneer visual observations of the high-altitude discharges from airplanes and orbital stations over 89–91 years of the last century (Boeck et al. 1994, 1998) have stimulated regular scientific research of an unknown phenomenon (Franz and Nemzek 1990; Sentman and Wescott 1993; Lyons 1994; Sentman et al. 1995;

K.V. Khodataev (✉)
FSUE "Moscow Radiotechnical Institute of RAS" (MRTI), Moscow, Russia
e-mail: k.v.k@home.ptt.ru

V. Bychkov et al. (eds.), *The Atmosphere and Ionosphere*, Physics of Earth and Space Environments, DOI 10.1007/978-94-007-2914-8_5,

Cummer 1997) devoted to accumulation of experimental data. The stream of publications devoted to the further study of phenomenology, and experimental and theoretical research of high-altitude discharges, proceeds to this day at an increasing rate. Review of works on this topic can be found in many references, in particular, in Pasco (2007) and Raizer et al. (2010).

By the present time, a large volume of observations of discharge processes in the stratosphere and mesosphere has been collected, and construction of the self-consistent closed theory of these phenomena is continuing on a wide front.

Among high-altitude discharges one can distinguish the ascending (blue jets) and the descending (sprites) discharges. This chapter is devoted to constructing a quantitative theory of the descending discharges of the elves and sprites types.

In brief, observational data of descending discharges observations can be summarized as follows.

On the night side of the Earth above the horizon on a background of the dark sky, luminescence flashes at altitude about 90 km from a luminous disk ∼100 km in radius are observed from time to time. Duration of the flashes is of the order of 0.1–1 ms. Figure 5.1 shows one of the first photographs of such flashes made from the Earth's surface in America in 1997 (Barrington-Leigh 2000) (Fig. 5.1a) and from on board the shuttle "Columbia" (19 January 2003) at night above the Pacific Ocean (Boeck et al. 1998; Yair et al. 2003) (Fig. 5.1b). The photograph in Fig. 5.1a was made from a distance of ∼200 km from the center of a thunderstorm and that in Fig. 5.1b from a distance of ∼1,600 km. In both cases, as well as in all others, the altitude of the luminous area is estimated in limits of 80–90 km. Such flashes have acquired the name "elves."

In some cases, probably at especially strong thunderstorms, large-scale cone-shaped asperities with a spatial period and amplitude about the depth of the luminous area develop on the bottom of the elf. Such formations are shown in Fig. 5.2 (Barrington-Leigh 2000). From the ends of the cones grow descending discharge filament structures, falling down to an altitude of ∼40 km. Development of cones and branching of the filamentary structure occurs during 10–20 ms at the already extinguished elf. The speed of the filamentary structure front is usually 10^8–10^9 cm/s. The cones and filamentary structures have the name "sprites."

In Fig. 5.3 (Barrington-Leigh et al. 2001; Cummer et al. 2006), one can see the dynamics of the consecutive development of the elf and sprites. It is possible to see that the elf's bottom border is moving downward by 1–2 km during a time of ∼1.5 ms, that is, with a speed of $\sim 10^8$ cm/s. The front of sprites goes downward, moving with a speed of $\sim 10^9$ cm/s.

A photograph of one of the powerful sprites is shown in Fig. 5.4 (Stenbaek-Nielsen et al. 2000). Temporal evolution of the elf into sprites is seen well in Fig. 5.5, where a luminosity waveform of all the discharge area is given.

The first peak of luminosity during a part of a millisecond corresponds to the elf, and the subsequent luminosity during 30 ms – to the sprites. Research of high-altitude discharges was executed also from specialized satellites, for example, from the satellite DEMETR (Błecki et al. 2009). With the purpose of spectrum

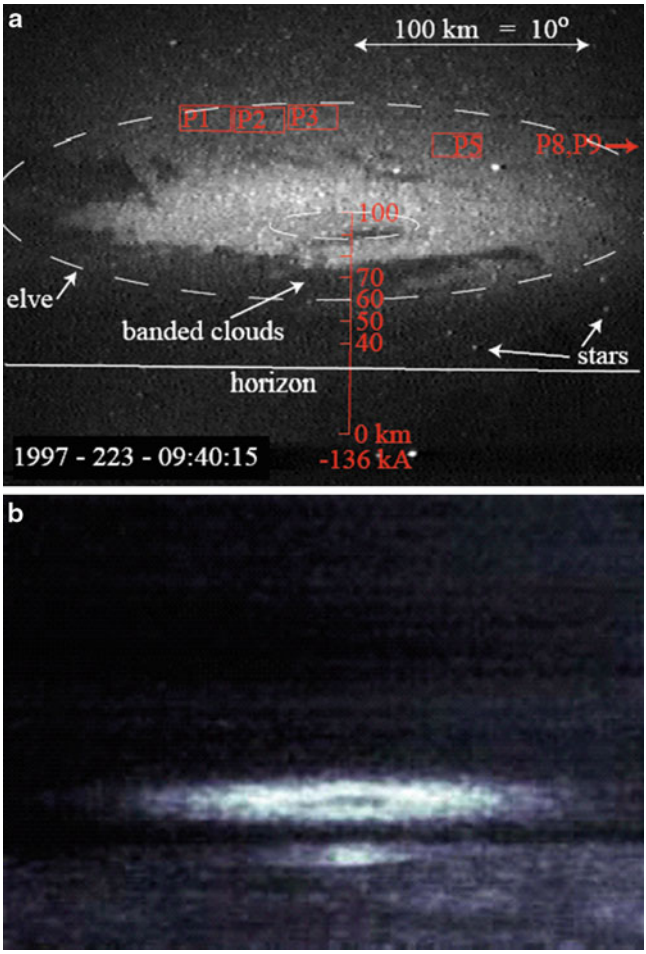

Fig. 5.1 (**a**) Photograph of elf from the surface of the ground in America. Reproduced with kind permission. (**b**) Photograph of elf from shuttle "Columbia" in January 2003. $h = 88 \pm 8$ km

registration of the UV and IR portions of the flashes, the satellites "Tatyana-1" and "Tatyana-2" (Sadovnichiy et al. 2011; Veden'kin et al. 2011) were launched. These satellites have reported the distribution of flashes over the Earth's surface (Fig. 5.6). Flashes occur mainly in the equatorial zone, not only above continents, where storm activity is the greatest, but also above the oceans.

For an explanation of high-altitude discharges, an assumption of an initiating role of powerful lightning discharges (Marshall and Inan 2007) and a supposition about a streamer mechanism of filamentary discharge formation development (Raizer et al. 2010) is usually used. With that, separate sides of the phenomenon without due quantitative analysis of the process as a whole are discussed.

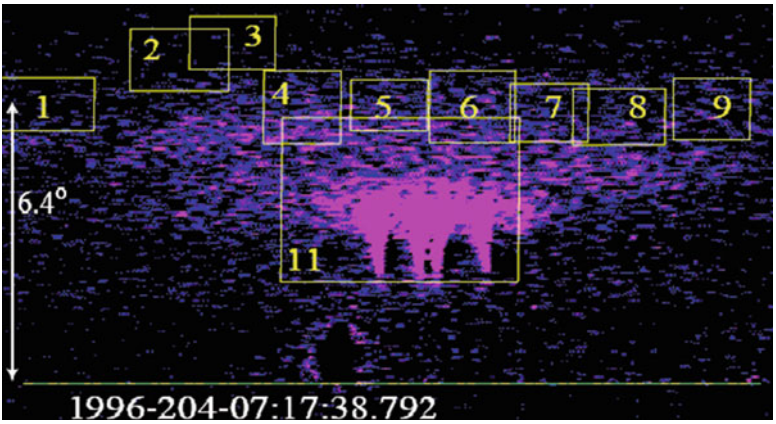

Fig. 5.2 Fast growth of large-scale regular hills

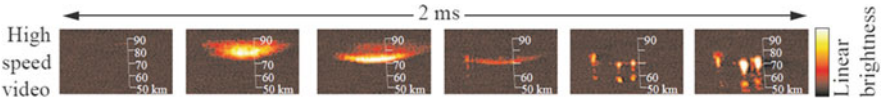

Fig. 5.3 Dynamics of transition from elf to sprites based on data from Barrington-Leigh et al. (2001). Reproduced with kind permission

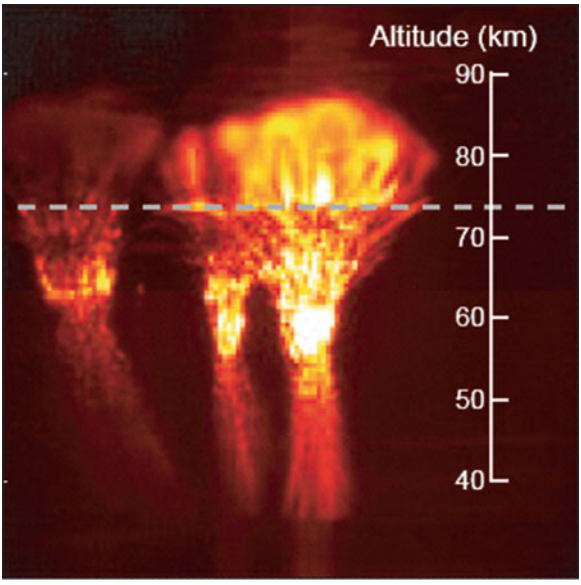

Fig. 5.4 A photo of the sprites (Stenbaek-Nielsen et al. 2000; Kramers 1923). Reproduced with kind permission

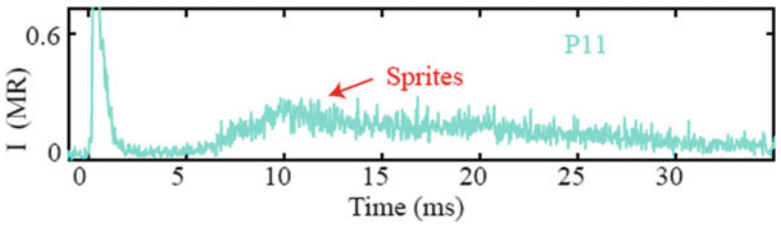

Fig. 5.5 Oscillogram of luminescence of all discharge areas of elf and sprites (Barrington-Leigh 2000). Reproduced with kind permission

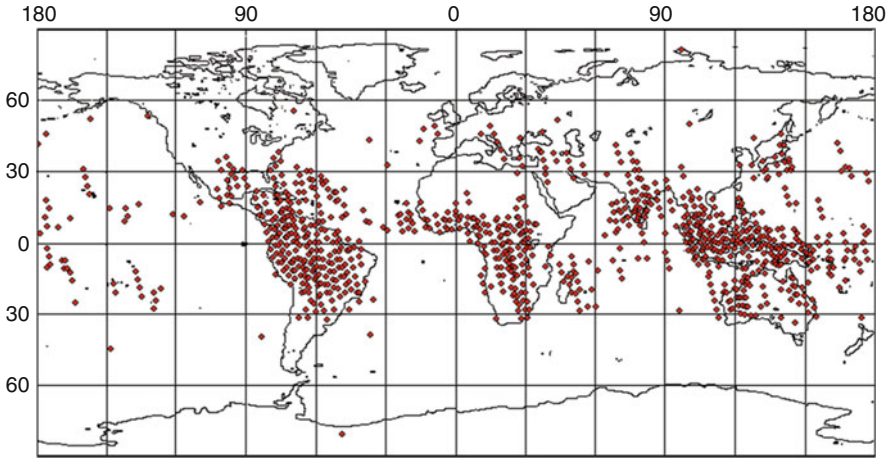

Fig. 5.6 Observations of flashes of UV and IR radiations on the night side from "Tatyana-2" (Sadovnichiy et al. 2011; Veden'kin et al. 2011) Reproduced with kind permission

Thus, many questions are left open:

- How does the initiation of ionization processes in the elves occur?
- Why are large-scale formations on their bottom border arising?
- What is the mechanism of the filamentary discharge initiation in the sprites?
- Why does sprite development occur during a time that essentially exceeds the duration of lightning discharges, etc.?

For the answer to such questions, it was necessary

- To find out all the dynamics of electric and electromagnetic fields behavior during a thunderstorm
- Based on experience of laboratory discharge observations in similar conditions, to carry out numerical calculations of ionization processes in the mesosphere

- Based on obtained results, to present a possible scenario of sprite development proved by quantitative estimations

The calculations and estimations as carried out have allowed to obtain a clear picture of the phenomenon "elf–sprites" at the quantitative level, having constructed the elementary model suitable for further specifications and complications.

5.2 The Elementary Model of Atmosphere Ionization by Solar UV Radiation (Layer E and Lower)

The calculations carried out earlier for determination of altitudes where the electric field generated by lightning discharges can exceed a critical value (a value at which excess the avalanche ionization takes place) assume an absence of conductivity below the ionosphere. At the same time it is known that a regular current with the average density of $\sim 10^{-16}$ A/cm^2 flows through the atmosphere from the terrestrial surface to the ionosphere; it assumes the presence of electric conductivity. Its presence can have an essential effect on a spatial-temporal distribution of the electric field above the storm cloud.

For the determination of conductivity distribution over altitude in the atmosphere, we use an elementary model of an ionization balance at which UV radiation of the sun and cosmic rays are present as sources of the ionization.

Let us assume that a distribution of air molecule concentration $N(h)$ over altitude h is described by the barometric formula (we neglect variation of air temperature with altitude for simplicity):

$$N(h) = N_0 \exp\left(-\frac{h}{h_0}\right), \quad h_0 = \frac{k_B T_{av}}{M m_n g} \approx 7.4 \text{ km}, \tag{5.1}$$

Here m_n = mass of a neutron; $M = 29$, the molecular weight of the air mixture, which structure is almost constant up to the altitude of 200 km; g = acceleration of gravity; k_B = the Boltzmann constant; and $T_{av} = 245$ K, the average air temperature at altitudes 0–120 km. Equation 5.1 approximates air density dependence on altitude for relatively standard atmosphere data with accuracy better than $\pm 50\%$ for altitudes less than 120 km. It is quite enough for our investigation.

Absorption of the sun radiation J_λ with a wavelength λ in the atmosphere caused by photo-ionization is described by the equation

$$\frac{dJ_\lambda}{dh} = S_{UV} \cdot N(h) \cdot J_\lambda, \tag{5.2}$$

where $S_{UV}(\lambda)$ is the cross section of photo-ionization.

The integration of Eq. 5.2 gives

$$J_\lambda(h) = J_{\lambda_0} \exp\left(-S_{\mathrm{UV}}(\lambda) \cdot h_0 \cdot N_0 \exp\left(-\frac{h}{h_0}\right)\right), \tag{5.3}$$

where J_{λ_0} is the source of the sun's radiation spectrum density.

Respectively, the source of the ionization is equal to

$$\Psi_{\mathrm{UV}_\lambda} = \frac{\mathrm{d}J_\lambda(h)}{\mathrm{d}h}. \tag{5.4}$$

After the substitution of Eq. 5.3 in Eq. 5.4 and differentiation, one gets

$$\Psi_{\mathrm{UV}_\lambda}(h) = J_{\lambda_0} \cdot S_{\mathrm{UV}}(\lambda) \cdot N_0 \exp\left(-\frac{h}{h_0}\right) \cdot \exp\left(-S_{\mathrm{UV}}(\lambda) \cdot N_0 \exp\left(-\frac{h}{h_0}\right)\right). \tag{5.5}$$

An effective photo-ionization cross section can be represented as (Kramers 1923)

$$S_{\mathrm{UV}}(\lambda) \approx S_0 \lambda^3, \quad \lambda < \lambda_{\mathrm{m}} = \left\{ \begin{matrix} 77 \rightarrow \mathrm{O_2} \\ 80 \rightarrow \mathrm{N_2} \end{matrix} \right\}, \ \mathrm{nm}$$
$$S_0 = 10^{-24}, \ \mathrm{cm^2/nm^3}. \tag{5.6}$$

A spectral density of UV radiation with wavelength shorter than 80 nm, generated, basically, by the sun crown, is represented in Fig. 5.7 (Chertok 1994).

It can be approximated by black body dependence with the appropriate temperature:

$$I_{\mathrm{UV}}(\lambda) = \frac{I_0}{\left(\frac{\lambda}{\lambda_0}\right)^4 \left(\exp\left(\frac{\lambda_0}{\lambda}\right) - 1\right)}, \ \mathrm{cm^{-3}s^{-1}} \quad \lambda_0 = \frac{\hbar 2\pi c}{k_{\mathrm{B}} T_{\mathrm{cor}}} = 100 \ \mathrm{nm}$$
$$T_{\mathrm{cor}} \approx 100 \ \mathrm{eV}, \quad I_0 \approx 3 \cdot 10^6 \ \mathrm{cm^{-2} \ s^{-1} \ nm^{-1}}. \tag{5.7}$$

The value I_0 corresponds to the average between a maximum and a minimum of the sun's activity.

The source of ionization by UV radiation is determined by the integral:

$$J_{\mathrm{UV}}(h) = \int_0^{\lambda_{\mathrm{m}}} I_{\mathrm{UV}}(\lambda) S_{\mathrm{UV}}(\lambda) N(h) \exp\left(-S_{\mathrm{UV}}(\lambda) N(h) h_0\right) \mathrm{d}\lambda, \quad \frac{1}{\mathrm{cm^3 s}}. \tag{5.8}$$

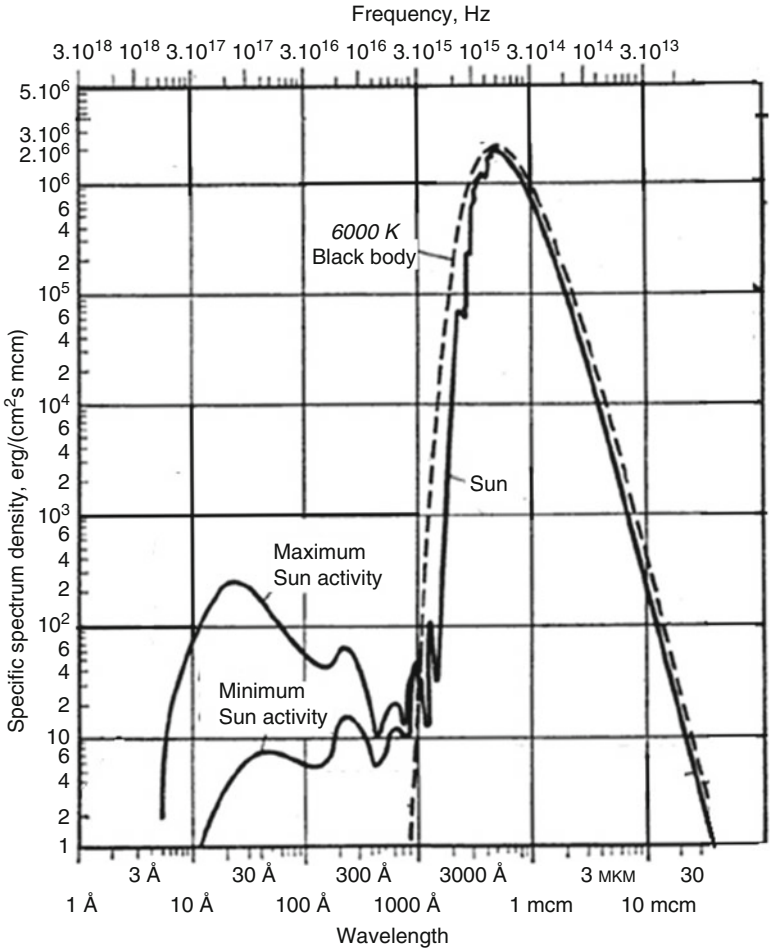

Fig. 5.7 Spectral density of radiation of the sun

Dependence of the ionization source by UV radiation on altitude is shown in Fig. 5.8.

It is known that a regular electric current proceeds through all altitudes (Imianitov and Chubarina 1965); at the surface of the Earth, the regular electric field is ~1 V/cm:

$$I_{\text{reg}} = 2 \cdot 10^{-16}, \quad \text{Acm}^{-2}. \tag{5.9}$$

Necessary regular conductivity at the surface of the ground is supported by cosmic rays. In the assumption of the high penetrating ability of space beams, the source of ionization by space beams can be approximated by dependence:

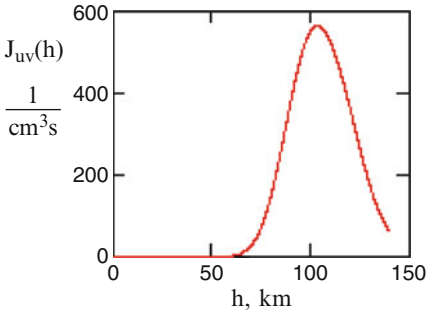

Fig. 5.8 Dependence of the ionizing UV radiation source on altitude

$$J_{\text{rays}}(h) = C_{\text{rays}} \frac{N(h)}{N(0)}, \quad C_{\text{rays}} \approx 2, \quad \frac{1}{\text{cm}^3\text{s}} \tag{5.10}$$

These factors (UV radiation of crown and cosmic rays) are sufficient for maintenance of the E-layer and weak ionization of mesosphere and stratosphere. At great altitudes and in the polar areas, the processes of ionosphere formation are also determined by events in the magnetosphere. For their description, more complicated models are required.

The ionization balance of stratosphere, mesosphere, and ionosphere is defined by three equations: balance of positive ions, balance of negative ions, and a condition of charge quasi-neutrality:

$$\begin{aligned} &J_{\text{UV}}(h) + J_{\text{rays}}(h) - \beta_{\text{i}} \cdot n_+ \cdot n_- - \beta_{\text{e}} \cdot n_+ \cdot n_{\text{e}} = 0 \\ &(K_{\text{a}}(T_{\text{e}}) + K_3(T_{\text{e}}) \cdot N(h)) \cdot N(h) \cdot n_{\text{e}} - \beta_{\text{i}} \cdot n_+ \cdot n_- = 0 \\ &n_{\text{e}} + n_- - n_+ = 0 \end{aligned} \tag{5.11}$$

where $\beta_{\text{e,i}}$ = coefficients of electron–ion and ion–ion recombination, and K_{a} and K_3 = constants of dissociation and three-body attachment reactions, depending on electron temperature, which are determined by the ratio of electric field and gas concentration *E/N*. The solution of system (5.11) is shown in Fig. 5.9.

At night the *E*-layer is recombining:

$$n_{\text{e}_{\text{right}}}(t) = \frac{n_{\text{e}_{\text{day}}}}{1 + n_{\text{e}_{\text{day}}} \beta_{\text{e}} t}. \tag{5.12}$$

In Fig. 5.10 the calculated distributions of electron concentration for daytime and nighttime are compared with well-known results of observations

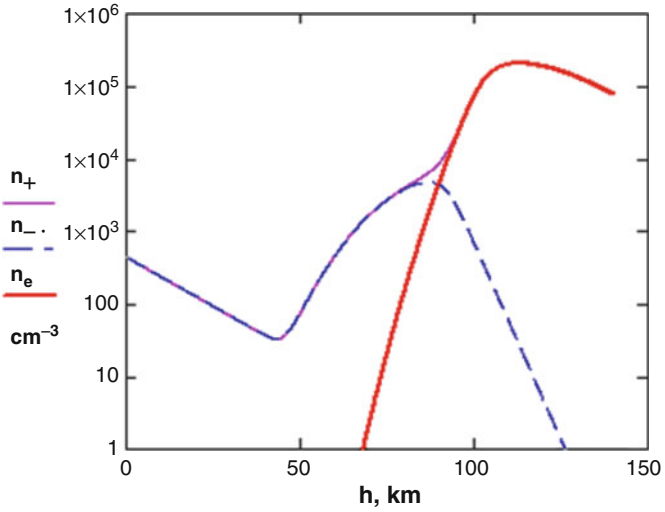

Fig. 5.9 Daytime distribution of concentration of ions and electrons on altitude

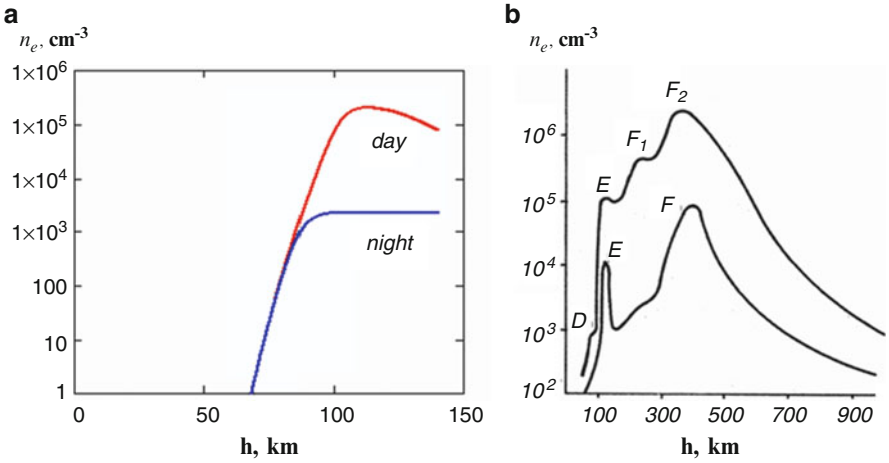

Fig. 5.10 Distribution of electronic concentration in the afternoon and at night. (**a**) Calculation result; (**b**) data of measurements

(Ivanov-Kholodnyi 1994). The satisfactory agreement for altitudes up to 150 km (layer *E* and lower) certifies applicability of use of the elementary model for further analysis.

Based on the obtained distributions of ion and electron concentrations, it is not difficult to calculate the appropriate conductivity with the account of magnetic field influence:

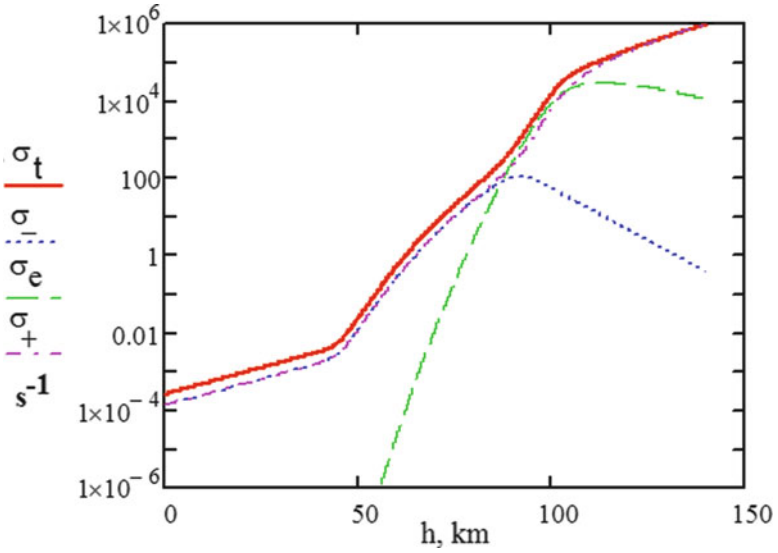

Fig. 5.11 Electric conductivity distribution on altitude: *dotted line*, electronic conductivity; *points*, conductivity of negative ions; *dashed line*, positive ions; *continuous line*, total conductivity

$$\sigma_\alpha(h) = \frac{n_\alpha(h)e^2}{m_\alpha \nu_{\mathrm{tr}_\alpha}(h)\sqrt{1+\left(\frac{\omega_{\mathrm{H}_\alpha}}{\nu_{\mathrm{tr}_\alpha}(h)}\right)^2}},$$

$$\nu_{\mathrm{tr}_\alpha}(h) = K_{\mathrm{tr}_\alpha}\left(\frac{E}{N(h)}\right)N(h), \tag{5.13}$$

and their sum

$$\sigma_{\mathrm{tot}}(h) = \sum_\alpha \sigma_\alpha(h) \tag{5.14}$$

Index α corresponds to negative ions, positive ions, or electrons, and K_{tr_α} is a constant of transfer collisions of particles α.

Distributions of the total and separate conductivities are shown in Fig. 5.11.

The regular current through media with the calculated total conductivity (Eq. 5.14) creates a regular electric field in the atmosphere, which distribution is shown in Fig. 5.12. The quantitative and qualitative agreement with the observations also confirms the applicability of the model used.

The relaxation time of the charge, appropriate to total conductivity, is defined by Eq. 5.15:

$$\tau_{\mathrm{q}} = \frac{1}{4\pi\sigma_{\mathrm{tot}}}. \tag{5.15}$$

It depends on the altitude, varying by many orders of magnitude (Fig. 5.13).

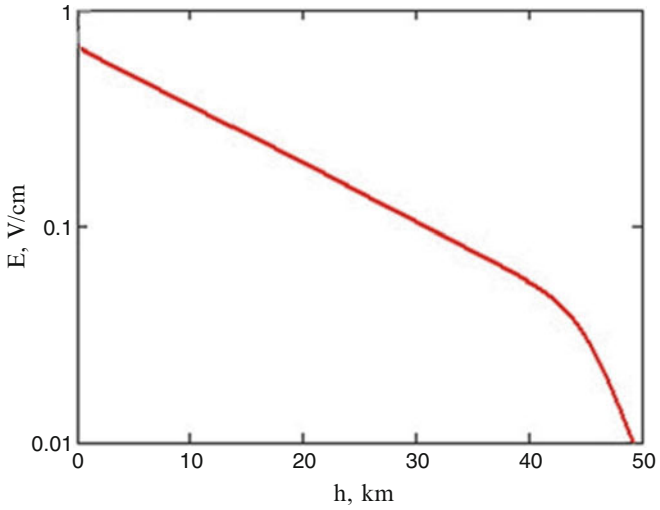

Fig. 5.12 Distribution of a regular electric field in the atmosphere

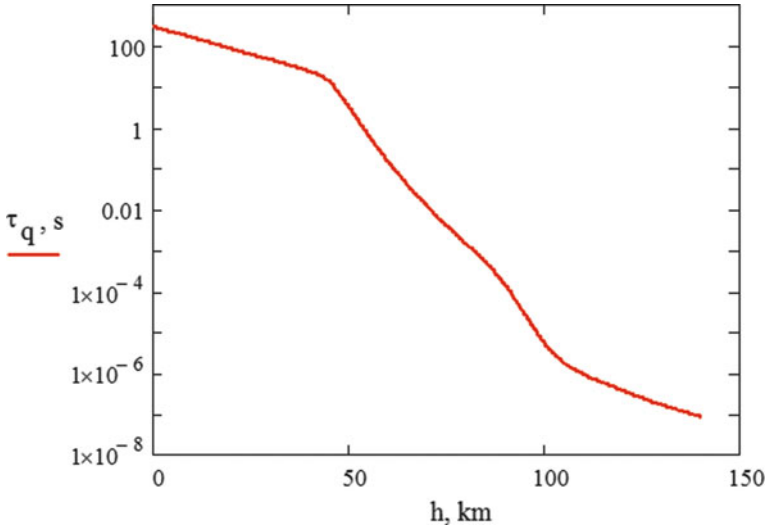

Fig. 5.13 Distribution of a charge relaxation time over altitude

If in the troposphere and lower stratosphere this time is many minutes, then in the mesosphere it is tens of milliseconds, and in the ionosphere it is microseconds. Because cloud charging caused by the convective processes in the troposphere occurs during a time period estimated in minutes, and the lightning discharge occurs during part of a millisecond, the dynamics of the electric field above the cloud demands calculations that take into the account the distribution of electric conductivity over the troposphere.

5.3 Dynamics of an Electric Field Above a Storm Cloud

Slow increase of the cloud charge causes a polarization in the stratosphere, mesosphere, and ionosphere. We present a cloud as a charged disk with radius L_c located above the surface of the ground at altitude h_0. The lightning discharge occurs on the axis of the cloudy disk (Fig. 5.14). The field of the cloud is determined by the sum of the cloud charge and its reflection under its terrestrial surface. The cloud and the ground are considered to conduct well.

The potential of the charged disk of radius R_c with charge q in emptiness is defined by Eq. 5.16:

$$\phi(r,z) = \frac{q}{R_c}\text{arctg}\left(\sqrt{\frac{2R_c^2}{r^2 - R_c^2 + z^2 + \sqrt{\left(r^2 - R_c^2 + z^2\right)^2 + 4R_c^2 z^2}}}\right). \quad (5.16)$$

The potential of the charged disk located above the conducting plane at altitude h_0 is equal to

$$\psi(r,z) = \phi(r, z - h_0) - \phi(r, z + h_0). \quad (5.17)$$

The module of the electric field is described by Eq. 5.18:

$$E_{\text{cloud}}(r,z) = E_0 \frac{\sqrt{\left(\frac{\partial\psi(r,z)}{\partial z}\right)^2 + \left(\frac{\partial\psi(r,z)}{\partial r}\right)^2}}{\sqrt{\left(\frac{\partial\psi(0,0)}{\partial z}\right)^2 + \left(\frac{\partial\psi(0,0)}{\partial r}\right)^2}}. \quad (5.18)$$

where E_0 is the field at the ground under the cloud.

The formula of Eq. 5.18 at $r = 0$ with good accuracy is approximated by the expression

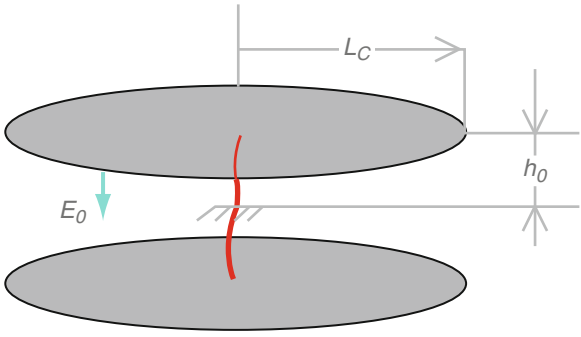

Fig. 5.14 A cloud and its "reflection"

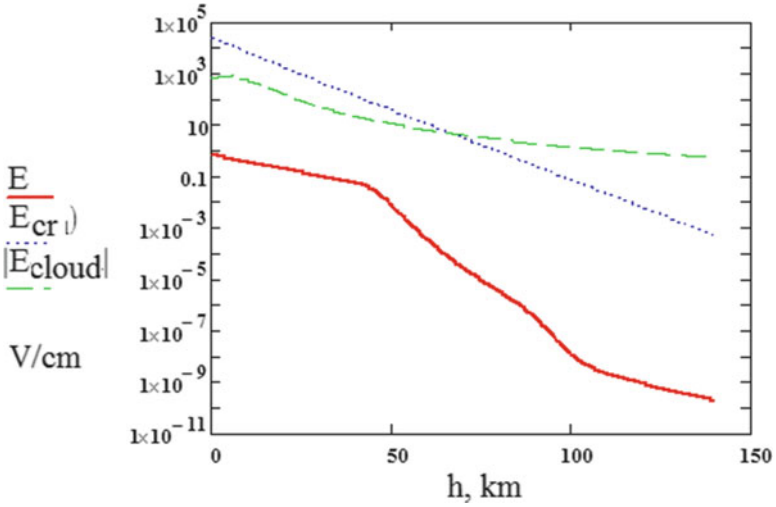

Fig. 5.15 Distribution of the field of the cloud before lightning discharge (*continuous line*), the field of the cloud without taking into account the conductivity of air (*dashed line*), and the critical field (*dotted line*)

$$E^0_{\text{cloud}}(z) \approx E_0 \left(\frac{h_0^2 + L_c^2}{(z + h_0)^2 + L_c^2} - \frac{h_0^2 + L_c^2}{(z - h_0)^2 + L_c^2} \right) \tag{5.19}$$

Let the cloud field increase by exponential law:

$$E_0 \sim \left(1 - \exp\left(-\frac{t}{\tau_{\text{ch}}} \right) \right), \tag{5.20}$$

where τ_{ch} is a characteristic time of charging in conducting media. It causes occurrence of a polarization field:

$$E_{\text{polarization}} = E^0_{\text{cloud}}(z) \left(\frac{\sigma_{\text{tot}} \tau_{\text{q}} \exp\left(-\frac{t}{\tau_{\text{ch}}} \right) - \exp(-\sigma_{\text{tot}} t)}{\sigma_{\text{tot}} \tau_{\text{q}} - 1} - 1 \right), \tag{5.21}$$

where τ_{q} is defined by Eq. 5.15

The resulting field of the cloud before lightning discharge is defined by the sum

$$E_{\text{before}} = E_{\text{cloud}} + E_{\text{polarization}}. \tag{5.22}$$

The field in the atmosphere before lightning discharge, depending on altitude, is shown in Fig. 5.15 ($r = 0$, $E_0 = 500$ V/cm, $\tau_{\text{cloud}} = 3{,}000$ s).

At all altitudes, the electric field is much smaller than the critical value, which for simplicity is approximated by Eq. 5.23:

$$E_{\mathrm{cr}} = 25 \cdot \exp\left(-\frac{h}{h_0}\right), \quad \mathrm{kV/cm} \tag{5.23}$$

After the lightning discharge, the charge of the cloud becomes small, and only the polarization field, which slowly relaxes with the local value of characteristic time, rests in the atmosphere (Eq. 5.15). This field is kept in the stratosphere and the mesosphere for tens and hundreds of milliseconds. In the mesosphere, at altitudes 70–90 km, the electric field exceeds the critical value during tens of milliseconds. The field of polarization and its relationship to the critical value at various moments of time after the lightning discharge are shown in Fig. 5.16.

After lightning discharge of the storm cloud at the bottom border of the E-layer, a zone of overcritical fields has appeared. Its radius can exceed 100 km. In Fig. 5.17 the distribution of the overcritical field zone, calculated using Eq. 5.18 for the time moment of 0.5 ms after the lightning discharge, is shown.

The size of the overcritical field zone is quite well co-ordinated with the observations (see Fig. 5.1a). The overcriticality ($E/E_{\mathrm{cr}} > 1$) is retained during several milliseconds with respect to the local value of electric conductivity. In the lower area of overcriticality ($h < 65$ km), the electric field is smaller than the critical one by several fold.

Because the electromagnetic wave pass-time between the ground and the ionosphere (3 ms) is comparable with the duration of the lightning discharge (<1 ms), the qualitative conclusion on the polarization field role in the process, obtained by the calculations carried out in the electrostatic approximation, requires verification within the framework of electrodynamics.

5.3.1 *Numerical Modeling of Electromagnetic Field Generation During Cloud Charging and Lightning Discharge*

The dynamics of the electromagnetic field in the vicinity of the storm cloud during a slow charging of clouds and after lightning discharge was investigated numerically. In contrast to previous research (Barrington-Leigh 2000; Veronis et al. 1999), the model takes into account the small, but final, conductivity of the stratosphere and mesosphere and the stage of slow cloud charging.

The problem formulation is shown in Fig. 5.18.

Between the ionosphere and the ground surface, which conductivity is assumed to be high, at the altitude of 8 km the disk-shaped conducting “cloud” is located. Above 20 km the area with final small conductivity is disposed. The slow charging of the “cloud” under the linear law during the time of several seconds is interrupted by the short circuit through the lightning channel with known conductivity,

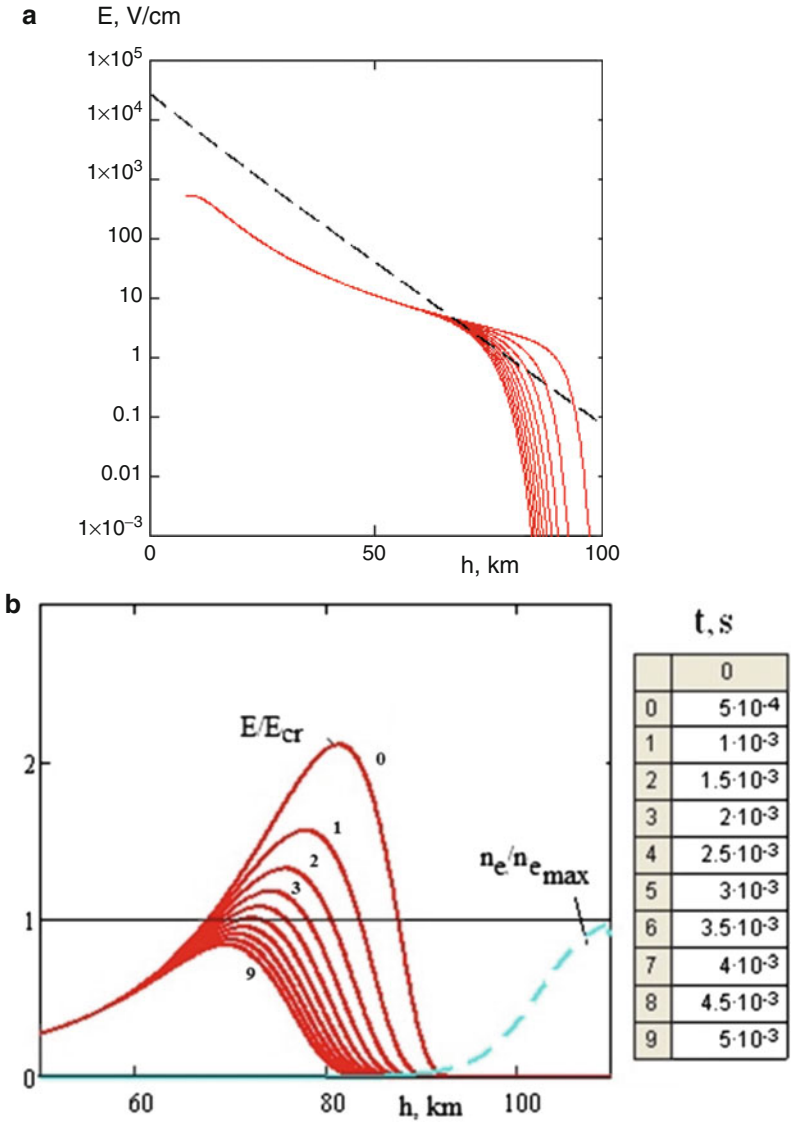

Fig. 5.16 Field of polarization (**a**) and its relationship to critical value (**b**). Minutes of time after the lightning discharge are specified in the table. *Curves* are numbered

connecting the "cloud" with the ground. Three-dimensional (3D) calculations of the electromagnetic field were carried out with the help of the standard code.

In Fig. 5.19 is shown the dependence of the lightning current magnetic field on time in the point located at the altitude of 1 km, at the distance of 1 km from the lightning channel. The maximum of the magnetic field corresponds to the maximum

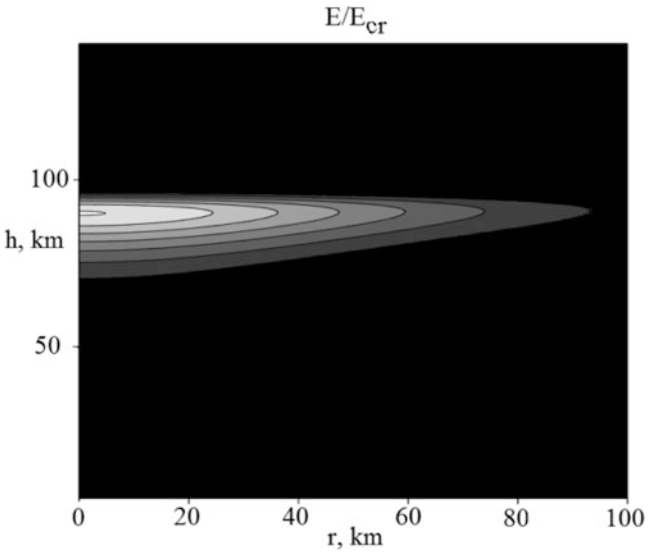

Fig. 5.17 Area of the electric field overcriticality after lightning discharge of the storm cloud

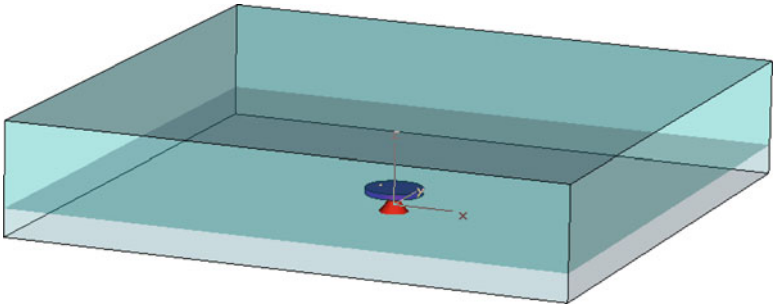

Fig. 5.18 Geometry of the problem formulation at modeling of electromagnetic field dynamics in the vicinity of a storm cloud during slow charging of the cloud and in time after lightning discharge

current in the lightning channel, equal to 13 kA. The discharge current in the lightning channel has a duration of about 0.5 ms.

In Fig. 5.20 the time dependence of the electric field above the cloud for various values of altitude is depicted.

Although the lightning discharge is finished during a time less than 1 ms, and the generation of the electromagnetic dipole radiation has finished, the electric field above the cloud under the ionosphere at all altitudes continues to exist during tens of milliseconds. This polarization field is caused by the separation of charges during the slow charging of the cloud. The electromagnetic wave, which has brought its contribution to the maximum of the field above the cloud, diverges radially in the waveguide channel, formed by ground and ionosphere, having left a zone with a

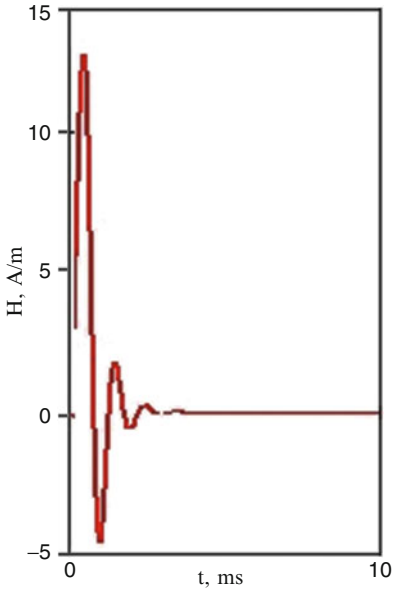

Fig. 5.19 Field *H* at altitude 1 km at distance of 1 km from the lightning channel

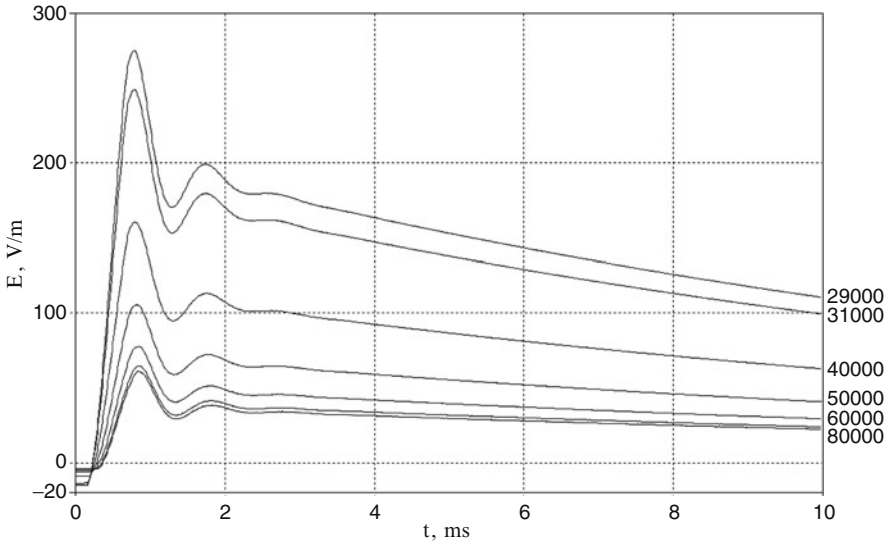

Fig. 5.20 Time dependence of electric field above the cloud for various values of altitude. *Numbers on curves*, altitude in meters

radius of 100 km during a time about of 1 ms. In Fig. 5.21 are shown spatial distributions of the electric field at the bottom border of the ionosphere after 1 ms (Fig. 5.21a) and 10 ms (Fig. 5.21b) from the moment of the beginning of the lightning discharge.

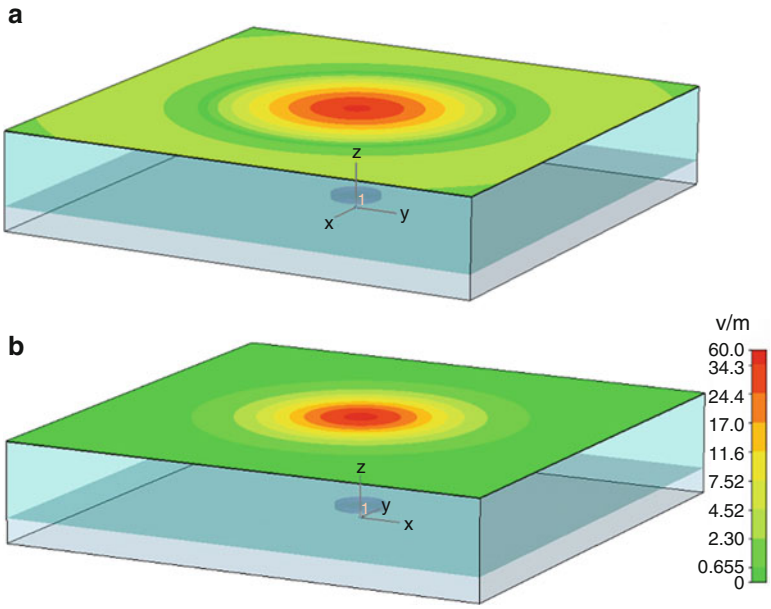

Fig. 5.21 Spatial distributions of electric field at the bottom border of the ionosphere after 1 ms (**a**) and after 10 ms (**b**) from the moment of the beginning of the lightning discharge

Thus, numerical modeling has confirmed that at the accounting of the finite conductivity of the space between the ionosphere and the cloud in the zone with a radius of about 100 km, the electric field after lightning discharge is retained during tens of milliseconds.

5.3.2 Appearance of the Plasma Layer on the Bottom Border of the Ionosphere

An excess of the electric field over the critical value by several times at the altitudes of 70–90 km, arising after the lightning discharge, causes quick ionization in this zone. We carry out research of this process by numerical modeling in one dimension (1D), using data about the electrical conductivity of the atmosphere already obtained, and the expressions of Eq. 5.19 for modeling description of the initial field distribution of the storm cloud over altitude, which scheme is submitted in Fig. 5.14.

The dynamics of the process is described by the system of Eq. 5.24, where designations are entered by Eq. 5.25. Rate constants of the dissociative attachment

K_a (E/N), and ionization by the electron impact $K_i(E/N)$ reactions and the coefficients of the ion–ion β_i and the ion–electron β_e recombination, are taken for the air mixture:

$$\begin{cases} \dfrac{\partial n_-}{\partial t} = K_a\left(\dfrac{E}{N(z)}\right) N(z) n_e - \beta_i n_- n_+, \\ \dfrac{\partial n_+}{\partial t} = K_i\left(\dfrac{E}{N(z)}\right) N(z) n_e - \beta_e n_e n_+ + \Psi(z), \\ n_e = n_+ - n_-, \\ \dfrac{\partial E}{\partial t} = -4\pi\sigma_{tot}(z) E + \dfrac{\partial E_{cloud}(z,t)}{\partial t}. \end{cases} \tag{5.24}$$

where $\sigma_{tot}(z)$ is defined by Eqs. 5.14 and 5.13.

The field of the cloud itself first rises during its charging up to the moment of time t_0, after which the lightning channel connects the cloud with ground. The resonant counter, formed by cloud capacity and lightning channel inductivity, starts the damping oscillations at the law given by Eq. 5.25:

$$E_{cloud}(z,t) = E^0_{cloud}(z) \begin{cases} \left(1 - e^{-\frac{t}{\tau_{ch}}}\right), & \text{if } t < t_0 \\ \cos\left(\Omega(t - t_0)\right) e^{-\delta\Omega(t-t_0)}, & \text{if } t > t_0 \end{cases}. \tag{5.25}$$

Here

$$\Omega \approx \frac{c}{L_c \sqrt{\pi \cdot \ln\left(\frac{2h_0}{a_{ld}}\right)}} \tag{5.26}$$

In the frequency of the contour, determined by geometric parameters of the model (see Fig. 5.14), a_{ld} is the lightning channel radius, c is the light velocity, and δ is the decay factor of oscillations caused by finite conductivity of the lightning channel. The decay factor is chosen equal to 0.4. Dependencies of the electric field of the cloud (Fig. 5.22a) and the current in the lightning channel (Fig. 5.22b) are shown at $t > t_0$.

Results of the modeling are shown in Fig. 5.23.

As one can see, the layer of ionization, which is retained for a long time under the bottom border of the ionosphere, appears during the time of the lightning discharge. The electric field inside the arisen layer is small, so the dissociative attachment ceases to play an appreciable role. The three-body attachment also is insignificant, as the concentration of molecules is small at the altitudes of the generation of the ionization layer. The layer lifetime is defined by the recombination and is as long as hours. Occurrence of the ionization layer has the character of an avalanche of ionization, which moves downward with a speed about of 10^8 cm/s, until it does not reach the border of the overcriticality region. The arisen layer of the ionization

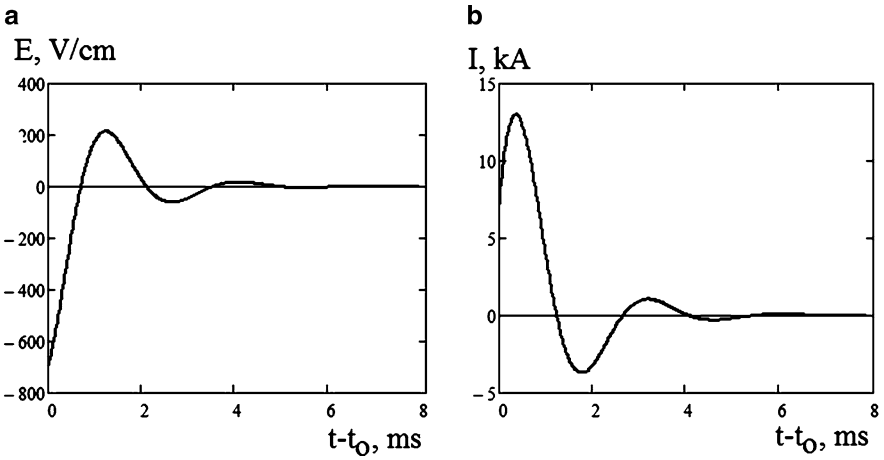

Fig. 5.22 Dependence of electric field of cloud on ground (**a**) and current in the lightning channel (**b**)

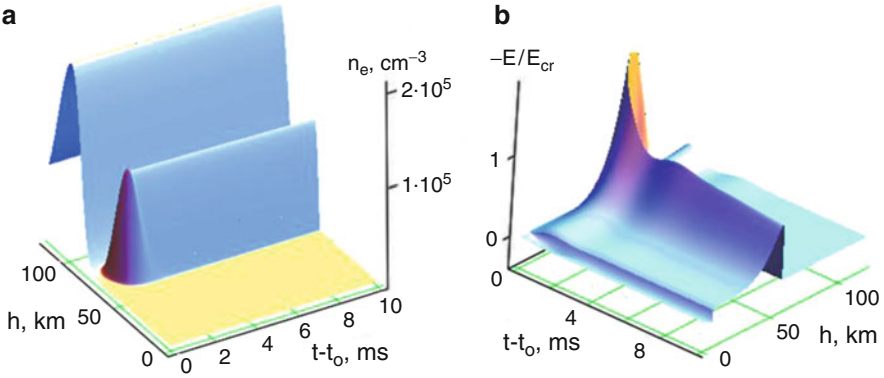

Fig. 5.23 Ionization in the zone of electric field overcriticality: electron concentration (**a**); electric field (**b**)

fills all the overcriticality zone (see Fig. 5.16). Luminosity of the ionization area, caused by the excitation of molecules by hot electrons, takes place if the electric field is comparable with the critical one and if the electron temperature, dependent on parameter *E/N*, is sufficient for the excitation of molecules. It is natural to assume that the intensity of radiation is proportional to the specific power of its ohm heating. The integration over the layer depth gives dependence, from which follows that the luminescence precedes only during the development of the avalanche and stops at its arrival at the border of the overcritical area. This time has a value of about 1 ms. The luminosity of the ionization area at the altitude of 70–90 km, arising during the thunderstorm at a duration of about 1 ms, is associated with the observations of "elves."

Although the arisen layer of the ionization stops shining, the long existence of its high ionization level influences the distribution of the electric field and further events.

5.4 Mechanism of the Occurrence of "Sprites"

The front of the avalanche of ionization is unstable with respect to large-scale perturbances of its surface (Khodataev 1995). Any asperity on a flat surface of a capacitor plate results in an increase of electric field on the asperity. The speed of the ionization avalanche is defined by Eq. 5.27:

$$V_{\mathrm{fr}} = 2\sqrt{D_{\mathrm{e}}(\nu_{\mathrm{i}} - \nu_{\mathrm{a}})}, \tag{5.27}$$

where D_{e} is the coefficient of free electron diffusion (Khodataev and Gorelik 1997);

$$\nu_{\mathrm{a}} = K_{\mathrm{a}}\left(\frac{E}{N(z)}\right)N(z) \tag{5.28}$$

is the frequency of the dissociative attachment; and

$$\nu_{\mathrm{i}} = K_{\mathrm{i}}\left(\frac{E}{N(z)}\right)N(z) \tag{5.29}$$

is the frequency of the ionization by electron impact. The greater the asperity, the faster it grows. Because the frequency of the ionization is a growing function of the electric field, the speed of the exserted part of the front exceeds the speed of the not-exserted part.

For estimation, we approximate the form of the asperity by half of the ellipsoid of revolution with the symmetry axis directed normally to the surface of the ionization avalanche front (Fig. 5.24a).

The conductivity of the layer, as the foregoing calculations show, is high enough for full shielding of the electric field during the time of the order of microseconds. Therefore, for estimation of the field increase at the top of the asperity, it is possible to consider the layer and the asperity as ideally conducting and to apply the known formula for the ideally conducting ellipsoid of revolution located in the external field represented by Eq. 5.30:

$$Q(a,b) \equiv \frac{E_{\mathrm{m}}}{E_0} = \begin{cases} \frac{2e_{\mathrm{long}}^3}{1-e_{\mathrm{long}}^2}\cdot\frac{1}{\ln\left(\frac{1+e_{\mathrm{long}}}{1-e_{\mathrm{long}}}\right)-2e_{\mathrm{long}}}, & e_{\mathrm{long}} = \sqrt{1-\left(\frac{b}{a}\right)^2}, \quad a > b \\ \frac{e_{\mathrm{flat}}^3}{1+e_{\mathrm{flat}}^2}\cdot\frac{1}{e_{\mathrm{flat}}-\mathrm{arctg}(e_{\mathrm{flat}})}, & e_{\mathrm{flat}} = \sqrt{\left(\frac{b}{a}\right)^2-1}, \quad a < b \end{cases} \tag{5.30}$$

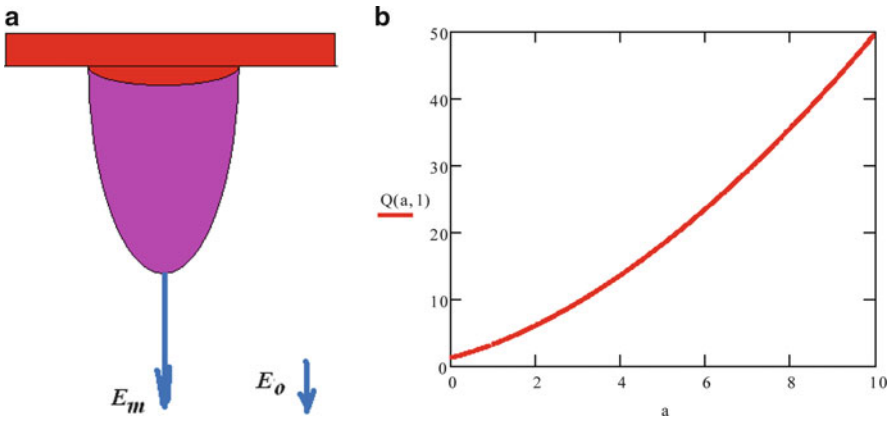

Fig. 5.24 An approximation of the form of a protuberance (**a**); dependence from Eq. 5.30 at $b = 1$ (**b**)

Here b is the radius of the basis of the ellipsoidal asperity and a is its height. The dependence given by Eq. 5.30 is shown in Fig. 5.24b.

Having applied for simplicity the known approximation of the ionization and the dissociative attachment sum of frequencies (Mayhan 1971):

$$\nu_i - \nu_a = \nu_a \left(\left(\frac{E}{E_{cr}} \right)^{\beta} - 1 \right), \quad \beta \approx 5.34, \tag{5.31}$$

and using Eq. 5.27, we estimate the speed of the asperity development in the coordinates of the front:

$$\frac{da}{dt} = V_{fr} \left(\frac{\sqrt{\left(\frac{E}{E_{cr}} Q(a,b) \right)^{\beta} - 1}}{\sqrt{\left(\frac{E}{E_{cr}} \right)^{\beta} - 1}} - 1 \right). \tag{5.32}$$

For small values of a the approximation is fair:

$$Q(a,b) \approx 1 + \frac{\pi}{2} \frac{a}{b}, \quad a \ll b. \tag{5.33}$$

Taking Eq. 5.33 into account, it is easy to determine the increment of the asperity development:

$$\gamma_{max} \approx \frac{V_{fr}}{b} \frac{\beta}{4} (E / E_{cr})^{\beta}. \tag{5.34}$$

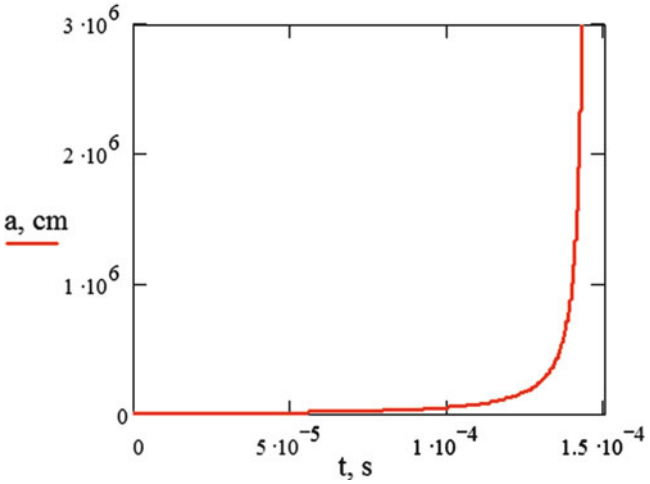

Fig. 5.25 Solution from Eq. 5.32 for the conditions of Eq. 5.35, describing the development dynamics of "sprites"

The small-scale heterogeneity of the electron concentration in the bottom of the ionosphere with horizontal sizes from several hundred meters up to tens of kilometers is formed as a result of the turbulence caused by numerous reasons (winds, magnetosphere electric currents, gravity-acoustic waves, etc.) (Gershman et al. 1984).The relative intensity of small-scale electron density fluctuations at altitudes from 80 up to 400 km is estimated by the value of about 10^{-2}. Assuming

$$V_{\text{fr}} = 10^8 \text{ km/s}, \quad b = 3 \text{ km}, \quad E/E_{\text{cr}} = 1.5, \quad a(t = 0) = 0.03 \text{ km}, \quad (5.35)$$

we get the estimated value of the increment $\gamma \approx 10^4$ s^{-1}. However, with the growth of the asperity the overcriticality E/E_{cr} at its top grows. Respectively, the increment grows. In the nonlinear case the development is defined by Eq. 5.32. Its solution for the considered case, given in Fig. 5.25, has an explosive character.

After a time of about 100 μs, the slow growth is replaced by sweeping development, and for 10 μs the asperity grows to 30 km.

In real conditions, the front of the ionization still moves within the limits of the zone of the overcritical field while the top of the asperity is already in the far subcritical field.

There can be several such asperities, caused by ionization front instability. These are the observed phenomena such as "sprites" (see Figs. 5.2 and 5.3). We have to note that the "elf" already is extinguished because its bottom front has reached the border of overcriticality and the electric field in it is already relaxed. But the "sprites" brightly shine, because their growth is accompanied by the action of the current that is taking a charge from the ionized layer of the elf to the tops of the asperities.

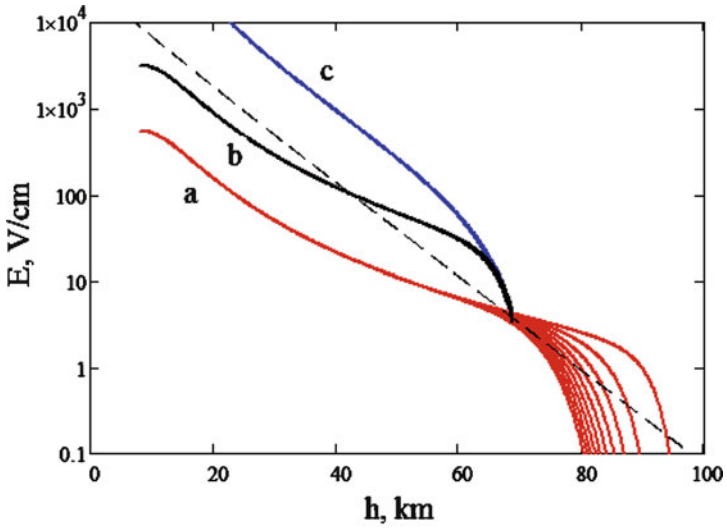

Fig. 5.26 Dependence of the electric field on altitude: *a* field under ionization layer in the absence of protuberances (same as that in Fig. 5.15); *b* field at top of system of protuberances; *c* field at the top of an individual protuberance (*dotted line*, critical field)

The electric field at the top of the individual asperity, which has reached the altitude h, remains at all altitudes greater than that of the critical value (curve (c) in Fig. 5.26). However, in the system of the asperities the field at their tops grows with their length up to a length comparable with the distance between them. For the system of the asperities, the field at their tops exceeds the critical one up to the altitude h, which is not lower than that of some definite value (a curve (b); Fig. 5.26).

During the development process the sharp peaks of the asperities initiate networks of thin streamer channels (Fig. 5.27) (Cummer 1997), playing the role of the initiator, without which the streamer discharge cannot appear in the subcritical field. Although the lightning discharge and the electromagnetic field caused by it are finished, the discharge processes proceed in the field of the polarization, obtaining from it energy necessary for ionization and heating of the channels.

The streamer nature of the filament structures, being the continuation of the large-scale asperities, was already indicated by Raizer et al. (1998). However, the question about the initiation of the streamer discharge in the subcritical field remained open. As the initiators, the tracks of the high-energy cosmic particles, the meteoric traces, and even the "running-up electrons" (Gurevich and Zybin 2001) were attractive.

The presence of the large-scale asperities, reliably providing the initiation of the streamer channels, makes other factors not necessary.

The phenomenology of the streamer subcritical discharges is investigated in sufficient detail. Their development can be accompanied by multiple branching, as one can see in Fig. 5.28 (Barrington-Leigh 2000).

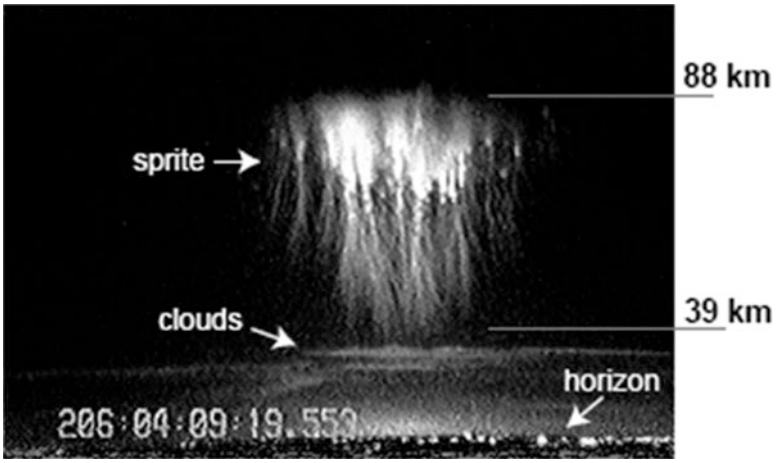

Fig. 5.27 Streamer channel initiation by large-scale protuberances (Cummer 1997). Reproduced with kind permission

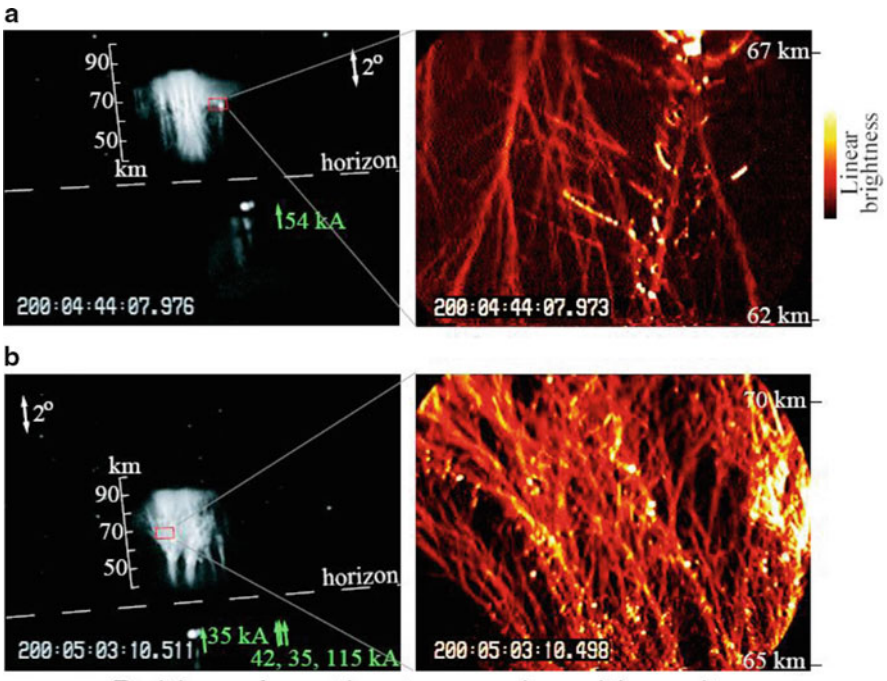

Fig. 5.28 Branching of channels in streamer discharge (Barrington-Leigh 2000). Reproduced with kind permission

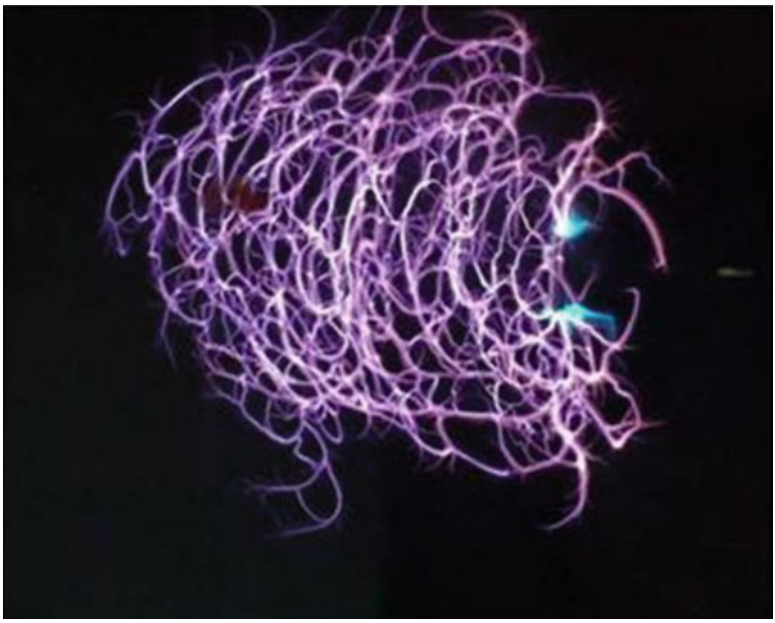

Fig. 5.29 Network of streamer channels in the microwave (*MW*) streamer subcritical discharge

In contrast to streamer subcritical discharges in the microwave (MW) field, which form no less complex networks of the filament channels (Fig. 5.29), the streamer subcritical discharge in the quasi-stationary electric field cannot leave the initiator, scooping from it the electric charge necessary for its development. However, the streamer heads, also known as the MW streamer discharge, are the powerful source of the UV radiation.

Thus, the streamer phase of the "sprites" generates the flash of UV radiation, registered by the equipment of satellites, in particular the satellites "Tatyana-1" and "Tatyana-2" (Veden'kin et al. 2011).

In Fig. 5.30 the spectrum of sprite radiation, registered by the ground detector (Barrington-Leigh 2000), and the spectrum of the MW streamer subcritical discharge, observed under laboratory conditions, are compared.

In the short-wave area, the spectra are essentially similar, which confirms the similarity of the processes in the streamer channels, in their head part, specifying their spark nature.

5.5 Conclusion

The slowly increasing charge of the cloud causes polarization in the atmosphere. Redistribution of charges in the atmosphere neutralizes the field of the cloud. After lightning discharge, the residual field of the polarization, which relaxes for a long time, remains.

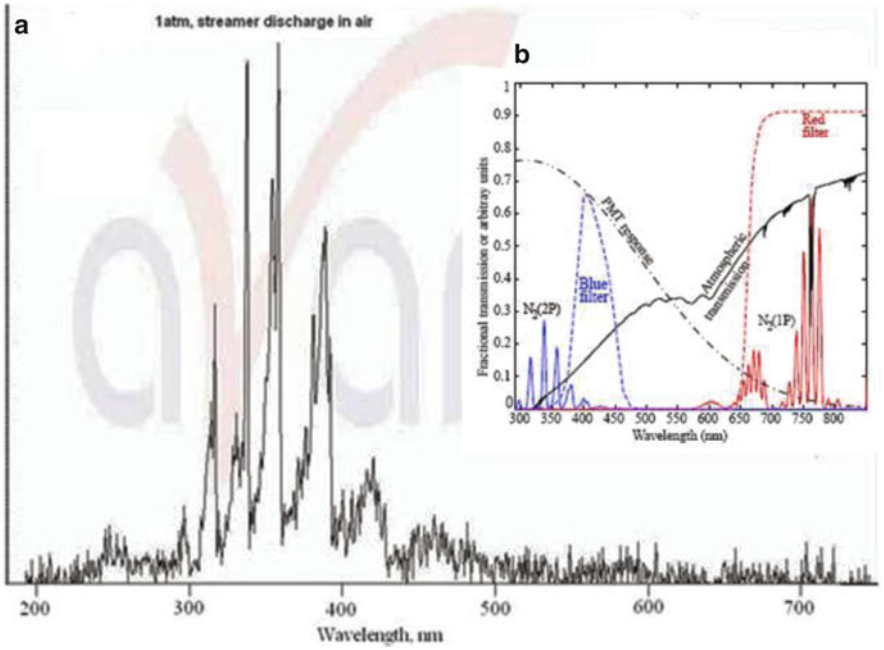

Fig. 5.30 Spectra of radiation: (**a**) spectrum of MW streamer subcritical discharge; (**b**) spectrum of the "sprites" (Barrington-Leigh 2000)

In a sufficiently strong thunderstorm, this residual field exceeds the critical value on the bottom border of the ionosphere. There originates the avalanche of ionization moving downward with the speed of 10^8–10^9 cm/s. This is the "elf."

The front of the avalanche ionization is unstable with respect to the growth of the asperities with sharpening peaks. The size of the bases of the asperities is determined by the depth of the avalanche front. When the asperities reach the zone of the subcritical field, the system of streamer channels appears at the tops of the asperities, sufficiently thin for development in the deeply subcritical field.

The relaxation time of the electric field is great enough for the development of the process during tens of milliseconds. The asperities with the attached streamer channels net are the "sprites."

Filamentation of the polarization currents at altitudes higher than 120 km creates the flash of IR radiation. The bright part of the elf and the streamer part of the sprites generate the flash of UV radiation that is registered by the satellites.

Acknowledgments The author thanks Boris Khrenov, who has attracted his attention to the most interesting problem of the high-altitude discharges, and the participants of the theoretical department of General Physics Institute of RAS seminar, headed by Prof. A.A. Rukhadze, for constructive discussion.

References

Barrington-Leigh CP (2000) Fast photometric imaging of high altitude optical flashes above thunderstorms. PhD dissertation, Stanford University, Stanford

Barrington-Leigh CP, Inan US, Stanley M (2001) Identification of sprites and elves with intensified video and broadband array photometry. J Geophys Res 106(2):1741

Błecki J, Parrot M, Wronowski R (2009) ELF and VLF signatures of sprites registered onboard the low altitude satellite DEMETER. Ann Geophys 27:2599–2605

Boeck WL, Vaughan OH, Blakeslee RJ, Vonnegut B, Brook M, McKune J (1994) Observations of lightning in the stratosphere. J Geophys Res 100(D1):1465–1475

Boeck WL, Vaughan OH Jr, Blakeslee RJ, Vonnegut B, Brook M (1998) The role of the space shuttle videotapes in the discovery of sprites, jets and elves. J Atmos Sol Terr Phys 60:669–677

Chertok IM (1994) The Sun. In: Prokhorov AM (ed) Physical encyclopedia, vol 4. Sovetskaya Éntsiklopedia, Moscow, p 394

Cummer SA (1997) Lightning and ionospheric remote sensing using VLF/ELF radio atmospherics. PhD dissertation, Stanford University, Stanford

Cummer SA, Jaugey N, Li J, Lyons WA, Nelson TE, Gerken EA (2006) Submillisecond imaging of sprite development and structure. Geophys Res Lett 33:L04104

Franz RC, Nemzek JR (1990) Winckler television image of a large upward electric discharge above a thunderstorm system. Science 249:48–51

Gershman BN, Erukhimov LM, Yashin YY (1984) Wave phenomena in ionosphere and cosmic plasma. Nauka, Moscow

Gurevich AV, Zybin KP (2001) Breakdown by run-out electrons during thunderstorm. Uspehi Fizich Nauk 171(11):1177–1199

Imianitov IM, Chubarina EV (1965) Electricity of a free atmosphere. Gidrometeoizdat, Leningrad (in Russian)

Ivanov-Kholodnyi GS (1994) Ionosphere. In: Prokhorov AM (ed) Physical encyclopedia, vol 2B. Sovetskaya Éntsiklopedia, Moscow, p 213

Khodataev KV (1995) On avalanche ionization of electronegative gas in DC field. Fizika Plasmy 21(7):605–610

Khodataev KV, Gorelik BR (1997) Diffusion and drift regimes of propagation of a flat ionization wave in MW field. Fizika Plasmy 23(3):236–245

Kramers HA (1923) The law of dispersion of X-ray absorption and of continuous X-ray spectrum. Philos Mag 46:836

Lyons WA (1994) Characteristics of luminous structures in the stratosphere above thunderstorms as imaged by low-light video. Geophys Res Lett 21:875–878

Marshall RA, Inan US (2007) Possible direct cloud-to-ionosphere current evidenced by sprite-initiated secondary TLEs. Geophys Res Lett 34:L05806

Mayhan JT (1971) Comparison of various microwave breakdown prediction models. J Appl Phys 42:5362–5368

Pasko VP (2007) Red sprite discharges in the atmosphere at high altitude: the molecular physics and the similarity with laboratory discharges. Plasma Source Sci Technol 16:S13–S29

Raizer YP, Milikh GM, Shneider MN, Novakovski SV (1998) Long streamers in the upper atmosphere above thundercloud. J Phys D Appl Phys 31:3255–3264

Raizer YP, Milikh M, Shneider MN (2010) Streamer- and leader-like processes in the upper atmosphere: models of red sprites and blue jets. J Geophys Res 115:a00e42

Sadovnichiy VA, Panasiuk MI, Yashin IV et al (2011) Cosmic media research on microsatellites "University- Tatiana" and "University -Tatiana-2". Astronomicheskiy Vestnic 45(1):1–27

Sentman DD, Wescott EM (1993) Observations of upper atmospheric optical flashes recorded from an aircraft. Geophys Res Lett 20:2857–2860

Sentman DD, Wescott EM, Osborn DL, Hampton DL, Haevner MJ (1995) Preliminary results from the Sprites 94 aircraft campaign 1. Red sprites. Geophys Res Lett 22:1205–1208

Stenbaek-Nielsen HC, Moudry DR, Westcott EM, Sentman DD, Sabbas FTS (2000) Sprites and possible mesospheric effects. Geophys Res Lett 27(23):3829–3832, doi:10.1029/2000GL003827

Veden'kin NN, Garipov GK, Klimov PA, Klimenko VV, Mareev EA, Morozenko VS, Pak I, Panasyuk M, Salazar U, Tulupov VI, Khrenov BA, Yashin IV (2011) Atmospheric flashes in UV and IR diapasons by data of satellite "University – Tatiana 2". Zurnal Eksper i Teoret Fiz 140(3(9)):1–11

Veronis G, Pasko V, Inan U (1999) Characteristics of mesospheric optical emissions produced by lightning discharges. J Geophys Res 104(12):645–656

Yair Y, Price C, Levin Z, Joseph J, Israelevitch P, Devir A, Moalem M, Ziv B, Asfur M (2003) Sprite observations from the space shuttle during the Mediterranean Israeli Dust Experiment (MEIDEX). J Atmos Sol Terr Phys 65:635–642

Chapter 6
Vortex Plasmoids Created by High-Frequency Discharges

A.I. Klimov

Abstract This experimental work is a continuation of the well-known work on microwave (MW) plasmoid physics carried out by the Nobel prize winner, P. L. Kapitsa. It is devoted to high-frequency (HF) plasmoid creation in low-temperature plasma, which is of interest from the point of view of ball lightning (BL) physics and the creation of artificial ball lightning. New experimental results on HF plasmoid generation in swirl flows are presented and analyzed. A good correlation is shown between Kapitsa's results and the new experimental results.

Keywords Plasmoids • Artificial ball lightning • Ball lightning • Experiments • Discharges • MW discharge • Capacity-coupled discharge • Swirl flow

6.1 Introduction

There are many reports on ball lightning (BL) creation in the atmosphere during thunderstorms and without them (Barry 1980; Avaramenko et al. 1994; Grigorjev 2006; Bychkov et al. 2010). Creation of BL and artificial ball lightning from the plasma vortex, created by either a lightning stroke or high power-electric jets, has been described in a number of works and is discussed by Bychkov et al. (2010). Thus, this work is the continuation of the work of Bychkov et al. (2010) devoted directly to BL investigations, but it is connected with experiments with discharge types, which have not obtained sufficient elucidation in the review literature until now. Well-known works on microwave plasmoids created by Japanese scientists headed by Y.-H. Ohtsuki and M. Ofuruton were discussed by Bychkov et al. (2010), so we do not address their works here.

A.I. Klimov (✉)
Joint Institute for High Temperature, Russian Academy of Sciences, Moscow, Russia
e-mail: klimov@ihed.ras.ru

V. Bychkov et al. (eds.), *The Atmosphere and Ionosphere*, Physics of Earth and Space Environments, DOI 10.1007/978-94-007-2914-8_6,

The famous scientist N. Tesla (Tesla and Childress 1993) and the Nobel prize-winner Russian scientist P. L. Kapitsa (1955, 1969) considered natural BL as a long-lived high-energetic structural plasma object (or a microwave [MW] plasmoid). BL theoretical models and experimental approaches based on a concept of the plasma vortex are very popular among many scientists up to the present (Avaramenko et al. 1994; Bychkov et al. 2010; Tar 2010; Vlasov 2006). Starting from the 1970s (latter twentieth century), a great number of experiments have been made on the different kinds of the vortex plasmoids (Tesla and Childress 1993).

These investigations were undertaken on realization of energy transportation for long distances and ball lightning analogues for possible aerodynamic applications (Avaramenko et al. 1994; Mirabo et al. 2001; Klimov 2009). These works created a basis for new scientific disciplines, called plasma aerodynamics and plasma combustion, which are intensively developing now (Avaramenko et al. 1994; Klimov 2009). Nowadays, investigations in these areas allow us to pose questions and find answers to phenomena connected with the nature of BL, unknown flying objects, St. Elmo's fire, and other plasma objects created in the lower troposphere.

We want to note that the artificial stable microwave (MW) plasmoid was obtained by Kapitsa in swirl gas flow. This MW plasmoid had unusual physical properties close to the observed properties of natural ball lightning. Let us indicate some of them:

1. Strong collective properties of the charged and the excited particles and the collective interaction between them;
2. Anomalous optical spectra (absorption of some optical lines by plasmoid, dissipation, and absence of the optical lines of testing deuterium gas);
3. Extremely high level of ultraviolet (UV) radiation power (so-called UV-catastrophe (Kapitsa 1969));
4. Extremely high plasma parameters: electron temperature $T_e > 10^5$ K and electron concentration $N_e > 10^{15}$ cm^{-3};
5. High efficiency of the MW energy conversion to plasma energy;
6. Neutron flux and others.

Kapitsa's hypothesis of the BL physical model is based on the combination of standing microwaves and swirl flow. He was certain that studies of the artificial plasmoid created in the laboratory help us to clarify BL physics. What is the role of swirl flow in the stable plasmoid creation in his experiment? The answer to this question was not given in his theoretical model and was left for further investigations. Now this question is studied in our work in detail.

First, let us clarify the notation "plasmoid" as used in this work.

1. The notation "plasmoid" is defined as a high-density plasma formation, consisting of excited and charged particles [including charged cluster ions, dusty particles, quasi-particles (holes, excitations, plasmons, etc., in special conditions with participation of the solid phase), cluster particles in the plasma stabilized by strong collective forces acting between them.

2. In addition to this definition, we propose that the plasmoid consists of a condensed charged plasma kernel, D_k in diameter, and an extended rarefied gas charged plasma halo with a typical diameter of about $D_h \sim (10–100)\, D_k$. Stable two-phase heterogeneous plasma formation can be created in special conditions by an initially nonequilibrium electric discharge, Klimov et al. (2011).
3. The plasma kernel and the plasma halo have opposite electric potentials, which are about several kilovolts (kV). An electrical double layer is present between these two plasma formations.
4. There is an energy gap (the "evaporation" energy of $E_c \sim 1–10$ eV) for the particles crossing the boundary between the plasma kernel and the plasma halo. However, there is an exchange between the kernel particles and those of the halo as a result of the high gas temperature (>1,000 K) in the plasma kernel, Klimov et al. (2011).
5. Strong collective forces inside the plasmoid can be of the following types: quantum body forces between the Rydberg excited atoms in the metastable condensed plasma kernel; strong magnetic forces that can stabilize the plasma pinch or the plasma focus (plasma kernel); strong Coulomb forces in the double electrical layers, which are created on the plasmoid surface (for example, plasma filaments); and others. Quantum models of the stable plasmoid are considered in the work presented by Avaramenko et al. (1994).
6. Gas dynamic disturbances with high gas flow gradients (such as a convergent shock wave, a vortex, a thermal [entropy] disturbance, etc.), created additionally in the initially diffuse gas discharge plasma, can considerably increase the probability of plasmoid creation.
7. An anomalous large lifetime after power supply switch off T_p* is an important feature of these plasmoids. A typical value of the lifetime T_p* of plasmoids is about 0.1–1.0 s. At that the plasmoid has to be supplied by the external energy flux (for example, by MW pumping), negative entropy flux (for example, an algorithmic modulation of the external MW radiation), and the mass flux during its lifetime period T is greater than T_p*: $T \gg T_p$*.
8. The erosive cluster plasmoid has a large energy storage value (range, 1–1,000 kJ), similar to a real BL (Avaramenko et al. 1994). This value of energy storage of a typical cluster plasmoid was measured by the calorimetric method. Electrical energy of the plasmoid is distributed between the extended plasma halo and the local plasma kernel with a considerably large distance. Thus, the nonlocal charged plasmoid is to be created by the erosive plasma generator. Nonlocal electrical damage (burning) of electric wires, radio devices, and electronics can be caused by this nonlocal charged plasmoid. In addition to this requirement, another is connected with the possible existence of a power converter inside the plasmoid. This power converter, a device that can transform one kind of energy (for example, mechanical) into another (for example, electrical), supplies the plasmoid with electrical energy extracted from the external medium (for example, from wind power (Klimov 2009; Klimov et al. 2009a), external turbulent flow, external MW pumping (Mirabo et al. 2001; Klimov 2009; Klimov et al. 2011), chemical power (Klimov et al. 2009b, 2010), etc.). The physical

mechanism of this power convertor operation is connected with charge separation by gas flow and may be close to the action of the well-known Van de Graaf generator.

The physical properties just listed were revealed and studied in the vortex plasmoid created by capacity-coupled high-frequency (HF) discharge. Some of the important experimental results of vortex plasmoid physics are considered in this chapter.

The main goal of this chapter is to describe studies of longitudinal plasmoids created by capacity-coupled high-frequency discharge in swirl flow. A longitudinal plasmoid was created by high-frequency discharge in swirl flow at normal atmospheric pressure.

The following tasks and problems were studied in this work:

- Stable vortex plasmoid creation by a capacity-coupled high-frequency discharge in swirl airflow. Study of the longitudinal plasmoid evolution and its structure at a pulse repetitive regime of external high-frequency power pumping.
- Physical properties of this plasmoid in swirl flow at a pulse repetitive regime of external high-frequency power pumping.
- Energy distribution inside the longitudinal vortex plasmoid created by the capacity-coupled high-frequency discharge.

Generally speaking, this work is the continuation of Kapitsa's work. Note that the listed tasks could be studied only with application of modern diagnostic instrumentation (such as high-speed CCD camera, optical spectrometer with high resolution, and electronic acquisition of measured data). This diagnostic instrumentation was not available during Kapitsa's experiments. Thus, the experimental results obtained in this work are actual and very important for the future development of plasmoids and BL physics.

6.2 Capacity-Coupled High-Frequency Discharge Parameters in High-Speed Gas Flow

It is shown that plasma formation created by capacity-coupled high-frequency discharge (CHFD) in high-speed gas flow has a number of unusual properties (Klimov 2004, 2009; Klimov et al. 2009a, 2011):

- A non-Maxwellian electron distribution function over energy. There is a group (or groups) of fast electrons (an electron beam with the energy of about 10–1,000 eV). Thus, it is possible to produce radicals and excited molecules by these fast electrons.
- The plasmoid can be created in the airflow by a capacity-coupled high-frequency discharge with a single internal electrode (one-electrode regime; the grounded electrode is connected with the high-frequency generator by a space capacity) or using two external electrodes, covered by a dielectric film (dielectric barrier discharge regime).

- A capacity-coupled high-frequency discharge is ignited and burned near a contact gas-mixing surface in the co-flow (near a high gas density gradient region) as a rule automatically. Modulated CHFD disturbs this contact surface and generates intensive acoustic waves and the gas turbulence. So, capacity-coupled high-frequency discharge can intensify a co-flow mixing of two jets.
- Fast transportation of the marked ions of a testing gas, injected in high-frequency filament, is found. The typical velocity of this marker ion transportation inside the high-frequency filaments is about $V_{fl} \sim 10^3$ m/s, or higher.
- The high-frequency filament in the high-speed gas flow (at the flow Mach number $M = 1.2$–2 and pressure $P_{st} < 10^5$ Pa) has extremely high plasma parameters. According to our measurements, the electron concentrations N_e are $N_e \sim 10^{15}$ cm^{-3} inside the streamer and $N_e \sim 10^{12}$ to 10^{13} cm^{-3} between the streamers. Specific energy storage Q inside the streamer is $Q \sim 1$–10 J/cm^3.
- Rotation temperature (T_R) of the excited nitrogen molecules in this filamentary discharge in the high-speed airflow is about $T_R = 1{,}200$ K.
- Vibration temperature (T_V) of the excited nitrogen molecules in this filamentary discharge in the high-speed airflow is about 4,000 K.

The T_R and T_V values depend considerably on high-frequency discharge parameters and airflow parameters. Thus, a high-frequency plasma filament is a nonequilibrium high-energetic plasma formation in the high-speed airflow.

6.3 Stable Longitudinal High-Frequency Discharge Plasmoid in Swirl Airflow

The longitudinal vortex plasmoid created by the capacity-coupled high-frequency discharge in swirl flow has additional important physical properties closely resembling those of natural BL.

The experimental setup SWT-1 used in our experiments was described in detail (Kilmov et al. 2011; Klimov and Moralev 2008). This setup SWT-1 was designed and manufactured to study a longitudinal vortex plasmoid created by a capacity-coupled high-frequency discharge in a tube in swirl airflow at high pressure $P_{st} \leq 10^5$ Pa and the maximal tangential velocity $V_t \sim 40$ m/s (Fig. 6.1). The setup consists of a swirl generator, a quartz tube (testing chamber), a high-frequency generator with a high-voltage Tesla transformer, high-frequency electrodes, and diagnostic instrumentation. The swirl generator was connected with a compressor. This modified setup, SWT-1M, was manufactured to study a longitudinal vortex plasmoid created by a longitudinal vortex in high-speed swirl flow at low static pressure, $P_{st} = 5 \times 10^3$ to 5×10^4 Pa, and the maximal tangential velocity $V_t \sim 140$ m/s. This setup was equipped with a vacuum chamber with a vacuum pump.

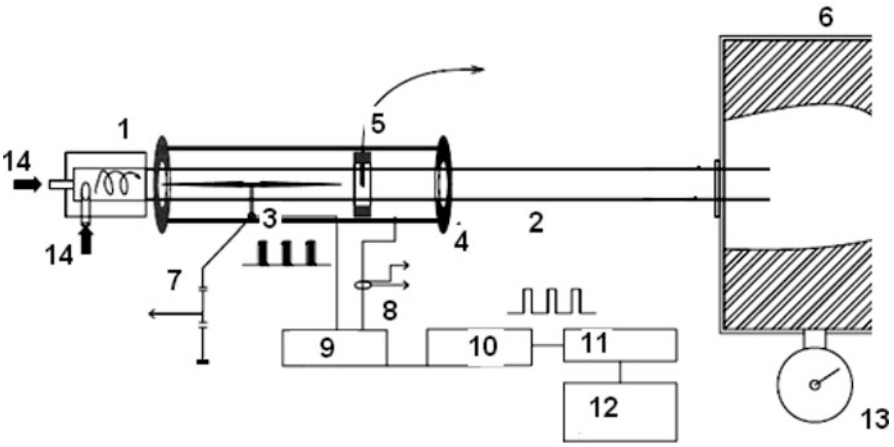

Fig. 6.1 Experimental setup SWT-1. *1* vortex generator, *2* quartz tube, *3* high-frequency electrode, *5* port with pressure sensor, *4* external grounded electrode, *6* vacuum chamber, *7* to high HF power supply, *8* current probe, *9* HF modulator, *10–12* command generator, *13* pressure manometer, *14* gas injector pressure manometer

The modified setup SWT-1F was used to study free longitudinal vortex plasmoids in the open atmosphere. The high-frequency plasma generator used in this work has the following parameters: high frequency, F_{HF}, =13.6 MHz, high-frequency power, P_{HF}, <2 kW, and two operation modes, a continuous mode and the pulse repetitive one. DC discharge was also used in some experiments ($U_{DC} < 8$ kV, $I_{DC} < 2$ A). The typical parameters of the pulsed repetitive high-frequency generator used in this work are the following: a maximal output pulsed voltage is ~60 kV, pulsed HF power was ~1–10 kW, high frequencies are $F_{HF1} = 13.6$ MHz, $F_{HF2} = 0.45$ MHz, pulse repetitive frequency was $F_M = 10–10^4$ Hz, and pulse duration is $T_i = 10$ μs to 100 ms.

Plasma and airflow parameters were measured by different diagnostic instruments including a shadow optical device with the excimer KrF laser ($\lambda = 248$ nm), an optical interferometer with a high-speed camera, Citius ($\lambda = 638$ nm), a voltage probe and current probe, an optical spectrometer ($\lambda = 200–800$ nm), an MW interferometer G4-108 ($\lambda = 1$ cm), etc.

6.4 Vortex Longitudinal Plasmoid Created by the Capacity-Coupled High-Frequency Discharge

A homogeneous longitudinal subcritical vortex plasmoid, created by a capacity-coupled high-frequency discharge in swirl airflow at continuous high-frequency discharge power pumping, is shown in Fig. 6.2. The typical length of this plasmoid varies from 30 to 150 cm at different high-frequency power values. Its diameter is about 10–15 mm.

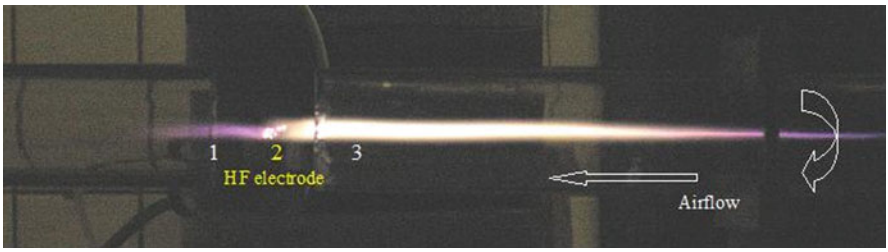

Fig. 6.2 Longitudinal vortex plasmoid created by a single high-frequency (*HF*) electrode in free space between two separated quartz tubes. *1* and *3* quartz tubes, *2* the "hot" high-frequency electrode

The typical relative ratio $K = E_{crit}/E_{HF}$ in this vortex plasmoid has been measured as about $K = 10$–100, where E_{crit} is the electric breakdown field, and $E = U/L$ (U is output high-frequency potential, E is the mean electric field intensity, and L the typical plasmoid length).

It is proven that the value $K = 100$ is too small to create the self-sustained capacity-coupled high-frequency discharge at atmosphere pressure ($L \sim 100$ cm, $U \sim 40$ kV). Actually, the relative electric field is about $E/N \sim 3$–6 T_d, and the average gas temperature inside a longitudinal vortex plasmoid is about $T_g = 600$–1,200 K (see following). This value of E/N is very small in comparison with the air breakdown field (the typical value of which, in air at atmospheric pressure, is 30 kV/cm), and it cannot realize an electric air breakdown and create a pulsed repetitive discharge. Thus, the physical mechanism of the creation of this subcritical vortex plasmoid in swirl airflow is not clear at present.

It was shown that this capacity-coupled high-frequency discharge propagates toward the oncoming airflow. This result can be connected with a reverse flow creation in swirl flow at a definite vorticity parameter value (Klimov 2009). Note that this type of high-frequency plasmoid is similar to BL and bead lightning going out of an electrical socket during thunderstorms (Grigorjev 2006; Bychkov and Bychkov 2006).

Different types of longitudinal plasmoids were created by capacity-coupled high-frequency discharge in swirl airflow at various mass flow rates in the range $2 < Q < 10$ G/s (or different flow velocities), and the various high-frequency power has values in the range $0.1 < P_{HF} < 1$ kW (Fig. 6.3). Co-flow plasmoids (frames 1, 2), counterflow plasmoids (frames 5–7), and combined forms (frames 3, 4) were created in the gas swirl flow (Fig. 6.3). The type of these longitudinal plasmoids is determined by the value Q (or of the tangential velocity) and of the value of the high-frequency power input in P_{HF}. Therefore, these vortex plasmoids can move against a wind, as can do some observed BL (Grigorjev 2006).

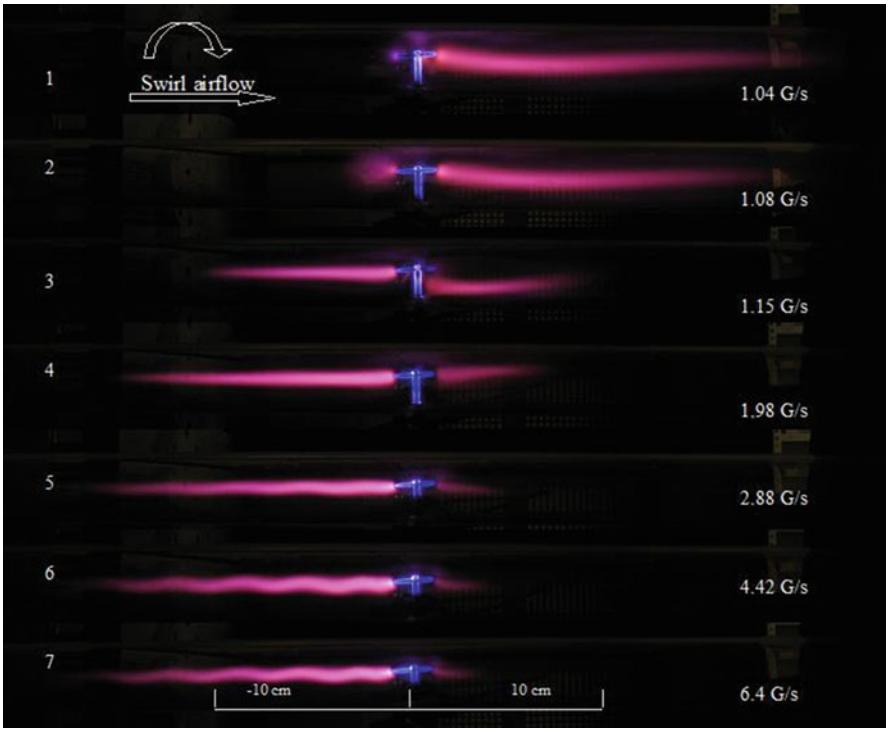

Fig. 6.3 Longitudinal high-frequency plasmoids at different mass flow rates Q. Vortex airflow, $P_{st} \sim 40$ Torr, $P_{HF} \sim 800$ W

6.5 Longitudinal Plasmoid Parameters Measured by a High-Speed Optic Interferometer

The longitudinal plasmoid evolution and its structure in swirl flow at the pulsed repetitive high-frequency power pumping was studied by both the high-speed camera and the optical interferometer simultaneously (Fig. 6.4) (Klimov and Moralev 2008; Klimov 2004; Klimov et al. 2009a, 2010, 2011; Bityurin et al. 2010). Note that a stable longitudinal vortex plasmoid was created at the pulse repetitive high-frequency power pumping was swirl flow at high modulation frequency $F_M > F_M^* \sim 1$ kHz (pulse duration $T_i = 0.5$ ms) only.

It is shown that the first high-frequency power pulse (of the pulsed repetitive capacity-coupled high-frequency discharge) creates a hot longitudinal vortex plasmoid (plasma kernel) near the vortex axis and a warm plasma cover (a halo or a low-density cavern) around it. A longitudinal vortex plasmoid consists of the longitudinal plasma filament (F) and the plasma corona (C) near its top. The second high-frequency filament, created by the new high-frequency pulse, propagates in this hot cavern created by the previous high-frequency pulse. The head propagation

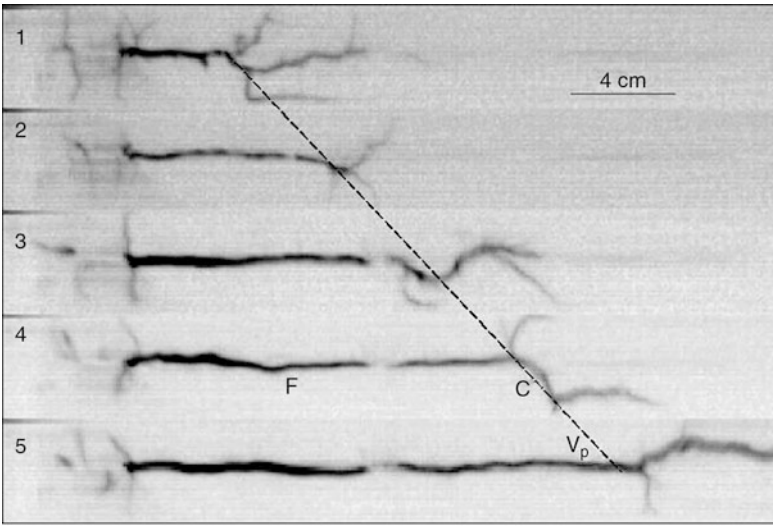

Fig. 6.4 High-speed frames of longitudinal plasmoid propagation in swirl flow. *F* plasma filament, *C* corona. Modulation frequency $F_M = 250$ Hz; $T_i = 0.5$ ms; $V_t \sim 20$ m/s; $V_{ax} \sim -8$ m/s; $U \sim 20$ kV; exposure time $t_{exp} = 1$ μs; time interval between the frames $T_f = 300$ μs; V_p, high-frequency (*HF*) filament propagation velocity

velocity of a longitudinal vortex plasmoid is close to the typical axial velocity of the counterflow (the reverse flow): $V_p \sim V_s \sim 10$–30 m/s was swirl flow (Fig. 6.4). The velocity V_p of longitudinal vortex plasmoid propagation is measured by the high-speed camera in swirl flow at low static pressure (40–100 Torr) also. The typical value of V_p is about 30–40 m/s, and it does not depend on the swirl flow velocity in this regime. In this connection one can recall that a typical velocity of BL flowing out of a socket is also about 1–10 m/s (Barry 1980; Grigorjev 2006; Bychkov et al. 2010).

Plasma parameters inside the longitudinal vortex plasmoid are studied both by optical spectroscopy and by the optical interferometer. The detailed optical spectra with a high space resolution were recorded in the different cross sections of the longitudinal vortex plasmoid created in swirl flow (Figs. 6.5 and 6.6). Nonequilibrium processes in the vortex plasmoid are optically studied. The typical optical spectrum obtained in the longitudinal vortex plasmoid is shown in Fig. 6.5. One can see the OH molecular bands and the N_2^{2+} molecular bands in this optical spectrum. These data are processed as represented in Fig. 6.6. A hot plasma kernel (with the rotational temperature $T_R \sim 1{,}500$–$2{,}000$ K and vibrational temperature $T_V \sim 3{,}000$–$4{,}000$ K) is seen inside the longitudinal vortex plasmoid. There is a "warm" plasma halo (with $T_R \sim 600$ K and $T_V \sim 4{,}000$ K) around the longitudinal vortex plasmoid kernel. There are large temperature gradients in the nonequilibrium longitudinal vortex plasmoid in this region. So, it is possible to suppose that there is some relaxation mechanism associated with the vibration–rotation (V-T) relaxation

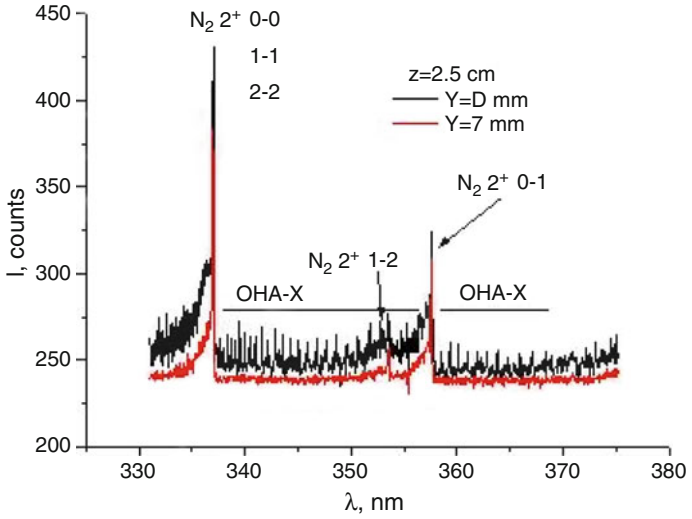

Fig. 6.5 Typical optical spectra of longitudinal plasmoid created by capacity-coupled high-frequency discharge in swirl flow. Distance $X = 2.5$ cm from the high frequency electrode for two different distances from the tube axis $Y = 0$ mm and $Y = 7$ mm; $V_t \sim 30$ m/s; $P_{HF} = 240$ W

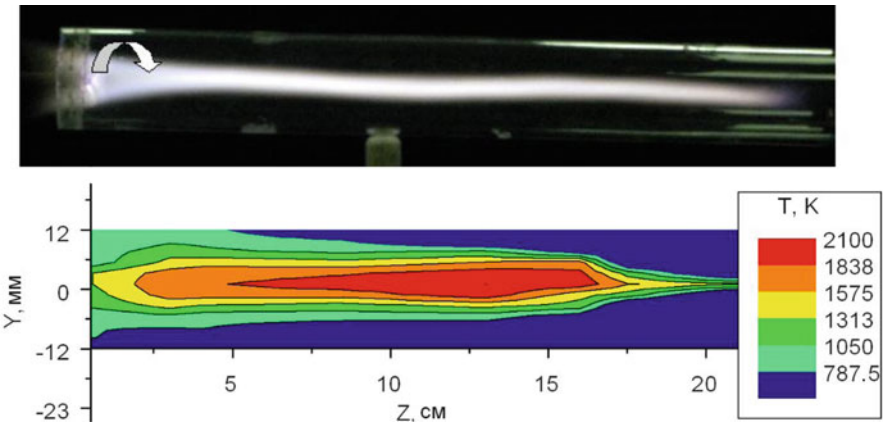

Fig. 6.6 Gas temperature (K) distribution in the high-frequency plasmoid, created in swirl flow. $V_t = 30$ m/s; high-frequency power $P_{HF} = 240$ W; pulse duration $T_i = 1$ ms; modulation frequency $F_M = 500$ Hz, $P_{st} = 10^5$ Pa. *Top*: Longitudinal high-frequency plasmoid in the swirl airflow

of the excited nitrogen molecules in this longitudinal vortex plasmoid. We have to note that we could not create the longitudinal vortex plasmoid in a noble gas (for example, argon), so it is most probably connected with the molecular features of the gas.

6.6 UV Spectra Obtained in a Longitudinal Plasmoid in Free High-Speed Swirl Flow

Recall that Kapitsa measured an intensive UV radiation and soft X-ray radiation (in the range 10^2–10^3 eV) generated by a longitudinal MW plasmoid in swirl flow in his work many years ago. He named this phenomenon the "UV-catastrophe" inside the longitudinal vortex plasmoid. The UV spectra ($\Delta\lambda = 270$–340 nm) of the longitudinal vortex plasmoid created by the capacity-coupled high-frequency discharge in swirl flow were recorded and analyzed in his work. The typical UV spectra of this longitudinal vortex plasmoid in free swirl flow recorded by the optical spectrometer AvaSpec 2048 are shown in Fig. 6.7. It was revealed that the intensity I of the optical lines and the optical bands in the wave range 250–300 nm is considerably increased in the constricted or filamented longitudinal vortex plasmoid (compared with the diffuse high-frequency discharge plasma in non-swirl flow in the same conditions). The value I was increased up to a factor of 10–20 during the transition from a filamentary (corona) high frequency discharge to the longitudinal high-frequency plasmoid (Fig. 6.7). This value I depends also on a duty cycle. So, this phenomenon depends on a plasma formation overheating (the average high-frequency power input in the plasma) (Fig. 6.8). UV radiation is increased in the

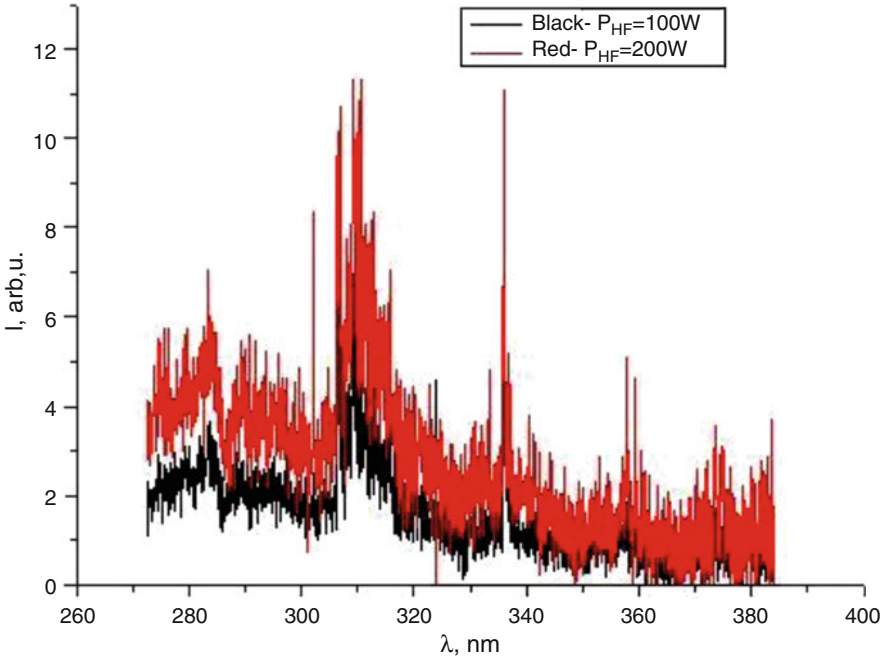

Fig. 6.7 UV optical spectra obtained in the longitudinal high-frequency plasmoid in free swirl flow. $P_{st} \sim 1$ bar; $V_t \sim V_{ax} \sim 30$ m/s

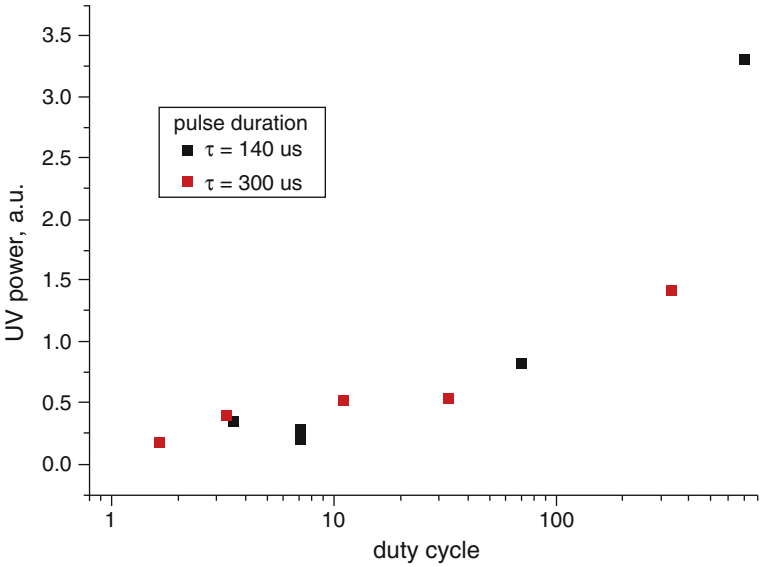

Fig. 6.8 UV intensity dependence on duty cycle in longitudinal high-frequency plasmoid in free swirl flow. $P_{st} \sim 10^5$ Pa; $V_t \sim V_{ax} \sim 30$ m/s

nonequilibrium longitudinal vortex plasmoid. So, the longitudinal vortex plasmoid is the source of the intensive UV radiation and, may be X-ray radiation (Kapitsa 1969). X-ray radiation connected with events of some BL impacts is also considered in some reports (Barry 1980; Avaramenko et al. 1994; Grigorjev 2006), but its nature has not yet been explained.

6.7 Gas Dynamic Characteristics of the Vortex Longitudinal Plasmoid

Airflow around the longitudinal vortex plasmoid was studied simultaneously by the optic interferometer and pressure transducers. The typical high-speed frames of this vortex plasmoid and the gas flow behind it (in the hot wake) obtained by this interferometer are shown in Figs. 6.9 and 6.10. It is noted that a hot gas wake is absent behind this longitudinal vortex plasmoid. It was seen that there is a considerable temperature jump on the plasmoid surface in swirl airflow. The gas temperature changes from $T_g \sim 2{,}000$ K inside the longitudinal vortex plasmoid up to $T_g \sim 600$ K outside it. The typical contact surface width in this plasmoid is about 3–5 mm (Fig. 6.9). This temperature jump was also measured by a thermocouple. The physics of this anomalous phenomenon is not clear today (see following). It is necessary to continue the experimental studies of this phenomenon to clarify the physical mechanism of this thermal insulation of a longitudinal vortex plasmoid in swirl airflow.

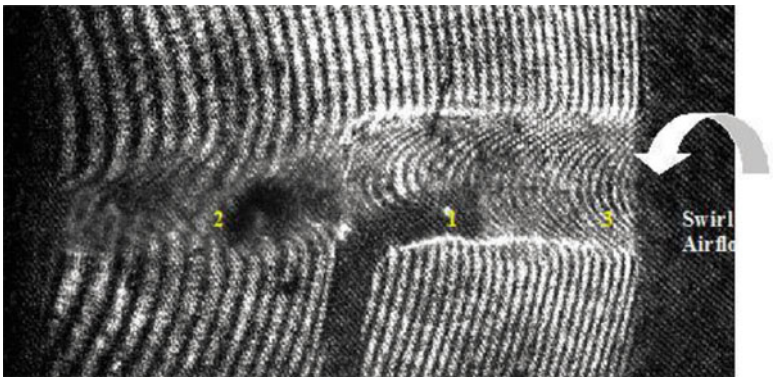

Fig. 6.9 Swirl airflow (hot wake) behind down electrode (*1*). Airflow axis velocity, 10 m/s; tangential velocity, $V_t \sim 30$ m/s; static pressure, $P_{st} \sim 10^5$ Pa; $P_d \sim 150$ W. *1* electrode, *2* hot wake, *3* vortex longitudinal plasmoid

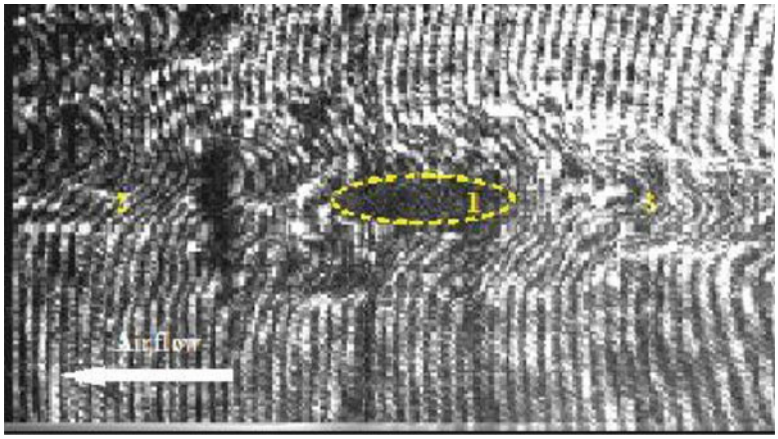

Fig. 6.10 Airflow (hot wake) behind plasma formation (*2*). Straight streamlined airflow. Airflow axis velocity, 10 m/s; static pressure, $P_{st} \sim 10^5$ Pa; *1* electrode, *2* plasmoid, *3* hot wake; $V_f \sim 30$ m/s; $P_{HF} \sim 100$ W

Comparison of results obtained in swirl flow with those obtained in non-swirl flow (in straight streamline flow) gives the following. The typical high-speed frame of the airflow around the plasmoid in Fig. 6.10 shows that there is a longitudinal turbulent hot wake behind the plasmoid in this regime. So, there is a considerable difference between this regime of straight streamline flow over the plasmoid and the previous one (in swirl flow). Note that an aerodynamic drag of this vortex longitudinal vortex plasmoid should be very small (because of the symmetrical streamlines around it, as is shown in Fig. 6.9).

There are many reports about BL motion (Barry 1980; Grigorjev 2006) near airplanes and contrary wind, and it is well known that in some observations of

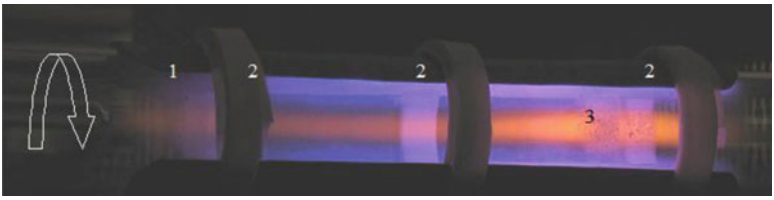

Fig. 6.11 Pressure ports (*2*) in the quartz tube (*1*) to measure pressure distribution inside longitudinal plasmoid created by capacity-coupled high-frequency discharge. $V_t \sim 140$ m/s; $P_{HF} = 1.7$ kW; $P_{st} = 40$ Torr; *1* quartz tube, *2* pressure sensor ports, *3* longitudinal plasmoid

BL motion near airplanes it has a very small drag. Note that BL long motion near airplanes represents a problem from the energy conservation point of view. So, studies of longitudinal vortex plasmoid aerodynamics can be helpful in clarification of the unusual aerodynamic properties of the real BL.

It is important to obtain a reliable information about a pressure distribution inside the longitudinal vortex plasmoid. The important task of the vortex control by a capacity-coupled high-frequency discharge can be studied in this experiment. However, correct measurements of a pressure distribution by the Pitot tube in two-dimensional (2D) swirl flow are a difficult technical task (for discussion, see (Klimov 2009; Bityurin et al. 2010)). A typical static pressure distribution in the vortex longitudinal vortex plasmoid measured by the pressure sensors is shown in Figs. 6.11, 6.12, and 6.13. One can see that the static pressure was increased up to 50% when the plasma was switched on. Therefore, there is the vortex attenuation and its dissipation by a capacity-coupled high-frequency discharge.

Some additional experiments were carried out to prove the vortex attenuation by capacity-coupled high-frequency discharge. A small helium jet was injected through a thin dielectric tube into the vortex region. This jet was deflected by the swirl flow at the plasma-off point. It was revealed that the helium jet marker was not deflected by the swirl flow at the high-frequency plasma-on point. The swirl flow is very weak to deflect the helium jet in this regime at plasma-on. Thus, there is a real vortex attenuation by the high-frequency plasma-on. This conclusion correlates with one obtained by pressure distribution analysis.

6.8 Measurements of a Power Balance in the Vortex Longitudinal Plasmoid

The experimental setup used to study the power budget in the longitudinal plasmoid vortex is shown in Fig. 6.1, Klimov (2004). The scheme of calorimetric measurements in this experimental setup is shown in Fig. 6.14. Thermocouples are arranged in a quartz tube behind the plasma formation. The optical pyrometer is

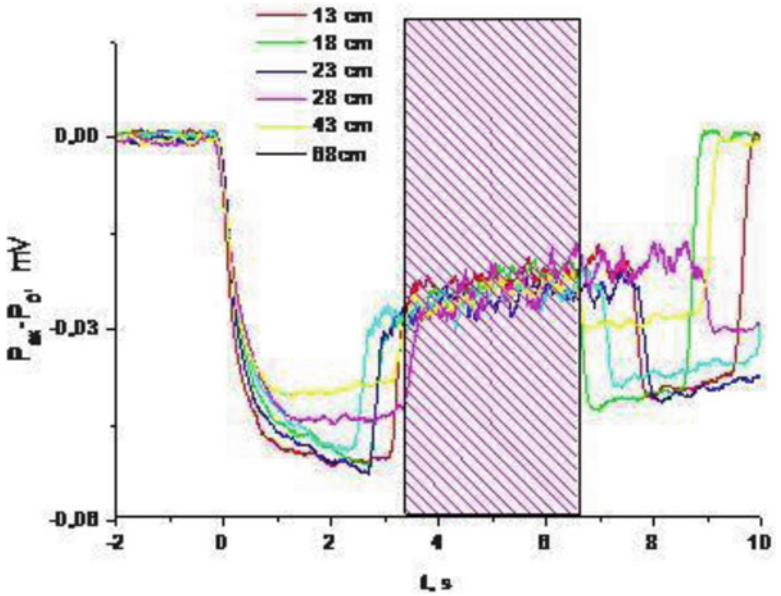

Fig. 6.12 Pressure sensor signals in different duct ports. Capacity-coupled high-frequency discharge in vortex airflow. $V_t \sim 140$ m/s, $P_{HF} = 1.7$ kW, $P_{st} = 40$ Torr. Minimal high-frequency plasma generator operation time is marked by *magenta lines*. A distance of a section from the high-frequency electrode, at which a measuring port was located, is in cm

used to measure gas temperature inside the plasma formation. We observed many erosive tungsten clusters created by the capacity-coupled high-frequency discharge (caused by tungsten electrode erosion). These particles help us to measure the gas temperature in the plasma by the pyrometer. The optical spectrometer AvaSpec 2048 (with wavelength resolution $\delta\lambda \sim 0.2$ nm) is used to measure the gas temperature inside the plasmoid (Klimov 2009).

The experimental conditions were the following:

High frequency	$F_{HF} = 13.6$ MHz
Electric power	$P_d = 1.9$ kW
Static pressure in airflow	$P_{st} \sim 10^5$ Pa
Airflow velocity (axial)	$V_{ax} \sim 30$ m/s
Tangential airflow velocity	$V_t \sim 30$ m/s

The following parameters were measured in this experiment: Q_{af}, the mass airflow rate in the quartz tube; δT, the average airflow temperature increase, measured by the thermocouples near the tube axis (X), and near the tube wall (W) at the high-frequency discharge plasma-on; T_w, wall temperature; T_{el}, electrode temperature; the chemical composition of the gas flow; and M_{el}, the erosion mass of the electrode material.

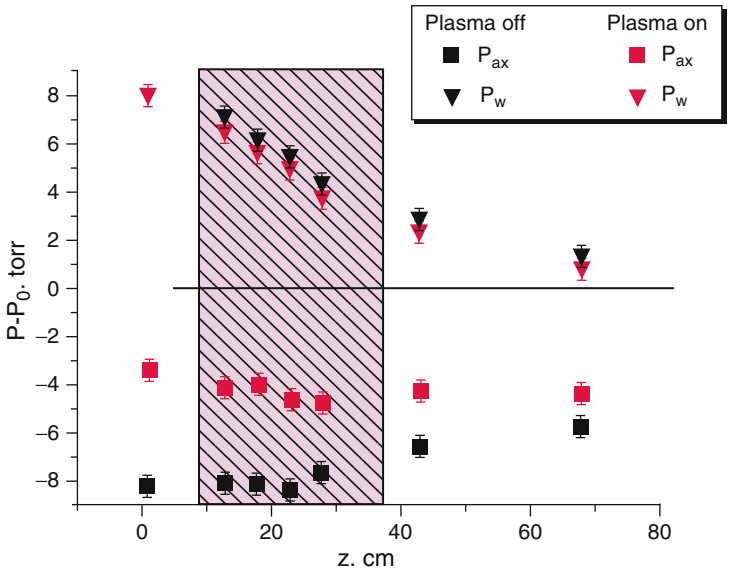

Fig. 6.13 Static pressure distribution along vortex of longitudinal plasmoid. Tangential velocity $V_t = 140$ m/s, $P_{HF} = 1{,}700$ W, $P_{st} = 40$ Torr. Discharge position in the quartz tube is marked by the *window*. P_{ax} and P_w are pressures measured near the axis and wall of the tube

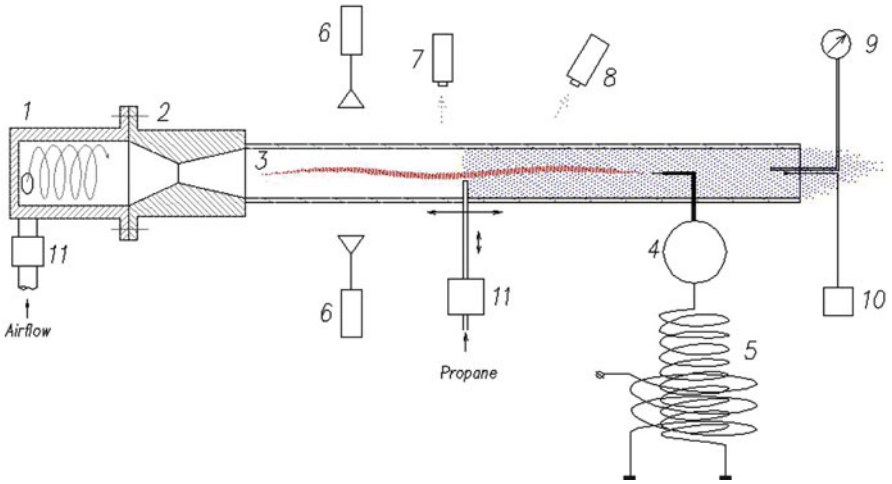

Fig. 6.14 Scheme of experimental setup with the vortex chamber *1* used in power balance experiment: *2* nozzle, *3* quartz tube, *4* high-frequency ball electrode, *5* Tesla transformer, *6* microwave interferometer, *7* video camera, *8* optical pyrometer, *9* pressure sensor, *10* thermocouple, *11* propane injector

Table 6.1 Vortex plasmoid parameters

Q_{af}, G/s	δT, K	P_T, W	$\eta = P_T/P_{HF}$
13.4	*X*, 530	7,000	3.7
14.4	*X*, 520	7,643	4.02
14.6	*X*, 420	6,284	3.3
14.65	*X*, 362	5,430	2.86
13.8	*W*, 437	6,174	3.25

Table 6.2 Capacity-coupled high-frequency discharge (CHFD) plasma parameters in the non-swirl (straight streamline) airflow

Q_{af}, G/s	δT, K	P_T, W	$\eta = P_T/P_{HF}$
14.65	*X*, 32	480	0.25
17.2	*X*, 33	583	0.31
17.2	*W*, 27	477	0.25

X corresponds to the temperature measurement near the duct axis; *W* corresponds to the temperature measurement near the duct wall

Table 6.3 Calorimetric calibration experiment results

Q_{af}, G/s	δT, K	P_T, W	I_H, A/U_H, V	P_E, W
7.11v	75	546	15/33	500
5.17s	84	445	15.5/33.6	521
5.17v	79	418	14.5/33.1	463.4
6.03s	76	469.3	15/33.1	496.5

s straight streamline airflow, v swirl flow

Thermal power P_T of the gas flow heated by a capacity-coupled high-frequency discharge was estimated by the formula:

$$P_T = Q_{af} C_p \delta T$$

where C_p is the heat permeability. The obtained experimental results are shown in Table 6.1.

One can see that airflow heating by the vortex plasmoid is more effective compared with the filamentary plasmoid, created in the straight streamline airflow (at the same high-frequency power input to the plasma). Note that the thermal power of the output airflow heated by a capacity-coupled high-frequency discharge exceeds the high-frequency power input to the plasma (~1.9 kW) by a factor of 3–4. This result is not clear today: one can suppose that there is additional power release connected with cluster creation in the plasma (condensation power) and their destruction in swirl flow. So, there is additional heating of the oncoming swirl flow by this power source. This principal question we plan to study in detail in future experiments.

One can see that there is a power loss in the straight-streamline airflow at the same experimental conditions as in the previous experiment (see Table 6.2).

The calibration experiment in this setup was carried out by the electric wire heater (using a tungsten wire). The obtained experimental results are shown in Table 6.3. Electrical voltage, current, and power were measured in this experiment.

One can see that the thermal power P_T of the output airflow is close to the electric power value P_E applied by the wire heater. So, these calorimetric measurements are correct and accurate ones (heat power losses were small in this setup). Therefore, the conclusion about the extra power release in the vortex plasmoid is correct also.

6.9 Study of a Longitudinal Plasmoid in a Free High-Speed Swirl Flow

Studies of the longitudinal vortex plasmoid created by a capacity-coupled high-frequency discharge in the free high-speed swirl airflow were carried out in this work for the first time. The experimental setup SWT-1F used in these experiments is shown in Figs. 6.1 and 6.15. A swirl generator was connected with a vacuum chamber by a conical nozzle in this experiment.

The conical nozzle had the following dimensions and parameters:

Contraction angle	60°
Outer diameter	20 mm

The experimental conditions were the following:

Mach number of axial flow	$M_x < 0.3$
Mach number of tangential flow	$M_t < 0.3$
Testing gas	Air
Flow static pressure	$P_{st} \sim 100$ Torr

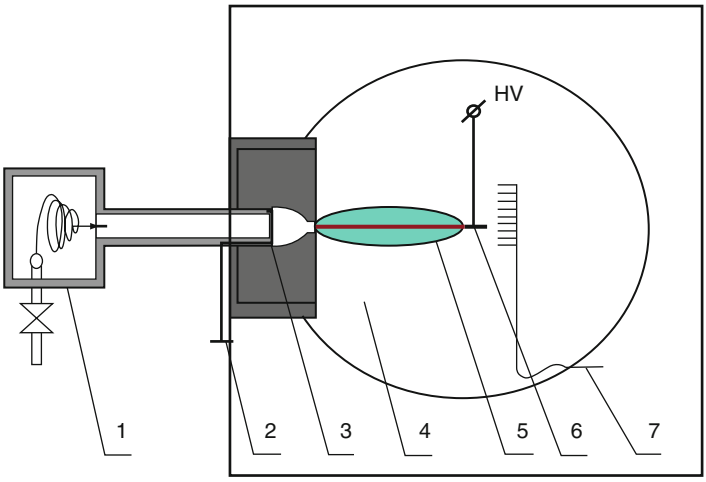

Fig. 6.15 Scheme of blow-down experimental setup SWT-1F. *1* Swirl generator, *2* grounded forming duct, *3* conical nozzle, *4* optical window, *5* capacity-coupled high-frequency discharge, *6* needle high-frequency electrode, *7* pressure sensors (grid)

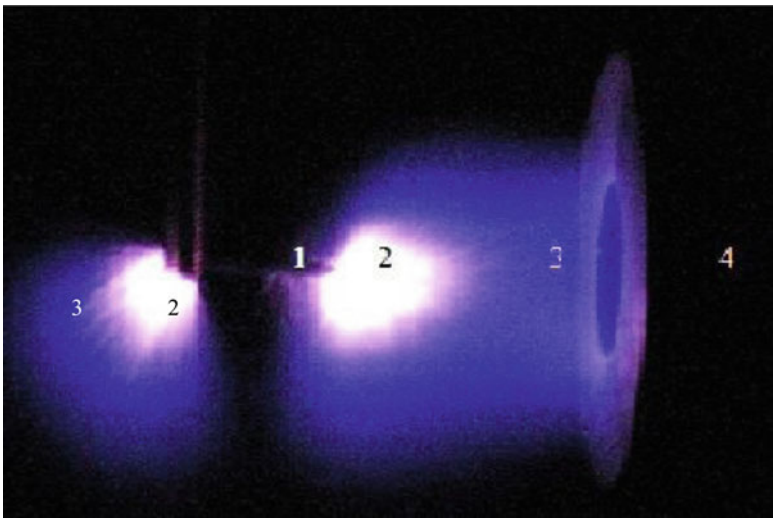

Fig. 6.16 Typical pictures of two plasma formations created by capacity-coupled high-frequency discharge in high-speed swirl flow. Charged longitudinal plasmoid with *blue halo* at $P_{st} \sim 300$ Torr, $V_{ax} \sim 90$ m/s. *1* needle HF electrode; *2* plasma kernel; *3* plasma halo; *4* nozzle

The high-frequency plasma generator had the following parameters:

Pulsed high-frequency power	$P_{HF} = 200$ W
Frequency	$F_{HF} = 1.2$ MHz; 13.6 MHz
Operation regime	Continuous, pulse repetitive
Modulation frequency	$F_M < 20$ kHz
Pulse duration	$T_i = 50$–500 μs

The typical picture of the free longitudinal vortex plasmoid created by the capacity-coupled high-frequency discharge in swirl high-speed airflow is shown in Fig. 6.16. One can see that this plasmoid consists of the bright plasma kernel and the blue plasma halo around it. The typical plasma halo diameter D_h exceeds the typical kernel diameter D_k by the factor $K = D_k/D_h = 2$–10. The value K depends on the initial pressure P_{st} and the initial flow velocity V_f.

The electrical potential of this plasma halo was measured by the electric high-voltage probe Tektronix P6018. The typical value of this electrical potential was about $\varphi \sim +(1\text{–}4)$ kV (Fig. 6.17). This value depends on the high-frequency power input P_{HF}, the pulse repetition frequency F_i, and the airflow velocity $V_f \sim V_{ax} \sim V_t$. The maximal value of $\varphi \sim +4$ kV is measured at the maximal high-frequency power input $P_{HF} \sim 800$ W, the maximal pulse repetition frequency $F_M \sim 10$ kHz, and the maximal airflow velocity $V_{ax} \sim V \sim 140$ m/s.

It is not clear why the measured halo potential is positive. From a conventional point of view, fast particles, that is, electrons, have to move from the kernel, so the potential of the halo has to be negative. However, it is not so. We plan to investigate this effect in future experiments.

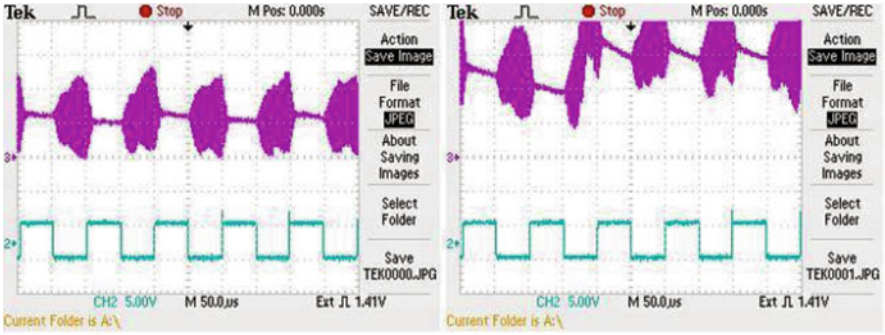

Fig. 6.17 Typical high-frequency plasmoid electric potential at different experimental conditions. SWT-1F. *Left*: Longitudinal charged high-frequency plasmoid with blue halo at $P_{st} \sim 300$ Torr, $V_{ax} \sim 90$ m/s. *Right*: Longitudinal charged high-frequency plasmoid with blue halo at $P_{st} \sim 300$ Torr, $V_{ax} \sim 140$ m/s. *Violet voltage signal*; *blue* command modulation signal

Mark that it is possible to create a DC power supply by this plasma–vortex converter. The main question is the efficiency of the plasma–vortex converter acting in this regime. We plan to study the converter physics in detail in future experiments. This study will probably help us to clarify the source of BL power supply.

6.10 Pressure Distribution in Swirl Flow at High-Frequency Plasma-On and Plasma-Off Conditions

The experimental results on temporal evolution of the static pressure inside the plasma kernel in high-speed swirl flow at plasma on and plasma off are shown in Fig. 6.18. One can see that there was considerable static pressure increase up to 20–50% (near its axis) at the high-frequency plasma-on. Note that the pressure jump signal was the difference between the stagnation pressure measured by the Pitot tube, and the static pressure measured inside the test section. So, the electric double layer created on the plasma kernel surface can play an important role in the pressure redistribution inside the kernel.

Therefore, it was revealed that the high-speed swirl flow parameters can be considerably changed by the capacity-coupled high-frequency discharge plasma. The obtained results may be used for flow control, lift control, advanced mixing, plasma aerodynamics, and plasma-assisted combustion of gas reagments.

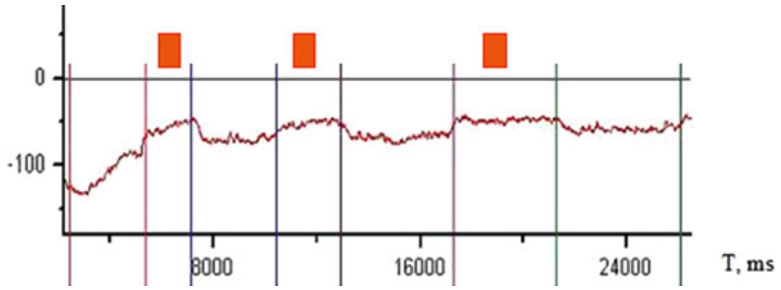

Fig. 6.18 Temporal dynamics of static pressure P_{st} (Torr) measured near swirl flow axis in setup SWT-1F at high-frequency plasma-on (below red rectangles) and plasma-off

6.11 Conclusions

This work is a continuation of Kapitsa's experiments on BL modeling (Kapitsa 1955; Kapitsa 1969). We repeated his experiments with the help of modern diagnostic instrumentation. His main experimental results were proved in our work. A number of new important data on the longitudinal vortex plasmoid creation and its physics have been obtained by us, namely:

1. A stable nonequilibrium heterogeneous longitudinal vortex plasmoid is created by a capacity-coupled high-frequency discharge in swirl flow. This longitudinal vortex plasmoid consists of a hot plasma kernel ($T_V \sim 3{,}200 \pm 400$ K, $T_R \sim 2{,}000$–$3{,}000$ K) and an extended warm plasma halo ($T_V \sim 3{,}200 \pm 400$ K, $T_R \sim 600$ K). This compact longitudinal vortex plasmoid is created by both the continuous high-frequency power pumping and the pulse repetitive high-frequency power pumping in swirl flow. Note that the stable longitudinal vortex plasmoid is created by the pulse repetitive high-frequency power pumping in swirl flow at high modulation frequency $F_M > F_M^* \sim 1$ kHz ($T_i = 0.5$ ms) only.
2. There is an energy exchange between the vibrational energy levels of the excited nitrogen molecules and the translation energy of these molecules in the longitudinal plasmoid (by the V-T relaxation process). This result is based on the analysis of the obtained optical spectra of the longitudinal vortex plasmoid luminescence at different swirl flow parameters, different high-frequency power settings, and different values of the initial pressure $P_{st} = 40$–760 Torr. Experimentally, it was impossible to realize this phenomenon in noble gas swirl flows (for example, in argon).
3. Vortex attenuation and its decay by the capacity-coupled high-frequency discharge plasma was found both in the duct and in the open air. The static pressure near the vortex axis increased up to 20–50% at the capacity-coupled

high-frequency discharge plasma-on. It is found that the pressure gradient was about zero near the vortex axis at plasma-on. So, there is a stationary immovable gas inside the central vortex region at plasma-on. The obtained results can be used for flow control, lift control, advanced mixing, plasma aerodynamics, and plasma-assisted combustion.

4. Aerodynamic properties of the longitudinal vortex plasmoid were studied. This longitudinal vortex plasmoid can move against a wind as can do a real BL. The typical velocity of the stable longitudinal vortex plasmoid is about $V_p \sim 30$–40 m/s, and it does not depend on the oncoming flow velocity. The aerodynamic drag of this vortex longitudinal vortex plasmoid should be very small (as a result of the symmetrical streamlines around it). It is well known that BL also has a very small drag. It can be important for aerodynamic applications and clarification of the unusual aerodynamic properties of a real BL.
5. We confirmed results of Kapitsa measurements of MW plasmoid UV radiation and discovered that the longitudinal vortex plasmoid can emit intensive UV radiation.
6. Measurements of the power budget in the longitudinal vortex plasmoid were made. An extra power release proved to be about 400% as measured inside the longitudinal vortex plasmoid. It can be connected with complex processes of cluster particle creation and destruction in vortex flows.
7. The plasma–gas dynamic power converter was created and studied in this work for the first time. We plan to study its physics in detail in future experiments. This study should help us to clarify the nature of the power supply of BL energy.

In conclusion, one can say the model of the plasma vortex created with the help of coupled-capacity high-frequency discharge proved to be fruitful for modeling of many BL features and understanding its physics.

Acknowledgments The author acknowledges I. Moralev for help in carrying out the experiments and Dr. V. Bychkov and Dr. A. Nikitin for fruitful discussions of this work.

References

Avaramenko R, Bychkov V, Klimov A, Sinkevich O (eds) (1994) Ball lightning in the laboratory. Khimia, Moscow

Barry JD (1980) Ball lightning and bead lightning. Plenum Press, New York

BityurinV KA, Moralev I, Tolkunov B (2010) Interaction of swirl flow with plasma created by capacity coupled RF discharge. High Temp Phys 58(1):151–156

Bychkov V, Bychkov D (2006) Ball lightning as unipolarly charged object with hot surface. 9th International Symposium on Ball Lightning, (ISBL-06), Eindhoven, The Netherlands, pp 26–32

Bychkov V, Nikitin A, Dijkhuis G (2010) Modern state of ball lightning investigations. In: Bychkov V, Golubkov G, Nikitin A (eds) Atmosphere and ionosphere: dynamics, processes and monitoring. Springer, Dordrecht/Heidelberg, pp 201–373

Childress D (1993) Fantastic invention of Nicola Tesla. Adventures Unlimited Press, Stelle

Grigorjev AI (2006) Ball lightning. YarGU Publishers, Yaroslavl

Kapitsa PL (1955) On nature of ball lightning. Doklady AN SSSR 101:245–248
Kapitsa PL (1969) Free plasma filament in high frequency field at high pressure. Zhur Exp Teoret Fiz 57(6):1801–1866
Klimov AI (2004) Calorimetric measurements in plasma vortex. In: Proceedings of 12th conference on cold nuclear transmutation and ball lightning. Dagomys, 19–26 Sept., Moscow, pp 246–225
Klimov A (2009) Strategy of plasma-aerodynamics researches today. In: Proceedings 3rd European conference for aerospace Science, Paris, p 16
Klimov A, Moralev I (2008) Longitudinal vortex plasmoid created by capacity HF discharge. In: AIAA Paper, Proceedings of 46th AIAA conference, Reno, NV, p 11
Klimov A, Bityurin V, Moralev I, Tolkunov B, Minko A (2009a) Study of a longitudinal plasmoid created by capacity coupled HF discharge in vortex airflow. In: AIAA paper 2009-1046. 47th AIAA aerospace sciences meeting & exhibit, Orlando, FL, p 14
Klimov A, Bityurin V, Moralev I, Tolkunov B, Kutlaliev V (2009b) Plasma assisted combustion of heterogeneous fuel in high-speed airflow. In: AIAA paper 2009-1046, 47th AIAA aerospace sciences meeting including the New Horizons forum and aerospace exposition 5–8 Jan 2009, Orlando, FL, p 11
Klimov A, Molevich N, Moralev I, Zavershinsky I (2010) Longitudinal plasma vortex created by transverse electric discharge. High Temp Phys 58(1):157–161
Klimov A, Bityurin V, Moralev I, Tolkunov B, Polyakov L (2011) Study of a longitudinal plasmoid created by capacity coupled HF discharge in vortex airflow. AIAA paper 2011-1272, 49th AIAA aerospace sciences meeting, 4–7 Jan 2011, Orlando, FL, p 18
Mirabo L, Nagamatsu H, Minucci M, Toro P, Pereira A (2001) Investigation of a laser-supported directed-energy "Air Spike" in Mach 6.2 air flow, AIAA Paper 2001-0641, 39th AIAA aerospace sciences meeting, 8–11 Jan 2011, Reno, NV, p 10
Tar D (2010) Ball lightning created by Thunder Shock Wave. In: Proceedings of 11th International Symposium on Ball Lightning (ISBL-10) and 4th International Symposium on Unconventional Plasmas (ISUP-10), Kaliningrad, Russia, pp 168–173
Vlasov AN (2006) Experimental modeling of ball lightning on a basis of electric explosion of a wire spiral rolled in torus. In: Materials of 13-th Russian conference on cold nuclei transmutation of chemical elements and ball lightning 2005. Dagomys, City of Sochi, Moscow, pp 290–297

About the Editors

Vladimir L. Bychkov is a leading researcher at the Department of Physics at Lomonosov Moscow State University. He has 40 years of experience in plasma physics studies, and the physics of elementary processes, gas discharges, plasma chemistry, and ball lightning.

Gennady V. Golubkov is a leading scientist at the Semenov Institute of Chemical Physics of the Russian Academy of Sciences. He has 45 years of experience in quantum scattering theory, the theory of atomic and molecular processes, and of low-temperature plasma.

Anatoly I. Nikitin is a principal researcher at the Russian Academy of Sciences Institute for Energy Problems of Chemical Physics in Moscow. He has 50 years of experience in quantum electronics research, chemical physics, plasma physics, plasma chemistry, and ball lightning.

V. Bychkov et al. (eds.), *The Atmosphere and Ionosphere*, Physics of Earth and Space Environments, DOI 10.1007/978-94-007-2914-8,

Index

V. Bychkov et al. (eds.), *The Atmosphere and Ionosphere*, Physics of Earth and Space Environments, DOI 10.1007/978-94-007-2914-8,